Study and control of three dimensional flow separations in a high pressure compressor stator blade row by boundary layer aspiration

Ankit Sachdeva

ÉCOLE CENTRALE DE LYON

N°ordre: 2010-12 Année 2010

THÈSE

en vue d'obtenir le titre de

DOCTEUR DE L'ÉCOLE CENTRALE DE LYON

ÉCOLE DOCTORALE M.É.G.A.

MÉCANIQUE, ÉNÉRGETIQUE, GÉNIE CIVILE ET ACOUSTIQUE

Par

Ankit SACHDEVA

STUDY AND CONTROL OF THREE DIMENSIONAL FLOW SEPARATIONS IN A HIGH PRESSURE COMPRESSOR STATOR BLADE ROW BY BOUNDARY LAYER ASPIRATION

SOUTENUE LE 21 JUIN 2010 À L'ÉCOLE CENTRALE DE LYON

- JURY -

L. JACQUIN	Directeur du DAFE, ONERA, Meudon	Président
G.GEROLYMOS	Professeur, UPMC, Paris	Rapporteur
G.BOIS	Professeur, ENSAM, Villeneuve d'Ascq	Rapporteur
F. LEBOEUF	Professeur, EC-Lyon, Ecully	Directeur de thèse
T. OBRECHT	Ingénieur, SNECMA, Villaroche	Examinateur
L. CASTILLON	Ingénieur, ONERA, Meudon	Examinateur

ACKNOWLEDGEMENTS

I express my sincere gratitude to the director of my thesis Professor Francis LEBOEUF for his kind support and continued guidance throughout the work of this thesis. An enlightening teacher and a very patient person, he has been like a guiding lighthouse in all the times.

I thank M. Armel TOUYERAS, M. Thierry OBRECHT and M. Michel DUMAS for their support and supervision over the entire duration of this work. Their experience and management skills have been crucial to meet the objectives of this work.

I extend my gratitude for our external partners such as ONERA, EPFL and LMFA for their contributions in making this thesis and project meet its objectives. I specially thank Lionel CASTILLON of ONERA for his support in advanced numerical modelling and computations. I thank M. Elia COLOMBO and M. François BARIO for their discussions involving their work on experimental setup and measurements.

I thank the secretary of our department at Snecma Mrs. Marie Claude CHEVALIER for her tireless contribution in managing the official work of this thesis such as travelling and lodging on various occasions.

Last but not the least; I thank all the colleagues of the high pressure compressor team at Snecma for their support and company during my stay at Snecma.

NOMENCLATURE

BLADE GEOMETRY NOTATIONS

β	Blade metal angle
c	Blade chord
z,H	Blade span
s	Blade pitch
AR	Blade aspect ratio (span/chord)
σ	Blade solidity (chord/pitch)
λ	Blade stagger angle
ζ	Blade camber angle

BOUNDARY LAYER NOTATIONS

$\overline{\delta}$	Boundary layer thickness
δ^*	Displacement thickness
$\overline{\theta}$	Momentum thickness

FLOW TOPOLOGY NOTATIONS

N	Node
F	Focus, Spiral node
S	Saddle point
ℓ	Separation line
τ	Friction vector

NON-DIMENSIONAL NOTATIONS

DF	Leiblein's Diffusion factor
DP	Diffusion parameter
Ma	Mach number
SI	Stall Indicator
Re	Reynolds number

GREEK SYMBOLS

ρ	Flow density
Ω	Vorticity
∇	Divergence operator
Ψ	Zweiffel loading coefficient
$\Delta\beta$	Boundary layer turning due to rotating wall
ϖ	Total pressure loss coefficient
η	Efficiency
α	Flow angle
δ	Flow deviation
γ	Ratio of specific heats
ε	Epsilon (rate of dissipation of turbulent kinetic energy)
μ	Coefficient of dynamic viscosity

υ	Coefficient of kinematic viscosity

ABBREVIATIONS

2D	Two dimensional
3D	Three dimensional
BLS	Boundary layer suction
CAD	Computer Aided Design
CFD	Computational Fluid Dynamics
DES	Detached Eddy Simulations
grad	gradient
HPC	High Pressure Compressor
LE	Leading Edge
LES	Large Eddy Simulations
OT	Off take (device to bleed air from blade passage)
PS	Pressure surface
P_S	Static Pressure
P_T	Total pressure
PVD	Prescribed velocity distribution
RANS	Reynolds averaged Navier Stokes
rot	rotational operator
SS	Suction surface
TE	Trailing edge
VG	Vortex generator

MISCELLANEOUS

u_o, V	Freestream / inviscid velocity
Cq	Aspiration/suction coefficient
y^+	Wall function
R	Universal gas constant
K	Turbulent kinetic energy
L	Characteristic length (m)
E(K)	Spectrum of turbulence

SUBSCRIPTS

1,2	Upstream, Downstream
abs	absolute
0	inviscid local condition
x	axial direction
θ	circumferential direction
r	radial direction
t	turbulent

ABSTRACT

The performance of the compression system of a gas turbine engine is limited for a large part by the three-dimensional separations occurring in the high pressure compressors. The effects of flow separation are more important in the endwall regions where the fluid tends to decelerate and accumulate in regions of low momentum. The theme of this research work is to implement boundary layer aspiration to control flow separations in high pressure compressors. This is achieved by implementing aspiration devices on the endwall and blade profile to judiciously remove low energy fluid in the boundary layers that enables higher pressure rise per stage. This thesis is a joint scientific work associating Ecole Centrale de Lyon (ECL), Ecole Polytechnique Federale de Lausanne (EPFL) and ONERA. The European Commission under the frame of the programme NEWAC and the enterprise SNECMA has financed this research work.

The test case is a stator blade row designed to operate with transonic inlet conditions. Three-dimensional steady state RANS computational studies are done to define the operating range of the cascade with emphasis on the study of blade-to-blade flow topologies to understand the formation and progression of the corner separation on the hub wall with increasing inlet incidences. Boundary layer aspiration is implemented on the hub wall to control the three-dimensional flow separations to improve the pressure rise and the operating range. The aspiration strategy is sensitive to the aspirated massflow; lower aspirated flow rate results in complex flow separation topologies with deteriorated performance, while higher aspirated flow rate is found to suppress the corner separation and improve the diffusion capability except at the highest incidence point. The analysis of flow topologies shows the recirculation of flow between the aspiration cavity and the blade passage; a highly complex three-dimensional flow phenomena that influences the blade performance. The study of flow topologies is instrumental in developing rationales for the implementation of flow control.

This aspiration strategy is studied experimentally at EPFL where aspiration has been implemented on the hub wall. A new set of numerical studies done with inlet conditions measured from the test bench associated with rational hypothesis concludes this task with reasonable agreement between the experiments and numerical simulation. In particular, the hub corner separation is predicted well by CFD.

Computational studies are done to implement aspiration on the blade profile to improve the diffusion capability of the blades; various sensitivity parameters such as aspiration slot locations, aspirated flow rate are studied and a configuration is finalised for the experiments to be followed. Some studies are performed with smaller and multiple slots on the blade profile. The results show the merit of applying localised flow control on the critical points associated with flow separation demonstrating the scope to achieve higher levels of performance with lower aspirated flow rates.

Keywords: High pressure compressors, three dimensional flow separations, boundary layer aspiration, flow topologies.

RÉSUMÉ

La performance du système de compression des turbomachines est limitée en grande partie par les décollements tridimensionnels; ils sont plus importants au niveau des parois internes où le fluide a tendance à décélérer dans les zones de faible impulsion. Ce travail de recherche met en œuvre l'aspiration de la couche limite afin de maîtriser les décollements dans les compresseurs. Ceci est obtenu par la mise en place de dispositifs d'aspiration sur le moyeu et le profil de l'aube afin de prélever judicieusement le fluide à faible énergie dans les couches limites et ainsi augmenter le taux de compression par étage. Cette thèse est issue de travaux de recherche réalisés conjointement avec l'Ecole Centrale de Lyon (ECL), l'Ecole Polytechnique Fédérale de Lausanne (EPFL) et l'ONERA. Ces travaux ont été financés par la Commission Européenne dans le cadre du programme NEWAC et l'entreprise SNECMA.

Le cas test est une grille annulaire de redresseur conçu pour fonctionner avec des conditions d'entrée transsoniques. Des calculs stationnaires tridimensionnels RANS sont réalisés afin de définir la plage de fonctionnement de la grille en mettant l'accent sur l'étude des topologies d'écoulement aube-a-aube afin de comprendre la formation et la progression du décollement de coin au moyeu avec des incidences d'entrée croissantes. L'aspiration est réalisée sur le moyeu par une fente afin de mieux maîtriser les décollements tridimensionnels et ainsi accroître le taux de compression et la plage de fonctionnement. L'aspiration est sensible au débit massique aspiré; de faibles débits aspirés conduisent à des topologies d'écoulements complexes avec des performances dégradées, tandis que des débits aspirés plus élevés permettent de supprimer le décollement de coin et d'améliorer la performance à l'exception du point de plus forte incidence. L'analyse des topologies montre une recirculation de l'écoulement entre la cavité d'aspiration et la veine. Ce phénomène d'écoulement tridimensionnel très complexe influe sur la performance des aubages. Ainsi l'étude des topologies permet d'orienter le choix dans l'implémentation de systèmes conduisant à une meilleure maîtrise des écoulements.

Cette stratégie d'aspiration est étudiée expérimentalement à l'EPFL où l'aspiration a été mise en œuvre au moyeu. Une nouvelle série d'études numériques réalisées avec les conditions d'entrée mesurées sur le banc d'essais associées à des hypothèses de calcul conduisent à une assez bonne concordance entre les mesures d'essais et la simulation numérique. En particulier, le décollement de coin est bien prédit par les calculs numériques.

Des études théoriques ont été menées afin d'appliquer l'aspiration sur le profil de la pale et ainsi améliorer la capacité de diffusion des pales. Des études de sensibilité ont été réalisées sur divers paramètres tels que le positionnement des fentes d'aspiration et le débit aspiré qui ont conduit au choix d'une configuration finale retenue pour les essais. Des études réalisées avec de multiples et plus petites fentes d'aspiration sur le profil de la pale montrent le bien-fondé de l'application d'un contrôle d'écoulement localisé sur les points critiques associés à des décollements. Ceci montre l'enjeu d'atteindre des niveaux de performance supérieurs avec des débits aspirés plus faibles.

Mots clés: Compresseurs à haute pression, décollements tridimensionnels, aspiration de la couche limite, topologie d'écoulements

INTRODUCTION

ENVIRONMENTAL CONTEXT AND EUROPEAN PROGRAM

Global air traffic is forecast to grow at an average annual rate of around 5% in the next 20 years. This high level of growth makes the need to address the environmental penalties of air traffic all the more urgent. As a result the aviation industry faces a massive challenge to satisfy this demand for increased air travel in an economic and safe way. Therefore alternative engine architectures with new technologies for the components need to be researched in order to achieve a significant reduction in pollution levels.

The Advisory Council of Aeronautical Research in Europe (ACARE) identified the research objectives for the gas turbine industry for 2020: a 20% reduction in CO_2 emissions per passenger-kilometre, 10 dB noise reductions per certification point and 80% reduction in NO_X emissions. The existing technology programmes have identified some innovative concepts and new technologies with a potential to contribute to these goals.

NEWAC is a European-level programme in which major European engine manufacturers, assisted by universities, and research institutes focus on new core engine concepts. NEWAC will develop and validate novel core engine technologies to further close the gap between the current emissions and the ACARE targets. One of the core concepts being studied in this programme is the Flow Controlled Core.

The Flow Controlled Core approach focuses on the compressor module by developing and integrating innovative technologies, providing a significant increase of efficiency and stall margin in the highly loaded high-pressure compressor. The strategy is based on the implementation of innovative concepts able of 'local control' of the compressor flow field. The optimised design of the compressor in association with the integration of these aero-oriented technologies leads to a global benefit. More precisely, these new and significant progresses in the field of highly loaded compressors will be made possible through the combination of several approaches. Implementation of breakthrough technologies is expected to control the flow locally, either near the operating line or near the stall line. When relevant, these technologies are integrated in an adapted and suited advanced aerodynamic design for both improved efficiency and stall margin.

This thesis studies the application of boundary layer aspiration on the hub wall and the blade profiles of a high pressure compressor stator cascade to increase blade diffusion capabilities by control of flow separations; this is provided through local modification of compressor flow field via aspiration devices to reduce the total pressure losses of a stator blade. This approach is one of the many approaches being investigated under the flow controlled core concept.

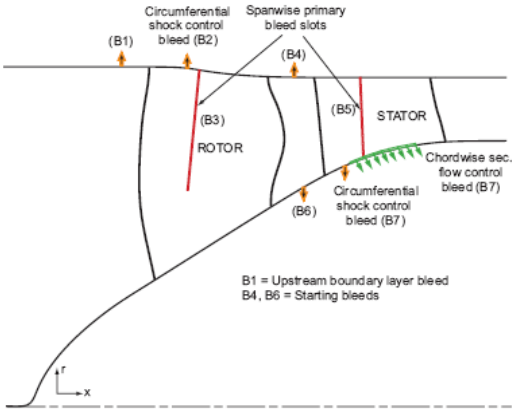

Fig A: Flow path of an aspirated compressor (Merchant et al. [11])

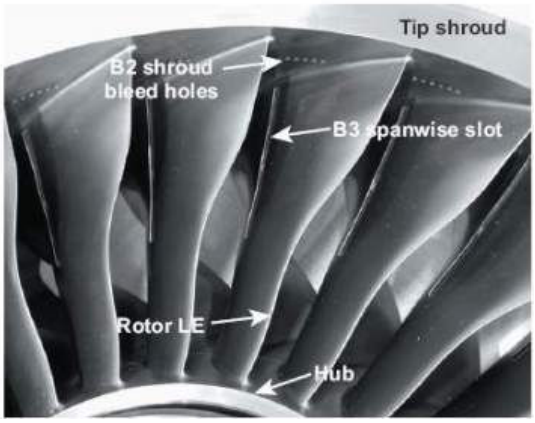

Fig B: Aspirated compressor rotor (Merchant et al. [11])

The present development for higher efficiency and thus higher turbine inlet temperatures and overall pressure ratios is limited by the overall machine length due to the mechanical integrity of the apparatus. Therefore, an overall increase in pressure ratio is only possible by increasing the stage pressure ratio in the compressor. An increased stage pressure ratio is also beneficial for jet engines as the reduction of the overall length and of the number of compressor stages will reduce as well the overall length and the weight of the compressor, leading to an increased thrust/weight ratio of the compressor. Presently the length of the compression system takes 50-60% of the overall machine length and 35-40% of the engine weight. The compressions system accounts for 30% of the total maintenance costs. (Steffens and Schaeffler 2002, extracted from Hubrich et al. [9])

Increasing the blade loading is the key to increase the total pressure rise capability of a compressor stage. Modern compressor blades diffuse the flow efficiently over the middle sixty to eighty percent of the span, and the endwall and corner regions are thus keys to aerodynamic blockage, loss production and compressor stability. Principally, the viscous effects in the blade passage and the endwalls hinder the pressure rise capability of the blades.

ORGANISATION OF THE REPORT

The report is divided into seven chapters; the contents of each chapter are briefly described in this section to provide a comprehensive overview of the contents of this report to the reader.

The **first chapter** presents the fundamental notions of boundary layer characteristics along with a brief introduction to the phenomenon of two-dimensional and three-dimensional boundary layer separation on the walls with relation to viscous effects. Further, we account for the effects of viscosity in gas turbine compressors, the origin of vortices in turbomachines due to various factors such as curvature of the wall, variation of blade channel section and viscosity.

The importance of analysis of vortices in turbomachines is expressed as this thesis principally studies the vortices, their influence and subsequently the control of vortices by flow control. The principal types of vortices existing commonly in turbomachines are described. These are complex three-dimensional phenomena and finally the influence of losses resulting from these phenomena is documented at the end of the chapter.

The **second chapter** is dedicated to the theoretical understanding of flow topologies related to boundary layer separation on the walls. The flow topologies are studied by the traces of skin friction lines on the walls and they form certain patterns when the flow separates and reattaches on the wall. These patterns, called critical points, are described. We study the existence of critical points that provide comprehensive description of flow behaviour on the walls.

Next, we describe the topological rules of closed separation patterns that have been well documented by several authors such as Délery [30], Tobak et Peake [31] and others. Recent developments made by Surana et al [20, 32] concerning the exact mathematical criterion of flow separation are discussed and subsequently applied on one of the study cases in chapter 4. A brief description of open separations is presented for general information to the reader. A new criterion for hub corner stall developed by Lei et al [14] is presented, the criterion establishes two quantities, namely Stall Indicator and Diffusion parameter based on the difference in relative loading of the flow in an inviscid region (blade mid-span) and in a zone under the influence of flow separation (close to the hub wall).

The **third chapter** introduces the concept of flow control for local modification of flow to change the flow behaviour on a larger scale. A general classification of flow control methods based on the location of application, energy expenditure and loop control is presented. Bibliographic review of application of flow control methods specific to gas turbine compressors and fans carried out by various researchers is discussed along with their respective analysis and conclusions.

The **fourth chapter** introduces the research work of this thesis. This chapter describes the design of the baseline stator blade row, computational methodology such as mesh, turbulence modelling and solver physics. The inlet and outlet boundary conditions along with the mesh planes are presented. The results obtained from CFD computations of baseline stator blade row are analysed and discussed in detail. The operating range of the blade row is determined to be limited by the presence of the progressive hub corner separation and the study of flow topologies is presented in detail. Recommendations are proposed for the possible aspiration strategies.

The **fifth chapter** presents the aspiration strategy employed on the hub wall via a slot. The numerical modelling of the aspiration cavity with chimera mesh technique is described. The results obtained from CFD studies are analysed, the sensitivity of suction flow rate in the aspiration strategy is discussed along with the advantages and limitations of the present aspiration strategy on the hub wall. The study of flow topologies is presented in detail to highlight the phenomenon of flow circulation between the aspiration cavity and the blade passage. The Stall indicator and Diffusion parameter developed by Lei et al [14] are plotted for all the cases studied. The values of Diffusion parameter obtained are found to be coherent with the critical limit established by the authors.

Two special parametric studies are presented, one with higher suction flow rate to control hub corner separation and the other one with an extension of aspiration slot closer to the leading edge to study the influence of aspirating critical point responsible for flow separation. The results and conclusions are presented at the end of the chapter.

The **sixth chapter** presents the experimental setup of the tests (from the thesis of E. Colombo at EPFL) for baseline stator blade row without and with hub aspiration. The experimental measurements are presented and a new set of CFD computations is done with the experimental conditions to compare the results from experiments and CFD. The computations are performed with some simplifying hypothesis in turbulence modelling and a good correlation is obtained between numerical and experimental results for most of the cases studied. The hub corner separation is found to be well predicted by CFD.

The **seventh** and the **final chapter** of the thesis is a numerical study of aspiration on the hub wall and blade suction surface. Various blade profile aspiration strategies are presented, the results from the CFD computations are analysed to study the influence of blade profile aspiration on the performance of the blade row.

TABLE OF CONTENTS

1. BOUNDARY LAYER SEPARATION

1.1 FUNDAMENTAL NOTIONS OF BOUNDARY LAYER

1.1.1 BOUNDARY LAYER

All solid surfaces interact with a viscous fluid flow because of the no-slip condition, a physical requirement that the fluid and solid have equal velocities at their interface. The portion of a fluid flow, near a solid surface, where shear stresses are significant is called the boundary layer. Boundary layer is dependent upon the Reynolds number. Because the velocity component along the wall is much higher than in the direction normal to the wall, then the pressure gradient in direction normal to the wall is very small. For this reason, the boundary layer is mainly driven by the pressure gradient generated by the inviscid flow at the edge of the boundary layer. This situation remains valid on a curved wall, such as on blade walls. However, it fails close to separation or reattachment of boundary layer as will be shown thereafter.

1.1.2 BOUNDARY LAYER THICKNESS

The boundary layer thickness is used for a thickness $\overline{\delta}$ beyond which the velocity is essentially the freestream or inviscid velocity u_o. This is customarily defined as the distance from the wall to the point where

$$u(y) = 0.99u_o \tag{1.1}$$

or any similar definition compatible with measurement capabilities.

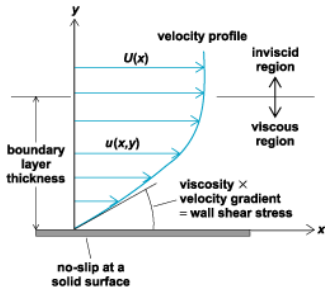

Fig 1.1: Boundary layer profile

1.1.3 DISPLACEMENT THICKNESS

The displacement thickness, δ^*, is the distance by which a surface would have to be moved parallel to itself towards the reference plane in an inviscid fluid stream of velocity u_0 to give the same mass flow as occurs between the surface and the reference plane in a real fluid.

In practical aerodynamics, the displacement thickness essentially modifies the shape of a body immersed in a fluid to allow an inviscid solution. It is commonly used in aerodynamics to overcome the difficulty inherent in the fact that the fluid velocity in the boundary layer approaches asymptotically to the free stream value as distance from the wall increases at any given location. The mathematical definition of the displacement thickness for compressible flow is given by:

$$\delta^* = \int_0^\infty \left(1 - \frac{\rho(y)u(y)}{\rho_0 u_0}\right) dy \tag{1.2}$$

1.1.4 MOMENTUM THICKNESS

The momentum thickness, $\bar{\theta}$, is the distance by which a surface would have to be moved parallel to itself towards the reference plane in an inviscid fluid stream of velocity u_0 to give the same total momentum as exists between the surface and the reference plane in a real fluid. The momentum thickness for an compressible flow is given by:

$$\bar{\theta} = \int_0^\infty \frac{\rho(y)u(y)}{\rho_0 u_0}\left(1 - \frac{u(y)}{u_0}\right) dy \tag{1.3}$$

where the vertical coordinate y is increasing upward from the boundary and u_o is the velocity in the ideal flow of the free stream. Compared to inviscid flow, this would be the distance that the surface would be displaced for the flow to have the same momentum. The influence of fluid viscosity creates a wall shear stress, τ_w, which extracts momentum from the mean flow. The boundary layer can be considered to possess a total momentum flux deficit due to frictional dissipation as expressed below:

$$\int_0^\infty \rho(y)u(y)(u_o - u(y))\, dy = \rho_0 u_0^2 \bar{\theta} \tag{1.4}$$

Integrating for the boundary layer the momentum equation written along x, in the thickness δ, we get the so-called Von Karman equation written here for a compressible flow : it shows that the wall shear stress τ_w is related to the evolution of the momentum thickness θ along the direction x:

$$\frac{C_f}{2} = \frac{\partial \bar{\theta}}{\partial x} + \delta^* \left(1 + \frac{2 - Ma^2}{H}\right) \frac{1}{u_0} \frac{\partial u_0}{\partial x} \tag{1.5}$$

with the friction coefficient defined as $C_f = \dfrac{\tau_w}{\frac{1}{2}\rho_0 u_0^2}$ (1.6)

and the wall shear stress $\tau_w = \left(\mu \dfrac{\partial u}{\partial y}\right)_{y=0}$ (1.7)

1.2 TWO DIMENSIONAL BOUNDARY LAYER SEPARATION

Fluid particles in a boundary layer are slowed down by wall friction. Owing to the presence of an adverse pressure gradient, the momentum of these particles will both be reduced by wall shear and the pressure gradient. In an adverse pressure gradient region, the remaining momentum may be too small to overcome the pressure rise and the motion of near wall fluid particles is eventually arrested or even directed towards the backward direction. At some point (or line), the viscous layer may then depart or break away from the solid surface. The surface streamline nearest to the wall leaves the body at this point, and the boundary layer is said to separate. At separation, the viscous flow region next to the wall abruptly thickens; the normal velocity component increases and the boundary layer approximations are no longer valid; the pressure direction normal to the wall is no more negligible. This is a classical mean time averaged explanation of two dimensional flow separation.

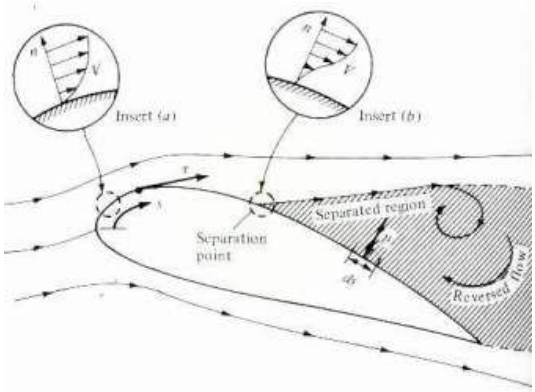

Fig 1.2: Two dimensional separation on an airfoil, Inserts (a) and (b) show the velocity profile at inlet and separation point respectively (Anderson [34])

1.3 THREE DIMENSIONAL BOUNDARY LAYER SEPARATION

Separations in three-dimensional flows do not behave in the simple way that is associated with those in two-dimensional cases where the separation from the surface is identified at a point where the shear stress vanishes by the inception of reversed flow. Three-dimensional separation can occur with no reverse flow and non zero friction and there is a wide variety of flows where three-dimensional separation appears nearly independent of the Reynolds number as opposed to the two-dimensional separation as pointed by Délery [30].

Three-dimensional separations are characterised by the convergence or divergence of the streamlines parallel to the surface and the curvature of streamlines under the influence of lateral pressure gradient.

In two dimensional flows the boundary layer separates from boundary points where the wall shear vanishes and admits a negative gradient; whereas three-dimensional flows tend to separate along lines.

In three dimensions, integral curves of the wall-shear vector field (also known as wall-shear lines or limiting streamlines) are the only viable candidates for separation lines, because they mark the intersection of two-dimensional stream surfaces with the boundary. More information will be given thereafter in the description of flow topology in the case of three-dimensional separation.

1.4 VISCOUS EFFECTS IN COMPRESSORS

In most compressor flows, the existence of shear stress is essential to overcome the adverse pressure gradients without separation. Generally, the stability of compressor improves, as turbulent stresses get stronger relative to laminar viscous stress with the increase in Reynolds number. Viscous effects have three major influences on flow in the compressors:

1) Viscous effects put a limit on the pressure rise that can be produced. Attempts to exceed this limit lead to local flow instability (unsteady fluctuations in flow behaviour resulting from three dimensional flow separations) that may eventually cause global flow instability involving the whole machine, such as in rotating stall or surge.
2) Viscous effects lead to blockage, an effective reduction in the flow area as a consequence of the growth of the boundary layer thickness δ. It affects the work input, particularly for axial compressors and can have enormous effects on mass flow capacity of the machine.
3) Viscous effects in shear layer are ultimately responsible for the main parts of the loss generation apart from the losses in the shock waves, or in the core of vortices embedded in the flow.

The general features of viscous flow in an axial compressor rotor stage are shown in the figure 1.3 below:

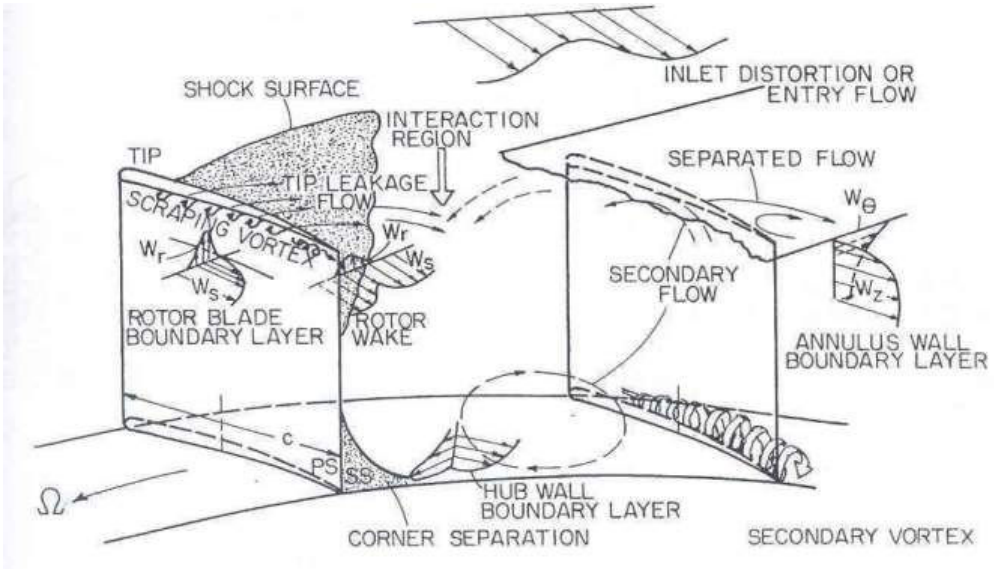

Fig 1.3: Nature of flow in an axial compressor rotor stage (Lakshminarayana [18])

Lakshminarayana [18] documents the special problems of viscous flows in compressors as follows:

- There are adverse pressure gradients in the flow both on the blades and the endwalls. The flow on the blades is often taken close to or beyond the point of separation and in this respect is like a heavily loaded wing. The viscous effects can be dominant on the endwalls in the corner regions between the blade and the endwall. Under certain conditions the corners may become the sources of very strong flow separations and thick boundary layers.

- The turbulence levels are very high in the freestream, typically of the order or greater that 5%. High levels of turbulence are thought to be most significant for their effect in transition from laminar to turbulent flows.

- The flows are highly unsteady because of the rotation of blade rows past one another. The unsteadiness takes the form of potential interactions between pressure fields and also wake and vortices interactions with downstream blades, the latter being particularly important for transition. As opposed to turbulence, this unsteadiness has a deterministic nature as it is related to the rotation of the machine.

- Owing to the energy transfer between the rotors and the flow, or to the flow redirection in stators, there are large gradients in every direction including along the span of axial blades. As a result, the static pressure is not constant across the viscous region; however, the pressure gradient in the direction normal to the wall is still imposed by the flow at the edge of the boundary layer thickness δ.

- For blades which are long with respect to the displacement thickness of the endwall boundary layers, it may be possible to treat the flow as two dimensional near the middle of the blade, since the variation in the blade shape is normally relatively small; near the endwalls and for low aspect ratio blades, there may be no region for which the two dimensional approximation is realistic.

- Dominant regions in terms of limiting the pressure rise, creating blockage and generating losses are the corners formed between blade surfaces and endwalls, mainly those on the suction surface of the blade. These are highly three dimensional flows with regions of separation; the flow is further complicated by the presence of tip clearance and by skewed non-uniform inlet flow.

1.5 ORIGIN OF VORTICES IN TURBOMACHINES

The three-dimensional flows in turbomachines are a complex set of interactions between the coupling of pressure gradients and the viscous forces. This coupling yields vortices in turbomachines that are important loss generating mechanisms in compressors and turbines. A brief analysis is presented here on the coupling of pressure gradients and the viscous forces in the turbomachines.

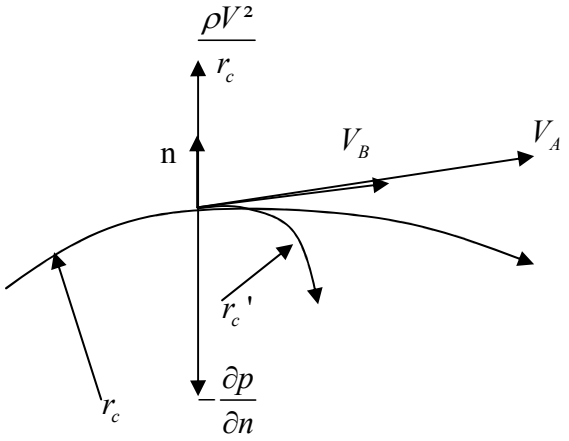

Fig 1.4: Motion of fluid particles on a curved trajectory (ECL study course [35])

Let A be a particle transported along a curved trajectory with radius r_c. Equilibrium exists between the pressure force $-\partial P/\partial n$ and the centrifugal force. Let a particle B introduced at A with a velocity vector tangent to the trajectory of particle A, but with a lower velocity modulus. Assume also the pressure field is not disturbed by the particle B, so that the pressure force imposed on B is the same as the one on A. Consequently B is transported towards the centre of curvature of the streamline A as its centrifugal force is lower that the one on A.

$$\left(\frac{\partial p}{\partial n}\right)_A = \left(\frac{\partial p}{\partial n}\right)_B \Rightarrow \left(\frac{\rho V^2}{r_c}\right)_A = \left(\frac{\rho V^2}{r_c}\right)_B \tag{1.8}$$

$$V_A^2 > V_B^2 \Rightarrow r_{cA} > r_{cB} \tag{1.9}$$

This simple model may be used to represent the transport of the endwall boundary layer towards the suction side corner in a turbomachinery blade passage. It is well known that under the influence of circumferential pressure gradient $\partial P/\partial \theta$, the endwall boundary layers (hub/casing) displace to the suction side of the blade.

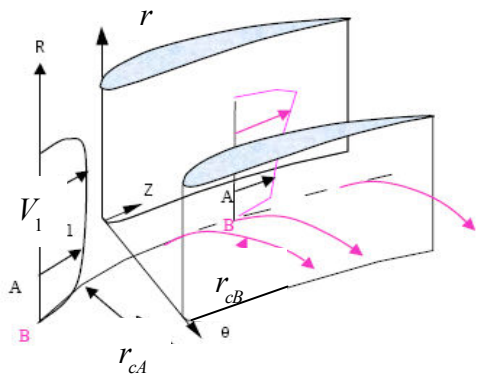

Fig 1.5: Motion of particles in a blade passage of a turbomachine (ECL study course [35])

Consider a simple model of a compressor blade row as sketched in fig 1.5. First of all, note that the radial pressure gradient is much smaller than the circumferential pressure gradient ($R\,\partial P/\partial R << \partial P/\partial \theta$). As a consequence, the circumferential pressure gradients experienced by the points A and B are roughly the same $(\partial P/\partial \theta)_A \approx (\partial P/\partial \theta)_B$; then as the velocity of the particle A in freestream is higher than those for the particle B close to the endwall $V_A > V_B$, so is the radius of curvature of A trajectory compared to B trajectory. Hence, under the influence of the tangential pressure gradient, the viscous layer slips towards the hub and casing endwalls.

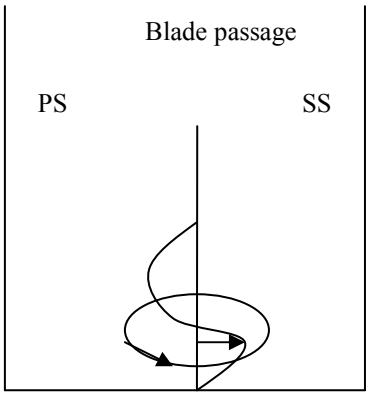

Fig 1.6: Formation of vortex in the blade channel of a turbomachine (ECL study course [35])

The viscous layer of the hub wall displaces then towards the suction side and tends then climbs on this wall towards the blade mid-span. The conservation of mass imposes a returning flow towards the pressure side outside of the viscous layer. The velocity of this flow is low only close to the wall. This creates a vortex motion in the blade-to-blade passage of the turbomachine.

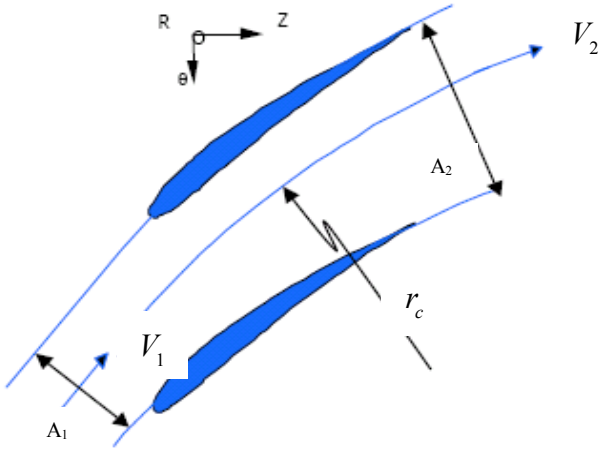

Fig 1.7: A diffusing blade channel of a turbomachine (ECL study course [35])

A better description of vector transport induced by the interaction of the pressure gradient and the velocity gradients associated to the endwall layer can be provided by the transport of vorticity. There are some important effects to consider:

1) The pressure gradient $\partial P/\partial n$ or $\partial P/\partial \theta$ that is linked to the streamline radius of curvature r_c in the blade-to-blade plane. For incompressible flows, the pressure gradient does not appear in the vorticity transport equation. The curvature of the streamline can be thought to represent the effect of the pressure gradient normal to the streamlines.
2) The variation of section of the blade channel ($A_1<A_2$ for compressor and $A_1>A_2$ for turbine). This effect represents the longitudinal pressure gradient in the main flow direction.
3) Effect of viscosity: generation of vorticity at the wall

1.5.2 EFFECT OF BLADE TO BLADE PLANE CURVATURE

This first simple configuration deals at presenting the effect of a curvature on a velocity gradient typical of a boundary layer on an endwall.

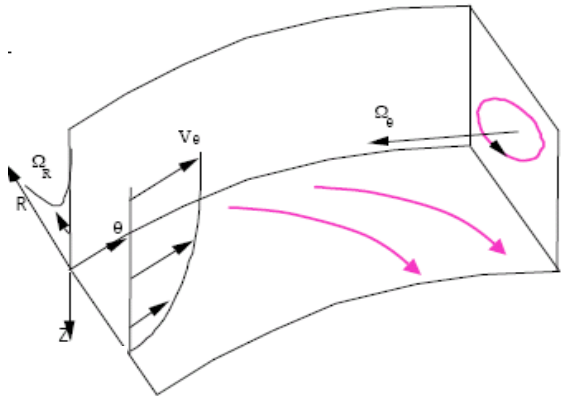

Fig 1.8: Cylindrical frame of reference of a turbomachine with circumferential flow (ECL study course [35])

Assume a stationary rectangular channel with a medium line θ in a cylindrical frame of reference (r,θ,z). At upstream $V_\theta(r,z), V_r = 0, V_z = 0$ and the rotational vector is $\vec{\Omega} = rot\left(\vec{V}\right)$ Hence, the components of $\vec{\Omega}$ at upstream are as follows:

$$\vec{\Omega}\left(\Omega_r = -\frac{1}{r}\frac{\partial r V_\theta}{\partial z}, \Omega_\theta = 0, \Omega_z = \frac{1}{r}\frac{\partial r V_\theta}{\partial r}\right) \tag{1.10}$$

The vortex vector transport (by convection) equation obtained by applying the rotational operator to the momentum equation can be written as:

$$\frac{d}{dt}\left(\frac{\vec{\Omega}}{\rho}\right) = \frac{\vec{\Omega}}{\rho}.grad\vec{V} - \frac{1}{\rho}grad\left(\frac{1}{\rho}\right) \wedge gradP + rot\left(\frac{\vec{F}_v}{\rho}\right) + rot\left(\frac{1}{\rho}div\vec{\tau}\right) \tag{1.11}$$

where

$\frac{\vec{\Omega}}{\rho}.grad\vec{V}$ is the redistribution (elongation) of vorticity

$-\frac{1}{\rho}grad\left(\frac{1}{\rho}\right) \wedge gradP$ is the effect of compressibility

$rot\left(\frac{\vec{F}_v}{\rho}\right)$ is the effect of external volume forces

$rot\left(\frac{1}{\rho}div\vec{\tau}\right)$ is the effect of viscosity

The transport equation of vortex vector in a local cylindrical frame is considered with some simplifying hypothesis:

- the flow is incompressible
- there are no external forces acting on the volume
- the viscosity does not influence the transport of vortex vector
- the boundary layer is two dimensional
- the convection is mainly performed by V_θ

With the above-mentioned simplifying hypothesis, the vector transport equation is reduced to:

$$\frac{d}{dt}\left(\frac{\vec{\Omega}}{\rho}\right) = \frac{\vec{\Omega}}{\rho}.grad\vec{V} \tag{1.12}$$

Developing expressions for Ω_R and Ω_z in terms of velocity gradients we get a relation between the circumferential vorticity component Ω_θ and the radial vorticity component:

$$\frac{\partial \Omega_\theta}{\partial \theta} = -2\Omega_r \tag{1.13}$$

This means that the circumferential vorticity component or the cross-flow Ω_θ is created by the radial vorticity component Ω_r included in the upstream viscous layer coupled with the angle of rotation $d\theta$. Hence, there is no creation of a vortex but simply a redistribution of the radial vorticity component Ω_r into the circumferential vorticity component Ω_θ or cross-flow in the blade-to-blade passage.

If Ω_r>0, Ω_θ is negative downstream implying transport of flow to the suction side and then to mid-span at the pressure side. This situation is typical of a hub endwall. If a tip endwall is considered, then Ω_r<0, Ω_θ is positive downstream implying again a transport of flow to the suction side of the blade channel.

1.5.3 VARIATION OF CHANNEL SECTION

The second configuration aims at presenting the effect of diffusion through the variation of section.

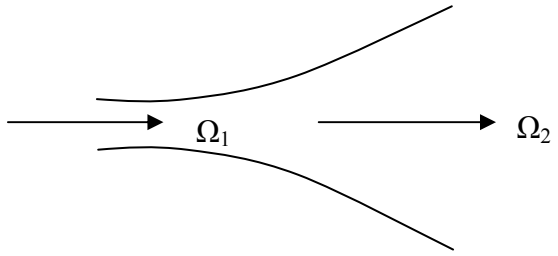

Fig 1.9: A 1D diffusing channel (ECL study course [35])

Consider a one-dimensional diffusing channel with exit section greater than the inlet section in the Cartesian frame of reference with certain simplifying hypothesis

- One dimensional non viscous flow
- No forces act on the volume

Assuming also a small component of vorticity upstream aligned with the main velocity component V_x, the vortex transport equation gives:

$$\Omega_x = K\rho V_x \tag{1.14}$$

Applying the conservation of mass from inlet to the outlet, $\dot{m} = \rho V_x A$

Consequently, the axial vorticity may be written as $\Omega_x = \frac{K\dot{m}}{A}$ (1.15)

Hence, in a divergent channel (compressor channel), Ω_x decreases and in a convergent channel (turbine channel) Ω_x increases under the effect of the variation of the section area.

1.5.4 EFFECT OF VISCOSITY

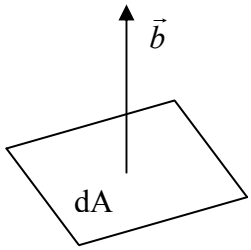

Fig 1.10: Elemental surface dA with a normal vector (ECL study course [35])

To understand the creation of vorticity on the wall let us assume a small elementary surface dA and a vector $\vec{b}$ normal to the surface. According to the Poincaré's formulation of the Navier-Stokes equation, the total force acting on the surface is the sum of the pressure force normal to the surface and the frictional force tangent to the surface being directly proportional to the local vorticity:

$$\vec{F}_S = -\Pi\vec{b} + \left(\mu_t + \mu\right)\vec{\Omega} \wedge \vec{b} \tag{1.16}$$

The vorticity is generated at the wall due to friction forces. The frictional force is contained on the wall and the particles do not exhibit translational velocity.

$$\vec{F}_{\tau_{wall}} = \tau.\vec{b} = -\mu\vec{b} \wedge \vec{\Omega}_{wall} \tag{1.17}$$

The particles exhibit rotational velocity related to viscosity on the wall.
Neglecting the viscosity variations in the vortex transport equation, we get:

$$\overrightarrow{rot}\left(\frac{1}{\rho}div\left(\vec{\tau}\right)\right)\approx \upsilon\Delta\vec{\Omega} \tag{1.18}$$

This translates into diffusion of vorticity to the freestream by molecular or turbulent agitation, but not loss of vorticity. This is expressed by the following equation:

$$\frac{d}{dt}\left(\frac{\vec{\Omega}}{\rho}\right)=\frac{\vec{\Omega}}{\rho}.\overrightarrow{grad}\left(\frac{1}{\rho}\right)\wedge\overrightarrow{grad}P+\frac{\overrightarrow{rot}\,\vec{f}}{\rho}+\upsilon\Delta\vec{\Omega} \tag{1.19}$$

1.5.5 THE IMPORTANCE OF THE ANALYSIS OF VORTICES

We may consider following principle reasons for analysing vortices in a flow:

- The vortices are a finer representation of the kinematic effect than the velocity field as they depend upon the velocity gradients.

- At large scales, the vortices are strongly mixing the flow. This is an important mechanism that may help to prevent or delay the separation of endwall layers as it introduces the free-stream momentum in the boundary layer. Hence, the increase of vortices allows the reduction of kinetic energy losses in the compressor or turbine channels.

- When the vortex vector is aligned with the velocity vector, the flow is known to have a non-zero helicity. Some experimental evidences show that the kinetic energy associates with a non-zero helicity at the trailing edge of a blade row is ultimately lost into heat. For that reason, helicity may be considered as a source of future loss, and these vortices are then responsible for significant losses in turbomachines.

- The vorticity is generated on the wall under the action of the friction force. It is also extracted from the wall by viscous and turbulent diffusion effects. At small turbulent scales, the vortices are dissipated by the viscous shear. This is a typical consequence from the well-known cascade of turbulent energy.

1.6 TYPES OF VORTICES IN TURBOMACHINES

Some commonly observed types of vortices found in turbomachines and analysed in the case studies of this thesis are:

- Leading edge horseshoe vortex
- Tip leakage vortex
- Hub corner vortex

1.6.1 LEADING EDGE HORSESHOE VORTEX

As the name suggests, the horseshoe vortex resembles the shape of a horseshoe and is associated with the leading edge of blades. When the inlet flow reaches the leading edge of the blade it is bifurcated into two streams of flow that go on to the suction and pressure sides respectively. This is associated with the formation of a system of vortices that is collectively called the horseshoe vortex. In fact, the horseshoe vortex is a bound vortex in front of a solid wall and two free trailing vortices that move to the two sides of the blade. In general, horseshoe vortex is observed for a flow in front of any hemispherical obstacle.

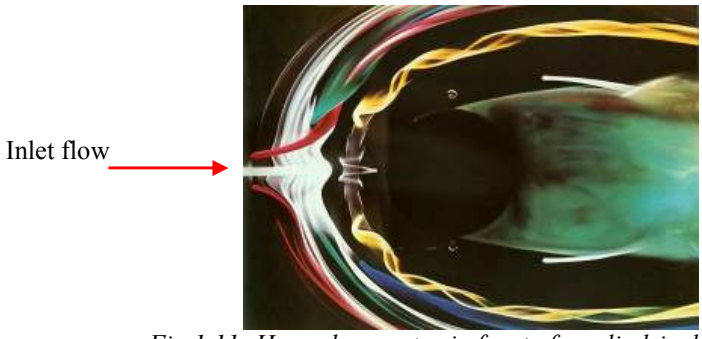

Fig 1.11: Horseshoe vortex in front of a cylindrical obstacle (Henri Werlé, ONERA, www.efluids.com)

In the figure 1.11 above, the inlet flow is bifurcated into two branches of trailing vortices (yellow coloured streak lines) that go on the upper and lower surfaces of the cylinder. The losses associated with the horseshoe vortex vary with its strength that is determined by the inlet conditions of the flow such as the Mach number, Reynolds number and the incidence. At nominal conditions, the bifurcation of the trailing vortices would occur at the centre of the leading edge and hence lower losses.

1.6.2 TIP LEAKAGE VORTEX

The un-shrouded rotors of turbomachines have a tip clearance gap between the tip of the rotor and the casing wall. Due to the pressure difference between the suction and the pressure surface, the flow is convected from the pressure side to the suction side in this tip clearance gap and rolls up in a vortex. The tip leakage vortex has deleterious effects on the performance of turbomachines. It reduces the work done in the tip clearance zone, decreases the stall margin of the compressor and increases the heat transfer in the blade tips. A tip leakage flow on a rotor tip of a turbomachine is illustrated in figure 1.12:

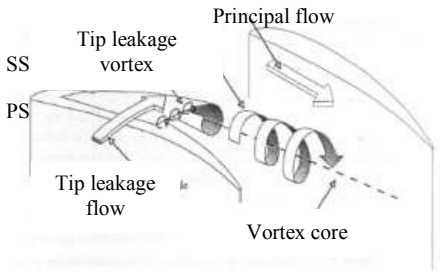

Fig 1.12: Tip leakage vortex formation on rotor tip in the blade to blade passage of turbomachine (ECL study course [35])

1.6.3 HUB CORNER VORTEX

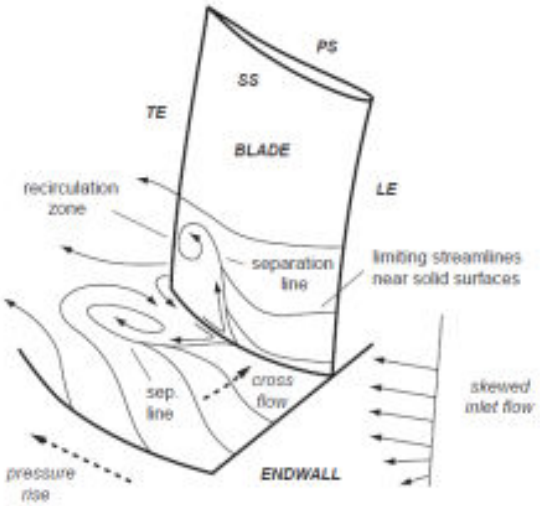

Fig 1.13: Basic processes governing the hub corner stall mechanism (Lei et al. [14])

Hub corner stall is a flow separation phenomenon that is characterized by flow reversal on both the suction side and the hub wall. The hub wall boundary layer has a lower velocity due to the viscous effects on the wall but experiences roughly the same cross-stream pressure gradient as the free stream. The streamline radius of curvature near the hub wall is therefore smaller than in the free stream, leading to cross-passage motion and the accumulation of low stagnation pressure fluid near the suction surface hub corner.

At increased blade loading conditions this low stagnation pressure fluid is not able to negotiate the pressure rise in the blade passage and hub corner stall occurs, increasing passage blockage, lowering the static pressure rise capability of the compressor blade row, and increasing the entropy rise from flow mixing downstream. The cross-flow, due to circumferential pressure gradient, transports low stagnation pressure, low momentum fluid, into the hub corner region.

The weakened boundary layer in the stream-wise direction along with the crossflow rapidly separates forming a large zone of reversed flow in the form of a vortex in the corner between the hub wall and the suction surface. The corner vortex mounts in the flow path and increases the aerodynamic blockage limiting the diffusion capability or the pressure rise capability of the blade. In addition the subsequent mixing of the flow in the separated region with the main passage flow may lead to a considerable total pressure loss and consequently reduction in compressor efficiency.

1.7 THREE DIMENSIONAL LOSSES IN TURBOMACHINES

1.7.1 GLOBAL VIEW

Lakshminarayana [18] gives a comprehensive account of three-dimensional losses in turbomachinery that include:

1) Profile losses due to blade boundary layer and wake: These are due to profile boundary layer as in a two-dimensional flow but involve three-dimensionality due to cross-flows. In addition to the losses due to two-dimensional parameters such as shock-boundary layer interaction, the losses depend on the radial distribution of the variables including $\partial p/\partial r$; three dimensional blade geometry including lean, dihedral, sweep, twist, aspect ratio, meridional curvature, rotation parameter and the flow coefficient. The profile losses depend then on the span-wise location.

2) Shock losses: Losses arise due to leading edge, passage, and trailing edge shocks, which are almost invariably three-dimensional both in strength and geometry. The shock losses and the boundary layer interactions are a major source of losses that limit the pressure ratio and the stability of the compression system. In addition to variables that control the two-dimensional shock losses, the three-dimensional blade geometry and radial variation of properties including inlet Mach number have a major influence on radial variation of shock losses.

3) Endwall losses: The viscous and turbulence dissipation associated with endwall boundary layers introduce flow losses and decrement in efficiency. These are direct losses associated with boundary layers. The endwall losses include both the secondary vorticity flow losses and the losses due to wall boundary layer.

   Practically, it is not simple to distinguish between these two sources: the wall boundary losses are direct local transformation of kinetic energy into heat through local turbulent and viscous shear stresses. The secondary vorticity losses are a local generation of helicity (corkscrew like motion of fluid particle exhibiting solid body motion) owing to flow curvature or span-wise variation of aerodynamic loading on the blade. In most cases, the kinetic energy associated to helicity will be transformed downstream into heat. Two others special cases of the endwall and secondary vorticity losses have to be identified, namely the corner and tip clearance effects; they are just local concentrations of the two previous losses.

   3.1) Corner flow: Corner flow is a crucial phenomenon of separation in the corner between the hub wall and the suction surface of the blade due to adverse stream-wise and tangential pressure gradients. The corner flow is associated with very strong flow separations that reduce the diffusion capability of the blades, increase aerodynamic blockage and increase the total pressure losses. At certain strength, the corner flow may also dictate the operating range of the cascade.

3.2) Clearance losses: The blade tip leakage flow and its eventual roll-up results in aerodynamic losses and decrement in efficiency. The leakage losses are associated with the loss of kinetic energy attributed to leakage velocity from pressure to suction side of the blade, the dissipation of leakage vortex linked to the local blade load and the interaction of the leakage flow with the main passage flow.

1.7.2 MORE ON ENDWALL LOSSES

The effects of endwall boundary layer growth on the performance are many:

1) Approximately one-third to one-half of the total losses in single-stage and multi-stage turbomachinery are due to endwall boundary layers including tip clearance and secondary flow effects.

2) The endwall boundary layers may cause aerodynamic blockage of the flow, amounting to as much as 5-20% span in terms of displacement thickness, depending on the type of blade row and blade height. In fact, the presence of a corner vortex in a highly separated zone is shown to have influence till mid-span (Sachdeva et al. [33])

3) In a multistage compressor, the endwall boundary layers has a direct influence on the stall and surge phenomena. The stall inception usually occurs near the tip and propagates downward.

4) Endwall boundary layers introduce off design conditions near the tip. For example, the reduction in axial velocity in the endwall boundary layer results in larger incidence to the succeeding blade row.

1.8 CONCLUSION

Viscous effects are inherent flow features of the high-pressure compressors where boundary layers are under the influence of adverse pressure gradients. The regions of adverse pressure gradients are well known to cause flow separations on the blade and the endwalls of the compressor leading to blockage in the flow path that puts a limit on the massflow entering the turbomachine and hence the work capacity of the machine is reduced. These regions of adverse pressure gradients on the blade suction surface and the endwalls foster complex three dimensional flow separations that are responsible for most of the losses in the turbomachines other than the shock losses.

The loss generating three-dimensional flow separation phenomena in turbomachines are complex vortex flow phenomena. The origin of vortices in turbomachines is related to redistribution of the three components of vorticity at the inlet: axial, radial and tangential. With simplifying hypotheses, the formation of flow phenomena is explained from the vorticity transport equation. The cross-flow in the blade-to-blade passage is essentially linked to a redistribution of the radial vorticity into circumferential vorticity by the effect of curvature of the blade-to-blade passage. In the divergent flow channels of a turbomachine (compressor), the axial vorticity decreases and in the convergent flow channels (turbine), the axial vorticity increases. More fundamentally, the creation of vorticity at the wall is linked to the friction forces induced by the viscosity on the wall.

Since vortices represent loss generating mechanisms in turbomachines, there are good reasons to undertake the study of vortices in this research work. The vortices are a finer representation of the kinematic effects as they depend on the velocity gradients. Analysis of vortices in turbomachines with their sources on walls and their diffusion in the free-stream may provide practical information to characterize the implementation of flow control on the wall, such as the location of device, geometry of device, massflow to bleed/blow, etc.

Some of the commonly observed vortex flow structures in turbomachines are the leading edge horseshoe vortex, tip leakage vortex and the hub corner vortex. These flow structures have been analysed in this research work for the test cases as they are found to represent most of the important losses. This list is, by no means, exhaustive for various other vortex flow structures are observed in experiments and numerical studies.

Three-dimensional losses in turbomachines primarily result from the span-wise blade profile losses and the wake, shock losses in rotors and the endwall losses. The endwall losses are often the largest contributors to the overall losses in the turbomachine. The wall boundary layer losses are direct transformation of energy into heat whereas the secondary vorticity losses are a local generation of helicity due to flow curvature or the span-wise variation of aerodynamic loading on the blade.

The tip leakage vortex and the corner vortex are major loss generating mechanisms in endwall losses. The tip leakage vortex rolls up and propagates downstream to the adjacent blade and is responsible for high losses in the tip clearance region, high heat transfer in the rotor tips and a decrease in compressor stall margin. The corner vortex in the region between the hub and the blade suction surface has a large impact on the pressure rise capability of the blades and increased aerodynamic blockage in the flow path leading to a reduction in the effective flow area and thicker wakes trailing downstream of the trailing edge of the blade.

In the following chapter we shall link the concepts of vorticity to the tools of flow topology for the analysis of three-dimensional separations.

2. FLOW TOPOLOGIES RELATED TO FLOW SEPARATION

2.1 SKIN FRICTION LINES AND THE VORTEX VECTOR

To define a three-dimensional separation, it is useful to study the flow properties on the surface of a body. This introduces the concepts that permit a rational definition of flow separation having the advantage of applying itself to the experimental observations.

Consider a body of surface B in a local frame of reference $\left(\vec{i},\vec{j},\vec{n}\right)$ formed by a unit vector $\vec{n}$ normal to the surface and two other unit vectors $\vec{i}$ and $\vec{j}$ in the plane tangent to the surface B. The global frame of reference is a cartesian frame $\left(x,y,z\right)$.

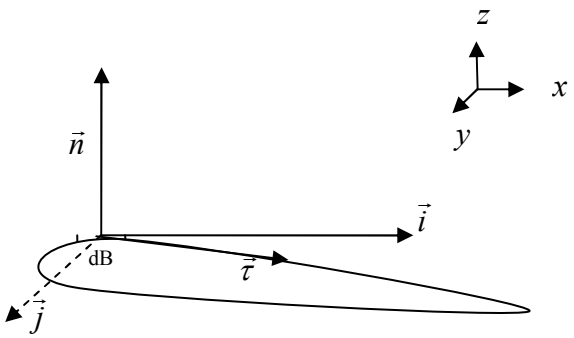

Fig 2.1: A body of surface B with skin friction vectors

The fluid motion around the surface B creates a force $\vec{F}$ on elemental surface dB. Consider the contribution of the shear stress tensor on the surface B. Let $\vec{\tau}$ be the vector induced by shear stress on the surface B. The friction vector $\vec{\tau}$ on the wall can be formed as

$$\vec{\tau} = \tau\vec{n} = \tau_x\vec{i} + \tau_y\vec{j} \tag{2.1}$$

The friction on the surface of the body is in the form of a vector field from which the skin friction lines can be determined. These lines are defined as the solution of the following differential system:

$$\frac{dx}{\tau_x(x,y)} = \frac{dy}{\tau_y(x,y)} = dt \tag{2.2}$$

where t is the parameter of integration.

Also, useful is the notion of the limiting streamlines (streamlines on the surface of the body) defined as the limiting position of a streamline when its distance at the wall tends to zero. It is a fictitious concept since the velocity on the surface is zero; but it is possible to demonstrate that the direction of the velocity vector $\vec{V}$ coincides with the direction of the friction vector $\vec{\tau}$. If u,v,w are the components of the velocity vector $\vec{V}$ in the frame of reference $\left(\vec{i},\vec{j},\vec{n}\right)$ in the vicinity of the wall (u,v,w are zero at the wall from the no slip condition), the first order derivatives of the velocity components can be written as:

$$u(x,y,z)=\left(\frac{\partial u}{\partial z}\right)_w z \approx \tau_x z \tag{2.3}$$

$$v(x,y,z)=\left(\frac{\partial v}{\partial z}\right)_w z \approx \tau_y z \tag{2.4}$$

$$w(x,y,z)=0 \text{ from the continuity equation.} \tag{2.5}$$

As one approaches the wall, the streamlines tend towards the lines in the friction field of vector $\vec{\tau}$, i.e. towards the skin friction lines. Hence, the "limiting streamlines and the skin friction lines are equivalent."

Consider the components of the vortex vector $\vec{\Omega}$:

$$\Omega_x=\frac{\partial v}{\partial z}-\frac{\partial w}{\partial y}, \quad \Omega_y=\frac{\partial u}{\partial z}-\frac{\partial v}{\partial x}, \quad \Omega_z=\frac{\partial w}{\partial x}-\frac{\partial u}{\partial y} \tag{2.6}$$

On the surface (wall), these components are

$$\Omega_x=-\left(\frac{\partial v}{\partial z}\right)_w, \quad \Omega_y=\left(\frac{\partial u}{\partial z}\right)_w, \quad \Omega_z=0 \tag{2.7}$$

The vortex vector on the surface of a body is tangent to the surface of the body. Also, $\vec{\Omega}$ is perpendicular to $\vec{\tau}$ as $\vec{\Omega}\cdot\vec{\tau}=0$. Hence, the lines of the vortex vector on the surface are orthogonal to the skin friction lines.

2.2 CRITICAL POINTS

As described previously, the skin friction lines are the solution curves of the system of the differential equations. In practice, it is exceptional to obtain an analytical definition of the skin friction lines. They have to be constructed step by step in the friction field $\vec{\tau}$ to trace their trajectories analogous to the streamlines. The only points that do not satisfy this general rule are the critical points of the system of differential equations (2.2) where simultaneously we have:

$$\tau_x(x,y)=0, \quad \tau_y(x,y)=0 \tag{2.8}$$

The critical points are the points where the skin friction vanishes altogether.

2.3 TYPES OF CRITICAL POINTS

The critical points can be broadly classified into two main categories:

- the nodes (including focus)
- the saddle points

2.3.1 THE NODES

A node is a point common to an infinite number of limiting streamlines or skin friction lines. At the node, all the skin friction lines are tangent to the straight line. At a nodal point of separation all of the skin friction lines are directed outward from the node. At a nodal point of attachment all of the skin friction lines are directed inward toward the node.

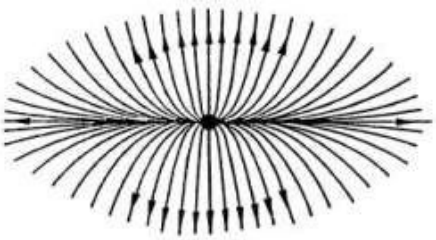

Fig 2.2a: Node of attachment (Délery [30])

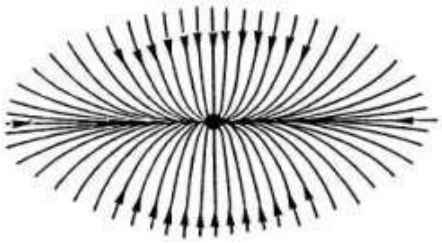

Fig 2.2b: Node of separation (Délery [30])

2.3.2 SPIRAL NODE OR FOCUS

A spiral node or focus is the point around which an infinite number of limiting streamlines or skin friction lines spiral around the node like the vortex like motion either away from it (focus of attachment) or either into it (focus of separation).

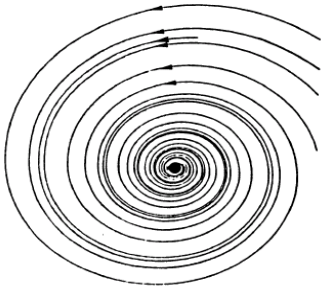

Fig 2.3: Spiral node or focus of separation (Délery [30])

2.3.3 SADDLE POINT

Saddle point is a point through which two particular (critical) lines pass, acting as barriers in the field of limiting streamlines or the skin friction lines, making one set of streamlines inaccessible to the adjacent set.

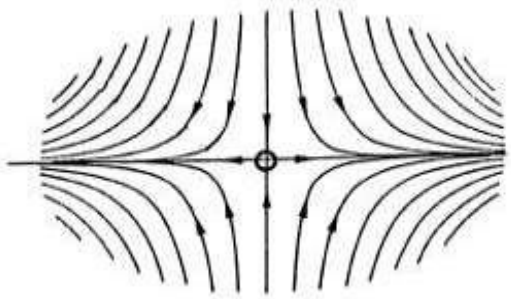

Fig 2.4: Saddle point (Délery [30])

2.3.4 DIVIDING LINES OF SEPARATION AND ATTACHMENT

The saddle point plays a key role in the phenomenon of three-dimensional separations. In the vicinity of a critical point all the skin friction lines avoid making contact with the critical point with the exception of two lines that pass through the saddle point. These lines are called the dividing lines.

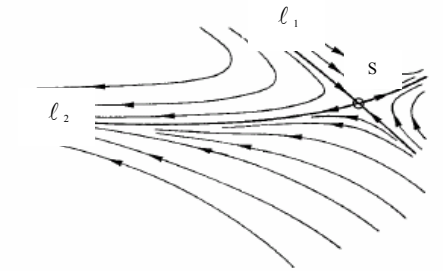

Fig 2.5a: Dividing line of separation (Délery [30])

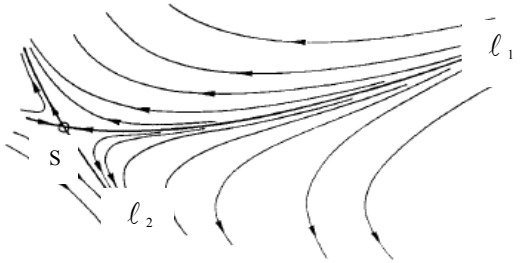

Fig 2.5b: Dividing line of attachment (Délery [30])

Figure 2.5a shows the two dividing skin friction lines, one coming from upstream and the other ℓ_1 coming from the opposite end, meet at the saddle point S and one family of lines turns towards the left and the other one to the right. After being separated, the lines tend to follow the second dividing line ℓ_2 where they approach ℓ_2 asymptotically without actually making contact with ℓ_2. Thus, ℓ_2 is the dividing skin friction line of separation issuing away from the saddle point. At the approach of the line ℓ_2, the other lines on the surface lengthen or "separate". The viscous layer of fluid is displaced transversally along the line ℓ_2. This is a typical characteristic of a three-dimensional separation. In this phenomenon, the regions of flow in contact with the wall leave the wall to mix in the free-stream with the non viscous flow.

The opposite type of flow (figure 2.5b) shows the dividing streamline of attachment approaching the saddle point S with the other lines that approach the saddle point asymptotically without actually making contact with ℓ_2.

2.4 NOTIONS OF CLOSED SEPARATIONS

Prandtl (1904) showed that a two-dimensional boundary layer separates on a slip boundary at isolated points where the wall shear (skin friction) vanishes and the flow reversal occurs. Three-dimensional flows separate along the skin friction lines and not on isolated skin friction zeros. However, the skin friction lines may originate from the skin friction zeros in the friction field on the walls.

Lighthill (1963) proposed a global view of three-dimensional separations of the convergence of wall-shear lines as a necessary criterion for separation. He concluded that separation lines always connect saddle points of the wall-shear field to stable spirals or nodes. This type of separation is called "closed" separation (Surana et al. [20]). Délery [30] has interpreted a number of flow phenomena based on this heuristic separation criterion. Tobak and Peake [31] define a skin friction line emerging from a saddle point to be a global line of separation leading to global separation. If the skin friction lines on which other lines converge do not emerge from a saddle point then this line is a local line of separation leading to local separation.

Recently, Surana et al. [20, 32] have derived an exact non-linear theory of three-dimensional separations and attachments of boundaries at rest in steady flows. In their theory, they obtain rigorous criteria for the separation points and the separation lines on fixed no slip boundaries in compressible flows. They link separation to the existence of unstable manifolds emanating from the no slip boundary. These manifolds are material curves or surfaces that collect and eject fluid particles from the vicinity of the boundary.

One-dimensional unstable manifolds (separation profiles) emanate from zeros of the skin-friction field; two-dimensional unstable manifolds (separation surfaces) emanate from specific skin-friction lines, the separation lines. The distinguishing feature of separation lines is their strong saddle type instability relative to an appropriately rescaled local flow near the boundary.

Such instabilities are identified by Surana et al. [20, 32] by solving the time-dependent equation of variations along scaled skin-friction lines. Asymptotic conditions for separation lines and explicit formulae for separation angles are deduced. Only four types of locally unique separation lines are possible in physical fluid flows:

(1) saddle–spiral connections
(2) saddle–node connections
(3) saddle–limit cycle connections and
(4) limit cycles.

Separations (1) and (2) are known as closed separations; Separations (3) and (4) are known as open separations. Recall that the closed separations are the separations that commence and terminate at singularities (critical points). These four types of unique separation lines are shown in figure 2.6:

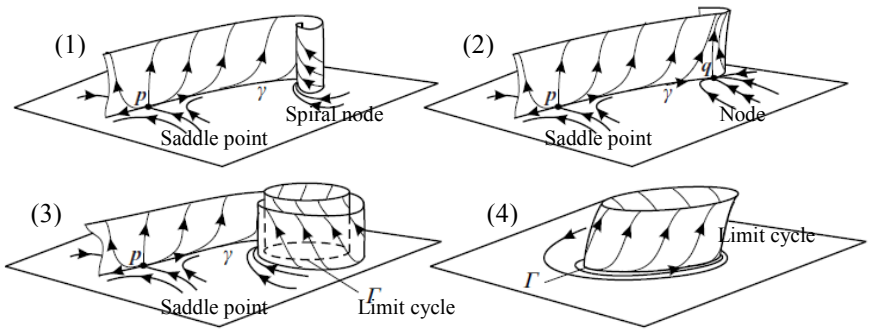

Fig 2.6: The four type of unique separation lines(Surana et al. [20, 32])

The flow separates at the boundary if fluid particles starting arbitrarily close to the boundaries converge to a streamline L (separation curve) or a separation stream surface S, along which they are ejected from the boundary. In the language of nonlinear dynamics, L is a one-dimensional unstable manifold of a boundary point (separation point) and S is a two-dimensional unstable manifold of a curve of boundary points (separation line).

Unstable manifolds are invariant: the particles starting on them remain on them for all times. Unstable manifolds, are, therefore material lines or surfaces that are not deformed by the flow in time. In steady flows, material lines are streamlines and stream surfaces respectively. To exclude unphysical cases, separation profiles and surfaces are subject to following properties:

1) Unique: no other separation profile or surface emerges from the same set of boundary points
2) Bounded: they intersect the boundary in a bounded set
3) Smooth: they are continuously differentiable
4) Robust: they smoothly deform but survive under small perturbations to velocity

Properties 1-3 express plausible physical features of separation; property 4 excludes degenerate separation patterns that are not reproducible experimentally or numerically. Such patterns include separation profiles and surfaces tangent to the boundary.

Attachment is defined as separation exhibited by the flow in backward time. Attachment points are, therefore, boundary points with a one-dimensional stable manifold (attachment curve), and attachment lines are boundary curves with a two-dimensional stable manifold (attachment surface). The separation and attachment manifolds are illustrated in figures 2.7a,b below:

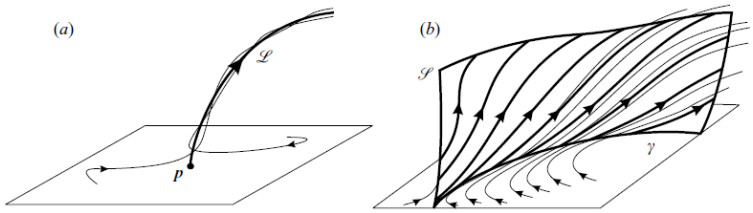

Fig 2.7a: Steady separation along (a)a streamline (1D unstable manifold L), and (b)along a stream surface(2D unstable manifolds) (Surana et al. [20, 32])

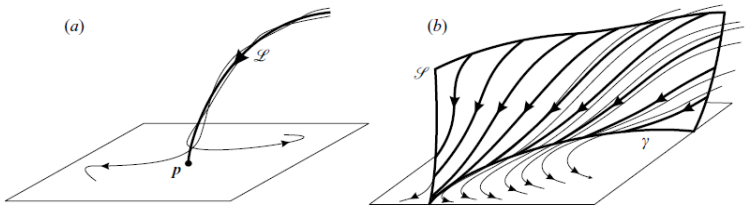

Fig 2.7b: Steady attachment along (a)a streamline (1D stable manifold L), and (b)along a stream surface(2D stable manifolds) (Surana et al. [20, 32])

2.4.1 SEPARATION AND ATTACHMENT CRITERION (CLOSED SEPARATIONS)

This section presents the rigorous criterion of separation and attachment deduced by Surana et al. [20, 32] that serves as necessary and sufficient conditions for the points and streamlines on the boundary to qualify as separation or attachment lines (unstable and stable manifolds). Later in this report, this criterion is applied to determine the characteristics of three-dimensional separations on the endwall of the stator blade in investigation.

Following Surana et al. [20, 32], in Cartesian co-ordinates (x,y,z) on a boundary $z=z_o$, a point P is a separation if and only if:

$$\tau_p = 0 \quad , \quad \nabla.\tau_p < 0 \, , \quad \det(\nabla \tau_p) > 0 \tag{2.9}$$

In the above equations, the first term represents the zero value of skin friction vector, the second term is the divergence of the skin friction vector and the third term is the determinant of the matrix (gradient of skin friction vector).

The above conditions imply that P is either a stable node or a stable spiral (focus) of the wall shear (skin friction) field.

Similarly, a point P is an attachment point if and only if

$$\tau_p = 0 \quad , \quad \nabla.\tau_p > 0 , \quad \det(\nabla \tau_p) > 0 \tag{2.10}$$

That is, P is either an unstable node or an unstable spiral (focus) of the wall shear (skin friction) field.

Furthermore, a line L is a separation line if and only if

1) the line originates from a saddle point P with $\nabla.\tau_p < 0$ and ends at stable spiral node (focus) q with $\nabla.\tau_q < 0$ ((1) in figure 2.7)
2) the line originates from a saddle point P with $\nabla.\tau_p < 0$ and ends at stable node q with $\nabla.\tau_q < 0$ ((2) in figure 2.7)

Similarly, a line L is an attachment line if and only if

1) the line originates from a saddle point p with $\nabla.\tau_p > 0$ and ends at stable spiral node (focus) q with $\nabla.\tau_q > 0$
2) the line originates from a saddle point p with $\nabla.\tau_p > 0$ and ends at stable node q with $\nabla.\tau_q > 0$

The conditions (1) and (2) are commonly observed in closed separations. For closed separations the divergence of the friction vector in the skin friction field is a necessary condition to determine the separation/attachment characteristics of points and lines.

In order to compute the divergence $\nabla.\tau_p$ here, we take the first order derivatives of the friction vector on the boundary. In physical terms, the sign of the divergence of a three-dimensional vector field is the extent to which the vector field flow behaves like a source or a sink at a given point. It is a local measure of the extent to which there is more exiting an infinitesimal region of space than entering it. If the divergence is nonzero at some point then there must be a source or sink at that position. A decrease in the divergence value of the friction vector below the zero value indicates the vanishing of the wall shear at the boundary, a confirmation of the skin friction zero and hence a separation point/line. The same logic applies for the attachment line/point in an inverse manner where the divergence of the friction vector is associated with non zero skin friction points that serve to re-attach the boundary layer.

2.4.2 TOPOLOGICAL RULES OF CLOSED SEPARATIONS

Délery [30] quotes some important topological rules of closed separations that serve as critical tools for analyses of closed separations.

Nodes and spiral nodes (foci) are topologically equivalent. They act as sources or sinks of the flows. On an isolated body, the skin friction lines originate from a nodal point of attachment. The skin friction lines can terminate only at a node or a focus. For a stable configuration, two nodal points or two saddle points cannot be connected to each other. There exists a saddle point between the two nodal points and a node or a focus between the two saddle points.

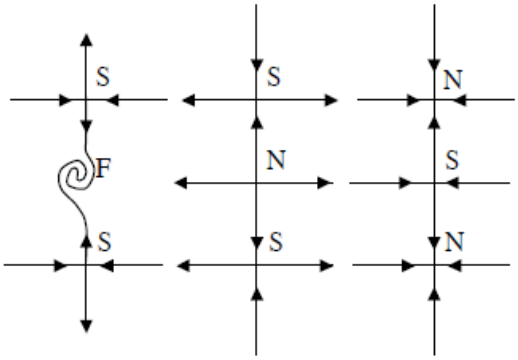

Fig 2.8: Stable configuration of closed separations (ECL study course [35])

The number of singular/critical points on a surface cannot be arbitrary. The number of critical points on a surface is a function of the genus property of the surface.

If all the curves on the surface can be reduced to a point by continuous deformation then this surface has the genus of zero or is a simply connected surface. This is the case of spheroids, ellipsoids, a finite surface of an infinite cylinder etc. The relation between the numbers of critical points on a surface is given as

$$\Sigma \text{ (nodes+foci)} - \Sigma \text{ (saddle points)} = 2 \qquad (2.11)$$

For a surface of genus non zero or a non simply connected surface, the curves cannot be reduced to a point but to a surface with a hole or simply a torus.

The relation between the numbers of critical points now becomes

$$\Sigma \text{ (nodes+foci)} - \Sigma \text{ (saddle points)} = 2-2g \qquad (2.12)$$

where g is the genus property of the surface. (Gbabedo et al. [21]). The second member of (2.12) is known as the Euler characteristic of the oriented surface: it is a topological invariant, a number that describes a topological space's shape or structure regardless of the way it is bent.

2.5 A CASE STUDY OF THREE DIMENSIONAL SEPARATIONS IN COMPRESSORS

Gbabedo et al. [28] have done a numerical and experimental study of the flow topologies associated with three-dimensional separations on two linear cascades with a subsonic inlet Mach number of 0.07. One of the cascades has a NACA65 blade profile and the other one is a cascade with PVD (Prescribed Velocity Distribution) blade. The surface flow visualisations have been done with surface mounted tufts and oil streak lines. The numerical code employed is MULTIP, a fully three-dimensional RANS code. The calculations were carried out using a control volume formulation on a structured 'H' mesh with y^+=11. The authors have a good correlation between the experiments and the CFD. The flow topology is analysed here for the cascade with PVD blade at the design incidence point:

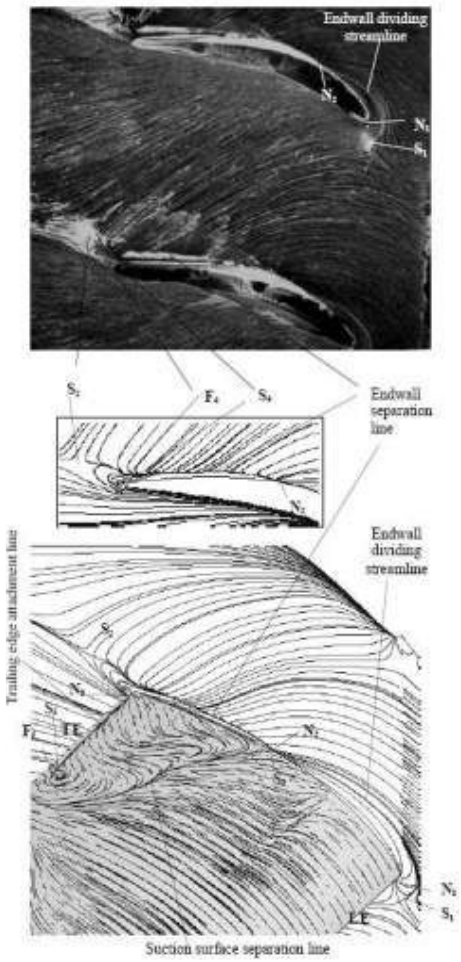

Fig 2.9: Oil streak lines on the endwall, limiting streamlines on the endwall and the blade suction surface (Gbabedo et al. [28])

Figure 2.9 shows the oil streak lines from experiments on the endwall followed by the limiting streamlines on the endwall and the blade suction surface (CFD) to study the three-dimensional separation. The flow topology can be explained in the following steps:

- The leading edge saddle point S1 and the corresponding nodal point of attachment N1 form the base of the leading edge horseshoe vortex. The endwall dividing streamline emerging from the saddle point S1 intersects the blade suction surface in the corner. This forms a node-saddle singularity on the corner between the suction surface and the endwall.

- The oil streak lines and the limiting streamlines on the endwall reveal the presence of a node N2 on the endwall.

- The endwall separation streamline emerging from node N2 is found to terminate at the saddle point S2 at the trailing edge.

- On the corner at the suction surface a saddle point S3 is revealed to be a singular point of separation.

- The authors claim that the suction surface separation line emerging from the saddle point S3 terminates at the trailing edge without encountering any critical point. Furthermore, the focus of separation on the suction surface F5 and the corresponding saddle point S5 is seen on the suction surface and their role is not discussed.

The analysis of three dimensional flow separations, as proposed by the authors, raises important doubts and questions. One of the questions is, "Can a limiting streamline originating at a critical point and terminate without encountering a critical point be qualified as a separation line?"

The suction surface separation line as described by authors is in violation with the theory of closed separations described in previous sections, and neither it can be described as open separation for it has a point of origin at a saddle point. As the origin of this separation line is associated with a critical point on a boundary, its termination must be either associated with another critical point such as node or focus in case of a closed separation or in a stable limit cycle in case of open separation as per Surana et al. [20, 32].

A simple termination into free stream at the trailing edge does not explain a complete stable topological configuration as indicated by Délery [30]. It is possible that the suction surface separation line terminates into the focus F5 on the suction surface or another critical point on the blade trailing edge but this analysis is not presented. The flow separations in the compressor cascades are more complex than many axisymmetric geometries studied by various authors previously. The application of the separation/attachment criterion developed by Surana et al. [20, 32] may prove to be instrumental for a better understanding of flow topologies on the compressor endwall and the suction surface.

2.6 NEW CRITERION FOR HUB CORNER STALL (CORNER SEPARATION)

Lei et al. [14] have developed new criteria for estimating the size and strength of three-dimensional hub corner stalls in rotors and shrouded stators of compressors. The two criteria are:

- Stall indicator and
- Diffusion parameter

The idea behind the stall indicator is to quantify the extent of hub corner stall via the reduction in local blade loading relative to flow conditions outside the separation zone. Assuming such conditions occur at mid-span, the size and strength of the hub corner stall can be expressed as the difference between the loading at mid-span and loading in the endwall region.

$$SI = \left[\int_0^1 \frac{P_{S_{ps}}(x) - P_{S_{ss}}(x)}{P_{T_1} - P_{S_1}} \left(\frac{dx}{c_x} \right) \right]_{z/c=0.5\times AR} - \left[\int_0^1 \frac{P_{S_{ps}}(x) - P_{S_{ss}}(x)}{P_{T_1} - P_{S_1}} \left(\frac{dx}{c_x} \right) \right]_{z/c=0.1} \tag{2.13}$$

where $AR = L / c$ is the blade aspect ratio.

Introducing Zweifel blade loading coefficient Ψ , the Stall indicator SI can be written as:

$$SI = \Psi_{z/c=0.5\times AR} - \Psi_{z/c=0.1} \tag{2.14}$$

The Zweifel loading coefficient is defined as the ratio of actual blade loading to the blade loading which would exist with isentropic diffusion to stagnation conditions.

For Diffusion parameter is developed in order to estimate the corner stall. It is assumed to depend on the stream-wise pressure rise (and gradient), the cross-flow pressure difference (and gradient), and the state and skew of the incoming endwall boundary layer. The three non-dimensional parameters thus proposed as being candidates for inclusion in the hub corner stall diffusion parameter are:

- the overall pressure rise, expressed in terms of blade and incidence angles
- the magnitude of the cross-flow, expressed in terms of the turning of the endwall region flow
- the solidity, which leads to a more local measure of the pressure rise (or pressure gradient) at the hub suction corner compared to the overall pressure rise value.

$$DP = \frac{1}{\sigma}\left[1 - \left(\frac{\cos\left(i + \lambda + \zeta/2 \right)}{\cos\left(\lambda - \zeta/2 \right)} \right) \right] \cdot \left(i + \lambda - \Delta\beta \right) \tag{2.15}$$

where σ is the blade solidity
λ is the blade stagger angle
ζ is the blade camber angle
i is the incidence angle
$\Delta\beta$ is the boundary layer turning due to upstream rotating hub wall (in rotor and shrouded stator)

Based on numerical simulations of over 100 different cascade geometries, the critical value of the diffusion parameter marking the onset of corner separation is DP = 0.4 ± 0.05. It is

possible to have flow separation on suction surface of the blade with DP<0.4 without corner separation on the hub wall.

Both blade stall and hub corner stall are diffusion driven and one would expect some correspondence between the diffusion parameter DP and the well-known Lieblein diffusion factor DF. For incompressible flow with equal velocity in and out of cascade, Lieblein Diffusion factor is:

$$DF = \left(1 - \frac{\cos\alpha_1}{\cos\alpha_2}\right) + \frac{\cos\alpha_1}{2\sigma}(\tan\alpha_1 - \tan\alpha_2) \tag{2.16}$$

The latter was originally defined (for two dimensional cascades) in terms of a correlation between deceleration of the suction surface flow and the wake momentum thickness. It was expressed in terms of cascade area ratio and turning through the blade row. The Diffusion parameter, DP, and the Lieblein diffusion factor, DF, both account for static pressure rise and flow turning in the blade passage. An explicit difference, however, is that DP incorporates the effect of incoming boundary layer skew.

The researchers demonstrate that both DP and DF correlate roughly well in cases without incoming boundary layer skew. However, DP does not correlate with DF when endwall boundary layer skew is introduced.

2.7 CONCLUSION

This chapter discusses several key elements of flow topologies for the analysis of three-dimensional separations. The trajectory of flow on the surface is derived from the friction field on the surface in the form of skin friction lines. The limiting streamlines deduced from the velocity components are topologically equivalent to the skin friction lines. Resolution of friction vectors at skin friction zeros yields the type of critical points and their physical interpretations in relation to the separations. Nodes are sources/sinks of skin friction lines, spiral nodes represent fully developed vortices on the wall and saddle points are the sources/sinks of dividing streamlines. The dividing streamlines are formed by the convergence of skin friction lines on the surface and they are physical representations of separation/attachment lines depending upon their connection to source/sink saddle points.

The notion of closed separation was first introduced by Lighthill (1963) and has been investigated by several others numerically and experimentally. The skin friction lines of separation (dividing streamlines) originate at saddle points and terminate at nodes. Tobak and Peake [31] have further shown that multiple lines relating to separation are possible on a body identifying them as global and local lines of separation. A global line of separation necessarily has its origin at a saddle point, whereas a local line of separation may be formed by convergence of skin friction lines on the wall originating from a node. Recent developments by Surana et al. [20, 32] have introduced rigorous criterion to confirm the already identified separation and reattachment patterns. Their criterion is deduced from the theory of non-linear dynamics and consists of studying the divergence of the friction vector on the critical points to identify them as source/sink of the skin friction lines to/from the wall.

The analysis of flow topologies in the case studies of this thesis will be done in relation to the rules and criterion of closed separations. We shall see the analysis of flow topologies of the various case studies later in this report beginning from chapter 4. The Stall indicator and Diffusion parameter are applied in chapter 5.

3. BIBLIOGRAPHIC REVIEW OF FLOW CONTROL

3.1 INTRODUCTION

Flow control is an attempt to alter the character or disposition of a flow-field favourably that is of concern to the enhancement of performance of the machine. A very relevant definition was offered by Flatt in 1961 as applied to the wall bounded flows but could also be easily extended to the free-shear flows: “Boundary layer control includes any mechanism or process through which the boundary layer of a fluid is caused to behave differently than it would normally were the flow developing naturally along a smooth straight surface.” (extracted from Gad-el-Hak [17]) Prandtl (1904) introduced the boundary layer theory, explained the mechanics of steady separation, opened the way of understanding the motion of the real fluids and described several experiments in which the boundary layer was controlled. Lord et al. [29] give a comprehensive overview of the various flow control methods and their applications in turbomachines.

Historically, Prandtl (1915) used active flow control of the boundary layer to show the great influence such a control exerted on the flow pattern. He used suction to delay boundary layer separation from the surface of a cylinder (figure 3.1):

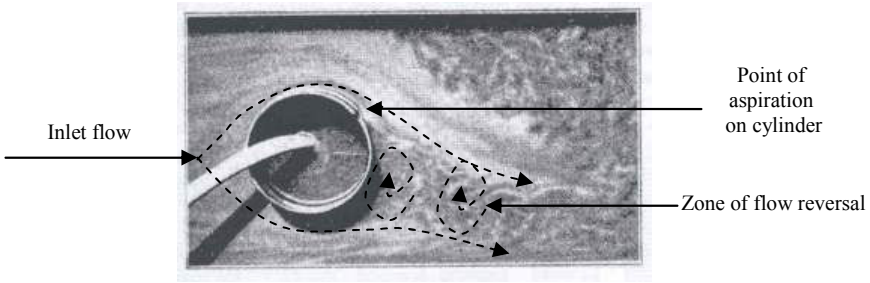

Fig 3.1: Flow around a cylinder with boundary layer suction at the upper rear part, showing an attached flow (Gad-el-Hak [17])

It is noted that with aspiration implemented on the upper surface of the cylinder, the flow separation has been retarded with a distinct reduction in the zone of reversed flow downstream of the cylinder.

3.2 CLASSIFICATION OF FLOW CONTROL

Gad-el-Hak [17] broadly classifies the flow control in two categories:

1) Flow control applied at the wall or away from the wall: Surface parameters that can influence the flow include roughness, shape, curvature, rigid wall motion compliance, temperature and porosity. Heating and cooling of the flow can influence the flow via the resulting viscosity and density gradients. Mass transfer can take place via a porous wall or a wall with slots. Suction and injection of primary flow can have significant effects on the flow field, influencing particularly the shape of the velocity profile near the wall and thus boundary layer susceptibility to transition and separation.

Control devices located away from the wall can also be beneficial. Large eddy break up devices, acoustic wave bombarding a shear layer from outside, additives introduced in the middle of the shear layer, manipulation of free-stream turbulence levels and spectra, gust and magneto and electro-hydrodynamic body forces are examples of flow control strategies applied away from the wall.

2) Flow control by energy expenditure and loop control: A device can be passive, requiring no auxiliary power and control loop, or active, requiring energy expenditure. As for action of passive devices, some refer to the term flow management rather than flow control reserving the latter terminology for dynamic processes. Active control requires a control loop and is further divided into pre-determined or reactive categories. Pre-determined control includes the application of steady or unsteady energy input without regard to the particular state of the flow.

   Reactive control is a special class of active control in which the control input is continuously adjusted based on measurements of some kind. The control loop in this case can either be an open feed forward one or a closed feedback loop. Classical control theory, for the most part, deals with reactive control.

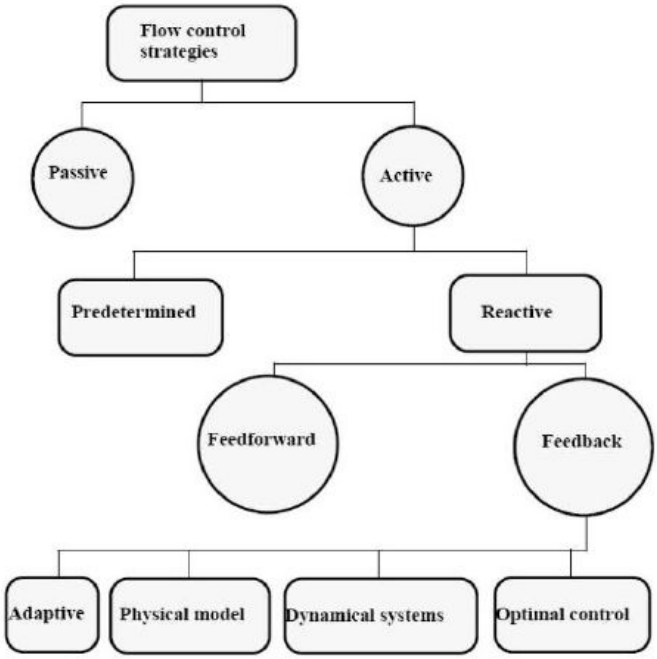

Fig 3.2 : Classification of flow control strategies (Gad-el-Hak [17])

The present research work is the study of "Active flow control by boundary layer aspiration applied at the walls of the high pressure compressor of an axial turbomachine"

3.3 BIBLIOGRAPHIC REVIEW OF ASPIRATED COMPRESSORS

The bibliography on the subject of boundary layer aspiration concerns mostly the application of aspiration on compressor blades to increase the diffusion capability of the blades. Along with the application of the aspiration some part of the literature also deals with the study of optimisation of blade geometric parameters and the blade design methodologies to be used with aspiration. Recent publications have explored the application of boundary layer aspiration to control the endwall losses. The following table gives a more comprehensive classification of the bibliographic literature according to its intent:

Authors	Type of flow control and devices	Type of study	Application	Flow control device position	$\dot{m}$ (% of inlet flow)
Loughery et al. [1]	Aspiration and blowing by slots	Experiments	Stator cascade	25-60%c	0.5-1.5%
Kerrebrock et al. [2]	Aspiration by scoops	CFD and experiments	Rotor cascade and compressor stage	Rotor:40-55%c, Stator: 50-85%c	Rotor:3.4%, stator:7.2%
Kerrebrock et al. [3]	Aspiration by slots	CFD and experiments	Fan stage	40%c	Rotor:3%, stator:3%
Merchant[4]	Aspiration by slots	CFD	Compressor stage	Rotor:40%c, 40-100% span, Stator: 40%c, 0-100% H	Rotor:1.5%, stator: 2%
Merchant et al. [5]	Aspiration by slots	CFD	Compressor stage	Rotor: slot (40-100%H), Casing: slot Stator: slots (0-100% H, 25-75%c), circumferential slot (hub)	Rotor: 3% Stator: 4%
Schuler et al. [6,7]	Aspiration by slots and holes	CFD and experiments	Fan stage	NA (Not available)	Rotor: 2.25% Stator: 2.45%
Dang et al. [8]	Aspiration by slot	CFD	Rotor cascade	NA (Not available)	Rotor:2% (baseline), 0.3% (optimised configuration)
Hubrich et al. [9]	Aspiration by slot	CFD and experiments	Rotor cascade	44% , 53% c	2%
Chen et al. [13]	Aspiration by slot	CFD	Stator cascade	40-80%c (parametric studies), slot span: 0-100% H	0.5%-1.5%
Gümmer et al. [12]	Aspiration by slot and holes	CFD	Compressor stage	Rotor: casing slot, stator: casing hole	Rotor:1%, stator:3%
Godard et al. [27]	Aspiration by slot	CFD	Diffuser	Diffuser slot at the separation (after selection)	3.2%
Chakraborthy et al. [22]	Aspiration by holes	Experiments	Stator cascade	Holes at 23- 59%c	0.15%
Gbabedo et al. [25]	Aspiration by slots	CFD and experiments	Stator cascade	Slots on blade and endwall	0.7%
Hergt et al. [23]	Passive control by vortex generators	CFD and Experiments	Stator cascade	NA	NA
Kirtley et al. [10]	Blowing by holes	CFD and experiments	Stator cascade	Holes on the blade suction side aft of the computed separation line	0% to 1.5%
Song et al. [30]	Blowing by holes (passive)	CFD	Stator cascade	Holes on blade suction side at 70-90%c and 10-15%span	1.35-1.49%

Table 1: Classification of the bibliographic literature

The bibliographic review presented here is specific to fans and high-pressure compressors of axial turbomachines. Broadly, the bibliographic review can be classified as the type of flow control such as aspiration, blowing or passive control.

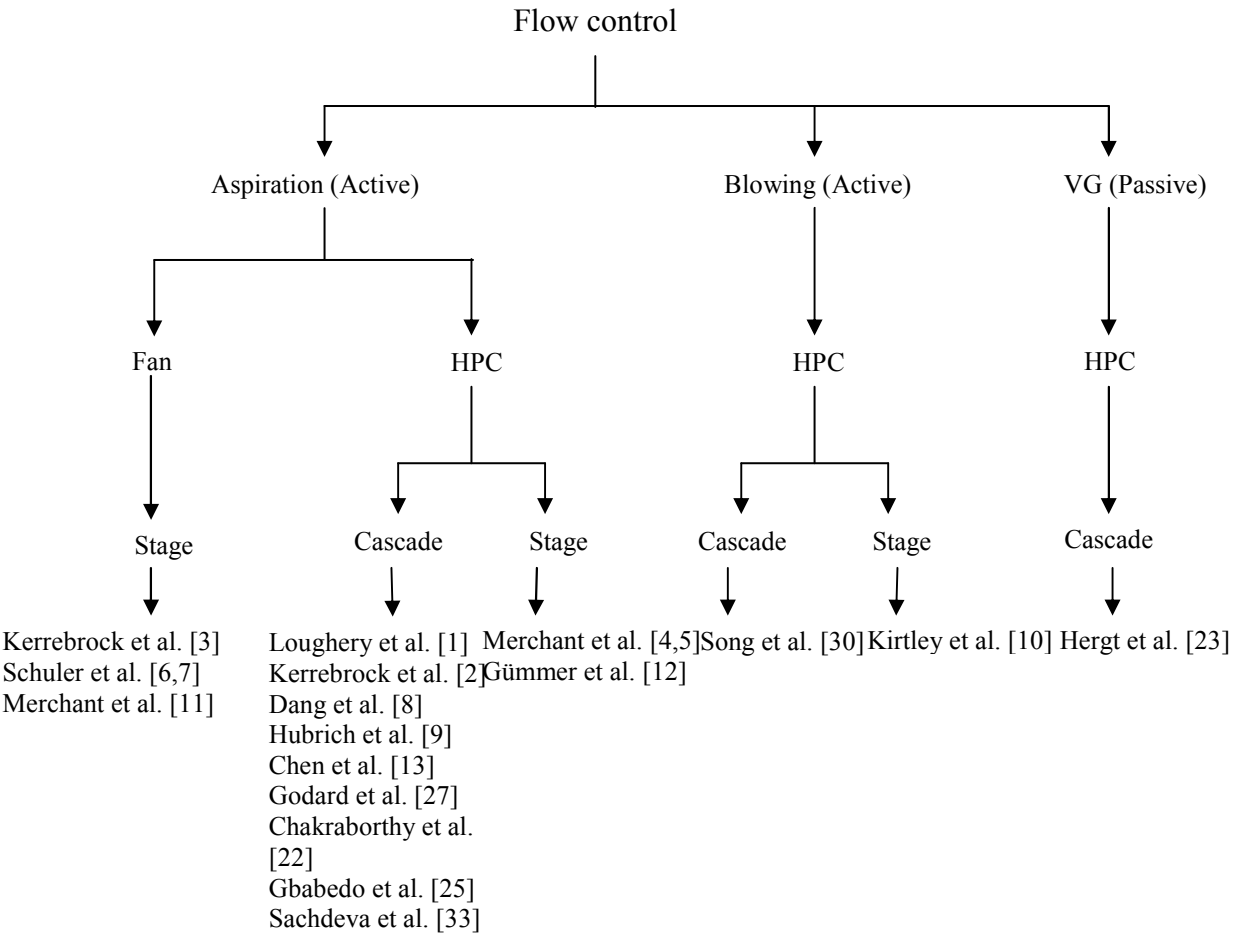

Fig 3.3: Breakdown of bibliographic review

3.3.1 BIBLIOGRAPHIC REVIEW OF ASPIRATION ON HPC CASCADES

In the 1970s, Loughery et al. [1] were few of the first researchers to experimentally study the effects of boundary layer blowing and aspiration on high lift stator blades. Their work examined both blowing and suction as means for increasing the flow turning capability of stator blades. Broadly, their results showed that blowing degraded compressor stator performance whereas suction enhanced it. But these interesting results were not investigated further due to difficulties to integrate the boundary layer suction and blowing with the existing compressor stator blades at that time. With the advance in modern technologies, flow control methods such as boundary layer aspiration are finding ways to integrate with the existing high-pressure compressor designs; however, complete integration with the entire engine requires more research. The research into aspirated compressors continues at a fast pace today with the advent of modern computers and the ever increasing sophisticated numerical simulation tools such as Computational Fluid Dynamics.

Kerrebrock et al. [2] were among the first few ones to revive the interest in the potential benefits of aspiration in the high-pressure compressors and his initial experiments with boundary layer aspiration in compressors sparked the Aspirated Compressors Research program at MIT. Kerrebrock et al. [2] studied the thermodynamic implications of the aspiration to study the potential benefits of boundary layer aspiration from the flow path of the compressors. They concluded that for most overall pressure ratios and bleed pressure ratios, the minimum inlet Mach number is between 0.3 and 0.5 to have benefits of aspiration. The inlet stages of most modern compressors satisfy this criterion.

An experimental investigation of the use of boundary layer control on the rotating blade row of the compressor was carried out by Kerrebrock et al. [2]. 5 out of 23 blades of an existing rotor designed to achieve a pressure ratio of 1.6 at a tip speed of 365 m/s are modified with suction scoops to bleed the blade boundary layer at the shock impingement location. Little difference is observed in the performance at design conditions, but at lower mass flow the modified blades show an increase in turning and higher static pressure ratio. This improvement was attributed to thinner boundary layers due to aspiration. Another beneficial effect observed is the delay in rotor stall.

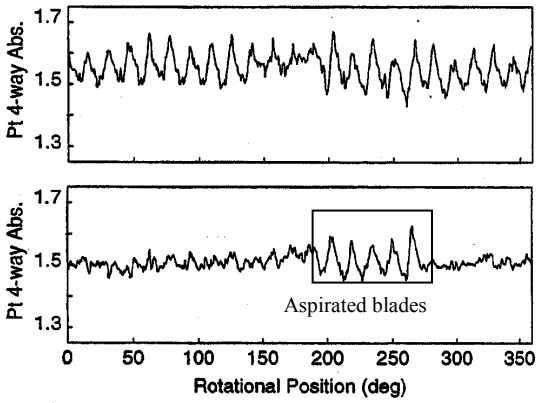

Fig 3.4: Comparison of exit total pressure of rotor with suction at design point (upper) and heavily loaded point (lower) (Kerrebrock et al. [2])

The clearest evidence of the effects of boundary layer aspiration on the rotor outflow comes from the comparison of exit total pressure for the aspirated rotor at the design point and the heavily loaded point. Referring to the top trace, the flow off the suction surface of each blade is clearly defined as a region of large total pressure except for three or four blades just ahead of the aspirated blades.

The aspirated blades, which appear in the phase range of 200° to 280°, have outflow structure not very different from the normal blades at design point. In the highly loaded case, the normal blades have lost the outflow structure of the design point but the aspirated blades clearly retain it. Thus, one effect of the boundary layer removal is to cause the blades to behave as though they are still at the design condition rather than a highly loaded condition.

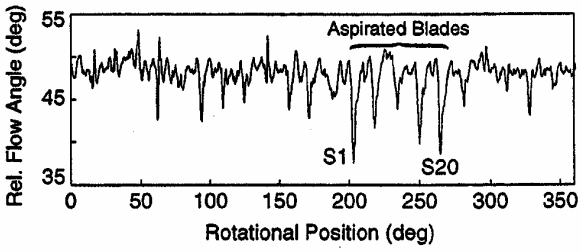

Fig 3.5: Exit flow angle from the rotor (Kerrebrock et al. [2])

The aspirated blades in the figure 3.5 exhibit a lower exit flow angle from the rotor indicating another important effect of the boundary layer removal to increase the blade turning capacity. This is more prominent for the first, fourth and fifth aspirated blades.

Since aspiration deals at the level of blade boundary layers, Kerrebrock et al. [3] give a comprehensive review of what happens at the boundary layer with suction and concludes that the best range of positions to apply aspiration is close to start of a strong pressure recovery region where the exponential magnification is greatest over downstream.

Godard et al. [27] conducted a parametric study of a two-dimensional aspirated diffuser at subsonic and high subsonic inlet Mach numbers with the objective of determining the optimal slot location for aspiration. Their approach is unique in a way that it combines passive control with the active control in the conception of the blade. The first part of the study demonstrates that the combination of strong curvature and diffusion variation can successfully restrict the separation point location in less than 0.5% of the total length of the curved section of the diffuser when the inlet Mach number increases from 0.55 to 0.75. In this way, the flow separation can be made dramatically less sensitive to this operating condition (inlet Mach number). The second part of the study studies the influence of three slot positions in proximity of the separation point: before separation, at the separation and just after the separation.

Their results show the best configuration to be the location of slot at the separation point (figure 3.6). This configuration requires the least amount of mass flow rate to reattach the flow. With the slot positioned upstream the separation point, the aspiration requires 1% higher mass flow rates than in other locations to achieve the same desired effect. In the configurations studied, one has a greater interest in keeping the aspiration device downstream the separation point to have the same control authority for lower aspirated massflow. The required aspirated massflow to suppress the separation is also found to be quite independent of the inlet Mach number (from subsonic to high subsonic range).

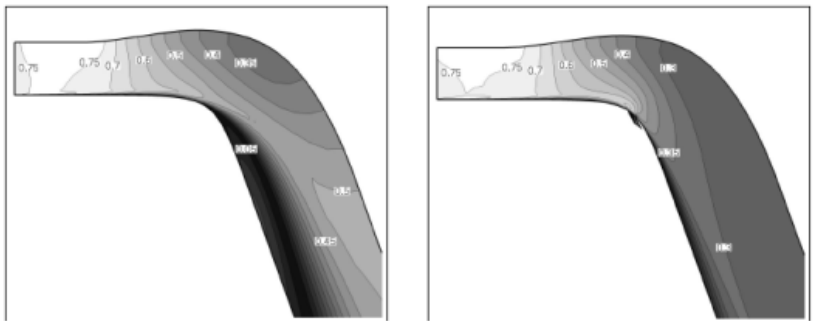

Fig 3.6: Mach number contours for diffuser without suction(left) and diffuser at suction position b(right) with inlet Ma=0.75 (Godard et al. [27])

Dang et al. [8] have come up with general design ideas and strategies that can be put into practice to easily convert some conventional blade designs into optimised aspirated blade designs. The underlying idea of their approach is to exploit the three-dimensional inverse design methods to have an optimum combination of tailored pressure loading with surface aspiration resulting in a minimal amount of sucked flow for a net aerodynamic performance improvement at on and off design conditions. In this method, the primary prescribed quantities are:

- The blade stacking line
- The blade thickness distribution
- The blade pressure distribution (defined as local static pressure difference between upper and lower surfaces at fixed axial positions)

For the input conditions, the camber geometry via flow tangency condition along blade surface is calculated. The challenge is to pick up values of blade stacking line, blade thickness distribution and pressure loading distribution for satisfactory design that can yield optimum performance and is aero mechanically acceptable. The amount and location of the flow transpiration (aspiration or blowing) is not derived by the method; it is user prescribed. The aspiration boundary condition along the blade surface is the prescribed aspirated velocity component normal to the blade surface.

To illustrate the potential merits of this method, the authors optimised the design of a supersonic rotor blade row with the above method. The suction rate required to prevent the boundary layer separation from the shock boundary layer interaction is reduced to 0.3% of the inlet flow from 2% of the inlet flow after optimization. This method demonstrates that aspiration, when used as an add-on to an existing design can require excessive amounts of suction, whereas, with a tailored pressure-loading distribution combined with the aspiration scheme and executed with the inverse design method, a significantly lower amount of suction is needed.

At the aerodynamic design point, the rotor inlet relative Mach number varies from 1.1 at hub to 1.4 at tip. The rotor contains 56 blades but it is not at critical condition necessitating aspiration. The blade count is reduced to 42 from 56 blades to create a critical state with strong adverse pressure gradients along the suction surface with an associated shock. This cascade with the same blade but with reduced solidity is referred to as “original blade”.

The CFD simulation indicated a spilled shock passage for the original blade at a casing backpressure of 3.6. At this backpressure to pull the shock back inside the blade passage at a location similar to that of R2-56 blade, a suction amount of 2% of the inlet massflow is needed to prevent boundary layer separation. The aspiration zone is located behind the shock on the suction surface of the blade from hub to 95% span. However, the suction coefficient Cq=0.02 is excessive in light of the blade internal volume and unacceptable due to its adverse potential system efficiency impact.

A re-design of the original blade is undertaken to significantly reduce the aspirated massflow and recover the performance of R2-56. This blade is called “new design”. The new design incorporates a tailored pressure loading that increases the loading in the inlet and exit zones of the blade and reduces the core loading. This is done without suction initially by the authors but to restore the conditions to that of R2-56, success is achieved by incorporating suction with Cq=0.003,i.e., 0.3% of the inlet massflow is aspirated in new design as compared to 2% in original design.

This loading strategy has an effect of reducing Mach number upstream of the shock that reduces the strength of the shock hence the strength of shock/boundary layer interaction. It is noted that this refinement process is successive and can take a number of trials to arrive at satisfactory designs. The improvement in rotor performance in the successive designs is shown below by the Mach number flow field in figures 3.8a,b:

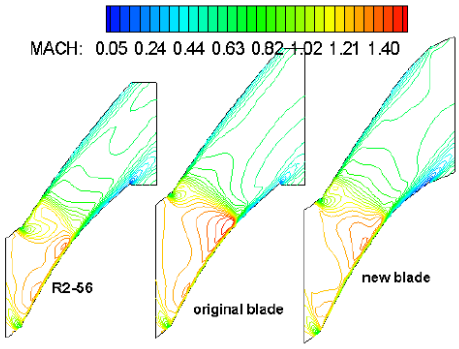

Fig 3.7a: Mach number at mid-span (Dang et al. [8])

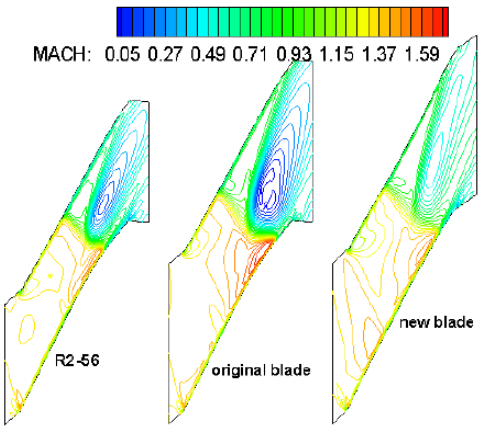

Fig 3.7b: Mach number at 95% span (Dang et al. [8])

The adiabatic efficiency of the rotor with and without aspiration is studied and compared by the authors. The upper limit of adiabatic efficiency is defined as the case where the aspirated massflow can be used fully and the lower limit of adiabatic efficiency is the case where the aspirated massflow is not thermodynamically useful.

Configuration	$\eta_{adiabatic}$ (%)
R2-56 blade (no aspiration)	92.7
Original blade (Cq=0.02)	89.5 (lower limit) to 91.3 (upper limit)
New design (Cq=0.003)	93.9 (lower limit) to 94.1 (upper limit)

Table 2: Adiabatic efficiencies of the rotor configurations (Dang et al. [8])

With better blade design and improved pressure distribution in the new design with lower aspiration flow rate the adiabatic efficiency of the rotor improves by approximately 1.5%.

Hubrich et al. [9] have studied the influence of boundary layer aspiration on the shock/boundary layer interaction to identify the possible benefits in a transonic rotor. An extensive numerical study is done for the datum blade (no aspiration) and for two aspiration location positions (44%c and 53%c) for one speed line and varying back pressure levels ranging from choked conditions to stall.

It is found that the working range of transonic rotor with an inlet Mach number of 1.2 and pre-shock Mach number of 1.35 can be increased by aspirating 2% of the inlet flow on the suction side of the blade in such a way that the maximum diffusion factor and maximum pressure ratio can be increased by 10% as compared to the datum case. For smaller pressure ratios with respect to design pressure ratio, the boundary layer aspiration is located in the supersonic region and thus creates additional losses due to flow acceleration in the divergent channel resulting in a higher pre-shock Mach number leading to higher losses.

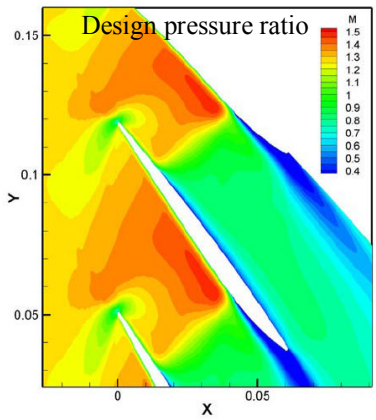

Fig 3.8a: Mach number, Datum, no aspiration, PR=100% (Hubrich et al. [9])

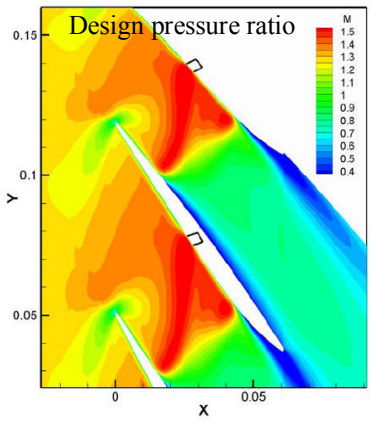

Fig 3.8b: Mach number, Aspiration at 44% c, PR=100% (Hubrich et al. [9])

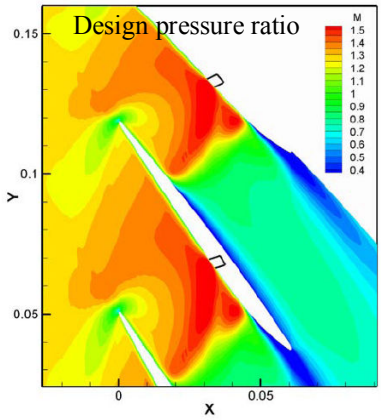

Fig 3.8c: Mach number, Aspiration at 53%c, PR=100% (Hubrich et al. [9])

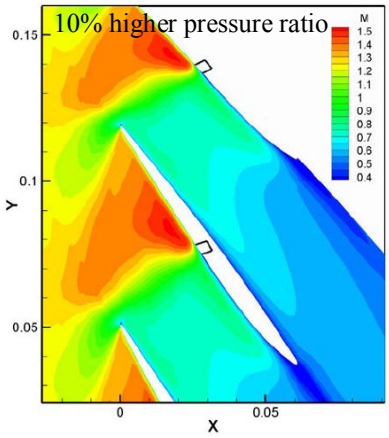

Fig 3.8d: Mach number, Aspiration at 44% c, PR=123% (Hubrich et al. [9])

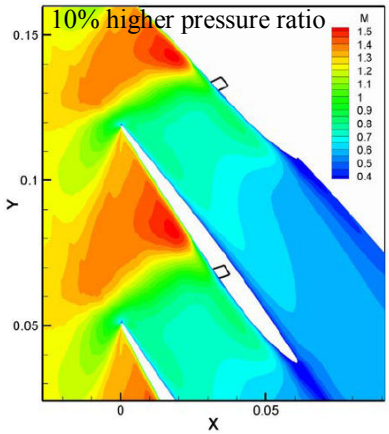

Fig 3.8e: Mach number, Aspiration at 53%c, PR=123% (Hubrich et al. [9])

In the figure 3.8a, the boundary layer thickens after interaction with shock on the suction surface and also on the pressure surface due to impingement of the passage shock on the pressure side. In front of the LE a detached bow shock wave is present which rejoins the flow in the passage and reaccelerates to supersonic flow. The high acceleration peak on the LE is due to the local acceleration caused by the high inlet flow angle. In fig 3.8b, the influence of aspiration at 44%c shows the interaction between the shock wave and the expansion wave.

The location of interaction between the expansion/recompression connected on the suction location and the passage shock is shifted from the normal shock wave to the pressure side. Also, the boundary layer on the pressure side is slightly thinned due to expansion of the passage shock. In fig 3.8c, the boundary layer is thinned due to aspiration and becomes thicker soon after the aspiration slot due to Prandtl-Meyer shock expansion wave. Both the aspiration configurations yield more or less the same flow structure at the design pressure ratio.

In figures 3.8d and 3.8e, the rotor is on the extent of stall at 10% higher pressure ratio resulting from the application of aspiration. In both the aspiration configurations, the shock foot bends locally to the suction location. Both the aspiration locations prevent the shock from moving further upstream that would stall the rotor.

Chen et al. [13] have done an extensive numerical study to investigate the influence of aspiration parameters to improve the performance of highly loaded compressors. These parameters are 1) location of the suction slot, 2) suction flow rate, 3) suction slot geometry and 4) aerodynamic parameters of the cascade (e.g. solidity and incidence). These studies were done on a NACA65 stator with the commercial flow solver FLUENT with K-ε turbulence model. The slot geometry is a hexahedron and the slot extends from the hub to the tip of the blade. The calculations have been done with a low subsonic inlet Mach number of 0.2 and the solidity has been modified to simulate high levels of loading in the cascade.

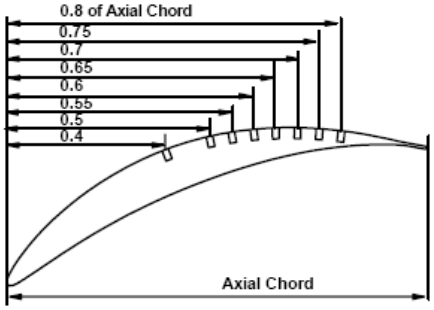

Fig 3.9: Location of suction slots on the blade suction surface (Chen et al. [13])

Figure 3.10 above shows the location of suction slots investigated by the authors. The suction slot has been positioned from 40-80%c_x of the blade. The suction flow rates studied are 0.5%, 1% and 1.5% of the inlet massflow in the cascade. In a cascade with solidity of 1.364 and 0° incidence, all the suction rates yielded lower total pressure losses and better flow deviations at all slot positions. The results got better as the suction rate was increased progressively. Also, the slot location at 70%c_x was found to be the optimum position in terms of cascade performance.

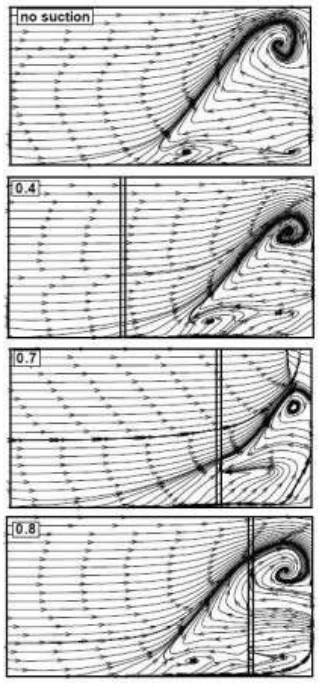

Fig 3.10 a: Limiting streamlines on suction surface with different axial slot locations (Chen et al. [13])

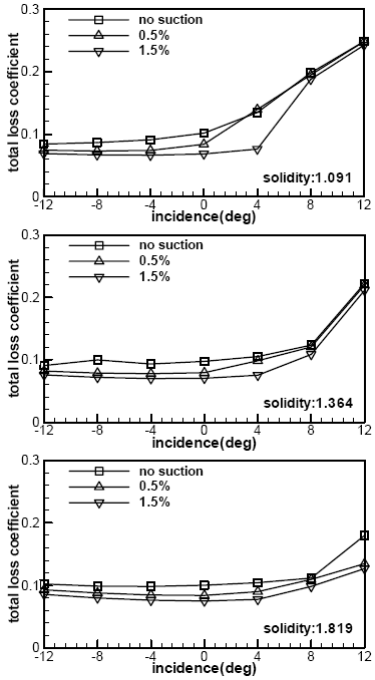

Fig 3.10b: Total pressure loss coefficient at different solidities (Chen et al. [13])

The limiting streamlines show the singularities on the wall associated with the flow losses. Generally, the singularities or critical points are enveloped in the dividing streamline on the walls in case of high level of losses. Figure 3.10a shows the flow topology on the wall when 0.5% of the inlet flow is aspirated in the slot. When the suction slot is placed at 0.4 of the axial chord, there is a slight improvement in the radial distribution of the flow, the radial extent of the separation is reduced at the tip of the blade and the strength of the focal point of separation on the suction side is reduced.

When the slot is placed at $0.8c_x$, it is placed in the separated region of the flow and does little to improve the flow separation. When the slot is placed at $0.7c_x$, the extent of flow separation is considerably reduced as seen from the diminishing strength of the focal point of separation and thin dividing streamline. As indicated by Merchant [4, 5, 19], Godard et al. [27] aspiration is effective in the vicinities of the separation point.

Fig 3.10b shows the influence of solidity and the suction rate on the total pressure losses with incidence when the slot is fixed at $0.7c_x$. As the solidity of the cascade reduces from 1.819 to 1.091, the total loss of the cascade increases rapidly within the positive range of incidence due to increased blade loading. For all the suction flow rates, the cascades with solidities of 1.364 and 1.819 have little change in total pressure losses until +8° incidence.

However, as the suction rate increases to 1.5% of the cascade inlet flow, the rapid increase in total loss for the cascade with solidity of 1.091 delays to 4° incidence indicating that boundary layer suction is an effective way to increase the stable operating range of a highly loaded compressor. At 8° and 12° incidences the suction has little effect on the control of losses. Any further increase in suction rate must be given consideration to the global engine cycle and hence the authors do not investigate the influence of increasing the suction rate beyond 1.5% of the inlet flow.

As for the suction slot itself, the authors also investigate the influence of width of the slot and the inclination of the slot with respect to the inlet flow. Increasing the width of the slot from 1mm to 2mm renders better flow control by aspiration; the slot inclined at –45° to the incoming flow offers the best results to trap the boundary layer.

Chakraborthy et al. [22] study the experimental application of a boundary layer aspiration on a compressor cascade in a different way. Their approach is to apply distributed boundary layer aspiration in forms of perforated holes positioned span-wise and chord-wise on the suction side of the NACA65 blade (figure 3.11). The experiments were done at low subsonic inlet velocity of 10 m/s on a linear cascade of 5 blades.

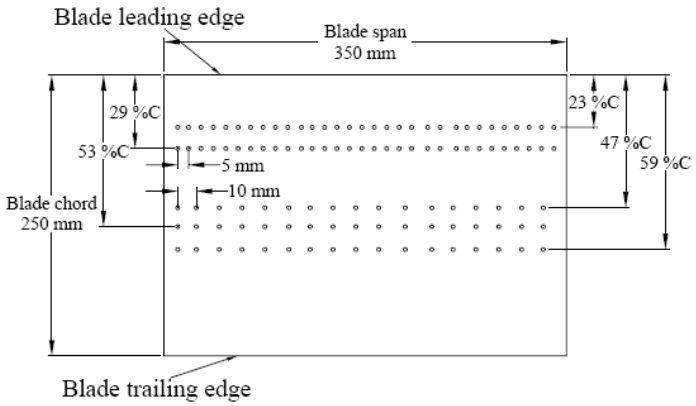

Fig 3.11: Perforated aspiration holes on the suction side of the NACA 65 blade (Chakraborthy et al. [22])

Figure 3.11 shows the perforated holes for aspiration on the suction side of the blade. The experiments were done over a range of incidences from –10° to 6° on the baseline blade without aspiration and with suction rates corresponding to 0.1, 0.15 and 0.2% of the inlet flow.

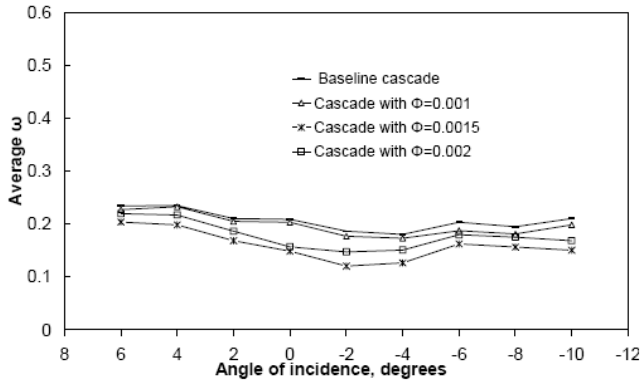

Fig 3.12: Total pressure loss coefficient at mid-span (Chakraborthy et al. [22])

The experimental measurements of the total pressure loss coefficient at mid-span (figure 3.12) show a reduction in total losses for all the incidence angles and the lowest level of losses are obtained with the suction rate of 0.15% of the inlet flow making it an optimum value of the suction rate in this case.

Increasing the suction rate to 0.2% of the inlet flow shows an increase in losses may be attributed to higher than necessary amount of aspiration leading to the removal of high energy free stream massflow. For all the suction rates, the lowest losses are observed for the incidence of –2°. It is due to lower level of adverse pressure gradients at negative incidence in the vicinity of the design point that we observe the lowest level of losses for this point.

Gbabedo et al. [25], in a numerical and experimental study on a PVD (prescribed velocity distribution) stator, demonstrate the control of three-dimensional separation by tailored boundary layer suction. Studying the three-dimensional flow topology with the limiting streamlines, they show that three-dimensional separation in the suction surface and endwall corner arises at the place where the limiting streamlines springing from the saddle point near the leading edge meet the suction surface.

Removing these limiting streamlines effectively removes the three-dimensional separation in the corner. Testing different aspiration slot configurations on the hub and the suction surface of the blade, they show that suction, which does not remove the limiting streamlines before it intersects the suction surface, reduces it but does not completely eliminate it.

The optimum slot location should be long enough to ensure the removal of limiting streamlines; the slot is recommended to run close to the suction surface from a position just downstream of the peak suction on the blade up to near the trailing edge. In their case, the researchers demonstrate that an appropriately applied boundary layer suction of up to 0.7% of inlet massflow can control and eliminate typical three dimensional hub corner separations over a range of operating incidences.

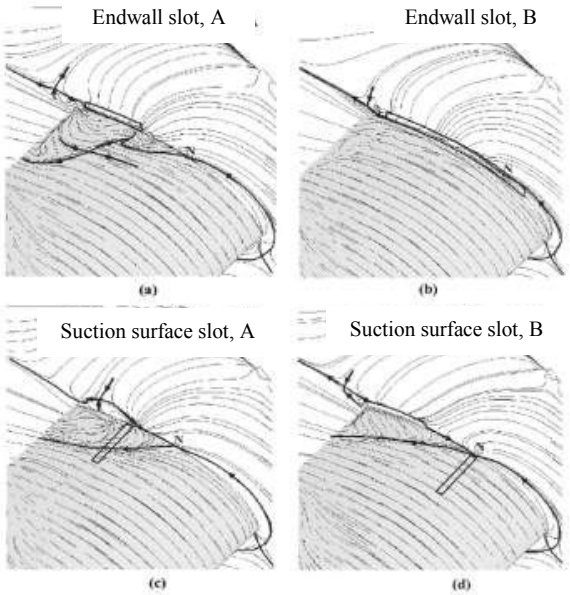

Fig 3.13: Limiting streamlines on the endwall and suction surface for the four configurations at the design point (Gbabedo et al. [25])

In the configuration (a) with the endwall slot A, the separation is clearly visible on the suction surface of the blade; as the slot is placed downstream of the separation point N, it is not very effective in controlling the separation.

In configuration (b) with the endwall slot B, the separation region has been practically eliminated since the endwall slot is extended upstream to capture the dividing streamline. The elimination of separation confirms that under inherent adverse stream-wise pressure gradient, the formation of three-dimensional separations is associated with the interaction of the dividing streamline with the suction surface. In the configurations (c) and (d), the aspiration slots on the suction surface are only able to reduce the separation marginally but not completely eliminate it. This shows that the separation which originates from the endwall may not be effectively removed by a flow control method employed on the suction surface.

3.3.2 BIBLIOGRAPHIC REVIEW OF ASPIRATION ON HPC STAGE

Merchant et al. [4, 5, 19] have designed a high-speed aspirated compressor stage to achieve a total pressure ratio of 3.43 at a tip speed of 457 m/s. This design is a substantial increase in the pressure ratio achieved by conventional compressors typically between 2 to 2.3 close to the maximum loaded operations. The bleed configuration of the aspirated stage is in figure 3.14:

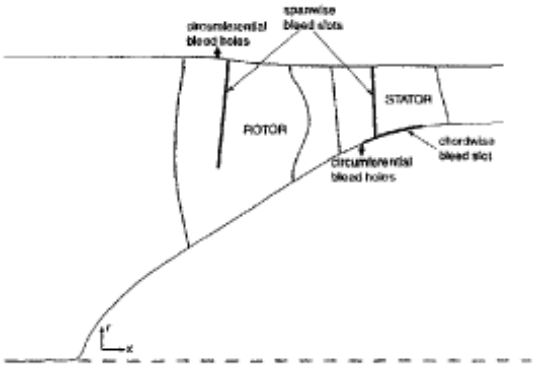

Fig 3.14: Schematic of the bleed configuration (Merchant et al. [4, 5, 19])

The span-wise slot on rotor extends from 40% span to the tip; the span-wise slot on stator extends from hub to tip, the circumferential slots span the entire pitch and the chord-wise slots extend from 25-75%c. The preliminary estimate of the location and bleed requirement of the circumferential slots is determined from shock impingement locations on the rotor shroud and the stator hub. Note that due to tip shroud on rotors, the tip clearance vortex is non existent.

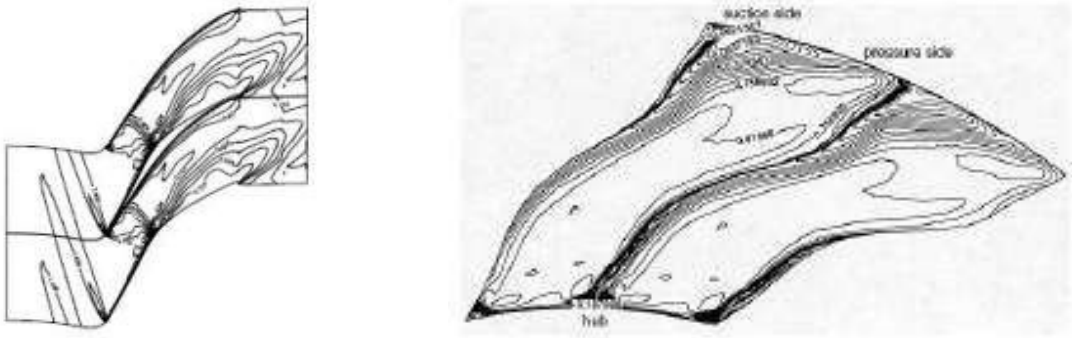

Fig 3.15: Rotor Mach number contours at 95% span (left) and the exit wakes (right)(Merchant et al. [4 ,5, 19])

The relative Mach number contours at 95% span show the foot of the shock structure retained at the point suction on the suction side of the blade. There is eventual growth and separation of the boundary layer at 70% chord.

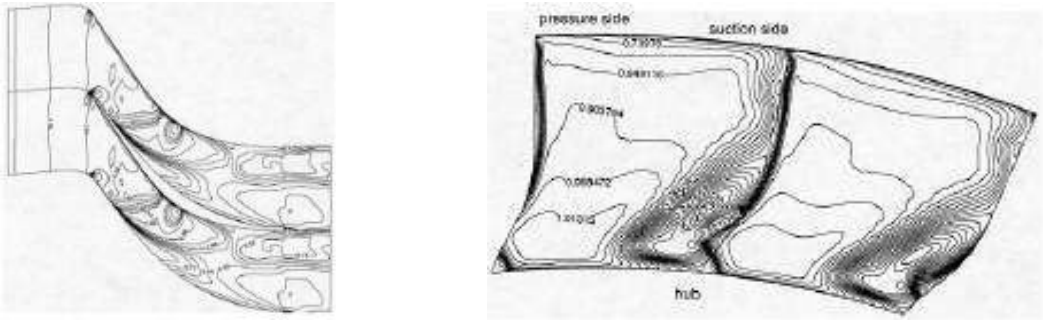

Fig 3.16: Stator Mach number contours at hub (left) and in the exit wake (right) (Merchant et al. [4, 5, 19])

Impingement of the passage shock at 10% chord and a high supersonic Mach number upstream of the shock is responsible for the separation on the pressure side. The effect of chord-wise suction slot to suppress the corner separation is limited. The stage achieves a peak efficiency of 86.8%.

Merchant [4] further provides an insight into the blade design methodology of the aspirated blades since their requirements are different from conventional blades. A few of the design considerations proposed are given below:

1) Thickness distribution: The position of maximum thickness is not critical for subsonic locations and is mainly driven by required pressure distributions. But for transonic and supersonic sections, the location of maximum thickness cannot be too forward on the blade.

2) Leading edge design: The thickness requirement of the aspirated blade constraints the design of the blade leading edge. The leading edge design must be so as to avoid the spikes or over-speeds in the pressure distribution, which may cause local flow-separation and loss of operating range. The primary consideration is to obtain a smooth pressure distribution near the leading edge.

3) Trailing edge design: Diverging trailing edge concept has been successfully applied to increase the aft loading of the aspirated blades. Another advantage of this concept is that pressure gradient on the suction surface can be relaxed and better flow deviation profiles are also obtained.

4) Pressure side design: The large turning combined with relatively high inlet Mach numbers leads to adverse pressure gradients on the blade pressure surface up to mid chord even for flat pressure surface; this is the consequence of the increase of local stream-tube section because of the suppression of the separation on the opposite wall under the influence of aspiration (Godard et al. [27]). The impingement of passage shock may lead to the separation of the pressure side boundary layer. Hence, pressure surface design is more critical for aspirated blades than in the conventional blades.

Gümmer et al. [12] numerically investigate the effects of aspiration on the rotor tip in the flow path of a high-speed research compressor and a shrouded stator hub. Using aspiration on the casing for both rotor and stator, they are able to eliminate the corner vortex on the stator hub efficiently and weaken the strength of the rotor tip vortices. They make the first numerical investigation of aspiration on an un-shrouded rotor. In their case, on the rotor, the use of 1% bleed rate taken at the radial tip clearance through an axisymmetric slot proved to give some control over the tip leakage vortex flow.

The tip leakage vortex and the associated three-dimensional separation line upstream of the vortex trajectory become more aligned with the main flow. The area covered by the reverse flow along the casing sidewall is reduced and there is lower blockage in the rotor tip region. Deviations are almost unaffected but the losses are reduced. On the stator, a bleed rate of 3% of the inlet mass flow taken through casing holes within the stator passage proves to give control over the suction side corner separation. Deviations and losses are significantly improved.

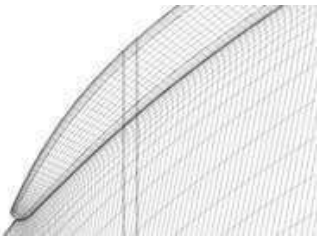

Fig 3.17a: Mesh of aspiration slot on rotor casing (Gümmer et al. [12])

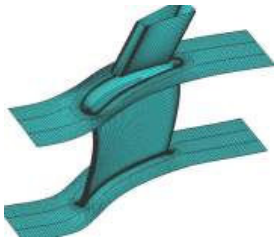

Fig 3.17b: Mesh of tailored OT(off take) on the stator casing (Gümmer et al. [12])

The above figures (3.17a, 3.17b) show the aspiration slot on the rotor casing and the tailored off take on the stator casing to bleed flow from the flow path. The tailored OT (off take) is a design iteration from a initially conceived circular OT that causes significant local perturbations in the flow field and is not efficient in the control of hub corner separation on the stator. Also, the boundary layer at the wall thickens at the intersection of the OT with the casing.

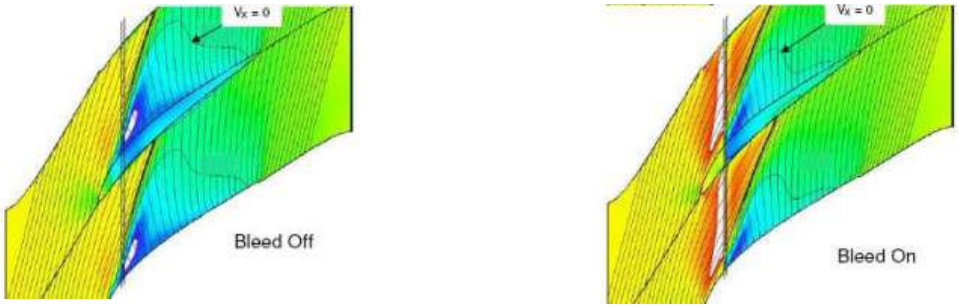

Fig 3.18: Contours of axial velocity and relative velocity streamlines at mid gap radial height without aspiration (left) and with aspiration (right) at the design point for rotor (Gümmer et al. [12])

When the bleed is not active the flow enters the passage at almost uniform axial velocity and approaches a three-dimensional separation line which originates at the suction side near the leading edge and impinges on the pressure side of the adjacent blade at 30% chord. The separation line is closely linked to the beginning of the tip leakage vortex. Just downstream of the separation line the separated zone with zero axial velocity is evident.

The activation of flow bleed accelerates the inlet flow as seen also upstream of the slot. The higher momentum flow retards the separation of the flow and displaces the separation line slightly. The separated zone with zero axial velocity is found to be reduced by 30% but not suppressed. This has an effect of decreasing the strength of the tip leakage vortex.

Fig 3.19: Stator surface Mach number contours and limiting streamlines without aspiration (left) and with aspiration by tailored OT (right) (Gümmer et al. [12])

The stator surface without active aspiration from the off take on the casing wall shows some level of separation on the blade suction side as seen by the limiting streamlines (figure 3.19). When the aspiration is activated by the tailored off take, the casing boundary layer close to the stator exit is removed. The tailored OT is able to capture the bulk of the cross passage flow approaching the suction side. At 70%c, a small fraction of the cross passage flow travels up to the suction side and then is drawn back towards the casing by the off take. The size of the separation zone has been reduced appreciably by the casing aspiration from the tailored OT.

3.3.3 BIBLIOGRAPHIC REVIEW OF ASPIRATION ON FAN STAGE

Merchant et al. [11] extend their experimental and CFD studies to design and test a high-pressure ratio aspirated fan stage that can achieve a pressure ratio of 3.4 at a tip speed of 457 m/s. The stage aspiration scheme and the aspiration in particular are shown in below (figure 3.20):

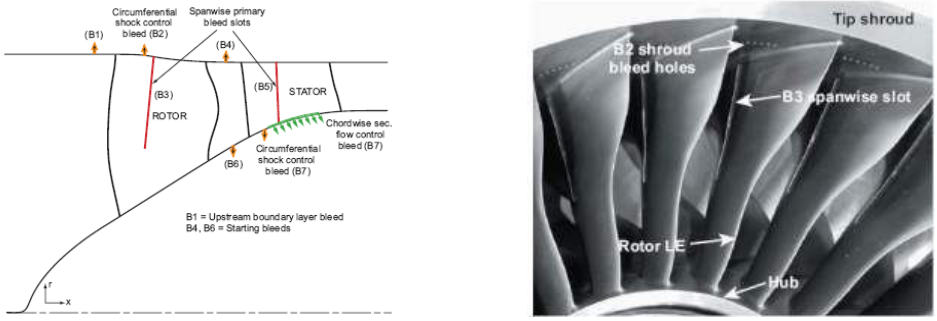

Fig 3.20 : Aspiration scheme of the fan stage (left) and the rotor (right)(Merchant et al. [11])

Stage pressure ratios exceeding 3 are obtained with an aspiration flow fraction of 3.5% of the stage inlet massflow. This is a massive improvement in terms of economising massflow over their previous studies. The design aspiration requirements are presented in table 3:

Aspiration location	Designation (in fig. 3.21)	Aspiration fraction (%)
Rotor shroud	B2	1
Rotor span-wise	B3	1.5
Stator span-wise	B5	2
Stator hub(circumferential)	B7	1
Stator hub(chord-wise)	B7	1

Table 3: Stage bleed requirements (Merchant et al. [11])

The aspirated fan stage is tested from 50% to 100% design speed. The measured pressure ratio and the efficiency of the stage are presented below (figures 3.21a,b)

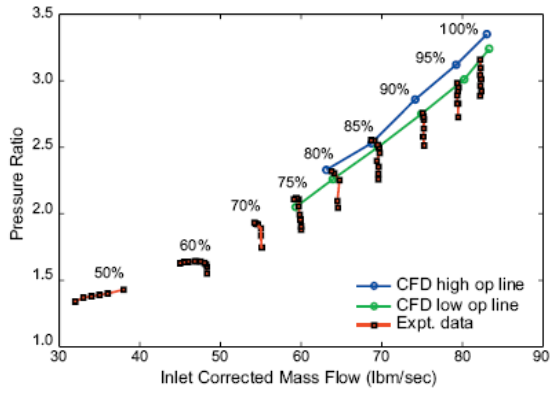

Fig 3.21a: Compressor pressure ratio map (Merchant et al. [11])

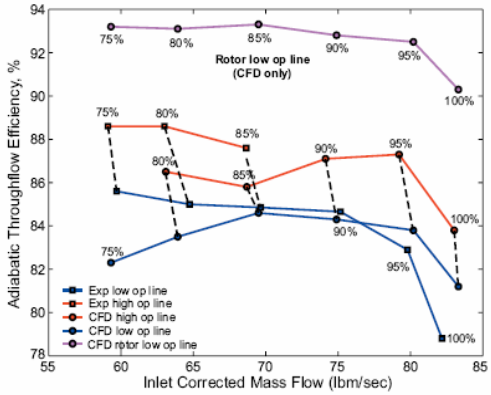

Fig 3.21b: Measured and calculated efficiencies on the low and high operation lines(Merchant et al. [11])

Their studies show that aspiration fixes the passage shock position, particularly in the tip region. The good correlation between experiments and CFD suggests that aspiration is effective in controlling the shock system and also achieving a started shock system at operating speeds above 90% which is necessary for obtaining the desired inlet massflow and pressure ratio. Good performance is achieved at the off-design conditions too. The measured stage performance is found to be less sensitive to reduction in aspiration flow than predicted by CFD. Performance close to the design intent and in good agreement with CFD predictions is obtained.

3.3.4 BIBLIOGRAPHIC REVIEW OF BLOWING ON COMPRESSOR CASCADE

An interesting study of boundary layer blowing is done by Song et al. [26] on the performance of highly loaded compressor cascades. Their approach to implement the flow control is passive blowing i.e. no energy expenditure is required. Their study is performed on a highly loaded linear compressor cascade having NACA65 blade with commercial CFD solver FLUENT and K-ε turbulence model. This study is well supported by the corresponding experimental correlation.

In their approach, the air injection is realised via hole/slot penetrating through the pressure side and the suction side of the blade under the effect of static pressure difference between two sides. The mechanism is to drive the high momentum fluid near the pressure side to energize the low momentum suction side flow to increase its ability to withstand the adverse pressure gradients.

Their parametric studies have investigated the influence of hole diameter (1.2mm to 4mm), hole axial position (70, 80, 90% c_x) and the hole radial location (2.5% to 25% of blade span). In all the cases, the hole orientation is kept at 30°. Also, several configurations such as one hole, two holes and three holes configurations were studied. The optimum performance was achieved when holes were located at 15% of the blade span with a hole diameter of 4mm. It is noted that the transported massflow from pressure side to the suction side of the blade increases with the number of holes due to increase in cross section.

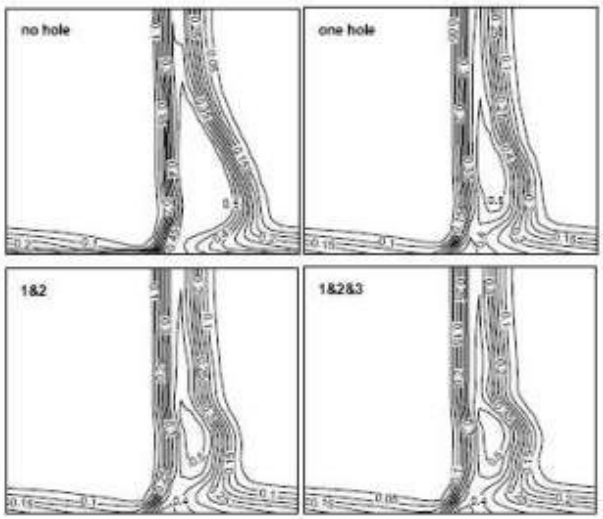

Fig 3.22: Contours of total pressure loss coefficient at the lower half of the cascade exit (Song et al. [26])

The results show that compared to the configuration with no hole, all the other air injection configurations reduce the size of high loss regions significantly. The multi-hole configuration (3 holes) transports larger quantity of high momentum flow from the pressure surface to the suction surface and offers better control of separation.

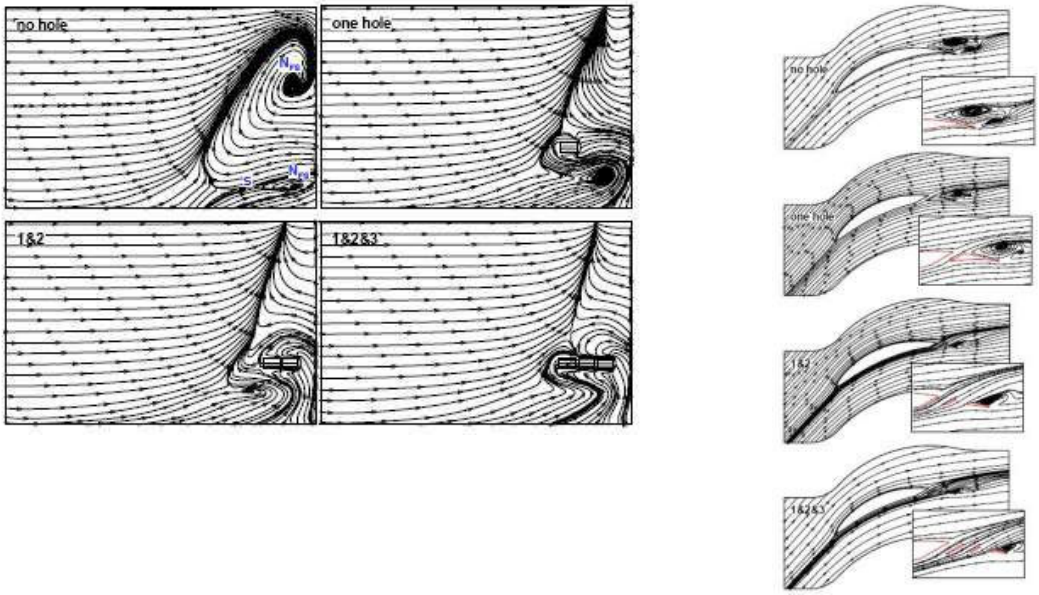

Fig 3.23: Limiting streamlines on the lower half of the suction side (left) and at 15% blade span (right) (Song et al. [26])

The limiting streamlines on the blade surface show the influence of the air injection on the flow structure (figure 3.23). The flow separation occurring on the suction side of the blade is a typical closed separation, starting from saddle point S and ending at the spiral node (or focus) N_{FS} located at 30% of the blade span. Another focus N_{FS} in the corner between the suction side and the endwall is associated with the corner separation. Air injection modifies the flow field of the cascade. The size of the flow separation in the axial direction is reduced by the three holes configuration.

Near the mid-span, the reverse flow occurs for the cascade with air injection. This is due to increased blade loading and the reverse flow does not increase the blade losses near the mid-span. The limiting streamlines in the blade-to-blade plane at 15% span show the progressive reduction in flow separation in the pitch-wise direction with the increasing number of holes. The flow separation is retarded progressively near to the blade trailing edge and decreases in strength with the increased transported massflow associated with the increasing number of holes.

Kirtley et al. [10] have designed and tested a full annulus of a fluidic flow controlled compressor stator ring in the third stage of a four stage GE Low Speed Research Compressor (LSRC). The design intent is to reduce the vane count by 30%, load the stator to the extent of stall and then employ boundary layer blowing via discrete steady jets on the suction side of the blade to control to re-attach boundary layers and restore the design point stage matching. The blade count of the cascade is reduced to 53 blades from 74 blades and the cascade solidity of near unity is achieved. Using three-dimensional RANS simulations, the flow separation characteristics of the boundary layer are studied. 19 flow control holes were drilled on the suction side of the blade just aft of the suction peak and upstream of the computed separation point. The flow controlled airfoil and the stator rig are shown below (fig 3.24a,b)

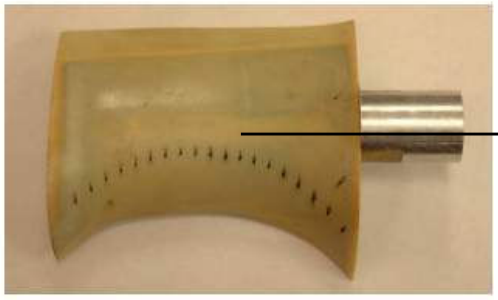

Fig 3.24a: Flow controlled airfoil(with blowing holes) (Kirtley et al. [10])

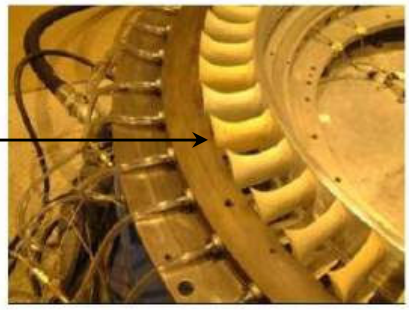

Fig 3.24b: Flow controlled airfoil installed in stator rig (Kirtley et al. [10])

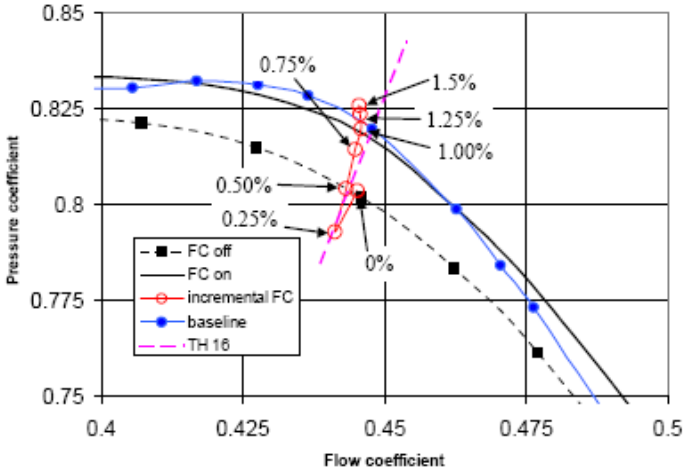

Fig 3.25: Compressor pumping with incremental flow control (Kirtley et al. [10])

Figure 3.25 shows the effect on the compressor of incrementally increasing the blowing rate from 0% to 1.5% of the through-flow at throttle point (TH 16 in figure 3.25). At 0.25%, the injected momentum is low enough to the extent of being detrimental because the correspondingly low velocity ratio further weakens by added massflow in the boundary layer through a retarding shear force. At 0.5%, the equivalent performance to the no blowing condition is restored. At 0.75% blowing, the injected momentum is sufficient to delay separation and reduce the stator 3 deviation angle. Past 1% blowing rate, the separated flow is fully attached and the gain in performance is mainly from the additional total pressure blown into compressor.

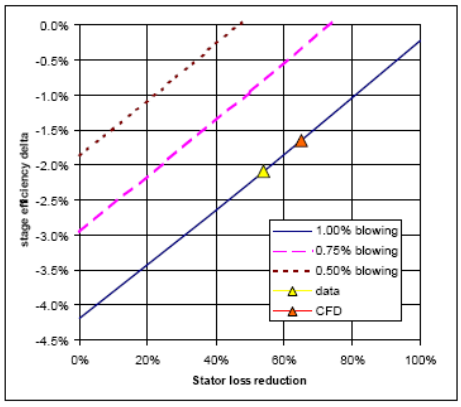

Fig 3.26: Stage efficiency characteristics (Kirtley et al. [10])

Figure 3.26 shows the casing static pressure rise characteristics for each of the stages. Stage 3 shows a significant improvement in performance due to reduced losses in stator by blowing. The stage 3 characteristics fall off towards stall due to high loading. The flow characteristics on the stage are healthier and the pressure rise is well beyond that from the blowing pressure. The pressure rise characteristic of the stage 4, while improved with blowing and parallel to stage 3 are still somewhat disappointing relative to that of stage 4 with the baseline conventional stator 3 in front of it which produces a 2.5% higher pressure rise.

The authors also employ a generalised analysis to calculate the system level penalty in an engine cycle study to achieve the increase in loading by 30%. The flow control air can be extracted from the compressor exit using a supplemental pump to represent the work from a downstream stage. Pump efficiency similar to the stage efficiency can be used as follows:

$$\eta_{compressor} = \frac{power_{ideal}}{power_{actual} + power_{blowing}} \tag{3.1}$$

For various levels of blowing and stator loss reduction the figure 3.26 above shows the stage efficiency penalty associated with stator flow control. For the current design, the CFD studies indicate a stator total pressure drop at 35% of the baseline high solidity stator for a 65% reduction. This results in a 1.6 penalty in stage efficiency for 30% increase in stator using 1% blowing. Penalty can be severe if the mixing losses are large and if the blowing is not as efficient as shown by CFD. If flow control can be optimised to blow 0.5% flow to achieve the same loading then the penalties can be significantly reduced. The experimental data shows a reduction of 54% in total pressure losses across the stator versus the baseline stator. The stage efficiency grows to 2.1 points, higher than CFD prediction.

Although the flow control is shown to be effective for this low solidity stator cascade, there are lot of other issues to consider. The weight reduction of the fewer stators is not great when one considers the stator rings are still in place with no reduction in engine length. A more promising approach would be to apply flow control to reduce the number of stages. Also, the complexity of the system, cost, weight and fail safe nature of the flow control schemes must be integrated into the study.

3.3.5 BIBLIOGRAPHIC REVIEW OF PASSIVE CONTROL (VORTEX GENERATORS) ON COMPRESSOR CASCADE

Hergt et al. [24] have experimentally investigated the effect of vortex generators on the compressor stator blade row as a passive flow control method. They used vane type vortex generators that generate two effects to influence the corner separation. The first is an accelerated nozzle flow that is directed into the corner region and the second is the longitudinal vortex that sheds from the tip of the vortex generator and produces a secondary flow on the surface of the vane thus pushing high momentum flow towards the wall. Both mechanisms transport high-energy flow from the outside of the boundary layer into the corner region so that the flow can overcome the adverse pressure gradient without being separated.

The investigation showed that as an application of vortex generators on axial compressor guide vanes, with an aspect ratio of 1, is possible to influence the flow. The loss behaviour could be significantly influenced; the profile losses decrease by 33%. The area of constant loss behaviour at mid-span is enlarged but in every investigated case a loss increase is obtained from 2% to 8.5% of the total pressure loss. Despite the loss increase, an enhancement of the flow deflection of the cascade is achieved.

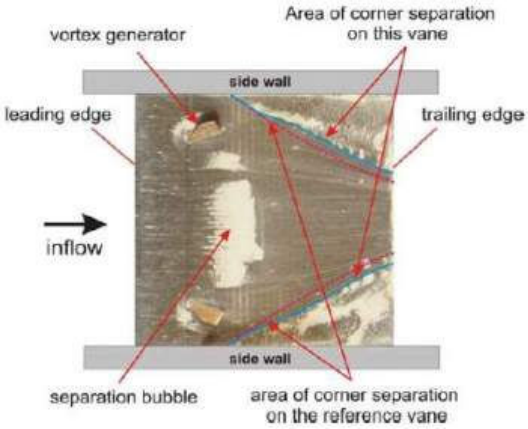

Fig 3.27: Flow visualisation on the suction side of the blade with mounted vortex generator at design point with inlet Ma=0.66 (Hergt et al. [24])

3.4 CONCLUSION

This chapter introduces the concept of flow control and its classification along with its historical demonstration by Prandtl to delay flow separation on a cylinder by boundary layer aspiration. This thesis is dedicated to investigate the application of boundary layer aspiration which is an active flow control method applied on the wall, more precisely the endwalls and blade surfaces of high pressure compressors.

The bibliographic literature on flow control is studied and classified based on its application on fan and compressor cascades and stages. Earlier experimental research to apply flow control techniques on stator cascades is attributed to Loughery et al. [1] in 1970s; they showed the benefits of aspiration on stator cascades over blowing. Technological limitations of that time hindered further progress until the turn of the new century when the aspirated research program at MIT led by Kerrebrock et al. [2] renewed the interested in aspirated compressors.

The bibliographic review introduces various types of flow control methods along with flow control devices studied till now. The most often-used flow control devices are the slots for aspiration as they are favourable to bleed quantities of air over larger spatial extents in regions of flow separations on the endwalls and the blade profiles.

Aspirated compressors capable of achieving pressure ratios of 3.5 have now been designed and tested that are proof of the capability of flow control technologies to dramatically improve the performance of turbomachines. Aspiration applied at various locations has the capability of reducing the endwall effects that cause highest levels of losses in turbomachines. Despite such potential benefits, there are some serious issues to be addressed that yet require meticulous attention. The studies show high levels of air to be aspirated in order to suppress the flow separations and improve the aerodynamic performance of the compressor. This issue has been addressed by some authors such as Godard et al. [27], Dang et al. [8].

Of particular interest is the approach of Dang et al. [8] who propose a redesign of blade adopted to achieve minimized rates of suction to achieve higher levels of blade performance. However, the impact of such methods is yet to be studied. Another issue is the reutilization of aspirated air. The disposal of aspirated air implies thermodynamic penalties on the engine cycle; it remains to be addressed.

The study of flow topologies on the wall has been undertaken by some researchers to implement suction optimally. This approach coincides with the principle intent of this thesis to concentrate on the fine comprehension of flow structures and implement aspiration accordingly.

We may identify some sensitive parameters of interest when implementing flow control in a compressor:

- The geometry of the flow control device (slot, scoop, hole, etc.): depends generally on the amount of flow to be aspirated, also the spatial extent of the device is to be considered.
- The position of the flow control device (numerical and experimental studies indicate vicinities of beginning of separations, particularly aspiration locations slightly downstream of separation start seem to be more effective)
- The suction flow rate: potential to optimise the suction flow rate is one of the critical aspects of flow control when the impact on global performance of the turbomachine is considered.

To conclude, this chapter presents the advancement of state of the art in application of flow control technologies over the past decades. Of more interest is the evolution of approach by researchers from simple implementation of flow control (example Chen et al. [13]) to ever increasing sophisticated approaches by study of flow topologies. (Dang et al. [8], Godard et al. [27], Gbabedo et al. [25])

4. BASELINE STATOR BLADE ROW: DESIGN AND ANALYSIS

4.1 GEOMETRIC CHARACTERISTICS OF THE STATOR BLADE AND THE BLADE ROW

For the present study, a baseline stator blade, that is representative of the first stage stator blade of a modern high-pressure compressor, is designed. The stator blade and the stator blade row represent the baseline test cases for the numerical studies. The design of the stator blade is in accordance to geometric characteristics of the test rig at EPFL on which the blade row is studied experimentally.

The blade has a radial tip clearance of 0.5mm, which introduces a tip leakage vortex and the blade is designed to have a maximum thickness at about $0.5c_x$ to make room for the internal aspiration cavities. In the test rig, the stator blade remains stationary and the tip leakage vortex emanating from the tip clearance region is not migrated towards the neighbouring blades as in a conventional rotor. The casing line is fixed by the overall architecture of the test rig; accordingly the blade height is constrained. These constraints result in AR values significantly lower than unity leading to stronger endwall effects being developed. Based on the sensitivity studies of aerodynamic performance and the operating range, a stator blade row with blade count of 18 is frozen as the baseline stator blade row.

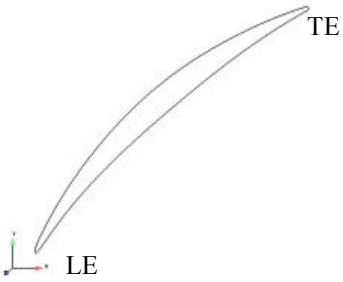

Fig 4.1a: 2D section of the baseline stator blade

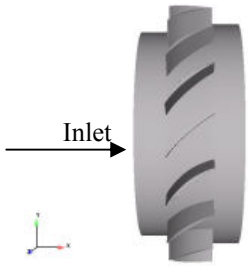

Fig 4.1b: CAD model of the stator blade row

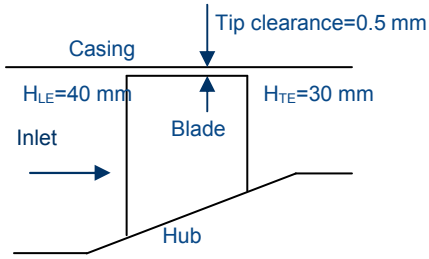

Fig 4.1c: Convergent flow path of the stator blade

The geometric parameters of the baseline stator blade are tabulated below:

Blade count	18
Solidity σ (c/s)	1.14
Blade AR (H/c)	0.41(mean value)
LE r_{hub} / r_{tip}	0.8
Blade metal inlet angle	60°
Blade metal outlet angle	28°

Table 4: Baseline stator blade row geometric characteristics

The inlet and exit blade angles present a stronger curve profile that may lead to stronger flow separations on the suction surface. With the blade count of 18, the blade row solidity is 1.14; higher solidity enables higher blade turning and thus increases the pressure rise in the hub and suction surface corner. With transonic inlet Mach number of 0.8, the stream-wise pressure gradients can be significantly adverse. Hence, the boundary layer momentum thickness and the losses also increase with higher inlet Mach number.

The blade profile is medium loaded; however the ratio of blade span to tip clearance amplifies the three dimensional effects of losses generated at the hub wall. This test case is an opportunity to study the influence on flow control on strong three dimensional separations.

4.2 COMPUTATIONAL APPROACH

A structured multi block mesh is created on the baseline stator geometry with commercial meshing software AUTOGRID. The structured mesh contains 1.5×10^6 cells with $y^+\sim1$. The mesh is shown in figures 4.2a,b.

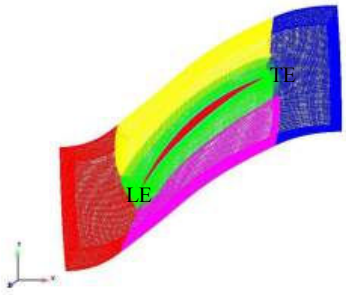

Fig 4.2a: Complete 3D mesh of the baseline stator blade

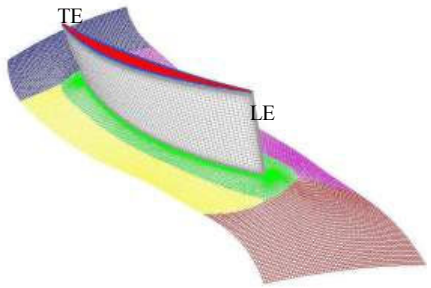

Fig 4.2b: 3D mesh planes

The CFD code used to carry out computational studies is elsA (developed by ONERA). The flow equations are solved by a cell-centred finite volume method using second ordered centred space discretization scheme. Centred schemes are stabilized by scalar or matrix artificial dissipation, including damping capabilities inside viscous layers. The semi-discrete equations are integrated by multistage Runge-Kutta schemes with implicit residual smoothing. The turbulence model chosen for this study is Launder Sharma K-ε model. More information on the solver can be found in Cambier et al. [37].

The methodology involves instructing the solver to run steady flow computations by the Object Oriented Programming approach. The initial computations are carried out using the Spalart-Allmaras turbulence model to ensure the robustness of the calculations. The partially solved flow-field is re-launched with the K-ε turbulence model where an additional turbulent variable is added to the flow field using Bradshaw hypothesis. The calculations were run on the supercomputer NEC SX-6 and a converged solution is obtained in 6000 to 10000 iterations consuming CPU time equivalent of 8 to 10 hours.

4.3 BOUNDARY CONDITIONS

4.3.1 INLET CONDITIONS

- Total Pressure (Profile of theoretical total pressure)
- Flow angle: from 60° to 65°
- Reynolds number: 5.35×10^5 (span-wise mass averaged value)
- Total Temperature (288 K, constant along the span)
- Mach number (Ma_1=0.8, adjusted by the downstream static pressure)
    - The Ma_1=0.8 corresponds to the inlet transonic velocities of the test rig that is expected by the blade row in experiments.
    - The first stage of modern high pressure compressors often experience inlet Mach numbers in the range of 0.7 to 0.8, hence, the Ma_1=0.8 may be considered as a representative condition of a real engine environment but not in a strict sense. The span-wise velocity gradients may vary considerably between the real engine environment and the CFD.

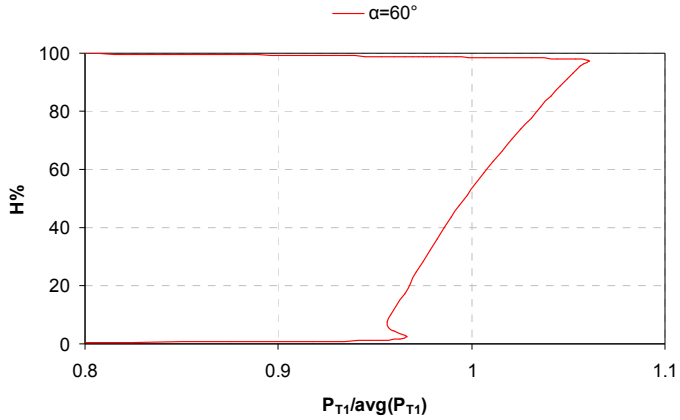

Fig 4.3a: Span-wise mass averaged non dimensionalized inlet total pressure at the design point

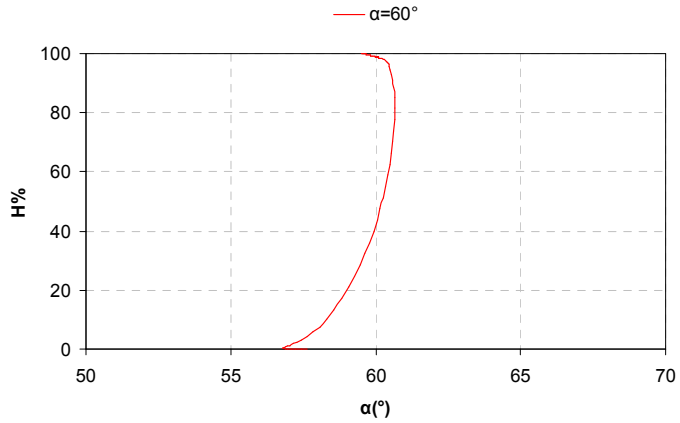

Fig 4.3b: Span-wise mass averaged inlet flow angle at the design point

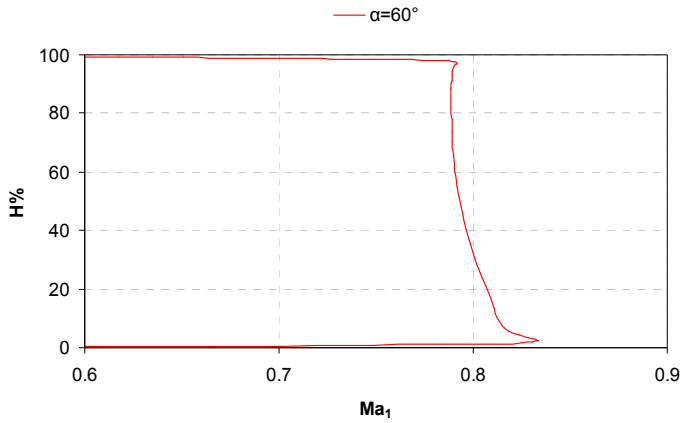

Fig 4.3c: Span-wise mass averaged inlet Mach number at the design point

The figures 4.3a-cshow the mass averaged span-wise inlet profiles of total pressure, flow angle and the Mach number at the design point (inlet α=60°).

4.3.2 OUTLET CONDITIONS

- Static Pressure: Adjusted to control the inlet Mach number (Radial equilibrium)
  - The radial static pressure gradient results directly from the swirl (tangential) velocity by the well known relation of radial equilibrium:

$$\frac{1}{\rho}\frac{\partial p}{\partial r} = \frac{V_\theta^2}{r} \tag{4.1}$$

4.4 MESH PLANES

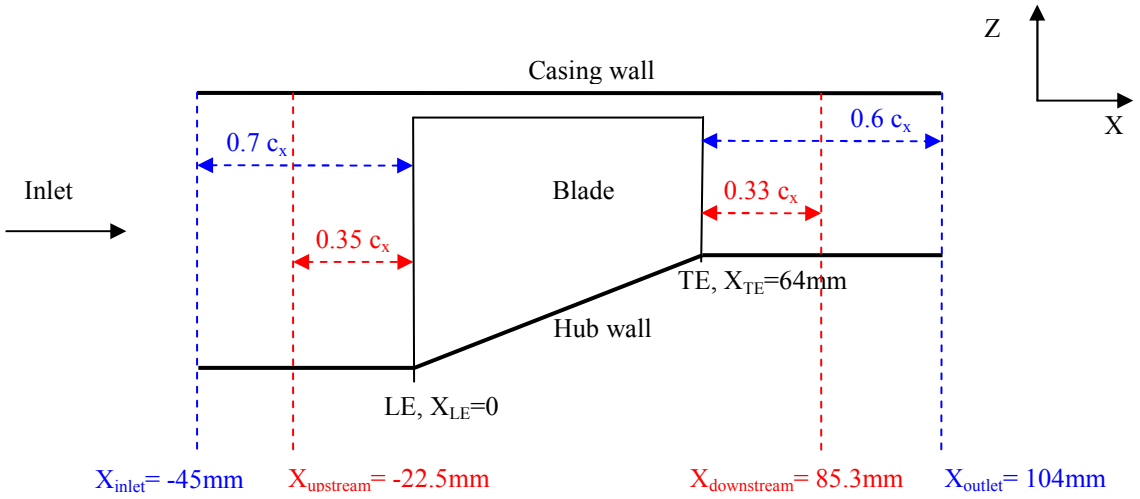

Fig 4.4: Mesh planes for boundary conditions and post-processing

4.4.1 BOUNDARY CONDITION PLANES

Inlet plane: X=-45 mm, Outlet plane: X=104 mm
The boundary condition planes are the planes at the extremities of the mesh.

- The inlet plane is $0.7c_x$ upstream of the leading edge to have enough axial distance for the smooth transport of the inlet variables to the leading edge.
- The outlet plane is $0.6c_x$ downstream of the trailing edge to have enough axial distance for the flow leaving the trailing edge to smooth out i.e., the flow fluctuations are stabilised.

4.4.2 POST PROCESSING PLANES

Upstream plane: X=-22.5 mm, Downstream plane: X=85.3 mm
The post processing planes correspond to the measurement planes of experiments in the test rig.

4.5 RESULTS AND ANALYSIS

The CFD studies have been done at the inlet transonic Mach number of 0.8 (in accordance to the test rig condition) at all the inlet flow angles from 60° to 65°. The results are discussed for the flow angle cases of 60° (design point), 63° (intermediate point) and 65° (highest loss point).

The global performance of the blade row can be analysed by studying span-wise averaged profiles of physical quantities such as the total pressure, Mach number, static pressure and the flow deviation at the downstream plane. The level of total pressure losses is estimated by plotting the total pressure loss coefficient.

Note:

- All physical quantities are mass averaged except the static pressure. The static pressure is geometrically pitch averaged.
- The Mach number and the flow angle are computed from the mass averaged velocity components V_x, V_θ and V_{abs}
- The physical quantities are averaged azimuthally and span-wise on the mesh planes.

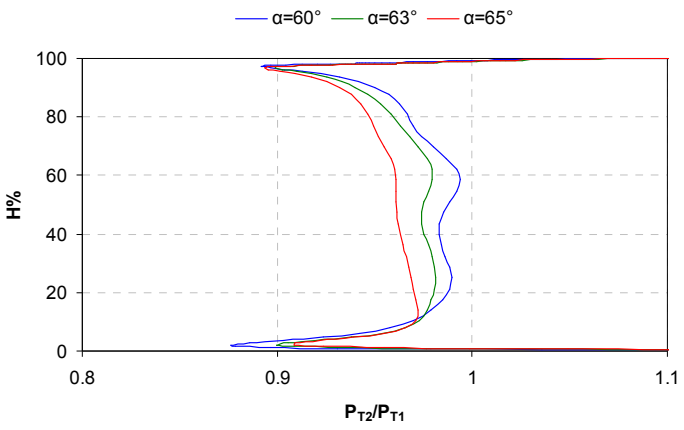

Fig 4.5a: Span-wise profile of total pressure ratio

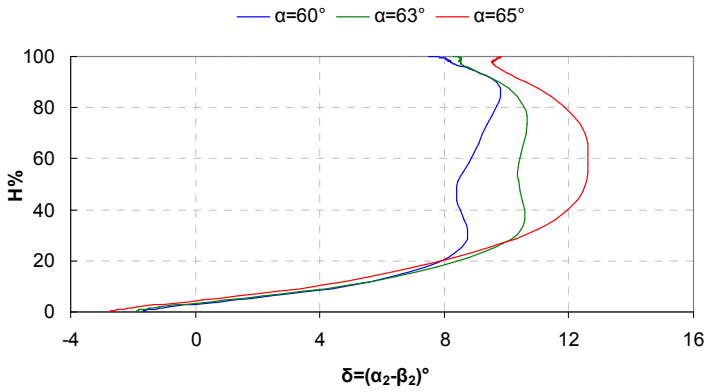

Fig 4.5b: Span-wise profile of downstream flow deviation

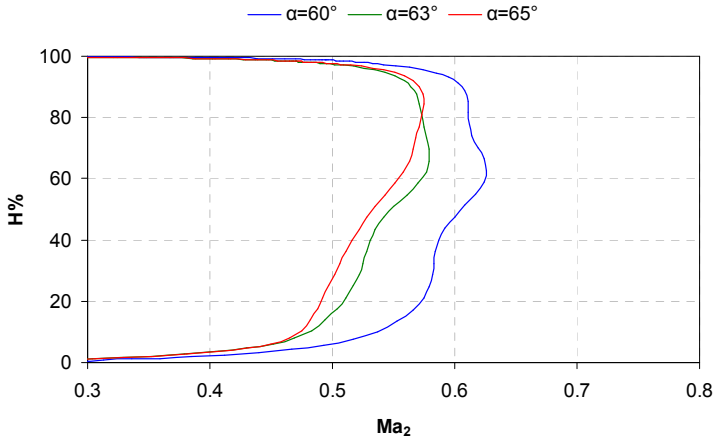

Fig 4.5c: Span-wise profile of downstream Mach number

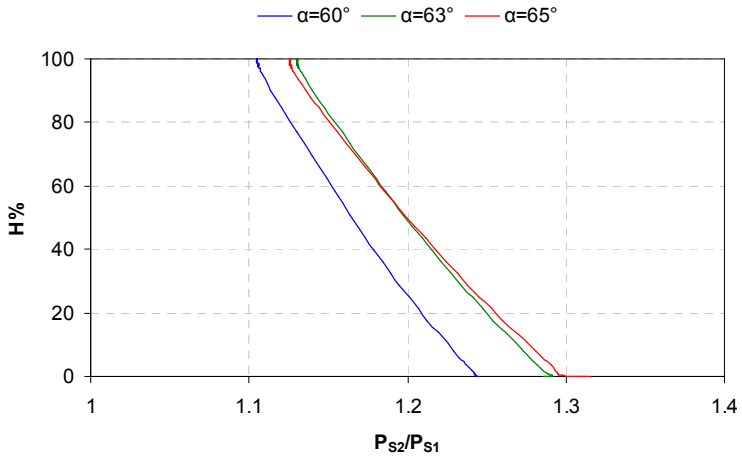

Fig 4.5d: Span-wise profile of static pressure ratio

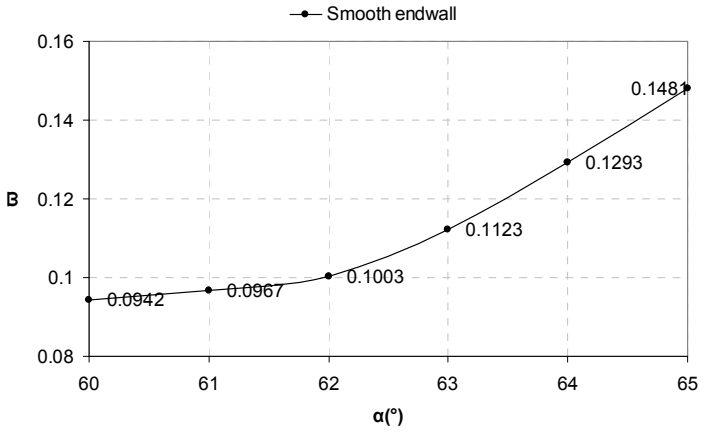

Fig 4.5e: Mass averaged total pressure loss coefficient over the operating range of the stator blade row

The total pressure loss coefficient is defined as:

$$\varpi = \frac{P_{T_1} - P_{T_2}}{\frac{\gamma}{2}.P_{S_1}.Ma_1^2} \tag{4.2}$$

These results show globally that as the inlet incidence increases the level of losses in the cascade increases also. The total pressure ratios show the zones of span-wise pressure losses. The important zones of pressure losses are the endwalls: the hub shows an increasing tendency to stall and the tip clearance losses are clearly important in the three cases but remain constant with the change in inlet flow angle. With the increasing inlet flow angles, the span-wise pressure losses increase and the case of α=65° shows a significantly reduced total pressure ratio indicating pockets of high losses at the hub that progressively intensify with the increase in incidence.

At the design point (α=60°), the total pressure ratio indicates some losses at the hub wall; the total pressure ratio profile is almost constant indicating good blade diffusion till 80% span after which the losses increase sharply under the influence of the tip corner effects. The endwall losses are clearly identified as the corner separation at the hub and tip clearance effects at the casing. The corner separation is found to be increased strongly with incidence. The flow deviation increases sharply with incidence along the span indicating thicker wakes downstream of the trailing edge. The total pressure loss coefficient shows a strong increase for inlet flow angles above α=62°.

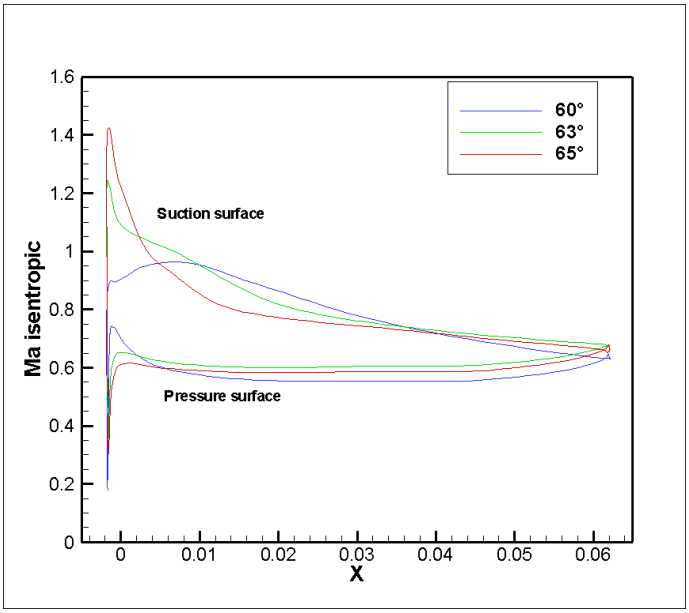

Fig 4.6: Isentropic Mach number evolution along the axial plane at 10% span

The isentropic Mach number is calculated from the reference total pressure and local static pressure as:

$$Ma_{isentropic} = \frac{2}{\gamma - 1} \sqrt{\left(\frac{P_T}{P_S}\right)^{\frac{\gamma-1}{\gamma}} - 1} \tag{4.3}$$

The isentropic Mach number plotted on the blade surface at 10% span in figure 4.6 clearly brings out the velocity spikes at the leading edge and the evolution of the flow velocity on the blade axial planes.

At the design point α=60°, the evolution of velocity is smooth with peak values reaching at X=0.02m followed by smooth deceleration towards the trailing edge. At α=63°, we observe a peak increase of velocity at the leading edge followed by flow deceleration along the blade axial plane. The peak velocity is very pronounced at α=65° on the leading edge is observed to surpass Ma=1.4. High Mach number at the leading edge tends to quickly destabilize the boundary layer on the suction side provoking earlier separation on the suction side and hub wall corner. A steep decline in the flow Mach number is observed downstream of the leading edge indicating strong flow separation on the hub.

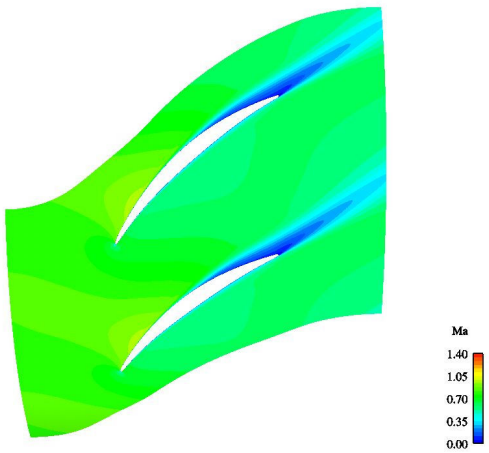

Fig 4.7a: Mach number at 10% span at α=60°

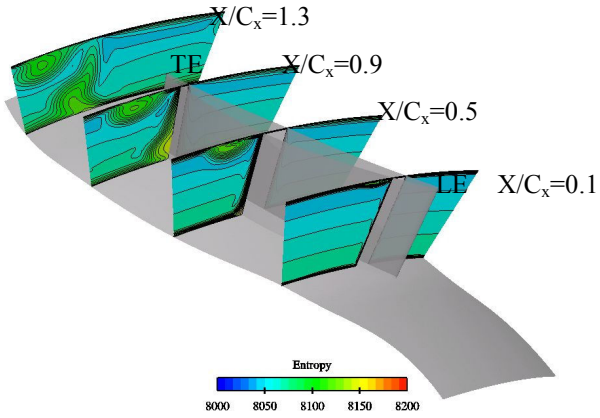

Fig 4.8a: Entropy in blade passage at α=60°

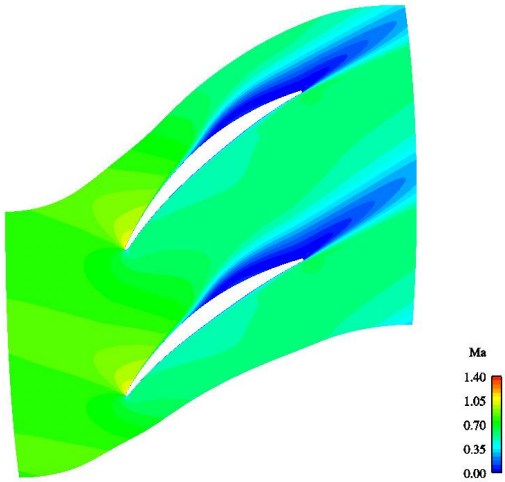

Fig 4.7b: Mach number at 10% span at α=63°

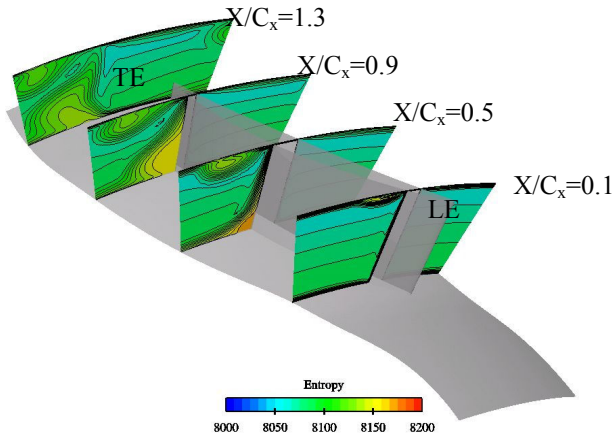

Fig 4.8b: Entropy in blade passage at α=63°

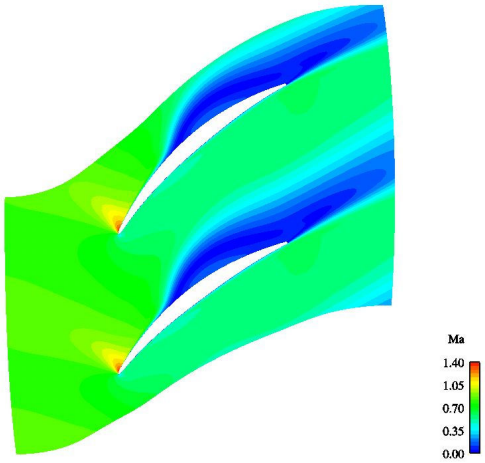

Fig 4.7c: Mach number at 10% span at α=65°

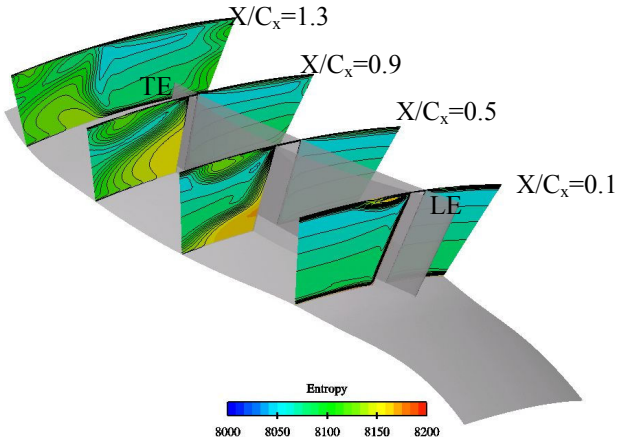

Fig 4.8c: Entropy in blade passage at α=65°

The visualisation of Mach number flow field at 10% span in figures 4.7a-c indicates the increase in strength of the corner separations with increase in incidence. The thick wake issuing from the trailing edge with α=65° indicates a strong corner separation that is seen to climb radially in the blade passage.

The entropy visualisations at chord-wise planes in figures 4.8a-c show the loss generating mechanisms such as the corner separation and the tip leakage vortex that are fully developed. The corner separation is found to be virtually absent in the flow path for the design point except for a small trace of separation visible at X/c_x=0.9. For α=63° the corner separation of a small magnitude is clearly visible at the mid-chord, which then advances downstream into a significant separated zone as seen at X/c_x=0.9. For α=65°, the corner separation progressively strengthens as it advances downstream; mixing with the tip leakage vortex in the wake.

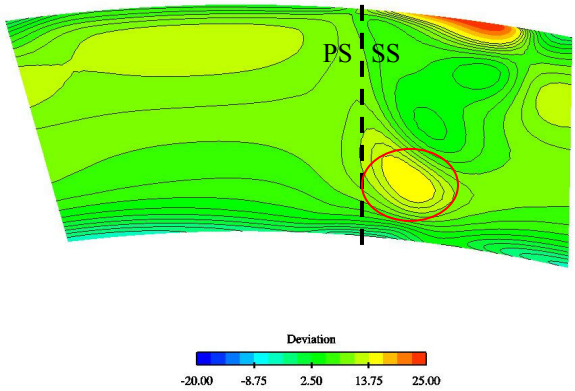

Fig 4.9a: Flow deviation at downstream plane, α=60°

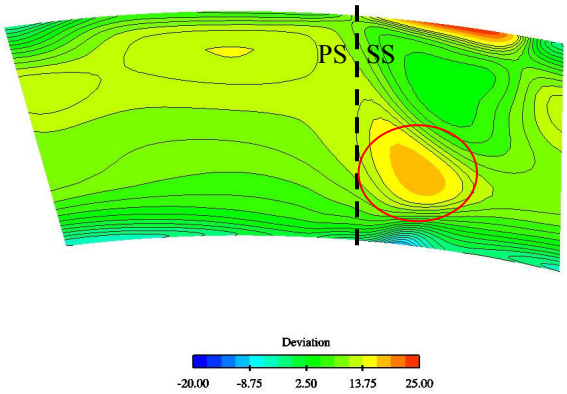

Fig 4.9b: Flow deviation at downstream plane, α=63°

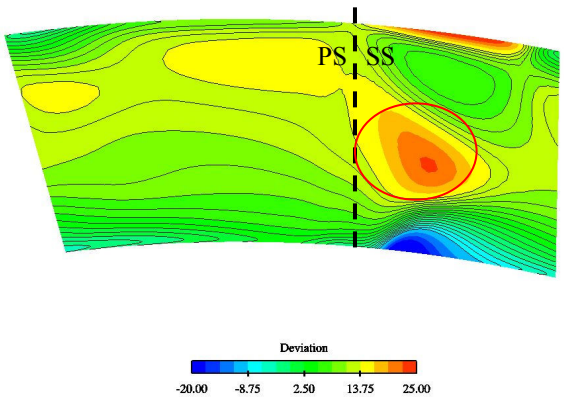

Fig 4.9c: Flow deviation at downstream plane, α=65°

Flow deviation from the blade metal angle is an indicator of the fluid behaviour in the wake, the stronger the wake the higher the flow deviation. Figures 4.9a-c show flow deviation at downstream post-processing planes for the cases of α=60°, 63° and 65°. As seen for the case of α=65°, the lower angle at the hub wall indicates boundary layer overturning due to strong flow reversal, the bright red spot in the centre of the flow path indicates strong fluid deflection due to boundary layer separation on the suction side of the blade and the bright red spot on the casing wall indicates the tip leakage vortex as it advances downstream and mixes into the free-stream.

4.6 ANALYSIS OF FLOW TOPOLOGY

The analysis of flow topology by critical points on the walls by skin friction lines is a powerful tool to better comprehend the separation and attachment of boundary layers by the fine study of flow field traces on the surface. The flow topology of three-dimensional separations on the baseline blade geometry is reviewed in this section by skin friction lines on the walls.

4.6.1 FLOW TOPOLOGY AT DESIGN POINT (α=60°)

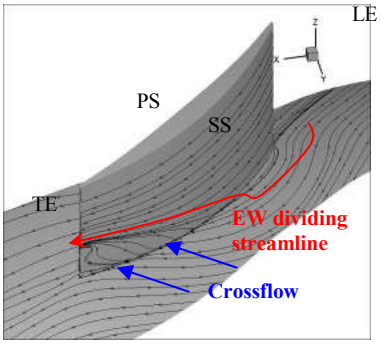

Fig 4.10a: Skin friction lines on the suction side and hub wall at α=60°

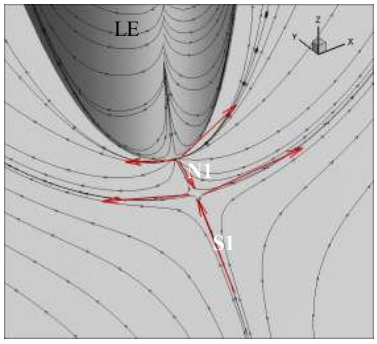

Fig 4.10b: Skin friction lines close to the blade leading edge and hub wall at α=60°

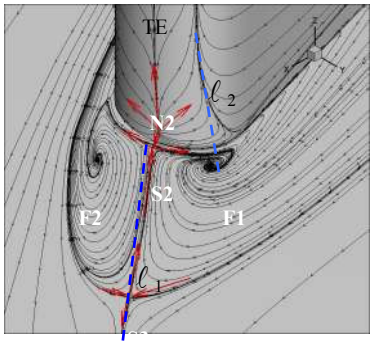

Fig 4.10c: Skin friction lines close to the blade trailing edge and hub wall at α=60°

The flow topology analysis at design point is simplified due to a very small magnitude of flow separation that is limited only to a small zone on the suction surface close to the trailing edge. Separation on the hub wall is non-existent. The flow structure can be described as follows:

- In the figure 4.10b representing the leading edge region, the traces of horseshoe vortex are observed. The boundary just upstream of the leading edge separates at the saddle point S1 owing to high adverse pressure gradient applied on the boundary layer and re-attaches at the nodal point of attachment N1 as the boundary layer is constrained by the stagnation line at the boundary layer edge. The saddle point is the origin of two endwall dividing streamlines that move to the suction and the pressure sides respectively.

- On the suction surface there is no specific evidence of separation (absence of critical points).

- In figure 4.10a, the suction surface leg of the endwall dividing streamline is transported on the suction surface under the influence of the crossflow from the pressure surface of the adjacent blade. As this suction surface of the endwall dividing streamline mounts it envelopes a number of streamlines following its direction of movement along the blade span. Close to the trailing edge a very small zone of separation on the suction side and it is not associated with strong flow reversal.

- In figure 4.10c, the flow topology in the trailing edge region is of particular interest. A saddle point S2 is identified that is the counterpart of the saddle point S1 at the leading edge at least for the friction line that comes from the blade pressure side. On the hub wall, two focal points F1 and F2 are observed that correspond to the extremities of two vortices whose axes are parallel to the blade span; these vortices are linked to a separated region, which is generated in the region of very high curvature at the trailing edge.

- On the blade surface two lines of convergence of the skin friction lines ℓ_1 and ℓ_2 are seen. ℓ_1 is attached to the critical points N2 and S3 and separates the regions of influences of the two vortices F1 and F2. ℓ_2 is linked to the vortex core F1; the vortex core attached to F1 pushes the friction line upstream; however the movement is prevented by the migration along the suction side induced by the passage vortex.

4.6.2 FLOW TOPOLOGY AT THE INTERMEDIATE POINT (α=63°)

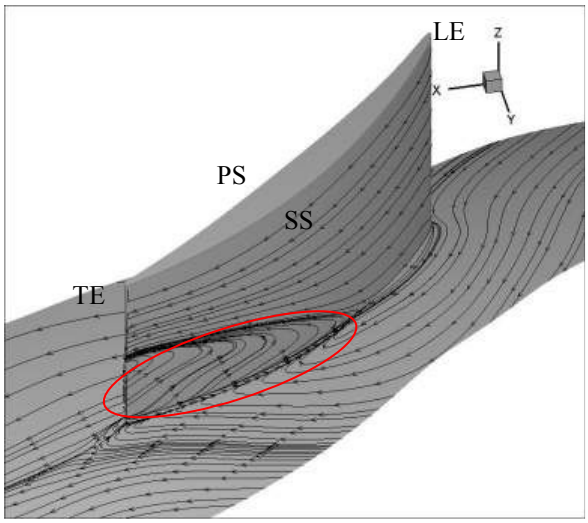

Fig 4.11: Skin friction on the suction surface and hub wall at α=63°

The flow topology for the intermediate point is similar to the design point with the exception of a larger zone of separation on the suction side of the blade and more flow turning on the hub wall. The larger zone of separation on the suction surface is marked in red bordered ellipse in the figure 4.11 above.

4.6.3 FLOW TOPOLOGY AT THE HIGHEST LOSS POINT (α=65°)

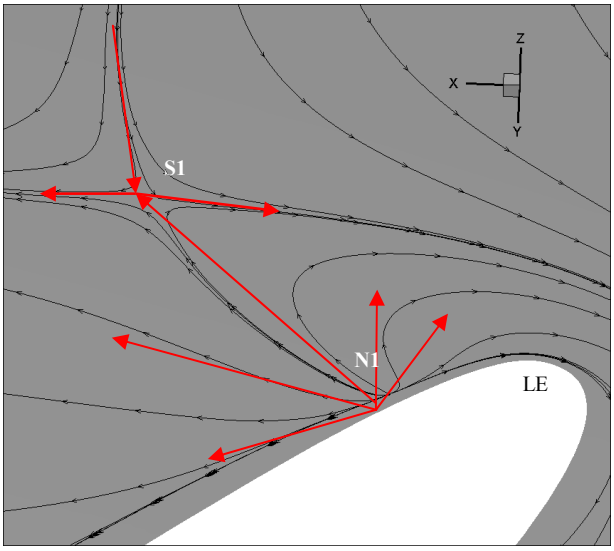

Fig 4.12a: Skin friction lines close to the leading edge at α=65°

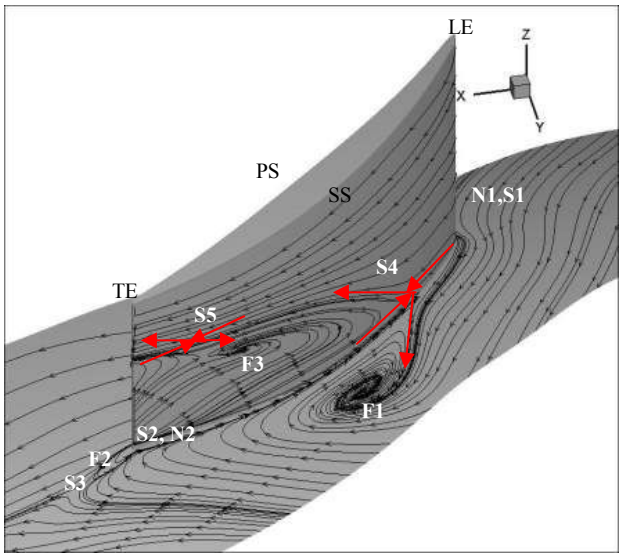

Fig 4.12b: Skin friction lines on the hub wall and suction surface at α=65°

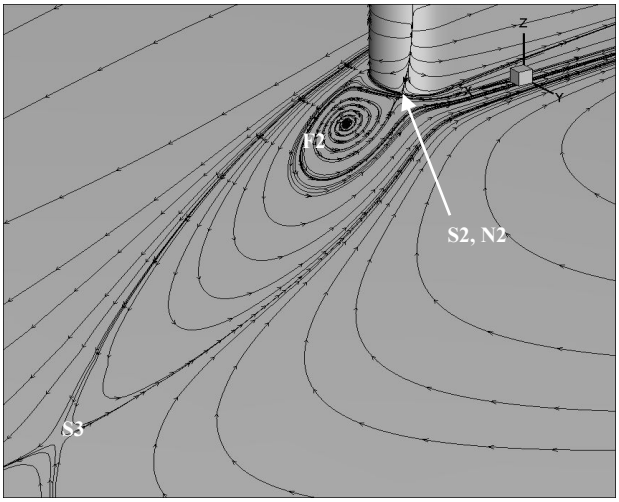

Fig 4.12c: Skin friction lines close to the trailing edge at α=65°

This particular case has strong flow separations on the hub wall as well as the blade suction surface. The distinguishing feature of this case is the separation of the wall shear line or the dividing streamline on the hub wall. The dividing streamline on the hub wall separates and spirals into a focal point of separation F1 similar to the focal point F3 on the suction surface. The flow topology is complex in this case of hub corner stall and is analysed to bring out as much detail as possible.

A visual examination of the skin friction lines in the figs. 4.12a-c can explain the flow separation in the following steps:

- In the figure 4.12a, the node-saddle point pair N1-S1 represent the horseshoe vortex system in the leading edge region. Two dividing streamlines spring from the saddle point in the leading edge region. The suction surface leg of the dividing streamline on the hub wall spirals into a focal point F1. The pressure surface leg of the dividing streamline flows towards the trailing edge of the adjacent blade and then spirals into the focal point F1 on the hub wall indicating strong influence of the crossflow. These dividing streamlines may be called hub wall dividing streamlines of global separation with saddle point S1 as their origin and focus F1 as their point of termination in direct relation to Lighthill's criteria of closed separation.

- The skin friction lines from the node N1 in the leading edge region intersect the corner between the blade and the hub wall at saddle point S4. S4 is seen as a semi saddle point on the hub wall and on the blade suction surface too. (figure 4.12b) As explained by Tobak and Peake [31], the convergence of these lines with their origin as another point other than the saddle point can be called local lines of separation.

- On the hub wall, the skin friction lines from the saddle point S4 form two separate local dividing streamlines: one spirals and terminates into the focal point F1; the other one spirals and terminates into the focal point F3 on the suction surface.

- The focal point F1 on the hub wall forms the base of the corner vortex and the vortex filament (vortex core) springing from it representing the radial motion of the vortex.

- The flow topology close to the trailing edge in figure 4.12c is similar to that of figure 4.10c for the design point. A striking difference is in the strength of the trailing edge vortex F3 that is stronger in the case of $\alpha=65°$ due to stronger flow separations. Also, F1 in figure 4.10c is found to be migrated upstream in the corner region becoming the centre of hub corner separation.

- The three dimensional separations studied here clearly obey the criteria of closed separation with the dividing streamlines originating from the saddle points and terminating at focal points. (saddle-spiral node connections)

- The trajectory of the dividing streamlines from the saddle point and the converging skin friction lines from the node passing through the critical points can be described as follows:
    - On the hub wall
        - S1 to F1 (global line of separation)
        - N1 to S4 to F1 (local line of separation)

- On the suction surface
  - N1 to S4 to F3 (local line of separation)

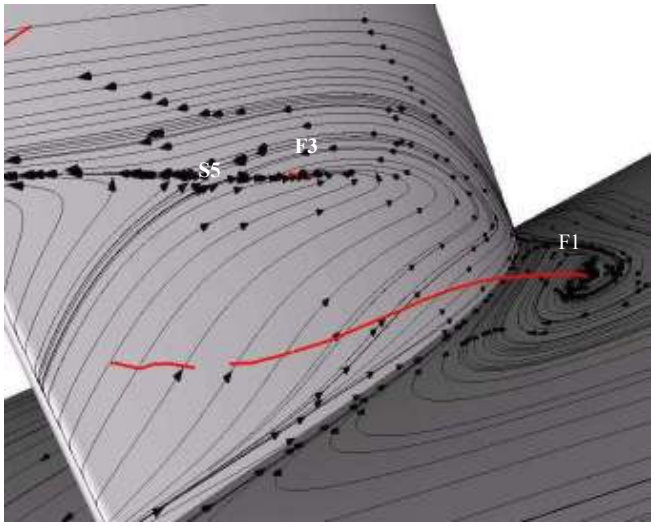

Fig 4.13: Vortex core from the centre of hub corner separation on the hub wall

The vortex core can be simply defined as the axis of the corner vortex i.e., a line central to the translation of the vortex from its origin at the endwall to its termination downstream (figure 4.13). It can be seen that the corner vortex plays an important role in intensifying the flow separation on the suction side as it reverses the flow to a large extent on the suction side.

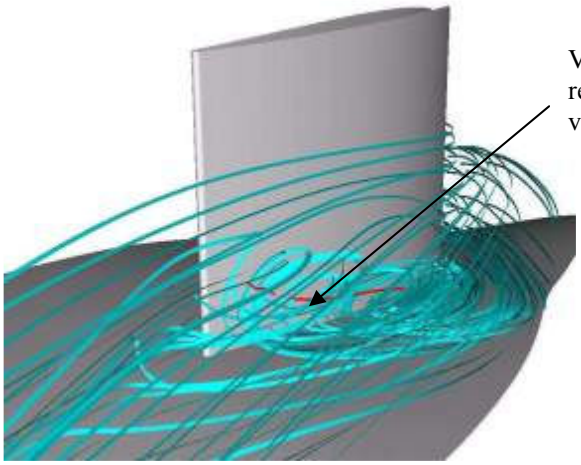

Fig 4.14: Volume streamlines around the vortex core (in red)

To visualise the effects of the corner vortex more clearly, figure 4.14 shows the streamlines in the volume domains around the vortex core. The corner vortex springing from F1 is seen to exhibit a radial and axial progression mounting in the flow path and reversing the flow on the suction side. It must be noted that the corner vortex is not responsible for the flow separation on the suction side but its influence is important to increase the extent of separation. The principal cause of losses in this case is the corner vortex limiting the diffusion capability of the blade, increasing the aerodynamic blockage in the flow path and consequently dictating a limit on the operating range of the blade row.

The above explanation of the flow separation is further verified by the criteria of Surana et al. [20, 32] for the non degeneracy of the critical points on the hub wall.

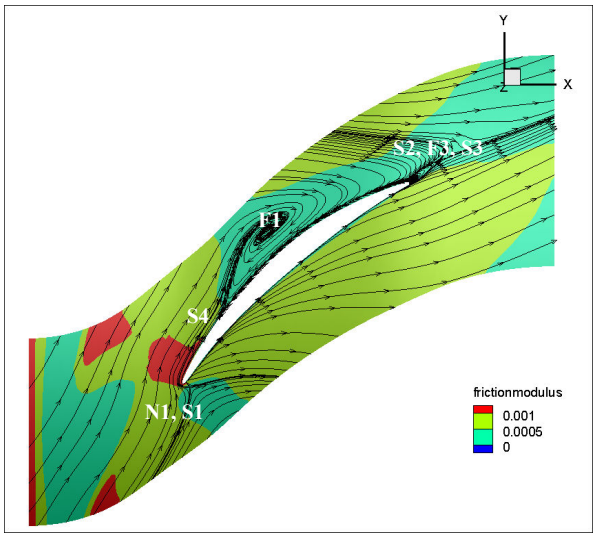

Fig 4.15a: Wall shear modulus on the hub wall

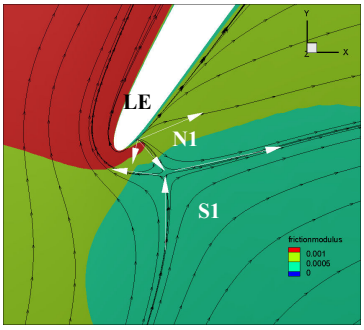

Fig 4.15b: Wall shear modulus on the hub wall close to the LE

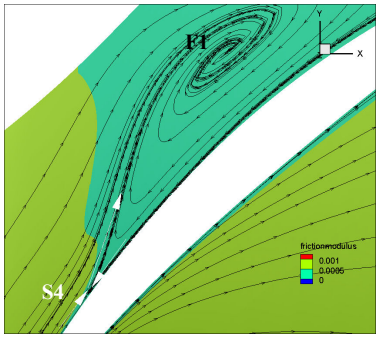

Fig 4.15c: Wall shear modulus on the hub wall close to the SS

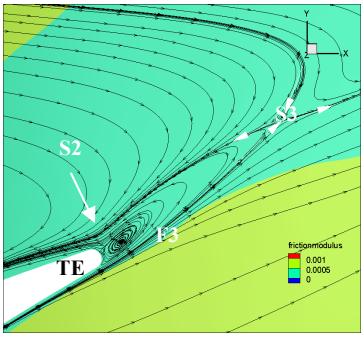

Fig 4.15d: Wall shear modulus on the hub wall close to the TE

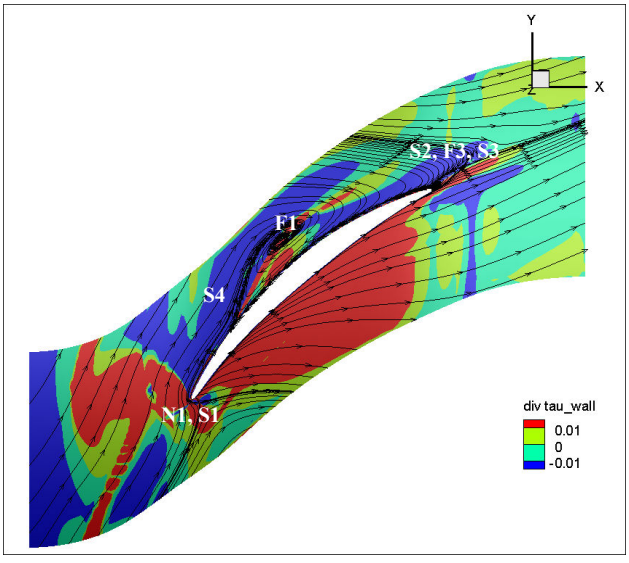

Fig 4.16a: Divergence of wall shear vector on the hub wall

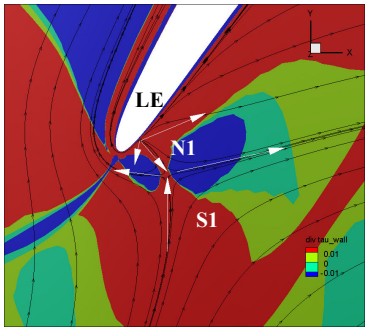

Fig 4.16b: Divergence of wall shear vector on the hub wall close to the LE

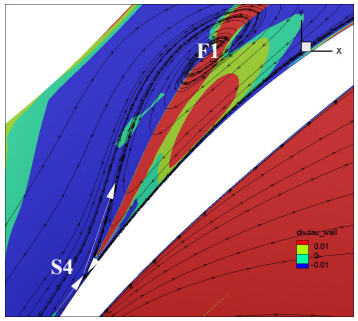

Fig 4.16c: Divergence of wall shear vector on the hub wall close to the SS

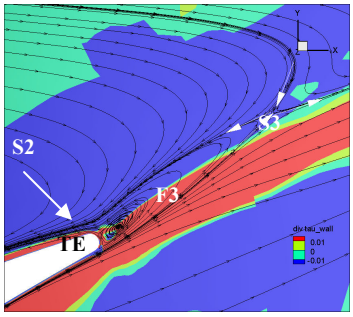

Fig 4.16d: Divergence of wall shear vector on the hub wall close to the TE

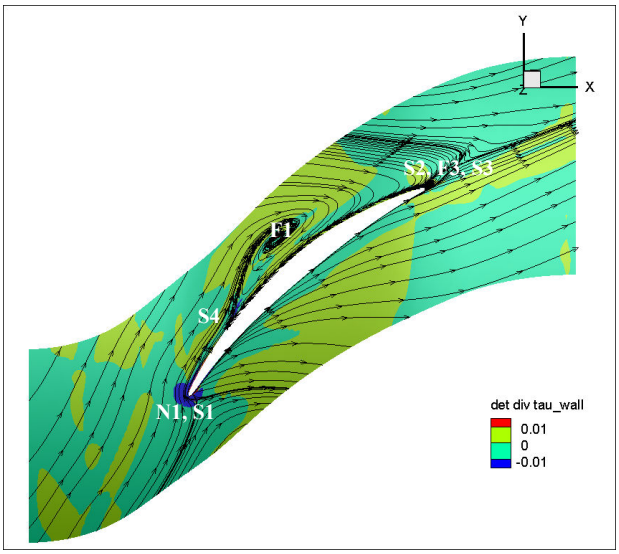

Fig 4.17a: Determinant of divergence of wall shear vector on the hub wall

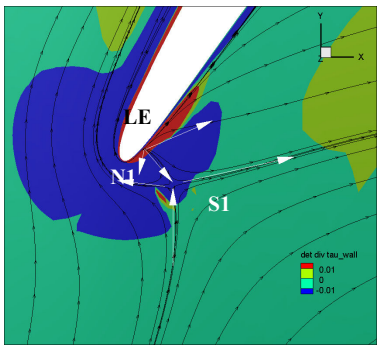

Fig 4.17b: Determinant of divergence of wall shear vector on the hub wall close to the LE

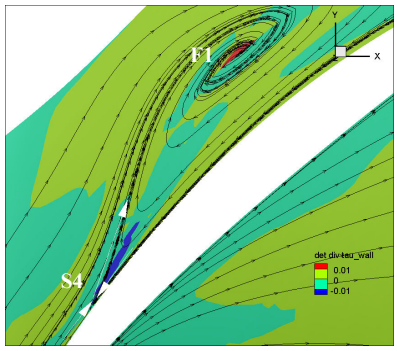

Fig 4.17c: Determinant of divergence of wall shear vector on the hub wall close to the SS

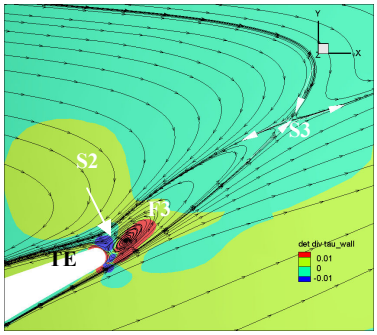

Fig 4.17d: Determinant of divergence of wall shear vector on the hub wall close to the TE

The values of the conditions of separation criterion of Surana et al. [20, 32] obtained for the critical points from figures 4.15-4.17 on the hub wall are tabulated below:

Critical point	τ_w	$\nabla \tau_w$ (+/-)	$\det(\nabla \tau_w)$
Node N1	<0.0005	+	>0
Saddle point S1	<0.0005	+	<0
Saddle point S4	<0.0005	-	<0
Focal point F1	<0.0005	-	>0
Focal point F3	<0.0005	+	>0
Saddle point S2	<0.0005	+	<0
Saddle point S3	<0.0005	-	<0

Table 5: Values of separation criterion obtained for critical points

The values in the vicinity of the absolute zero value are judged to qualify as separation/attachment points/lines. It is not clear, at this moment, to determine if this is a limitation of our numerical modelling or if absolute zero values in the skin friction fields are approximations of close to zero values of the friction field vectors. In any case, this approximation still seems to serve as a satisfactory indicator of separation/attachment on boundaries. Perhaps, a more refined modelling of the boundary layer with denser mesh and lower Reynolds number can bring out such details more clearly.

From the above calculated values it is clear that only the saddle point S4 and the focal point F1 satisfy the conditions of non degeneracy to be the points of separation. The line connecting the saddle point S2 to the focal point F1 is the line of separation on the hub wall in the region of adverse pressure gradient. It is noted that all saddle points, including S4 exhibit negative values of $\det(\nabla \tau_w)$. This violation may not qualify the saddle points to be rigorously non degenerate. The calculation of $\nabla \tau_w$ and $\det(\nabla \tau_w)$ neglects the wall curvature. This may have an effect close to the leading edge, trailing edge and the suction surface corner on the hub wall. Hence, we are not certain about the validity of the results obtained for the critical points.

We also suspect that the mesh employed in these areas for the numerical simulation should have been denser in order to properly capture all the local flow structures. We may also think to use the verification of the conditions of rigorous non degeneracy by the simulation as indicators of the mesh quality.

The purpose of analysing the three dimensional separations is to understand the location of implementation of a flow control method. The analysis presented here shows that the hub corner stall is a mechanism of the endwall effects. Although, the horseshoe vortex at the leading edge is the origin of endwall dividing streamlines, it is also an essential mechanism for the flow bifurcation on the blade sides.

One interesting method may be to implement aspiration at the leading edge on the hub to displace the horseshoe vortex from the pressure side to the centre of the leading edge that may alter the pressure distribution in a beneficial way. If successful, the flow around the blade may be restored closer to the design point pressure distribution giving a possibility to extend the operating range of the blade. On the other hand it may even cause a high level of flow instability to divert the inlet flow drastically.

A safer way to implement flow control may be in the region of adverse pressure gradient in the corner between the hub wall and the suction surface where the three dimension separation is prominent. The analysis shows the hub corner stall to be dominant downstream of the saddle point S4. A control method implemented in the vicinity of the saddle point S4 can prove to be beneficial as it would allow to aspirate the separated flow from the origin S4 in the corner. The line connecting S4 and F1 on the hub wall from the analysis of Surana et al. [20, 32] qualifies to be the separation line. It is the application of flow control along this line that offers prospects of a successful control of corner separation on the hub wall. The elimination of this corner vortex by boundary layer aspiration can lead to an important reduction in the total pressure losses and also the scope to increase the operating range of the cascade.

4.7 CONCLUSION

The focus of the present chapter has been the numerical study of the baseline stator blade cascade at various points of operation. This numerical study has covered the study of the flow features of the cascade; the blade performance has been studied by averaged physical quantities at the upstream and downstream planes. At the fixed inlet transonic Mach number of 0.8, the change in incidence is found to progressively increase the endwall losses on hub that increase the total pressure losses of the cascade. Flow reversal occurs on the suction surface of the blade even at lower incidences indicating weaker boundary layer due to local velocity spikes close to the leading edge.

The crossflow transporting the flow from the pressure side of the adjacent blade helps to resist the flow separation on the hub wall at lower incidences. However, beyond $\alpha=63°$, the flow separation on the hub wall is clearly dominant. The flow topological studies show the separation on the blade suction surface and the hub wall by focal points that represent vortices of separation. The corner vortex mounts on the hub wall mounts in the flowpath increases the flow deviation and a drop in pressure rise capability of the blade leading to higher total pressure losses.

In the case of suction surface and corner separation, Lighthill's criterion of closed separation has been found to be satisfactorily observed where the separation line originates at the saddle point in the corner between the hub wall and the blade suction surface and terminates at the focal point.

The criterion developed by Surana et al. [20, 32] has been applied on the hub wall at the highest loss incidence point. The analysis of wall shear field on the hub wall by this criterion confirms the saddle point S4 in the corner between the hub wall and the blade suction surface to be a point of origin of the three dimensional separation (with exception of the non degeneracy condition that we suppose to be a limitation of our numerical modelling). The focal point F1 on the hub wall representing the corner separation vortex is also identified as a separation point. The line connecting the saddle point S4 and the focal point F1 may be called the separation line.

The reattachment points and lines have not been identified with this analysis of the wall shear. It is possible that the mesh is not dense enough to properly identify the characteristics of the wall shear everywhere in the flow field that can satisfactorily analyse the characteristics of separation and reattachment. Also, there are a number of critical points in the corner between the hub wall and the blade surface whose influence in the separation and attachment is not well understood. The presence of these critical points may be physical or non physical in nature. The three dimensional separation is an unstable phenomenon and the steady state RANS calculations force a stable solution to the set of problems. It is, therefore, possible that many of the critical points existing in the corner regions of the flow field may not be physical critical points observed in reality. The approach has been to identify those critical points that serve to understand a global view of separation in the flow field.

5. NUMERICAL STUDIES OF BASELINE BLADE WITH HUB WALL ASPIRATION

The aerodynamic performance analysis of the stator blade row has shown the performance to deteriorate with increasing incidence due to the formation and progressive increase in strength of the corner vortex. The separation line associated with the corner separation on the hub wall has been identified with the studies of flow topologies and this chapter presents the implementation of boundary layer aspiration by an aspiration slot on the hub wall.

5.1 HUBWALL ASPIRATION SLOT CONFIGURATION

ONERA performed numerical studies of various hub wall aspiration slot configurations on the stator cascade to control the corner separation. Five hub wall slots were designed by varying the axial and tangential limits of the slots and studied numerically at various points of operation. The figure 5.1 below shows the various slot configurations studied:

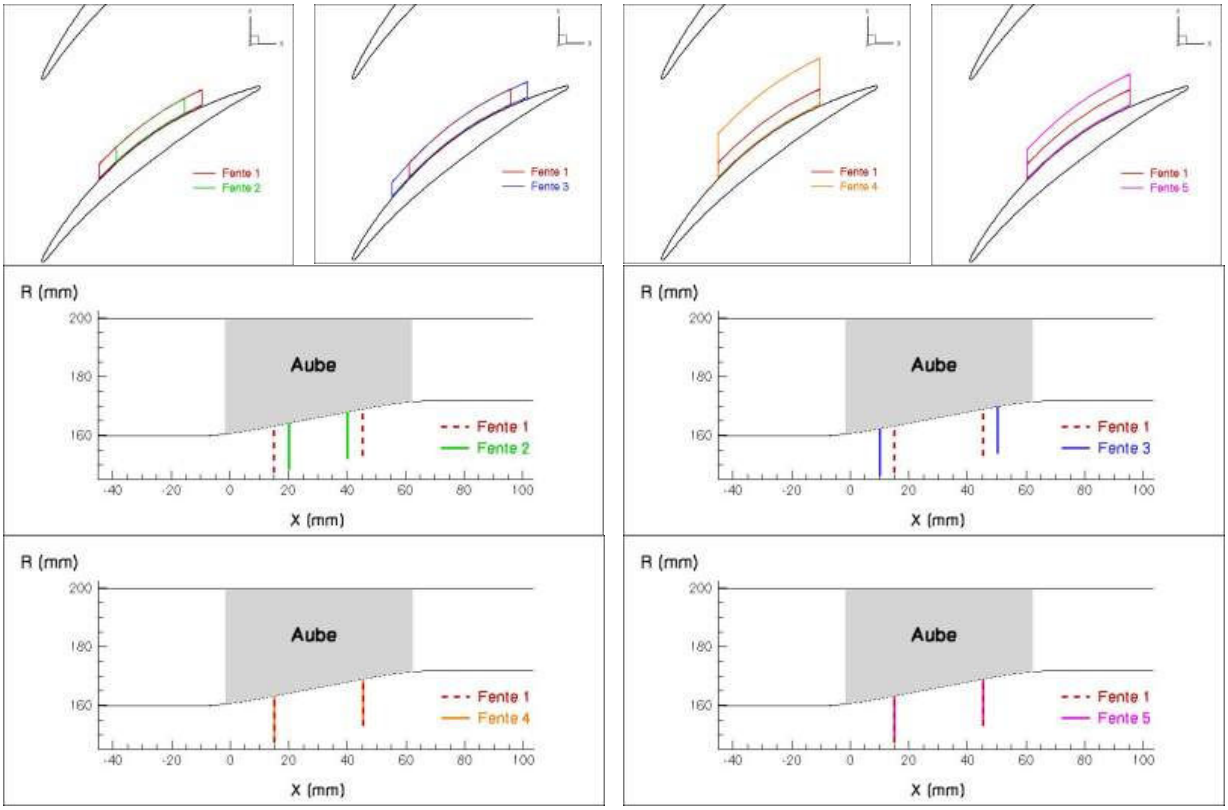

Fig 5.1 : Various hub wall slot configurations studied
(Note: Aube=blade, Fente=slot, Courtesy ONERA)

Slots 1 to 3 exhibit same circumferential dimensions and slots 4 and 5 exhibit larger circumferential dimensions in the blade channel. Slots 1,4 and 5 have the same longitudinal dimensions and slot 3 has the largest longitudinal dimensions. This parametric study aims to study the sensitivity of the slot dimensions for their aerodynamic performances. The parametric studies for all the above slot configurations have been performed for α=60°, α=63° and α=65°.

The slots that are larger in circumferential dimensions (slots 4 and 5) encourage large flow separations on the end-wall as they tend to accelerate and bleed the cross-flow in the blade channel resulting higher quantity of massflow being transported to the corner region. It is, therefore advised, to restrict the circumferential dimensions of the slot so as not to extend higher (circumferentially) into the blade channel.

Slot 3 is found to be most effective for the control of corner separation that becomes dominant at the highest loss point. For the upstream flow conditions of this study, the corner separation initiates close to the leading edge and the only slot that extends close enough to the origin of corner separation is slot 3. Hence, it has been decided to finalise slot 3 for the detailed analysis.

The meshed endwall aspiration configuration is finalised with slot 3 and is shown below:

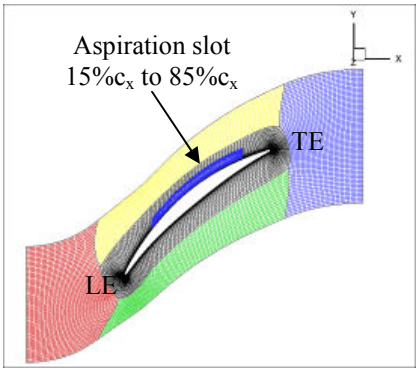

Fig 5.2a: Aspiration slot on hub wall

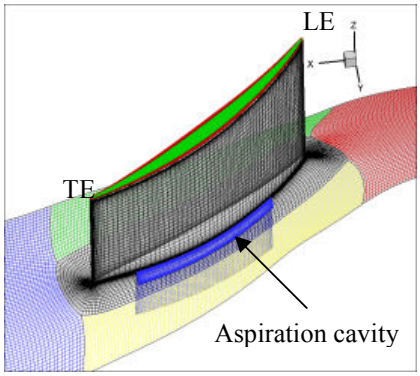

Fig 5.2b: Aspiration cavity with hub wall

The aspiration cavity mesh is joined with the flow-path mesh by chimera connections. The aspiration cavity mesh slightly overlaps the hub wall mesh planes and joins with the 'O' block mesh. The chimera mesh technique enables simplified meshing of complex geometries as additional mesh blocks can be easily added to the existing multi-block structured mesh. Advantageously, the elsA solver is designed to easily adopt its physics to the chimera mesh structures.

5.2 RESULTS AND DISCUSSIONS

The CFD studies of the cascade with endwall aspiration were done to study the influence of aspiration on the performance of the blade row with the same inlet boundary conditions. The massflow aspirated in the aspiration cavity is expressed as fraction of the total inlet mass flow in the cavity. The suction coefficient Cq is defined as

$$Cq = \frac{\dot{m}_{aspirated}}{\dot{m}_{inlet}} \tag{5.1}$$

For instance Cq=0.01 represents that 1% of the total inlet massflow is aspirated

The quantitative and qualitative assessment is made on three important operating points of the cascade: the nominal point (60°), the intermediate point (63°) and the highest loss incidence point (65°).

5.2.1 TOTAL PRESSURE RATIO

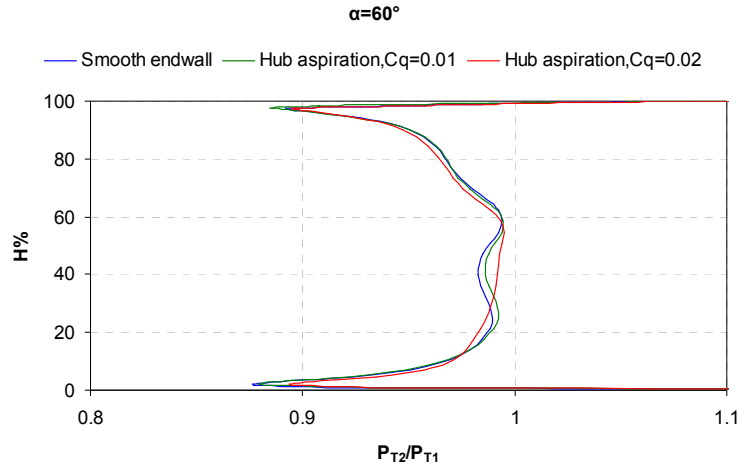

Fig 5.3a: Span-wise profile of total pressure ratio at α=60° (Smooth endwall/hub aspiration)

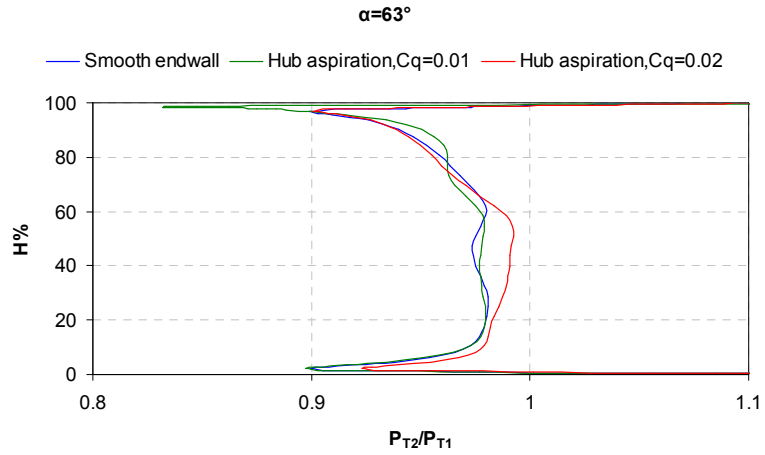

Fig 5.3b: Span-wise profile of total pressure ratio at α=63° (Smooth endwall/hub aspiration)

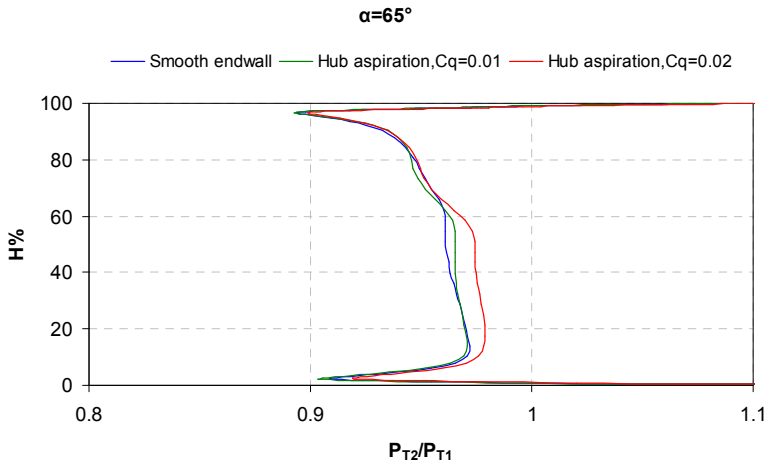

Fig 5.3c: Span-wise profile of total pressure ratio at α=65° (Smooth endwall/hub aspiration)

The total pressure ratio profile is improved from 10-60% span with hub wall aspiration (Cq=0.02) for all the operational points and there is very little increase in total pressure ratio resulting from aspiration with Cq=0.01 as shown in figs 5.3a-c. Also, the improvement is highest for α=63° making it an optimum operational point with aspiration on as the zone of separation on the suction side is suppressed. The gain at the design point α=60° with aspiration is not appreciable as there is no loss generating mechanism that is controlled by aspiration. Hence, aspiration has little influence on the design point.

At the highest loss point α=65°, the hub corner stall is well developed on the hub wall and is responsible for most of the losses. With aspiration there is some control exercised over this hub corner stall and its strength is reduced. This improvement is seen in figure 5.3c in the profile of total pressure ratio from the hub wall to mid-span. Aspirating 1% of the inlet massflow does not create enough depression in the cavity against the adverse pressure gradients and hence has a very weak influence on the blade row. The flow topology studies of the aspiration cavity are presented in the later sections of this chapter.

5.2.2 TOTAL PRESSURE LOSS COEFFICIENT

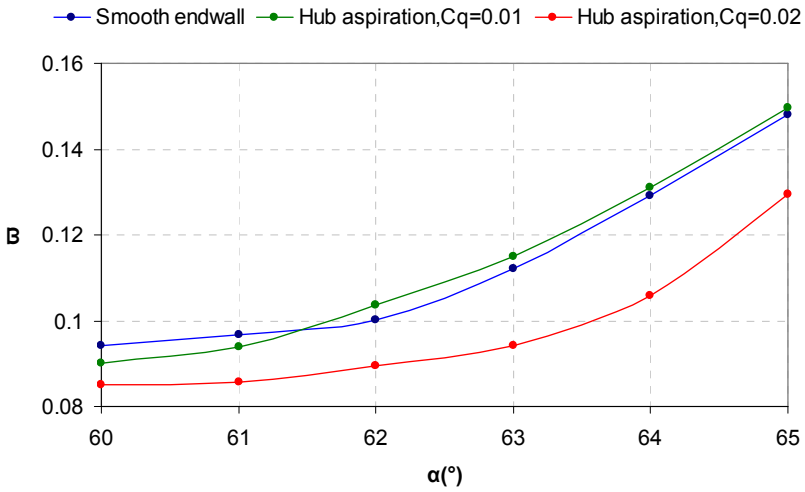

Fig 5.4: Total pressure loss coefficient ϖ (Smooth endwall/hub aspiration)

Figure 5.4 shows the influence of hub aspiration on the total pressure losses of the stator blade row. The total pressure loss coefficient ϖ is calculated as

$$\varpi = \varpi_{hub} + \varpi_{flowpath} \tag{5.2}$$

$$\varpi = \left[\left(\frac{Cq_{hub}}{100}\right).\frac{P_{T_1} - P_{T_{hub}}}{\frac{\gamma}{2}.P_{S_1}.Ma_1^2}\right] + \left[\left(\frac{100 - Cq_{hub}}{100}\right).\frac{P_{T_1} - P_{T_2}}{\frac{\gamma}{2}.P_{S_1}.Ma_1^2}\right] \tag{5.3}$$

This expression of ϖ allows accounting for the loss in the core of the flow transported with the massflow exiting the cascade $\left(1 - 0.01Cq_{hub}\right)$, and the mechanical energy exiting in the slot but also lost for the downstream flow, with the mass flow $\left(0.01Cq_{hub}\right)$

The total pressure loss coefficient is seen to increase with hub aspiration, Cq=0.01 over the baseline stator blade row after α=62°. However, the values of total pressure loss coefficient obtained from hub aspiration, Cq=0.01 closely match those of the baseline stator blade row with smooth endwall. This indicates that hub aspiration, Cq=0.01 is not efficient to control the flow separation and the resulting losses in the blade row.

There is a significant decrease in total pressure loss coefficient with hub aspiration, Cq=0.02 over the entire operating range of the cascade. The decrease in losses is higher with the increase in the inlet flow angle. This indicates efficiency of the aspiration strategy with increased flow rate to control stronger flow separations with increasing inlet flow angles.

With hub aspiration, Cq=0.02 the total pressure loss coefficient reduction over the baseline case with smooth endwall is 9.7% at α=60°, 16% at α=63° and 12.5% at α=65°. This indicates that the maximum gain is derived from the present aspiration strategy not at the design point with lower losses neither at the highest loss point with stronger flow separations but somewhere in between at the intermediate point. From the engine-application point of view, the potential benefit of the technology would be an increased pressure rise capability over the operating range. The application of such a technology would then require a complete redesign of the compressor (maybe even re-distribution of pressure ratio between rotor and stator) to get full benefit of lower losses and extra stability from the aspirated stator row.

5.2.3 FLOW DEVIATION

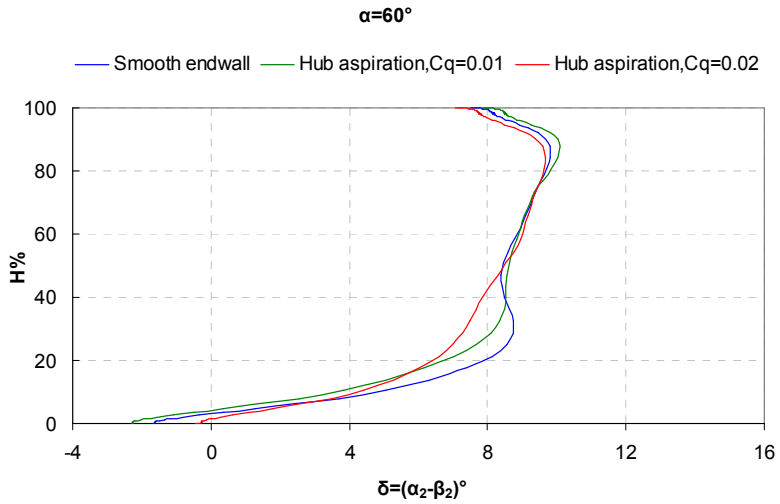

Fig 5.5a: Span-wise profile of flow deviation at α=60° (Smooth endwall/hub aspiration)

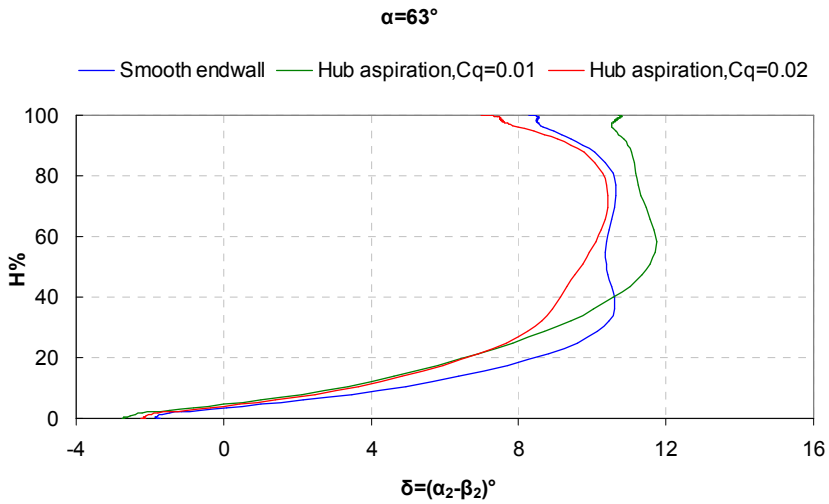

Fig 5.5b: Span-wise profile of flow deviation at α=63° (Smooth endwall/hub aspiration)

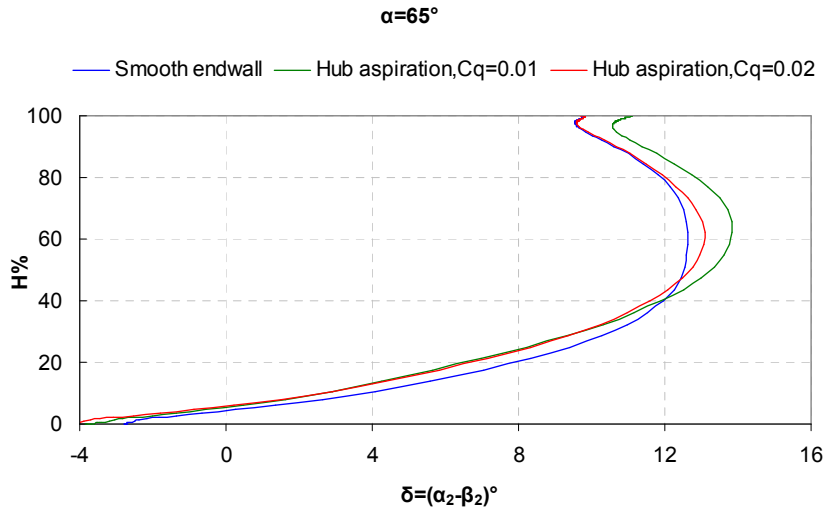

Fig 5.5c: Span-wise profile of flow deviation at α=65° (Smooth endwall/hub aspiration)

The flow deviation is interesting as aspiration has different effects on flow deviation at different operational points under investigation. At the design point, α=60°, aspiration offers little improvement on the flow deviation from the hub wall to 40% span as the boundary layer is more strongly attached at the corner of hub and the blade due to increase in cross-flow under the influence of aspiration.

At the intermediate point α=63°, the flow deviation is appreciably increased over the blade span when 1% of the inlet massflow is aspirated and conversely the flow deviation is appreciably reduced when 2% of inlet massflow is aspirated. The reduction is highest at 30% span as the flow deviation is reduced by 2° as compared to the baseline. The zone of flow reversal on the suction surface resulting from the radial displacement of flow on the suction surface by the cross-flow is suppressed as the flow is aspirated downwards in the aspiration cavity.

At the highest loss point α=65°, the flow deviation remains approximately the same for both the mass flows aspirated with aspiration from the hub endwall to 40% span. This indicates that aspiration is not very effective in controlling the hub corner stall locally at the endwall. When 1% of the massflow is aspirated the flow deviation is increased all over the span compared to the baseline and is slightly reduced from 40% to 60% span when 2% of inlet massflow is aspirated. Although aspiration is not effective in suppressing the hub corner stall it is marginally reduced as indicated by a slight reduction in the flow deviation at mid-span.

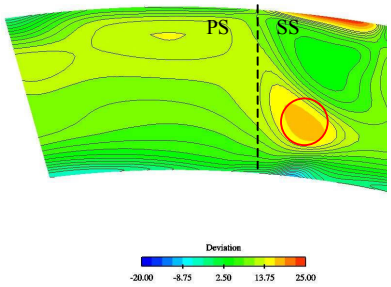

Fig 5.6a: Downstream flow deviation at α=63°, smooth endwall

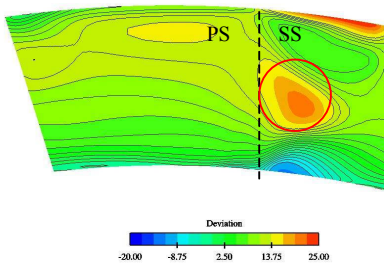

Fig 5.6b: Downstream flow deviation at α=63°,Cq=0.01

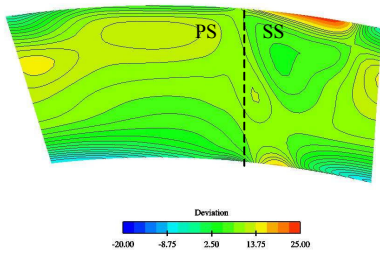

Fig 5.6c: Downstream flow deviation at α=63°, Cq=0.02

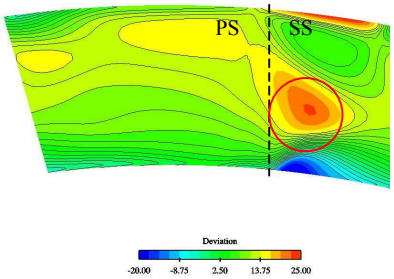

Fig 5.7a: Downstream flow deviation at α=65°, smooth endwall

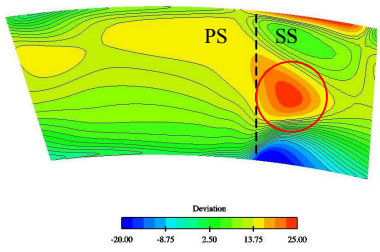

Fig 5.7b: Downstream flow deviation at α=65°, Cq=0.01

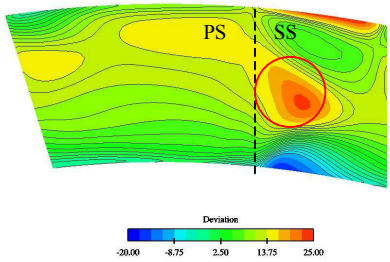

Fig 5.7c: Downstream flow deviation at α=65°, Cq=0.02

In the figures 5.6 and 5.7, the flow deviations on the downstream plane for α=63° and α=65° respectively, hub aspiration corresponding to Cq=0.01 is found to increase the flow deviation for both the points as compared to the case without aspiration, except very close to the hub wall; this is because the separation on the suction side is not really affected by the aspiration slot on the hub.

However, with aspiration, the negative angles are clearly higher close to the hub meaning that the aspiration tends to reinforce the cross-flow from pressure to suction side (passage vortex effect). Aspiration corresponding to Cq=0.02 successfully suppresses stronger flow deviations from the blade suction surface for 63°; however the improvement is only marginal in the case of α=65°.

5.2.4 MACH NUMBER

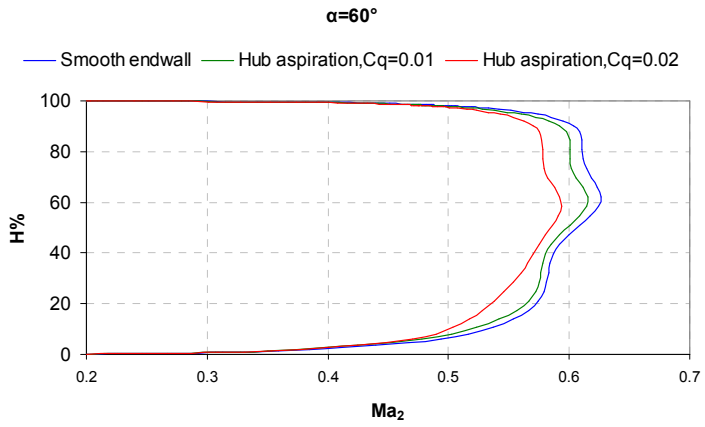

Fig 5.8a: Span-wise profile of downstream Mach number for α=60° (Smooth endwall/hub aspiration)

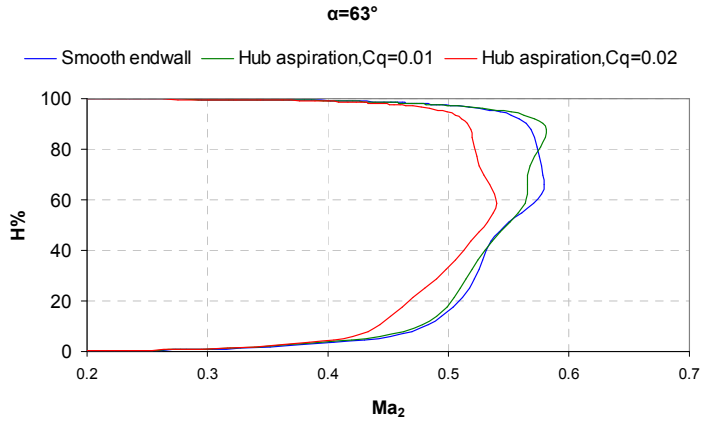

Fig 5.8b: Span-wise profile of downstream Mach number for α=63° (Smooth endwall/hub aspiration)

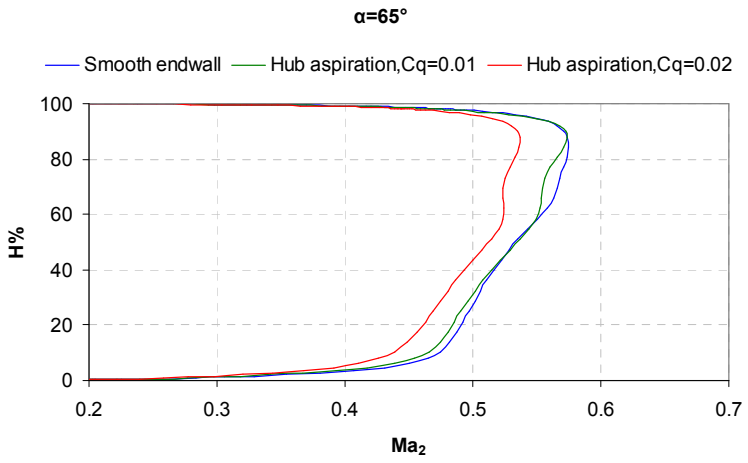

Fig 5.8c: Span-wise profile of downstream Mach number for α=65° (Smooth endwall/hub aspiration)

The downstream Mach number is appreciably reduced with aspiration (Cq=0.02) owing to a better static pressure compression on the blade. It is observed that the aspiration with Cq=0.01 does not offer much improvement over the baseline blade without aspiration for all the three operational points under discussion.

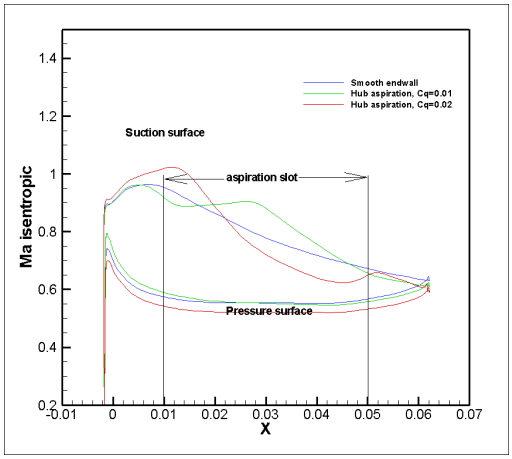

Fig 5.9a: Isentropic Mach number at 10% span at α=60°, (Smooth endwall/hub aspiration)

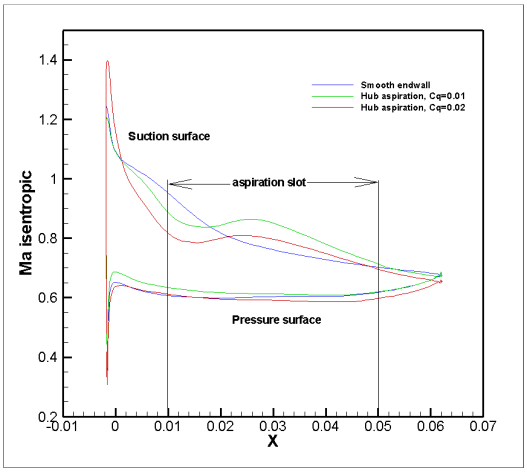

Fig 5.9b: Isentropic Mach number at 10% span at α=63°, (Smooth endwall/hub aspiration)

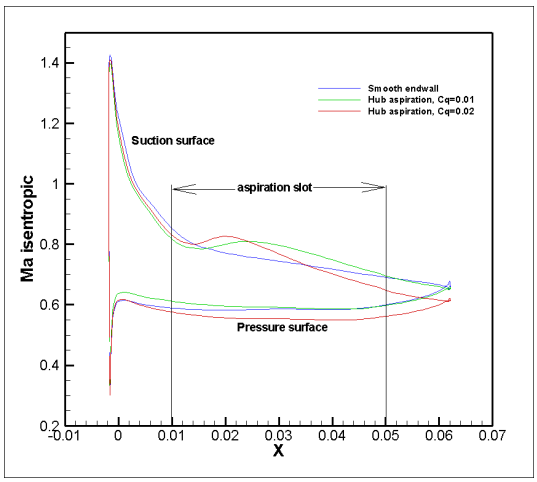

Fig 5.9c: Isentropic Mach number at 10% span at α=60°, (Smooth endwall/hub aspiration)

Figures 5.9a-c show the evolution of isentropic Mach number along the blade chord at 10% span. For all the cases studied here, the local velocity spikes at the leading edge are evident by the high peak isentropic Mach number values. The local isentropic Mach number values get higher with aspiration as the flow is accelerated by the depression created in the cavity.

For α=60° and 63° with hub aspiration Cq=0.01, there is a local increase in isentropic Mach number from X=20mm to X=40mm on the suction surface. This is due to radial outflow of fluid from the cavity to the flow path and a probable presence of the vortex due to recirculation of fluid. The corner region between these axial limits (X=20 to 40mm) may be susceptible to flow separation. This will be verified by the analysis of flow topologies on the walls. While hub aspiration with Cq=0.02 is found to decelerate the flow on the suction surface for α=60° and 63°, the traces of radial outflow are clearly seen in the case of α=65°.

Next, we shall see the Mach number flow field visualisation at 10% span.

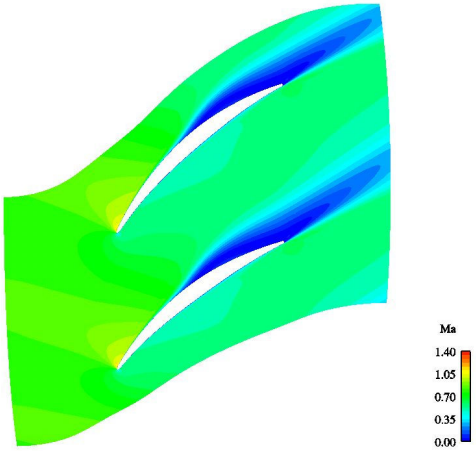

Fig 5.10a: Mach number at 10% span, Configuration: Smooth endwall at α=63°

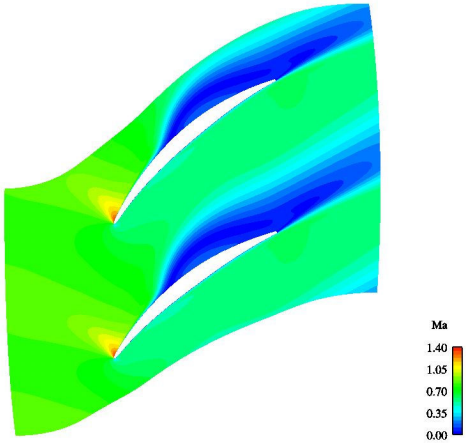

Fig 5.11a: Mach number at 10% span, , Configuration: Smooth endwall at α=65°

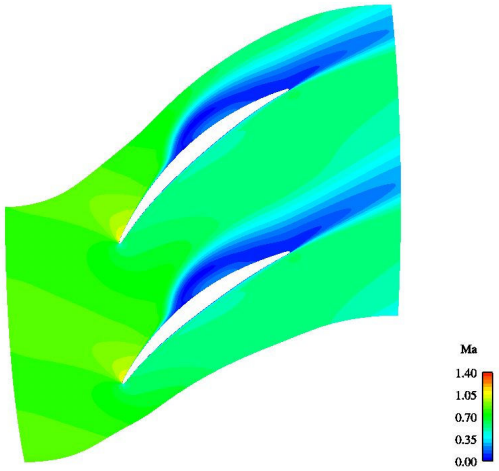

Fig 5.10b: Mach number at 10% span, Configuration: Hub aspiration, Cq=0.01 at α=63°

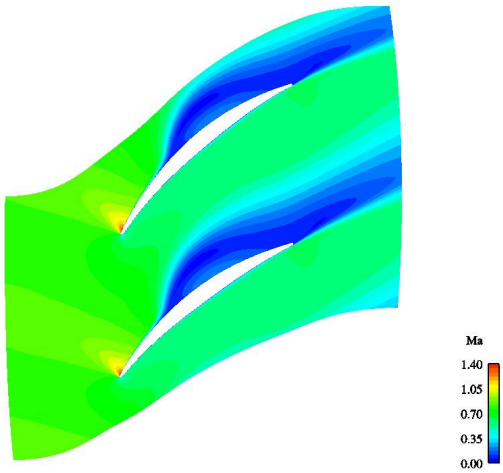

Fig 5.11b: Mach number at 10% span, , Configuration: Hub aspiration, Cq=0.01 at α=65°

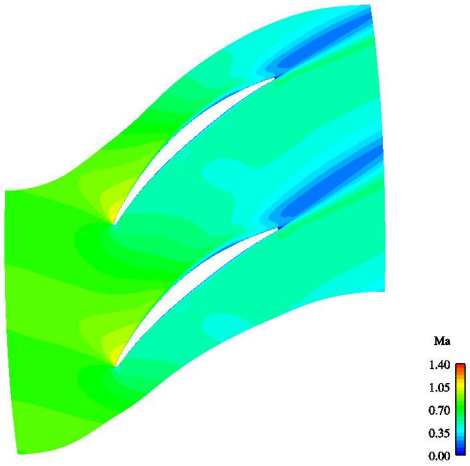

Fig 5.10c: Mach number at 10% span Configuration: Hub aspiration, Cq=0.01 at α=63°

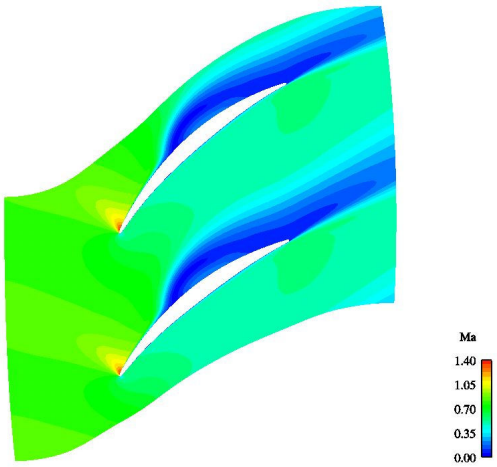

Fig 5.11c: Mach number at 10% span, , Configuration: Hub aspiration, Cq=0.02 at α=65°

Figures 5.10-5.11 show the Mach number at 10% blade span for flow visualisation in the blade-to-blade plane for α=63° and α=65°. At α=63°, the flow separation is found to increase with hub aspiration, Cq=0.01 and is completely suppressed by hub aspiration, Cq=0.02.

At α=65°, the flow separation increases with hub aspiration, Cq=0.01 and is only slightly reduced with hub aspiration, Cq=0.02. The growth of flow separation with hub aspiration, Cq=0.01 is again attributed to the recirculation of fluid from the aspiration cavity to the flow path.

5.2.5 ENTROPY IN THE BLADE TO BLADE PLANE

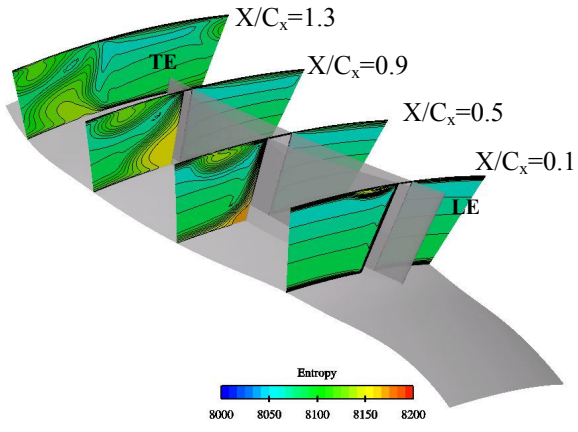

Fig 5.12a: Entropy in blade passage, Configuration: Smooth endwall at α=63°

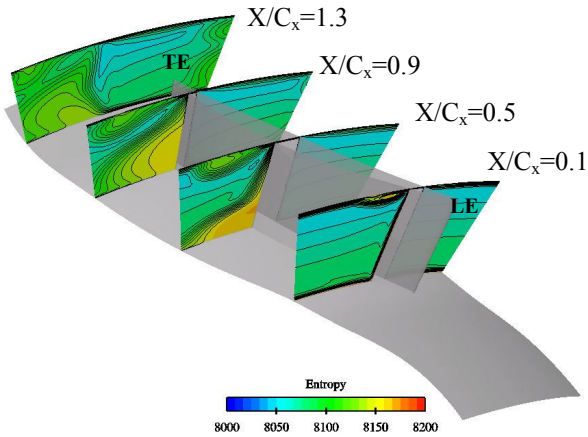

Fig 5.13a: Entropy in blade passage, Configuration: Smooth endwall at α=65°

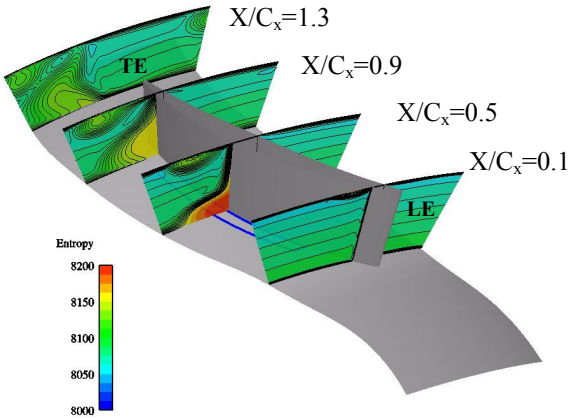

Fig 5.12b: Entropy in blade passage, Configuration: Hub aspiration, Cq=0.01 at α=63°

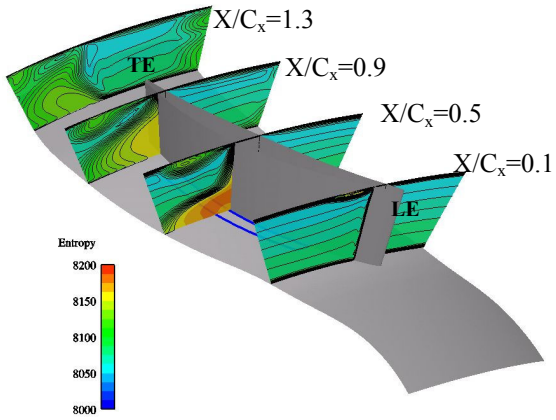

Fig 5.13b: Entropy in blade passage, Configuration: Hub aspiration, Cq=0.01 at α=65°

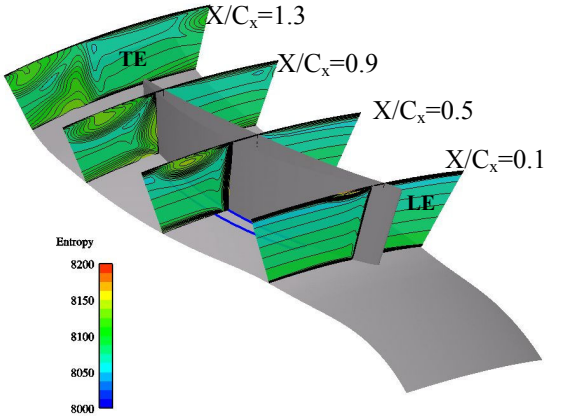

Fig 5.12c: Entropy in blade passage, Configuration: Hub aspiration, Cq=0.02 at α=63°

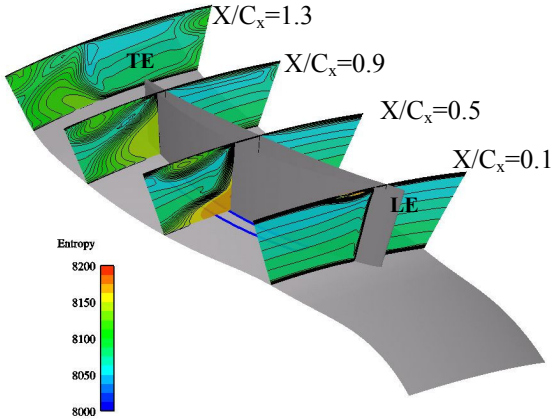

Fig 5.13c: Entropy in blade passage, Configuration: Hub aspiration, Cq=0.02 at α=65°

The visualisation of entropy in blade passage in figures 5.12-5.13 shows the evolution of the corner separation and the tip leakage vortex from the blade inlet to the downstream plane for α=63° and α=65°. In the case of aspiration with Cq=0.01, the corner separation is found to be clearly visible at mid chord while it is non existent in the baseline at the design point.

The corner separation visualised at both the points with Cq=0.01 is stronger than the other configurations due to recirculation of fluid between the flow path and the cavity. The corner separation is almost suppressed with aspiration flow rate of 2% at α=63° whereas at α=65°, the corner separation is found to increase with 1% aspiration flow rate and there is only a marginal reduction of corner separation with 2% aspiration flow rate. The above results lead to the conclusion that due to strong corner separation, the operating range is limited at the highest loss point even with hub aspiration strategy using different aspirated flow rates.

5.3 ANALYSIS OF FLOW TOPOLOGY

5.3.1 FLOW TOPOLOGY AT THE DESIGN POINT (α=60°)

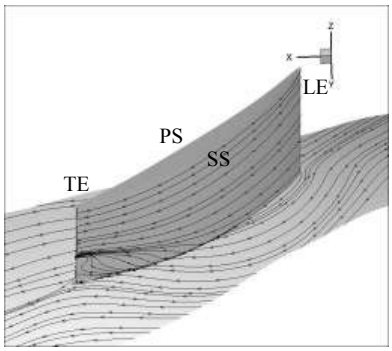

Fig 5.14a: Skin friction lines on blade and hub wall, Configuration: Smooth endwall at α=60°

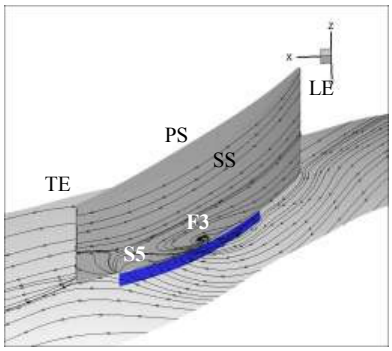

Fig 5.14b: Skin friction lines blade and hub wall, Configuration: Hub aspiration, Cq=0.01 at α=60°

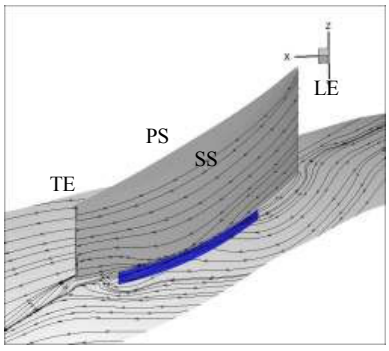

Fig 5.14c: Skin friction lines blade and hub wall, Configuration: Hub aspiration, Cq=0.02 at α=60°

The flow topologies are discussed here on the hub wall and the suction side for all the cases excluding the leading edge and the trailing edge. Both the leading edge and the trailing edge exhibit similar flow topologies as discussed in the previous chapter for the design point and hence they are not repeated. The baseline case without aspiration shows the suction surface dividing streamline enveloping a very small zone of suction side separation close to the trailing edge.

In the case of aspiration with Cq=0.01, the flow topology is complex with a focus F3 appearing on the suction surface of the blade followed by a saddle point S5. This is due to the recirculation of fluid between the cavity and the flow path and will be discussed immediately in the next section.

Aspiration with Cq=0.02 completely suppresses the suction side separation and the entire flow path is free of critical points. There is however, a radial displacement of limiting streamlines from the cavity to the flow path after mid-chord indicating decreasing effect of aspiration along the blade chord. Downstream of the aspiration slot, the fluid tends to accumulate in the corner from the secondary flow (passage vortex) as well as the recirculation of flow from the cavity. Together, they tend to form a single dividing streamline on the hub wall as they exit the blade passage. This leads to a local rise in the entropy in the downstream region at the hub wall.

5.3.1.1 RECIRCULATION OF FLUID IN THE FLOW PATH

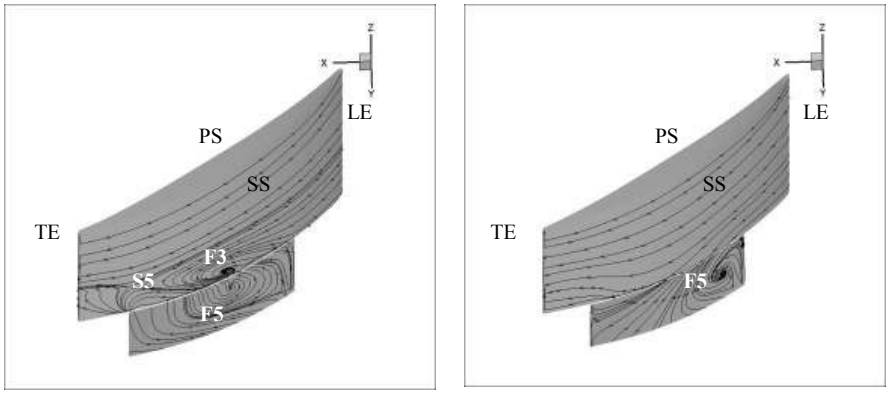

Fig 5.15: Skin friction lines on the suction surface and the aspiration cavity for aspiration with Cq=0.01(left) and Cq=0.02 (right)

In the figure 5.15 above the hub wall is not shown; only the suction side of the blade and of the aspiration cavity wall are shown with skin friction lines to give an insight into the vortex flow interaction. When 1% of the flow is aspirated, the flow enters the aspiration cavity but it is not confined into it. It re-circulates in the form of a vortex normal to the wall of the suction side and the wall of the aspiration cavity to introduce a three-dimensional vortex circulating between the flow path and the cavity.

This vortex is seen as focal point F3 on the suction surface and F5 in the aspiration cavity. This forms a system of vortices connecting and re-circulating with each other in a complex way on two walls. The flow aspirated in the aspiration cavity separates forming a vortex F5 that tends to propel out of the cavity in the flow path where it interacts with the vortex F3. The reason of vortex F5 propelling radially from the aspiration cavity into the flow path is that aspirating lower massflow (Cq=0.01) does not create enough depression to hold the vortex inside the cavity or eliminate it. The consequence is more critical for the flow path as it compromises the aspiration capability of the slot itself.

Hence, an important conclusion can be drawn: **"For a given blade geometry and an aspiration strategy, there exists a critical value of the aspirated massflow, below which the aspiration may be rendered ineffective"**

A second important factor is the shape of the cavity itself. As the cavity is large enough the aspirated massflow under the adverse pressure gradients is able to form a large re-circulating vortex in the absence of geometric constraints (length constraints). Simply put, the magnitude of the re-circulating vortex is dependent upon the volume of the cavity defined by its geometric parameters.

As the cavity is not wide enough in the circumferential direction, the recirculation vortices, although present, do not have a major contribution to the total pressure loss generation due to their limited strength at the design point. In fact, there might still be a gain in terms of total pressure losses. However, under the influence of increasing adverse pressure gradients with increasing incidence the corner separation is likely to become more intense and so is the recirculation (if not controlled well). This might indicate a risk of compromising the efficiency of aspiration strategy as a whole. The recirculation might interact and increase the intensity of the corner vortex on the hub wall or vice versa. Such an interaction happens in the case of very strong flow separation and will be observed later for the case of α=65°.

On the contrary, with hub aspiration, Cq=0.02, the vortex of separation inside the aspiration cavity F5 is well confined within the cavity and does not propel into the flow path. The flow path is clear of critical points and hence aspiration can be determined to have successfully suppressed the separation.

5.3.2 FLOW TOPOLOGY AT THE INTERMEDIATE POINT (α=63°)

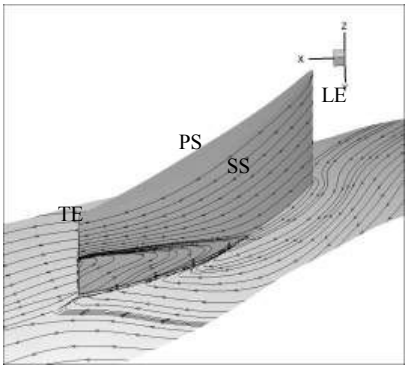

Fig 5.16a: Skin friction lines on blade and hub wall, Configuration: Smooth endwall at α=63°

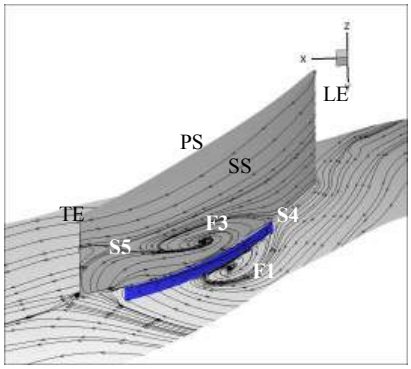

Fig 5.16b: Skin friction lines on blade and hub wall, Configuration: Hub aspiration, Cq=0.01 at α=63°

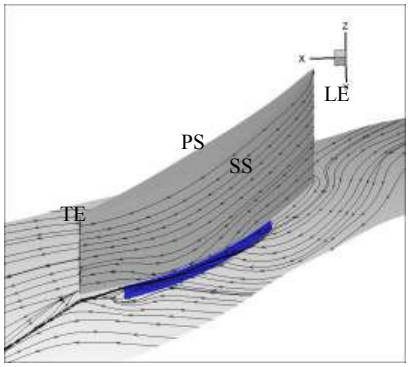

Fig 5.16c: Skin friction lines on blade and hub wall, Configuration: Hub aspiration, Cq=0.02 at α=63°

The flow topology in this case is very similar to the previous case with the exception of a focal point F1 appearing on the hub wall when 1% of the inlet massflow is aspirated. As with the case of increasing incidence, the regions of flow separation on the suction surface are larger for the cases of smooth endwall and hub aspiration with Cq=0.01 but all the singularities associated with flow separation on the suction surface and the endwall are completely suppressed when 2% of the inlet massflow is aspirated indicating the efficient control of aspiration at this suction rate.

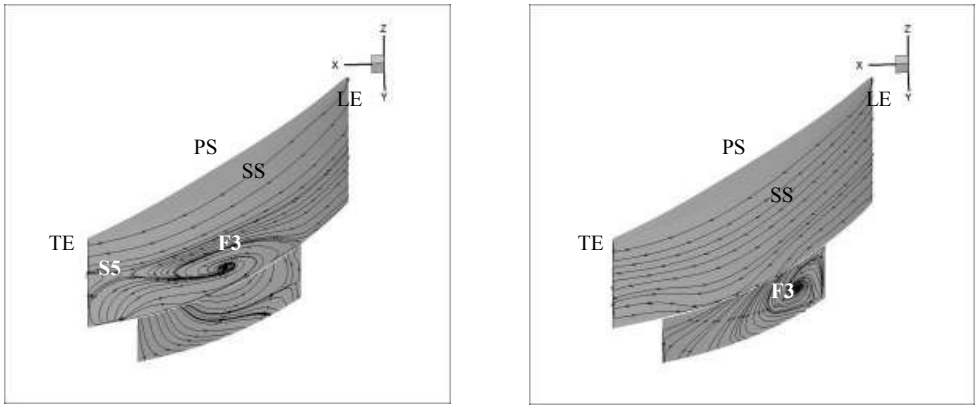

Fig 5.17: Skin friction lines on the suction surface and aspiration cavity for Cq=0.01(left) and Cq=0.02(right)

The flow topology exhibited by skin friction lines between the flow path and the aspiration cavity is comparable to that of the previous case of design point analysis where hub aspiration, Cq=0.01 leads to the amplification of vortex F3 on the suction surface due to recirculation from the aspiration cavity. It is noted, however, that there is no centre of focal point in the aspiration cavity. This indicates that the vortex in the aspiration cavity has merged with the vortex on the suction surface wall making it stronger and hence a much larger region of flow separation on the hub wall as compared to the previous case. The vortex in the aspiration cavity F3 in this case is well confined in the cavity with hub aspiration, Cq=0.02 similar to the previous case. The singularities in the flow path are eliminated.

5.3.3 FLOW TOPOLOGY AT THE HIGHEST LOSS POINT (α=65°)

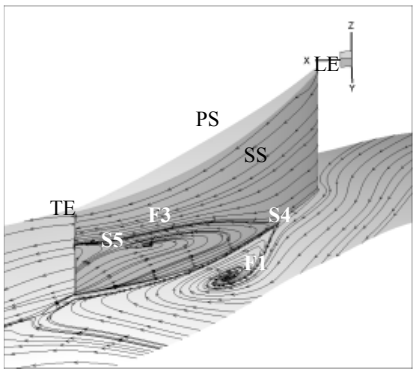

Fig 5.18a: Skin friction lines on blade and hub wall, Configuration: Smooth endwall at α=65°

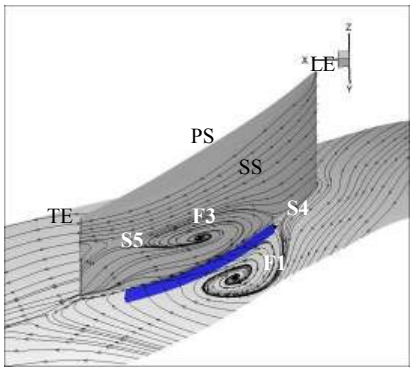

Fig 5.18b: Skin friction lines on blade and hub wall, Configuration: Hub aspiration, Cq=0.01 at α=65°

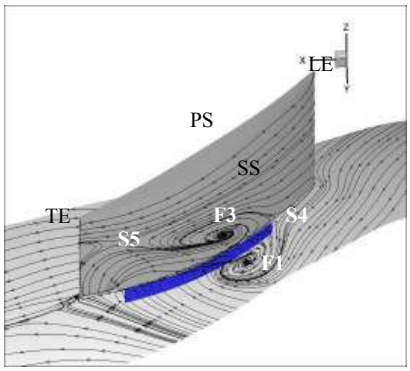

Fig 5.18c: Skin friction lines on blade and hub wall, Configuration: Hub aspiration, Cq=0.02 at α=65°

The flow topologies for the smooth endwall and the hub aspiration cases at the highest loss point are strikingly similar. Fully developed corner separation is evident in all the cases as it is not controlled by hub aspiration.

With hub aspiration, Cq=0.01 the focus of corner separation on the hub F1 is found to be stronger whereas F3 on the suction surface is displaced closer to the corner region as compared to the baseline case with smooth endwall. The radial leakage of fluid from the cavity intensifies the vortex F1 on the hub wall and it is found to mount in the flow path and actually connect with F3. The same phenomenon is observed in the case of hub aspiration, Cq=0.02 and is illustrated in figure 5.19:

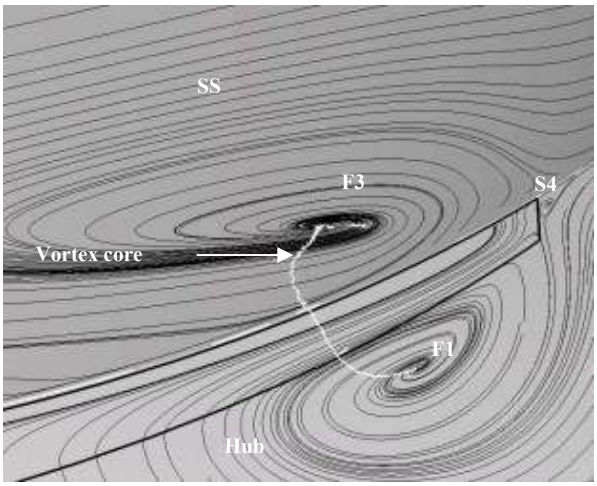

Fig 5.19: Vortex core connecting the foci F1 (hub wall) and F3 (suction surface), Configuration: Hub aspiration, Cq=0.02 at α=65°

It is noted that a common vortex core connects the vortices F1 and F3, only in the case of hub aspiration. As seen in the previous chapter with smooth endwall (figure 4.14) the vortex core of F1 mounts radially in the flow path and is carried downstream by the flow leaving the blade channel. A question now arises, "Is there only one principal flow separation on the hub wall and the suction surface, so that the suction surface separation is simply the extension of corner separation on the hub wall" It may seem so. However, a more probable explanation for this complex phenomenon may be that both the separation phenomena on hub wall and suction surface represented by F1 and F3 respectively are brought closer to each other in the corner region due to the depression in the cavity, giving them a tendency to merge.

The displacement of vortices F1 and F3 towards the corner region under the influence of aspiration indicates that if the depression can be increased in the cavity by increasing the quantity of aspirated massflow, it may just get strong enough to pull both F1 and F3 closer to each other, join them into a unified vortex, aspirate and confine this unified vortex into the cavity clearing the corner region and the flow path of the critical points. A parametric study to control the corner separation at the highest loss point with increase in aspirated massflow has been performed and will be discussed in the next section.

We can also observe that for this high incidence, the upstream part of the slot does not aspirate the saddle point S4, so that the efficiency of the control is probably smaller for this reason. Compare with α=63° where S4 has been aspirated in the slot for Cq=0.02.

Before proceeding, the recirculation of fluid between the aspiration cavity and the flow path for the highest loss point with hub aspiration, Cq=0.02 is presented in figure 5.20:

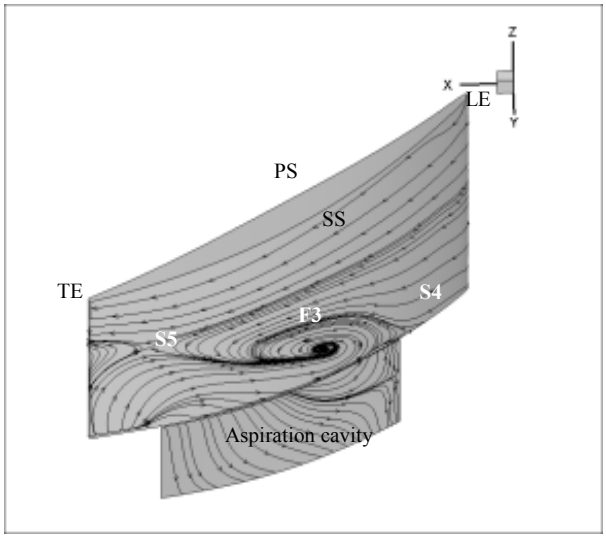

Fig 5.20: Skin friction lines on the wall of aspiration cavity and suction surface, Configuration: Hub aspiration, Cq=0.02 at α=65°

Most of the flow entering the aspiration cavity is propelled radially into the flow path rendering aspiration ineffective in this case. There is no trace of an independent vortex in the cavity indicating that F3 is a single strong vortex re-circulating between the flow path and the cavity.

5.4 STALL INDICATOR AND DIFFUSION PARAMETER

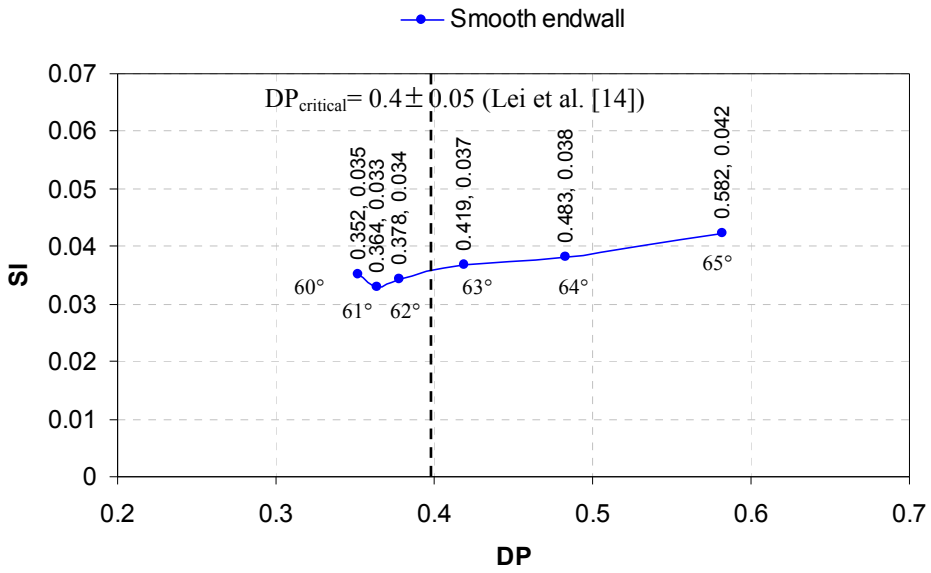

Fig 5.21a: Stall indicator (SI) and Diffusion parameter (DP) at operating points, Configuration: Smooth endwall (DP, SI values are plotted, e.g. At α=60°,(DP,SI)=(0.352,0.035))

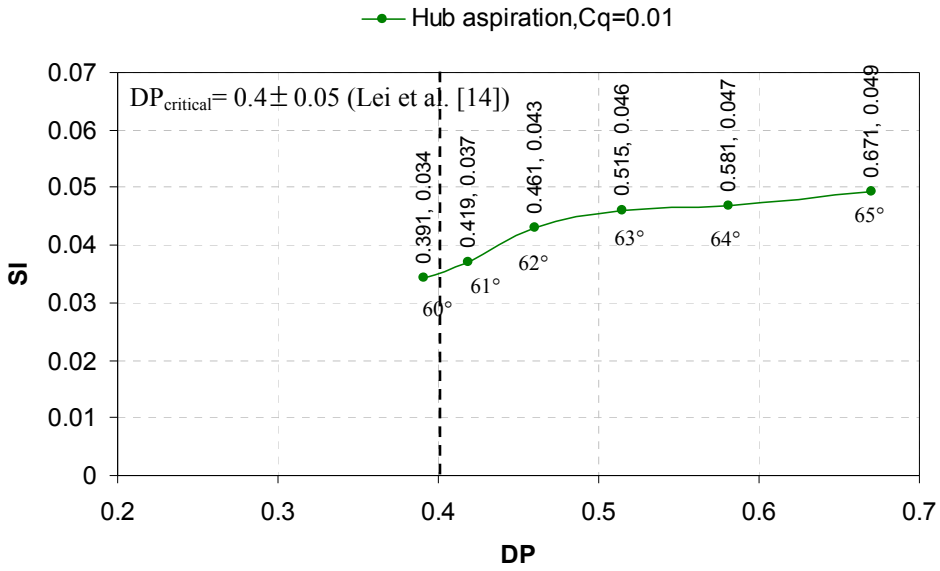

Fig 5.21b: Stall indicator (SI) and Diffusion parameter (DP) at operating points, Configuration: Hub aspiration, Cq=0.01 (DP, SI values are plotted, e.g. At α=60°,(DP,SI)=(0.391,0.034))

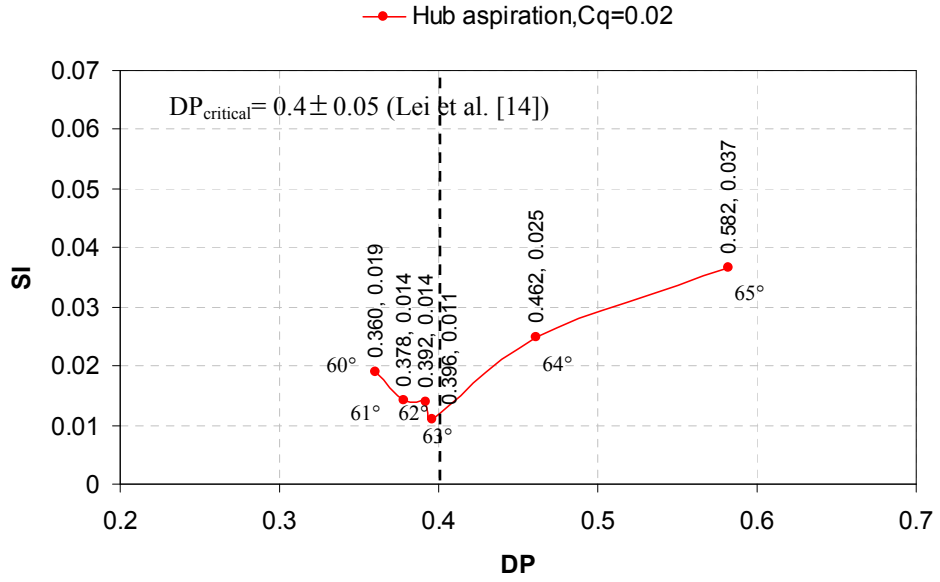

Fig 5.21c: Stall indicator (SI) and Diffusion parameter (DP) at operating points, Configuration: Hub aspiration, Cq=0.02 (DP, SI values are plotted, e.g. At α=60°,(DP,SI)=(0.360,0.019))

The Stall indicator and Diffusion parameter, introduced in chapter 2 (section 2.1) are plotted here for all the configurations studied. The values of Stall Indicator vary little in the configuration of smooth endwall over the operating range of the blade row. The suction surface flow separation is found to increase gradually with increasing incidence. The Diffusion parameter passes the critical value $DP_{critical}$=0.4 at α=63°. The flow topology of smooth endwall at α=63° in figure 5.16a shows that there is no corner separation on the hub wall. However, the skin friction lines are seen to curve strongly on the hub wall indicating that the onset of corner separation on the hub wall. The flow topology at α=64° verifies the development of corner separation on the hub wall and it is seen to get stronger at α=65° in figure 5.18a. Correspondingly, the DP values at α=64° and α=65° are higher than the critical value of DP.

With hub aspiration, Cq=0.01, we get higher values of DP over the entire operating range of the blade row. DP at design point α=60° exhibits a value close to the critical value of DP. The flow topology with hub aspiration, Cq=0.01 at α=63° in figure 5.18b shows the corner separation to be well developed on the hub wall, confirming the higher value of DP associated to hub corner stall. The corner separation is intense over the entire operating range of the blade row with hub aspiration, Cq=0.01. As the suction surface flow separation grows stronger with hub corner stall, we see higher values of SI over the entire operating range of the blade row.

With hub aspiration, Cq=0.02, it is surprising to see higher values of DP from α=60° to α=62° as compared to its corresponding values for the case of smooth endwall. Furthermore, the SI values are found to be lower indicating reduction in suction surface flow separation. The influence of hub aspiration, Cq=0.02 in suppressing the corner separation is clearly evident from visualisation of flow topologies in figures 5.14c and 5.16c at α=60° and α=63° respectively. The higher values of DP perhaps result from localised low-pressure regions associated with span-wise turning of cross flow in the hub corner.

Interestingly, at α=63°, we see a radical drop in values of DP and SI indicating the efficiency of hub aspiration, Cq=0.02 to control the corner separation when it is just on the verge of complete development as visualised in figure 5.16a. However, with the increase of incidence beyond this point, the corner separation fully develops and higher than critical values of DP beyond this point are in correlation with the visualisation of corner separation from previous study of flow topologies.

Based on the numerical studies and formulation of elements associated with hub corner stall, the Diffusion parameter developed by Lei et al. [14] (introduced in section 2.7) is applied to our case of blade without and with hub aspiration and the values obtained are found to correlate well with the numerically deduced value of $DP_{critical}$ to indicate the presence of hub corner stall in the blade row.

5.5 INFLUENCE OF INCREASING THE ASPIRATED FLOW RATE

In this parametric study performed at the highest loss point (α=65°), the aspirated flow rate is increased to 4% of the inlet mass flow rate, i.e., Cq=0.04, the results are compared against the baseline case with smooth endwall and hub aspiration, Cq=0.02.

5.5.1 TOTAL PRESSURE LOSS COEFFICIENT

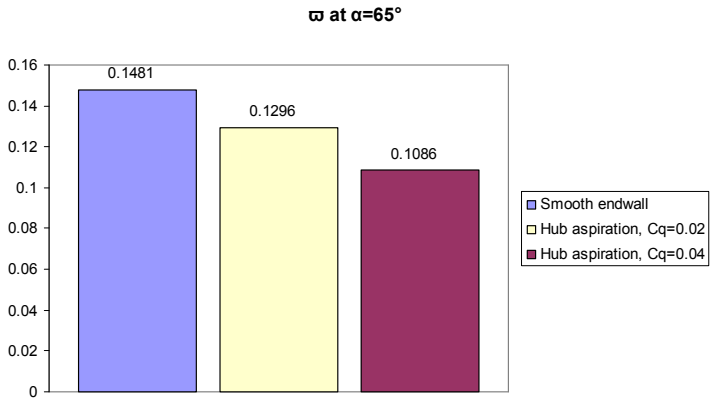

Fig 5.22: Total pressure loss coefficient at α=65° (Smooth endwall/Hub aspiration)

With hub aspiration, Cq=0.04, the total pressure loss coefficient is lowered by 26.6% over the baseline case of smooth endwall and 16.2% over hub aspiration, Cq=0.02. The total pressure losses are very sensitive to the aspirated massflow, higher aspirated flow rates lead to forced removal of separated flows in the corner region and favouring higher pressure rise capability of the blades.

5.5.2 MACH NUMBER

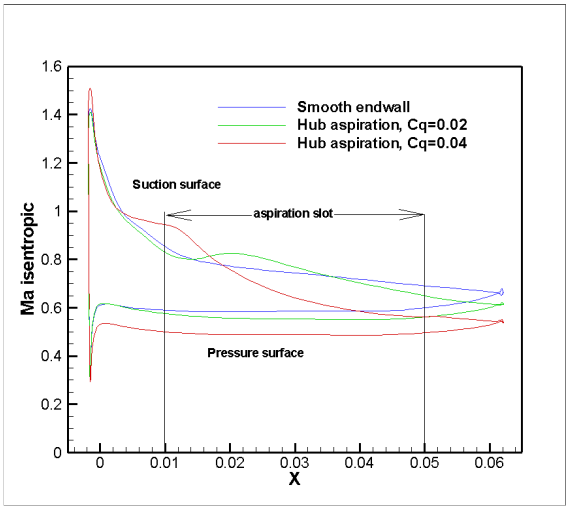

Fig 5.23: Isentropic Mach number at 10% span for α=65°

There is a local increase in the value of the isentropic Mach number with hub aspiration, Cq=0.02 in the axial zone from X=20 to 40mm as the flow propels radially into the corner region from the aspiration cavity. With hub aspiration, Cq=0.04, the recirculation vortex is confined into the aspiration cavity and hence the flow is smoothly decelerated as indicated by the evolution of isentropic Mach number on the blade chord.

5.5.3 ANALYSIS OF FLOW TOPOLOGY

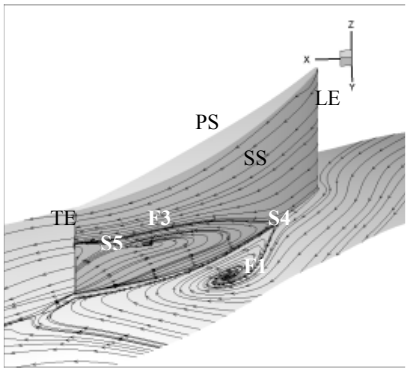

Fig 5.24a: Skin friction lines on blade and hub wall, Configuration: Smooth endwall at α=65°

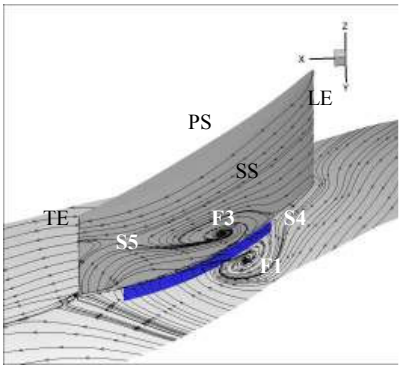

Fig 5.24b: Skin friction lines on blade and hub wall, Configuration: Hub aspiration, Cq=0.02 at α=65°

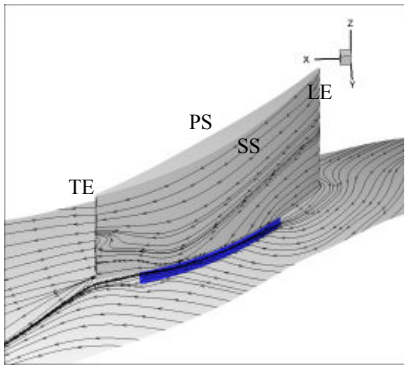

Fig 5.24c: Skin friction lines on blade and hub wall, Configuration: Hub aspiration, Cq=0.04 at α=65°

As seen from the figure 5.24c, the corner separation is completely eliminated with hub aspiration, Cq=0.04. Doubling the aspirated flow rate in the aspiration cavity is a way to improve the performance of the blade row and also increase its operating range; however, it is not easy to justify this strategy.

Aspirating such a higher flow rate may incur system level penalties that could influence the global performance of the system. The objective of this study is limited to show the efficiency of increasing the aspirated flow rate to control the flow separation and no claim is made to recommend such a strategy.

5.6 INFLUENCE OF ASPIRATION BY EXTENDED HUB SLOT

Since the saddle point S4 is the origin of dividing streamlines on the hub wall and the suction surface, we may reason that aspirating S4 would be a better way to implement flow control. We have made a parametric study to understand the influence of an extended slot at α=65° with Cq=0.02 and 0.04. The hub slot has been extended 4% chord upstream of the existing hub slot. We shall limit the discussion of results to the analysis of flow topologies associated with this study.

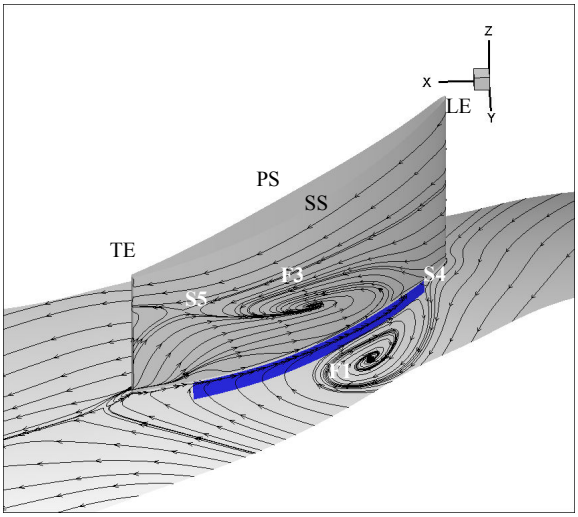

Fig 5.25a: Skin friction lines on blade and hub wall, Configuration: Hub aspiration (extended slot), Cq=0.02 at α=65°

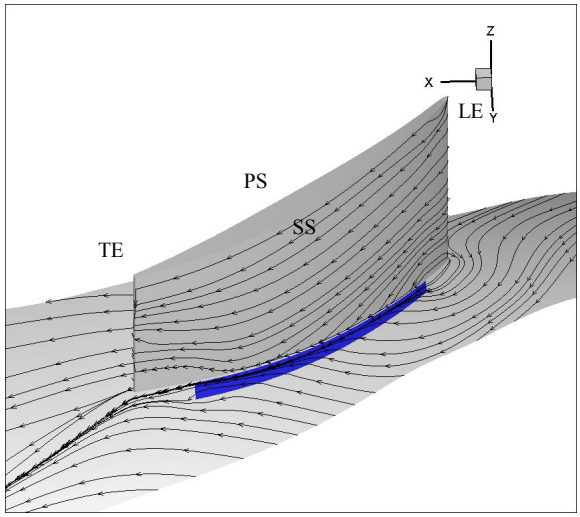

Fig 5.25b: Skin friction lines on blade and hub wall, Configuration: Hub aspiration (extended slot), Cq=0.04 at α=65°

The flow topologies in figures 5.25a,b are directly comparable to those in figures 5.24b,c. The flow topologies are strikingly similar with the extended hub slot when compared to those with the original hub slot. The saddle point S4 is displaced further upstream when the slot is extended upstream, making the flow separation stronger with the extended slot. We may say that it would not be advisable to implement aspiration close to the leading edge due to the sensitive nature of the flow in this zone. We are faced by the limitation of the present aspiration strategy to improve the operating range of the blade row. A different aspiration strategy is required to overcome this limitation.

5.7 CONCLUSION

The present chapter has focussed on the influence of hub aspiration on the cascade performance parameters and the associated phenomena of the aspiration on the flow topologies in the cascade. Globally, hub aspiration with Cq=0.01 has been detrimental to the cascade performance and increasing the aspirated massflow coefficient to Cq=0.02 has yielded beneficial results for the cascade.

Both the aspirated massflow coefficients associated to the hub aspiration have not been effective in increasing the operating range of the cascade. The flow topology remains particularly complex with critical points in the flow path at the highest loss incidence point. This establishes the influence of the sensitivity of the aspirated massflow. It is necessary to aspirate a certain amount of massflow below which the aspiration will be rendered futile. In this case, endwall aspiration with Cq=0.01 does not create enough depression in the aspiration cavity to completely confine the separation vortex in the cavity.

In absence of stronger depression in the cavity, the flow entering the cavity quickly separates and forms a re-circulating vortex between the cavity and the flow path. The separation vortex slips out of the aspiration cavity and weakens the suction surface wall boundary layer. The interaction of the vortices in the cavity and the flow path is revealed to be a complex three-dimensional interaction. At lower incidences, the centres of the vortices on the wall of aspiration cavity and the wall of the blade suction surface are found to be distinct and only their outer layers are found to interact. As the incidence increases, the vortices seem to merge into one single large vortex circulating between the flow path and the cavity. The weaker depression in the cavity propels the flow separation vortex upwards in the flow path.

Increasing the aspirated massflow rate to Cq=0.02 has been beneficial for all the parametric points in terms of reduction of total pressure losses. The flow topology visualisations on the walls of the suction surface and the aspiration cavity show the confinement of the flow separation vortex in the cavity for all the incidence points except the highest loss incidence point. There appears to be one large vortex circulating on the walls of the suction surface and the aspiration cavity; an indication of the merging of the two vortices as seen in the previous cases. However, a net reduction in total pressure losses is still achieved for this case. This may be due to the lower strength of the vortex as compared to the case of Cq=0.01.

The presence of critical points in the flow path along with the strong corner separation at the highest loss incidence point with both the aspiration flow rates presents the limitation of the boundary layer aspiration strategy in this case to improve the operating range of the cascade. A simple way to achieve this improvement in the operating range is the increase of aspirated massflow in the cavity. When Cq is increased from 0.02 to 0.04, the corner separation is completely suppressed providing scope to increase the operating range of the cascade. However, such an attempt must be considered while taking into account the system level penalty on the engine cycle. Due to very high suction rate, this aspiration strategy with Cq=0.04 is demonstrated only as a possibility and is not recommended.

Furthermore, the extension of hub slot in the upstream zone close to the leading edge to aspirate saddle point responsible for flow separation has been futile. The saddle point is displaced further upstream with the extended slot, making flow separations stronger. We recommend a different aspiration strategy for the effective control of flow separation.

6. COMPARISON OF RESULTS: EXPERIMENTS/CFD

6.1 INTRODUCTION

This chapter is discusses the experimental results of the tests performed at EPFL and the validation of numerical results. The first campaign of tests was carried out at EPFL on the baseline stator blade row without and with hub aspiration. The setup of the test rig and cascade instrumentation is defined briefly along with a description of the two methods employed for experimental observations: aerodynamic probe and LDA (Laser Doppler Anemometry). Some incoherencies are observed in the experimental measurements and are discussed.

CFD studies are done with upstream experimental measurements as inlet boundary conditions and the numerical results are compared with experimental measurements with some hypothesis in turbulence modelling. The results are analysed and discussed for various cases along with the differences between experiments and CFD results. The CFD parameters leading to an acceptable agreement with the test results have been assessed and frozen.

6.2 EXPERIMENTAL RIG

The test rig used for these experiments is a non rotating annular cascade test rig in which the inlet flow is pre-swirled by the adjustable guide vanes.

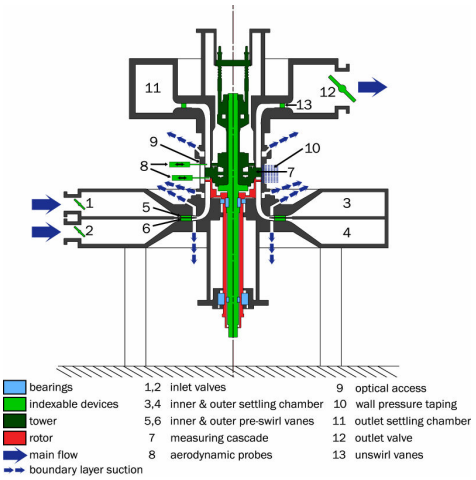

Fig 6.1a: Schematic view of the test rig (Colombo et al. [36])

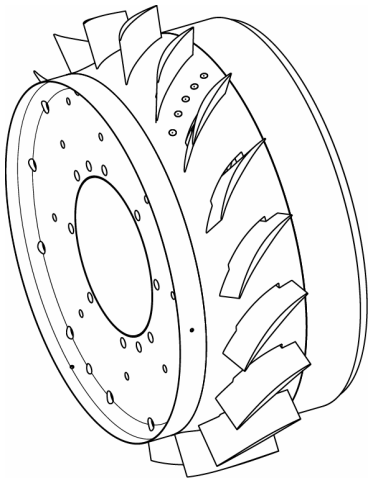

Fig 6.1b: CAD design of the stator blade row (Colombo et al. [36])

Figures 6.1a,b show the test rig and the annular stator blade row with hub aspiration slot on the hub wall. The inlet conditions as Mach number and flow angle can be varied over a large range and a two settling chamber system allows adjusting the radial flow distribution at the inlet to the blade channel.

The non-rotation of the stator allows for direct access of optical and aerodynamic measurement equipment. The test facility is supplied with air by a four stage radial compressor with a maximum mass flow of 10 kg/s and a maximum pressure ratio of 3.5. Heat exchangers allow adjusting the air temperature that is set to 298K during the experiments.

An additional compressor is used to suck off the wall boundary layers as well as the flow from the hub slots. Upgraded measurement equipment allows controlling the flow conditions and ensuring the repeatability of the tests, which is essential for the comparison of the aspirated cases to the reference measurements. The cascade instrumentation is complex with more than 60 pressure taps installed for sensing information. Air enters the cascade via two inlet chambers and this mixing of the air causes a thick boundary layer at the cascade inlet that is aspirated by a boundary layer suction trap to reduce the thickness of the boundary layer. (Colombo et al. [36])

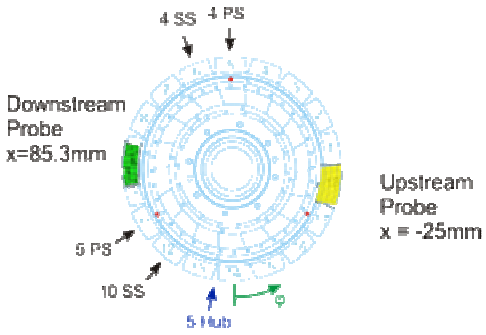

Fig 6.2: Stator blade row instrumentation with probe positions in the blade channel (Colombo et al. [36])

6.3 STATOR BLADE ROW INSTRUMENTATION

6.3.1 AERODYNAMIC PROBE

The aerodynamic probe measurements were performed with a conical five-hole L-probe having a diameter of 2.5 mm. It is used to determine the velocity vector as well as stagnation and static pressure upstream and downstream of the blade channel. The position is 0.6 chord lengths upstream of the leading edge (in flow direction) for the inlet measurements and 0.3 chord lengths downstream of the trailing edge (in flow direction). The measurement grid consisted of at least 14x20 points per blade channel respectively in radial and circumferential direction.

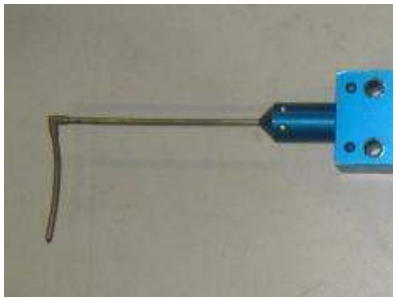

Fig 6.3: Aerodynamic probe (Colombo et al. [36])

6.3.2 PRESSURE TAPS

Static wall pressures were measured by 25 pressure taps situated at different axial positions on the inner and outer rig walls. As with the aerodynamic probe measurements, indexed rotation of the cascade permitted to obtain circumferential profiles. Additionally different blades are instrumented with pressure taps at mid-span.

Fig 6.4: Static pressure taps on the hub wall of the stator blade row (Colombo et al. [36])

6.3.3 LDA SETUP

A Dantec BSA 2D system with 250 mm focal laser probe is used for LDA measurements. The probe is fitted on an automatic 3-axis displacement system. Measurements are made in a radial-tangential (r,θ) frame of reference with a remote displacement of the probe in the radial direction and a remote displacement of the cascade in the tangential direction. The seeding system includes probes, automatic displacement, seeding generators and controlling devices. The seeding probes are fitted far upstream of the cascade on the two inlet pipes of the test rig. The seeding particles are olive oil droplets. A window equipped with optical access for the upstream and downstream measurement locations has been designed. The measurements have been performed up to the casing but were limited to a distance greater than 3 mm from the hub because of the very strong noise from the back-scattering light. For each measurement point, 100,000 samples are acquired simultaneously for both velocity components. The measurement grid consisted of at least 21x21 points for one blade channel. Axial and tangential mean velocity components, their velocity fluctuations and the corresponding shear stress are then obtained.

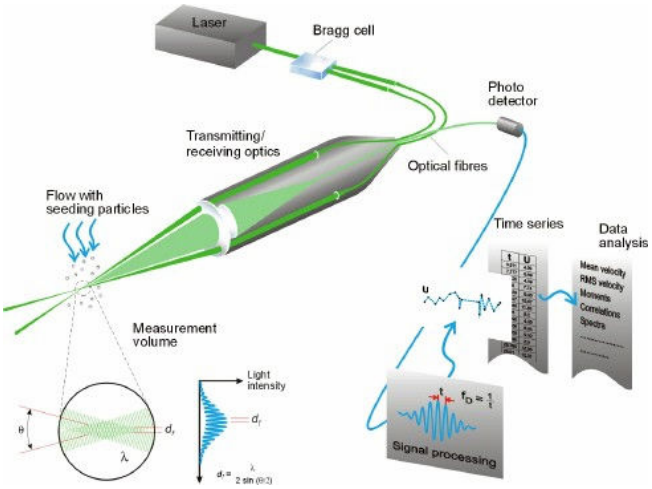

Fig 6.5: Illustration of working of LDA (www.dantecdynamics.com)

LDA is a well-established technique that gives information about flow velocity. Its non-intrusive principle and directional sensitivity make it very suitable for applications with reversing flow, chemically reacting or high-temperature media and rotating machinery, where physical sensors are difficult or impossible to use. It requires tracer particles in the flow.

The method's particular advantages are: non-intrusive measurement, high spatial and temporal resolution, no need for calibration and the ability to measure in reversing flows.

The basic configuration of an LDA (Figure 6.5) consists of:

- A continuous wave laser;
- Transmitting optics, including a beam splitter and a focusing lens;
- Receiving optics, comprising a focusing lens, an interference filter and a photo detector;
- A signal conditioner and a signal processor.

(Source: www.dantecdynamics.com)

To sum up the measurement techniques used are:

- Aerodynamic probe measurements on a grid of points at inlet (X=-25 mm) and outlet (X=85.29 mm) (figure 4.4)
- LDA measurements at inlet and outlet of a blade channel for one flow condition on the same axial positions as the aerodynamic probe measurements
- Static pressure taps
    - 15 positions distributed on different blade suction and pressure sides at mid-span
    - 8 positions on the hub, 5 of which are situated inside the blade channel
    - 18 positions on the outer the rig walls

6.4 EXPERIMENTS

The experiments were done to study the flow characteristics of the stator blade row under the influence of:

- Different inlet flow angles
- Hub aspiration with Cq=0.02 and Cq=0.04
- No aspiration by sealing the hub slot with plugs (creating smooth endwall condition)
- No aspiration with open hub slot

6.4.1 CONFIGURATIONS OF EXPERIMENTS

The experiments have been performed on four configurations at different inlet flow angles and are tabulated below:

Configuration	α (Inlet flow angle)
Smooth endwall, No aspiration	61°,63°,65°
Open hub slot, No aspiration	61°,63°,65°,67°
Hub aspiration active, Cq=0.02	61°,63°,65°,67°
Hub aspiration active, Cq=0.04	61°,63°,65°,67°

Table 6: Configurations of cases in comparison studies

The measurements for all the configurations have been done by the aerodynamic probe. LDA measurement is done only at the operating point of α=63° with hub aspiration, Cq=0.02. The test measurements on this particular point have been done by both probe and LDA. We define this point as the "reference point" for the present studies as it enables to study the discrepancies in both the measurement techniques.

6.5 EXPERIMENTAL MEASUREMENTS

The experimental measurements have been done by the aerodynamic probe and LDA; the LDA and probe are introduced at two different circumferential positions in the test rig, both upstream and downstream. There are some discrepancies found in the measurements carried out by both techniques.

The aerodynamic probe senses the total pressure, static pressure and flow angle measured in the (θ, z) plane; flow velocity and variables such as the Mach number are derived from the primitive variables.

LDA measures the velocity components while variables such as the Mach number, flow angle, intensity of turbulence, etc. are derived from the measured variables.

The measurement uncertainty for LDA measurements is estimated to be ±0.5° for the flow angle and ±1.5% for the velocities. To look at the discrepancy in measurement between LDA measurement technique and the aerodynamic probe let us look at the "reference point". Recall that the "reference point" corresponds to the case of α=63° with hub aspiration, Cq=0.02. The discrepancies in experimental measurements between probe and LDA are discussed at the reference point.

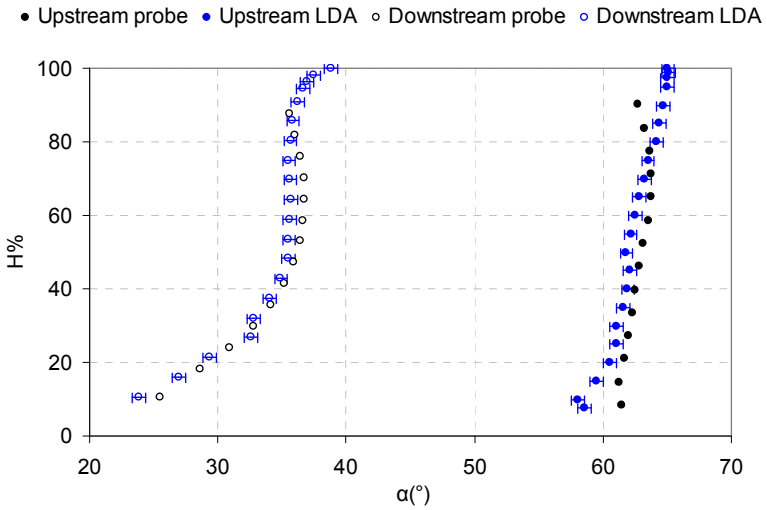

Fig 6.6: Span-wise profiles of circumferential averaged flow angle from experiments (Probe/LDA with uncertainties marks)

The 2D maps are presented in figure 6.7 in the (θ, r) plane. On the LDA results, we present with dotted lines the limit of the probe domain of measurement: the comparisons between the LDA and probes results should then be made in the inner side of these dotted limits.

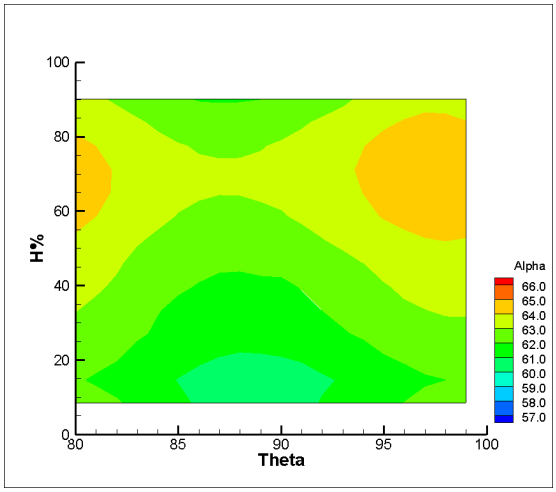

Fig 6.7a: Flow angle at upstream measurement plane from probe

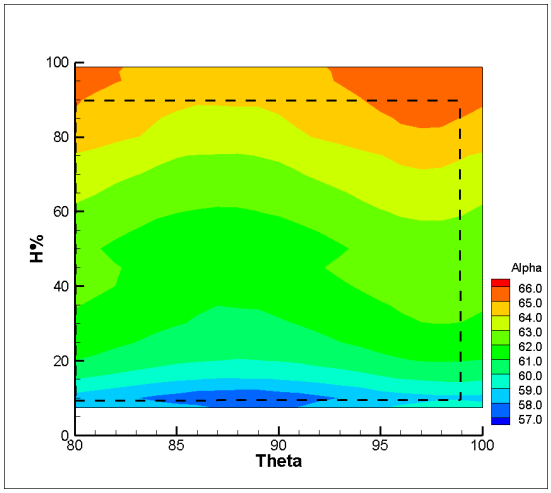

Fig 6.7b: Flow angle at upstream measurement plane from LDA

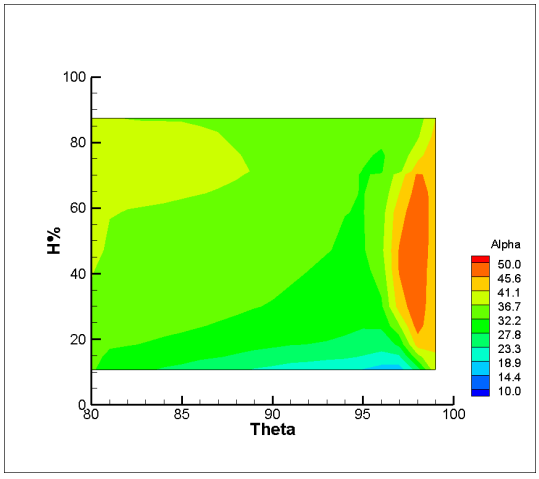

Fig 6.7c: Flow angle at downstream measurement plane from probe

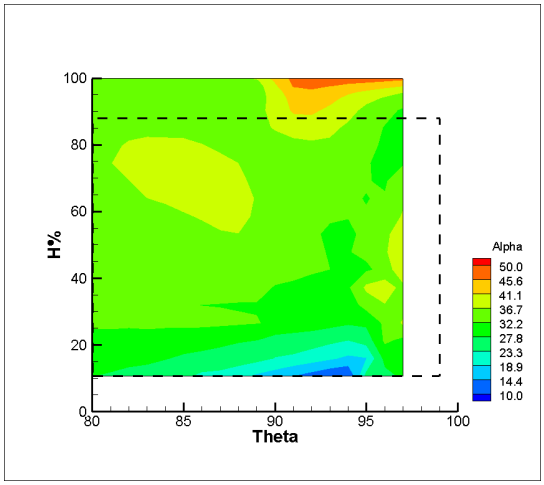

Fig 6.7d: Flow angle at downstream measurement plane from LDA

The upstream flow angle measured by LDA and the aerodynamic probe is found to have differences of 1-2° in their magnitude in their base values. The plot of uncertainty of flow angle measurements by LDA shows this difference to be small between 20-80% span. Also, the probe measurements show stronger gradients close to the hub and casing walls showing a greater discrepancy of the flow angle measurement close to the walls.

The downstream flow angle shows a good agreement between LDA and probes except between 40-80% span. The LDA measurements show a lower deflection than probe measurement from 40-80% span. Close to and at the casing wall there is noticeable increase of the flow angle by LDA due to the tip leakage vortex.

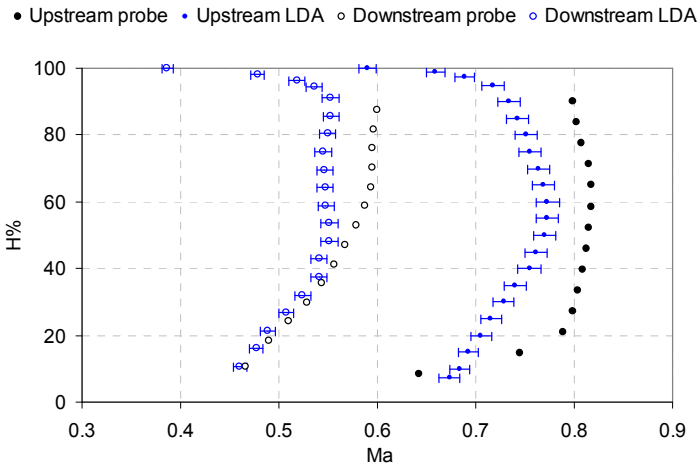

Fig 6.8: Span-wise profiles of Mach number from experiments (Probe/LDA)

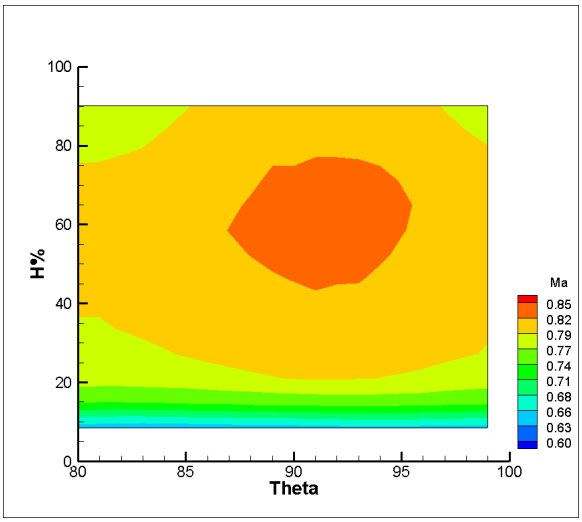

Fig 6.9a: Mach number at upstream measurement plane from probe

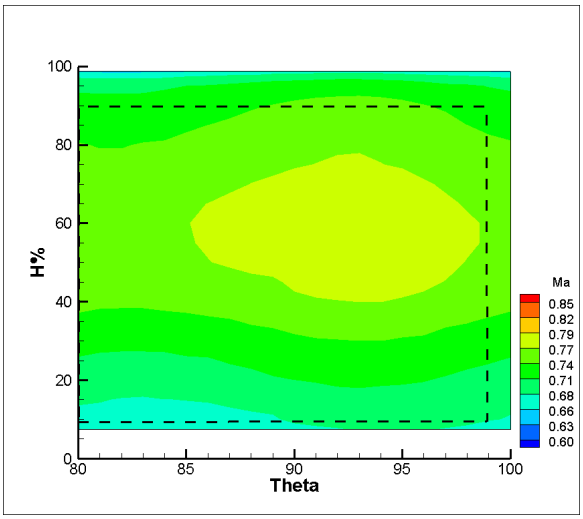

Fig 6.9b: Mach number at upstream measurement plane from LDA

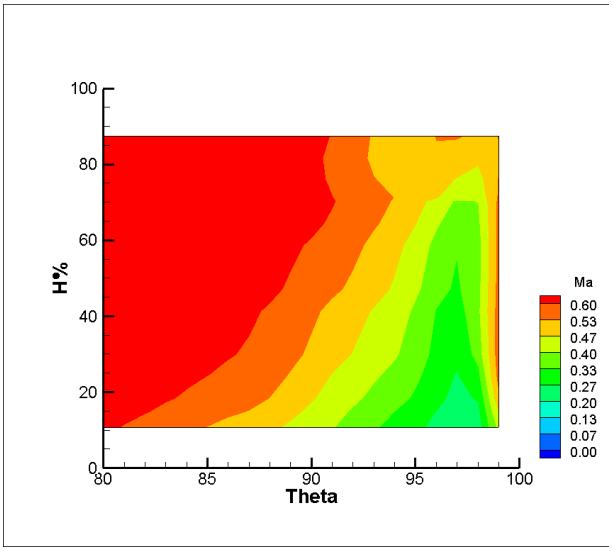

Fig 6.9c: Mach number at downstream measurement plane from probe

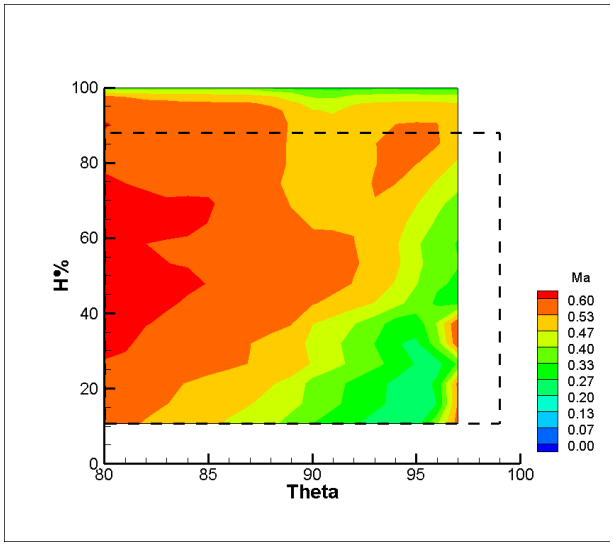

Fig 6.9d: Mach number at downstream measurement plane from LDA

The upstream Mach number deduced from LDA and the probe at the upstream measurement plane presents a high level of discrepancies in the magnitude and at a lower extend in the gradients. The probe Mach number is obtained from the total pressure and the static pressure measurements whereas the LDA Mach number is deduced from the measured velocity components and the available upstream averaged stagnation temperature. The hypothesis considered is the conservation of the stagnation temperature upstream to the location of LDA measurement plane.

LDA shows very strong gradients from the hub wall to the casing wall; the gradients are found to be altered approximately at mid-span. LDA Inlet flow is found to have a lower magnitude of the velocity and hence lower Mach number as compared to that deduced by the probe. The probe measurement shows a strong Mach number at inlet over most of the span (Ma>0.8) while LDA measurement shows the Ma to be significantly lower (Ma=0.76 at highest).

The discrepancy in the magnitude of Mach number by both the techniques has been a difficult issue to resolve for comparison with the CFD results. It has been speculated that the probe might cause local aerodynamic blockage leading to a higher velocity being measured but this has not been proven. The Mach number deduced from probe measurements is 5% higher than that deduced from LDA; blockage of the order of 5% does not seem realistic.

We have suspected that most of the discrepancies are linked to a circumferential distortion introduced upstream by the test rig. Some specific studies conducted at LTT-EPFL seem to confirm this hypothesis.

6.6 INLET BOUNDARY CONDITIONS: EXPERIMENTS AND CFD

All the CFD studies during the design phase prior to the experiments were done with theoretical conditions, in a way that the inlet variables are imposed as uniform or constant pressure gradients. Moreover, the turbulence intensity at the inlet domain has been neglected, and the boundary layer is assumed to start at the most upstream location of the computational domain. The objective of this section is to highlight the differences between the experimental and theoretical inlet conditions. We shall continue with the case of α=63° and hub aspiration, Cq=0.02

6.6.1 INLET TOTAL PRESSURE

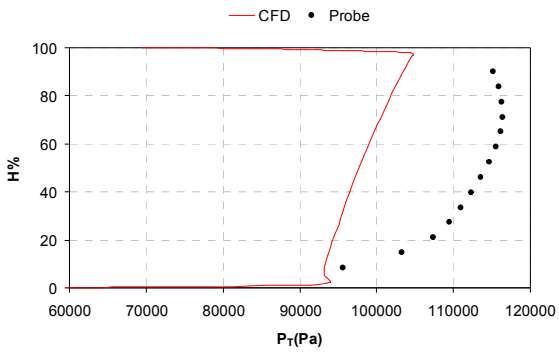

Fig 6.10: Span-wise profile of upstream total pressure (CFD/probe)

As seen in figure 6.10, the theoretical total pressure in previous CFD simulations has almost no gradients at the hub wall indicating a virtual absence of the boundary layer. The span-wise distribution of total pressure by the probe is marked by strong gradients with higher values as compared to its theoretical counterpart. The total pressure at inlet close to the hub wall shows very strong gradients due to the presence of thick boundary layers; it indicates the inefficiency of the boundary layer suction traps located upstream of the blade row inlet to smoothen the strong pressure gradients of the inlet flow.

6.6.2 INLET FLOW ANGLE

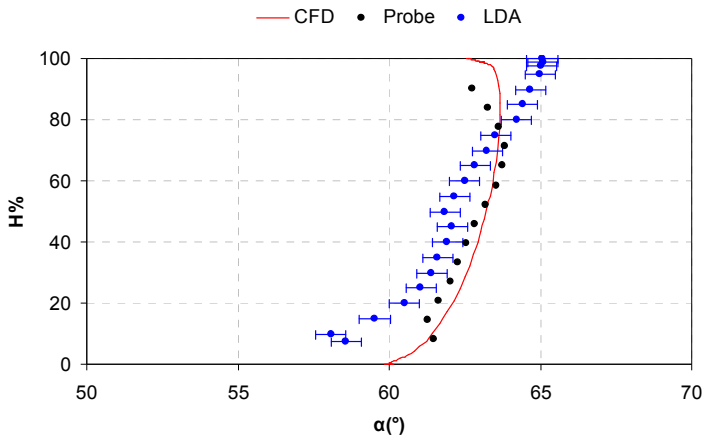

Fig 6.11: Span-wise profile of upstream flow angle (CFD/probe/LDA)

The inlet flow angle measured by probe and LDA also show stronger gradients than the theoretical condition. Considering these differences between the theoretical conditions and the experimental conditions, it is necessary to redo the numerical studies with the experimental inlet conditions.

6.6.3 INLET TURBULENCE

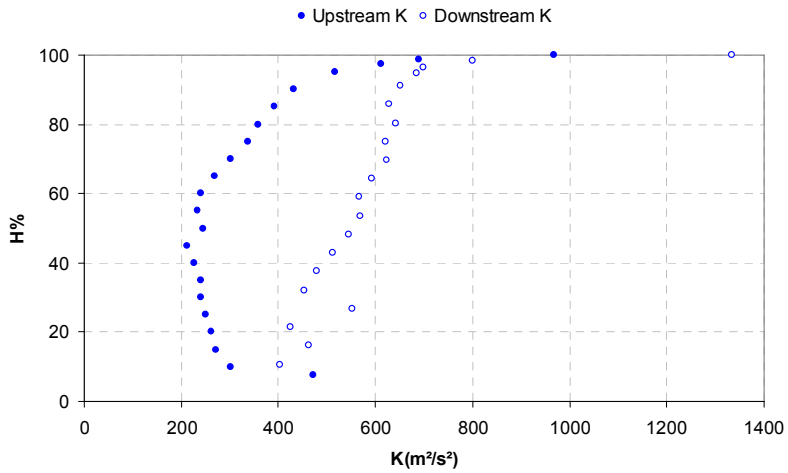

Fig 6.12: Span-wise profile of turbulent kinetic energy at upstream and downstream planes (LDA)

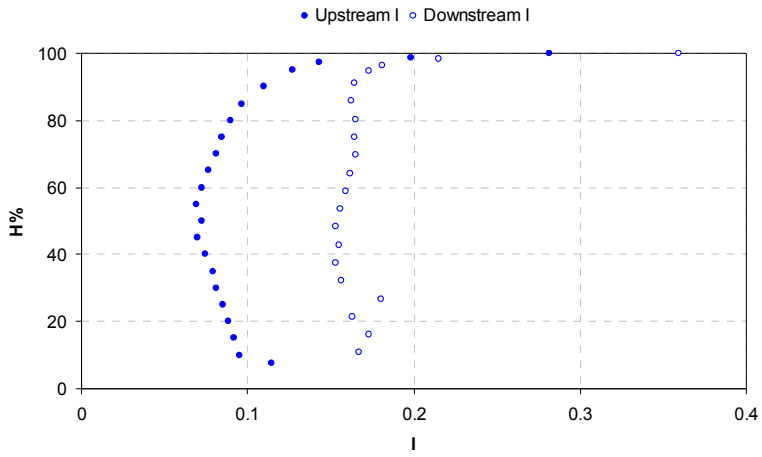

Fig 6.13: Span-wise profiles of intensity of turbulence at upstream and downstream planes (LDA)

The turbulence kinetic energy and the intensity of turbulence are deduced from the velocity components measured by LDA as:

$$K = \frac{1}{2}(u'^2 + v'^2 + w'^2) \tag{4.1}$$

$$I = \frac{\sqrt{u'^2 + v'^2}}{V} \tag{4.2}$$

LDA measures velocity fluctuations u' and v'; we assume isotropy for w' so that $w' = v'$. I is given as an indication of the intensity of turbulence for information; w' is not added to the formulation of I. From figures 6.12 and 6.13 showing the span-wise profiles of upstream and downstream turbulent kinetic energy and the intensity of turbulence, it is clear that inlet levels of turbulence intensity in the blade row are high: 5% to 10%. The inlet turbulence is much higher than the orders of turbulence in real compressor environments that range from 2% to 5%. This is due to a specific problem induced by the upstream portion of the test rig. The intensity of turbulence in the CFD studies done with theoretical conditions is almost non-existent. It is thus necessary to assign proper values of turbulence corresponding to LDA measurements in the turbulence model.

In the K-ε turbulence model, the upstream turbulent kinetic energy (K) from LDA is added to the set of boundary conditions. The rate of dissipation of the turbulent kinetic energy is defined by $\varepsilon = \frac{K^{3/2}}{L}$. The characteristic length of turbulence (L) is required to determine ε.
L was not immediately available after the tests; the span-wise profile of L was deduced much later when the CFD studies were concluded.

The span-wise profile of L is presented in figure 6.14:

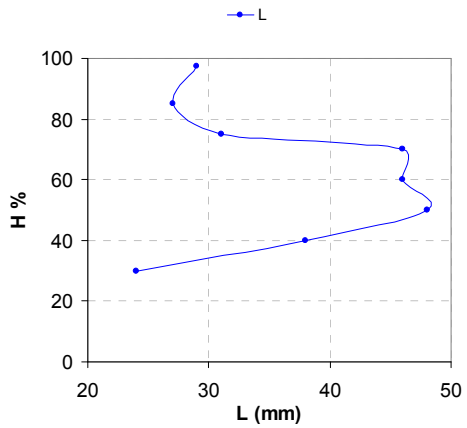

Fig 6.14: Characteristic length at the upstream plane (LDA)

The span-wise profile of L at the upstream plane as deduced by LDA is shown here for information; L is deduced from the spectrum of turbulence by measured velocity fluctuations from LDA. Rotta(1951) proposed to define the scale of the large structure in function of the average spectrum of energy E(k):

$$L = \frac{1}{K}\int_0^{\infty} \frac{E(K)}{K} dK \tag{4.3}$$

Where $E(K)$ is the average spectrum of turbulence.

Owing to these very high values of deduced L, we decided not to use them to model ε in the CFD studies. We suspect some specific vortices to be generated in the upstream part of the test rig, and to be responsible of the very high measured values of L.

A sensitivity study of various values of L was performed to determine a value of L that could model ε to yield closest match between the experiments and CFD. Based on this sensitivity study, L corresponding to 10% of the blade span at the leading edge is finalized, i.e., L=4mm. This is a simplifying hypothesis adopted in absence of the measurements of L at the time when comparison studies were initiated and is not representative of the true energy dissipation in the blade channel.

From the preceding discussions, some important points are summarized:

- The upstream total pressure gradients in the experiments are stronger than the theoretical inlet conditions used during the design phase of the blade.

- Using the experimental flow conditions, the CFD results show a deep modification of the flow at the hub wall close to the leading edge. In the figure 6.15b, we observe flow separation on the wall upstream of the cascade, as visualized by tracing limiting streamlines on the hub wall and blade surface.

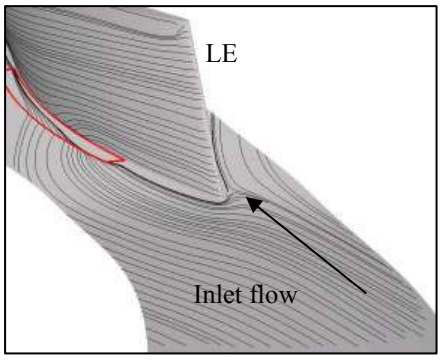

Fig 6.15a: Limiting streamlines upstream of blade (Theoretical inlet conditions)

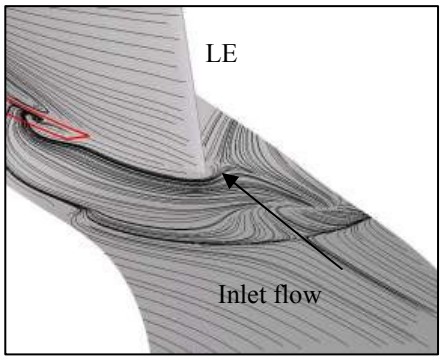

Fig 6.15b: Limiting streamlines upstream of blade (CFD using experimental inlet conditions)

- Finally, to allow the comparison with experimental results, a new set of boundary conditions has been used, that are based on adapted experimental values that account for the discrepancies observed between LDA and probe values.

The boundary conditions for CFD studies to compare experimental and numerical results are thus defined as following:

- Inlet boundary conditions:
  - Total pressure (P_T) from the probe
  - Total temperature (T_T) from the upstream rig measurement
  - Flow angle (α) from the probe/LDA
  - Turbulent kinetic energy (K) from LDA
    - For all the configurations at all the inlet flow angles, K deduced by LDA at the "reference point" is introduced as an inlet boundary condition.
  - Rate of dissipation of turbulent kinetic energy (ε) from K and L (L=4mm)

- Outlet boundary conditions:
  - Aspiration: mass flow in the cavity
  - Outlet plane of the flow path: Static Pressure (radial equilibrium hypothesis, similar to previous CFD studies in chapters 4 and 5)

6.7 METHODOLOGY FOR VALIDATION CALCULATIONS

6.7.1 COMPUTATIONAL MESH AND METHODOLOGY

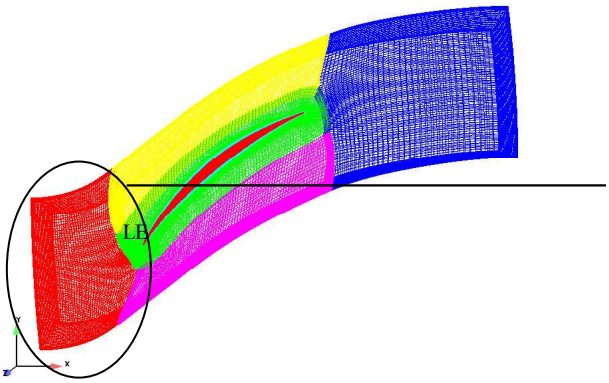

Fig 6.16a: 3D mesh for CFD studies

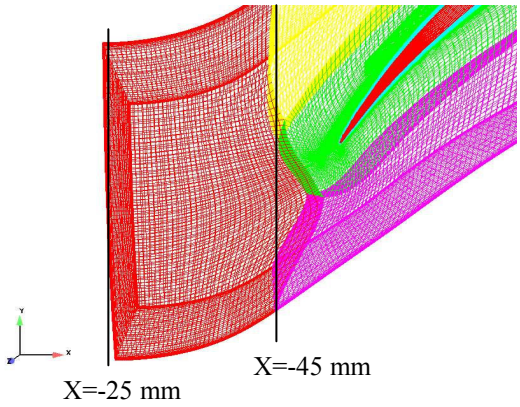

Fig 6.16b: 3D mesh close to the LE

The computational mesh employed for this study is same as the mesh used for previous studies. The mesh has been slightly extended downstream with the exit mesh plane terminating at X= 145 mm or 1.2 chords downstream of the leading edge. Experimental measurements at plane X=-25mm are extrapolated as inlet conditions at the mesh inlet plane X=-45mm with the in house 2D meridional calculations.

6.8 RESULTS AND DISCUSSIONS

This section presents a detailed analysis of the configurations studied in the comparison of experimental and numerical studies. The configuration of open hub slot without aspiration has been studied to serve as a reference. Firstly, we shall study the comparison of results at the "reference point α=63°, C_q=0.02" for which measurements from both probe and LDA are available.

6.8.1 THE REFERENCE POINT: HUB ASPIRATION, C_q=0.02 AT α=63°

The LDA measurements were done on a different blade channel of the same cascade that has a slightly higher radial tip clearance of 0.6mm. In the previous CFD studies, the tip clearance values employed is 0.5mm. The corresponding CFD simulations are done with the tip clearance value of 0.6mm. Since the measurements at the reference point have been taken by both probe and LDA, two sets of CFD studies are done with different inlet boundary conditions corresponding to probe and LDA measurements respectively. We define two cases of this CFD study as follows:

- Case: Probe
    - All the inlet conditions, except the turbulent kinetic energy are the experimental measurements of the probe.
    - The downstream static pressure level is regulated to achieve the inlet Mach number as measured by the probe.

- Case: LDA
  - All the inlet conditions are the experimental measurements of LDA, except the total pressure obtained from the pressure probe. The static pressure is deduced from the velocity and the total pressure.
  - The downstream static pressure level is regulated to achieve the inlet Mach number as measured by LDA.

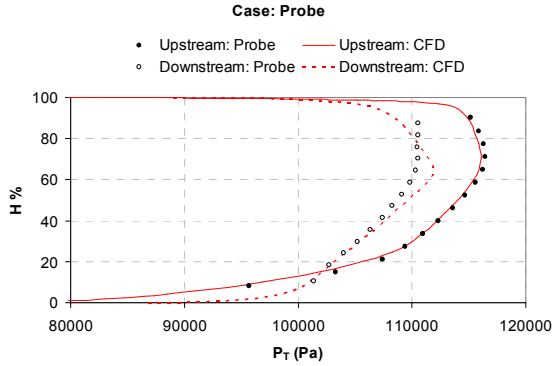

Fig 6.17a: Span-wise profile of total pressure at upstream and downstream planes (Probe/CFD for Case: Probe)

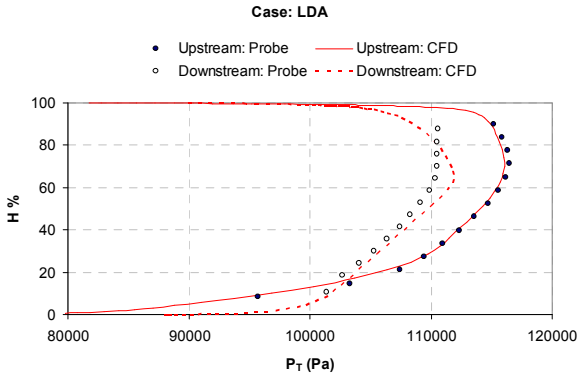

Fig 6.17b: Span-wise profile of total pressure at upstream and downstream planes (Probe/CFD for Case: LDA)

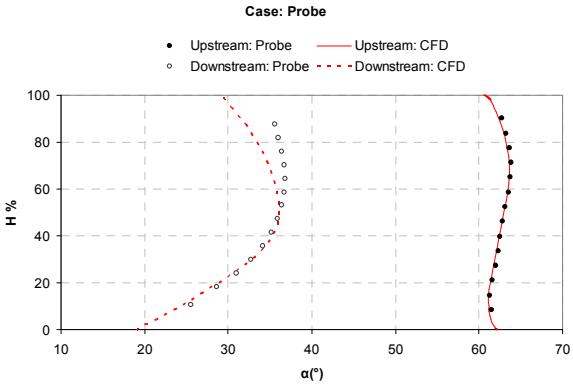

Fig 6.17c: Span-wise profile of flow angle at upstream and downstream planes (Probe/CFD for Case: Probe)

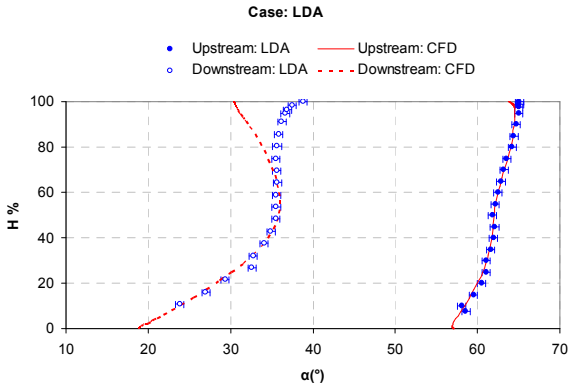

Fig 6.17d: Span-wise profile of flow angle at upstream and downstream planes (Probe/CFD for Case: LDA)

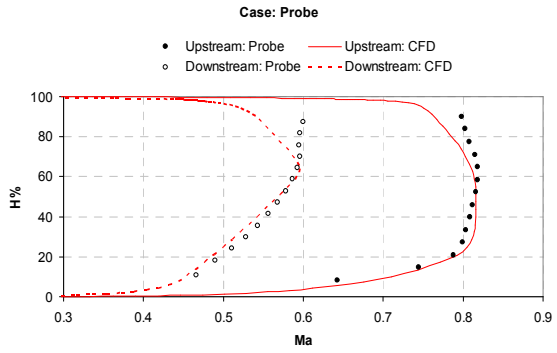

Fig 6.17e: Span-wise profile of Mach number at upstream and downstream planes (Probe/CFD for Case: Probe)

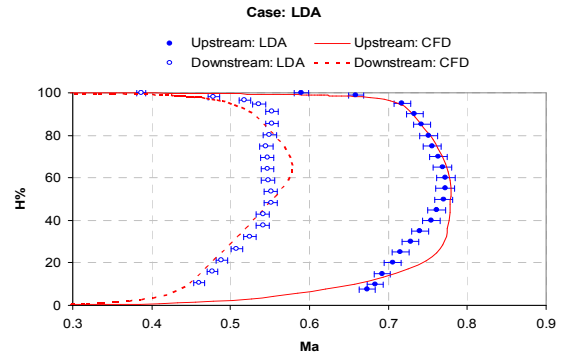

Fig 6.17f: Span-wise profile of Mach number at upstream and downstream planes (LDA/CFD for Case: LDA)

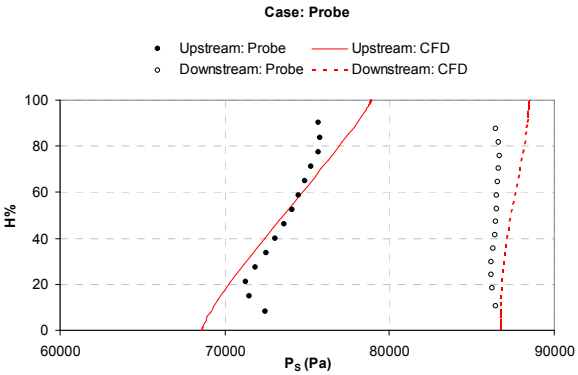

Fig 6.17g: Span-wise profile of static pressure at upstream and downstream planes (Probe/CFD for Case: Probe)

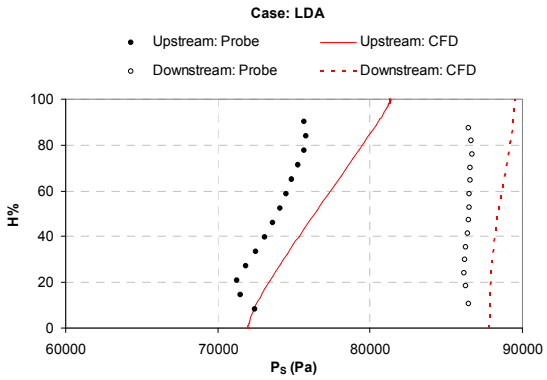

Fig 6.17h: Span-wise profile of static pressure at upstream and downstream planes (Probe/CFD for Case: LDA)

- The inlet boundary conditions are well imposed in terms of inlet flow angle and the total pressure; an appreciable difference exists in the gradients close to the hub wall in the Mach number between CFD and experiments for case: LDA (figure 6.17f). As the total pressure measured by the probe is used as a boundary condition, the gradients of Mach number in CFD (case LDA) hence resemble the gradients of the total pressure.

- The calculated (CFD) downstream total pressure is in good agreement with the measured total pressure for both the cases (‘Case: Probe’ and ‘Case: LDA’ in figures 6.17a,b).

- In the case: probe, the downstream flow angle is in good agreement with the flow angle deduced from probe measurements till mid-span. From the mid-span to close to the casing wall, the probe flow angle shows higher deviation than CFD in the range of 2° to 3° (figure 6.17c). In the case: LDA, the CFD/experimental correlation is good till 70% span after which the flow deviation is remarkably stronger in the experiment till the casing wall (figure 6.17d). This reveals the possibility of a stronger tip leakage vortex in the experiments compared to CFD.

- In the Case: probe, the calculated downstream Mach number is in good agreement with the experimentally deduced values till 60% span followed by an increase in the experimental Mach number close to the casing wall (figure 6.17e). This is due to the lower static pressure observed near the casing wall in the experiments (figure 6.17g). The measured static pressure gradients are surprising as they increase and decrease at the hub and casing walls respectively causing local modifications close to the endwalls in the deduced Mach number. It is possible that when the probe is close to the casing wall, the probe might interfere and cause local blockage of the flow between itself and the casing wall and thus a lower static pressure is sensed by the probe. On the contrary, the probe close to the hub wall might cause a venturi effect resulting in a higher static pressure being sensed by the probe. Considering this, we may conclude that the probe static pressure measurements close to the endwalls are probably erroneous.

- In the case: LDA, the downstream Mach number correlates well with the deduced experimental values from LDA (figure 6.17f). Note that the experimental value of the Mach number is deduced from the velocity measured from LDA and the stagnation temperature upstream.

The static pressure measured by the pressure taps on the endwalls and the blade surface at mid-span along is traced to compare the experimental and numerical results.

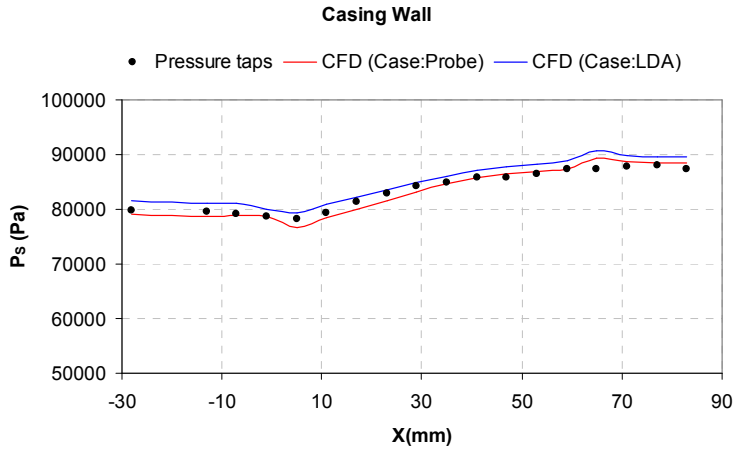

Fig 6.18a: Static pressure on the casing wall (Probe/CFD)

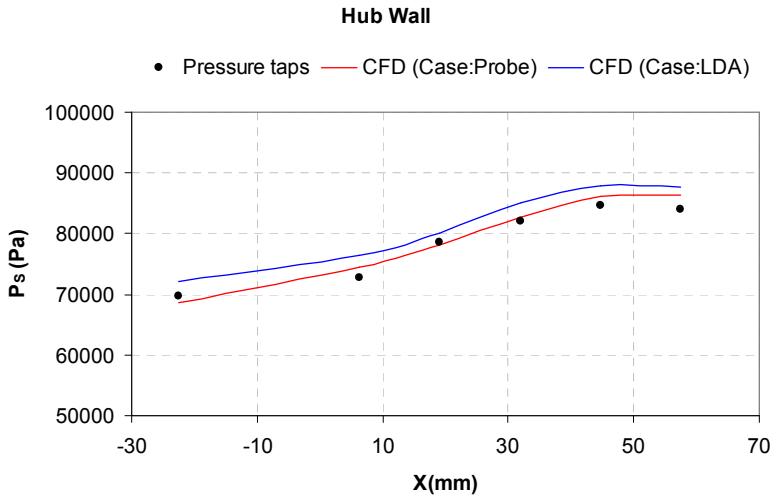

Fig 6.18b: Static pressure on the hub wall (Probe/CFD)

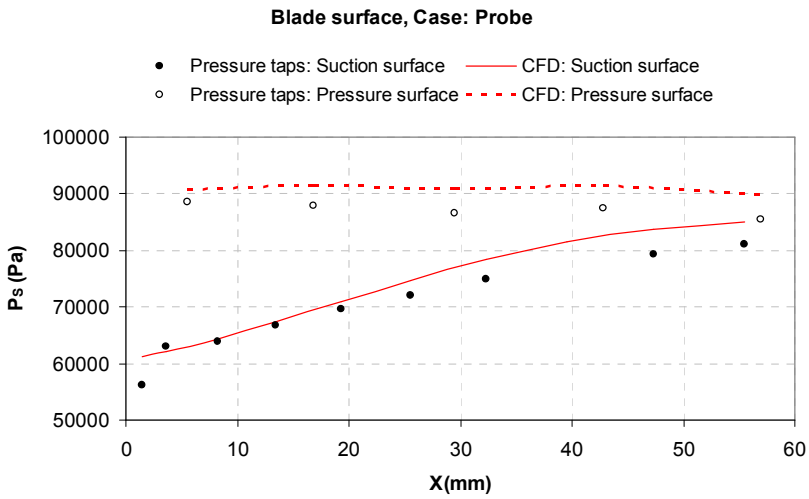

Fig 6.19a: Static pressure on the blade surface at mid-span (Probe/CFD (Case: Probe))

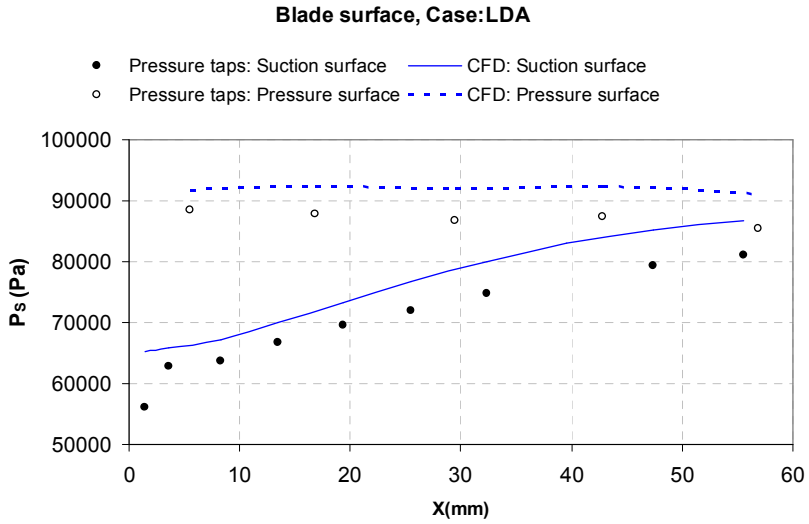

Fig 6.19b: Static pressure on the blade surface at mid-span (Probe/CFD (Case: LDA))

- The CFD traces of static pressure for the Case: LDA have been given as supplementary information. It is more practical to compare the Case: Probe CFD traces to the experimental values as they correspond to the probe measurements. Since, Case: LDA is calibrated to match the inlet Mach number deduced by LDA, a lower value of static pressure is obtained for all CFD traces of Case: LDA as compared to Case: Probe.

- The static pressure from Case: Probe on the casing wall is in good agreement with experimental values of the same over most of the axial planes (figure 6.18a)

- On the suction surface of the blade at mid-span, the CFD values correlate well with experimental values from X=3mm to X=20mm, after which the CFD values are remarkably higher over the rest of the blade chord (figure 6.19a). This indicates that hub aspiration in experiments is less efficient than CFD for the control of flow separation in the blade row.

- It can be said that although CFD predicts the experimental nature of the flow well over the first few chords, the dissipation of energy is not totally the same in both the cases and the evolution of quantities finally makes room for the discrepancy.

- Interestingly, the static pressure on the pressure surface of the blade is appreciably different between the experiments and CFD signifying as if the solidity of the blade row in both the cases is not the same (figure 6.19a,b). It has been verified that the blade count of the cascade is the same in both the cases and further analysis is required to figure out the reason for this difference. As will be shown later, this is suspected to be a measurement error.

Next, we shall compare the flow quantities (flow angle and Mach number) visualized at the downstream plane in experiments and CFD.

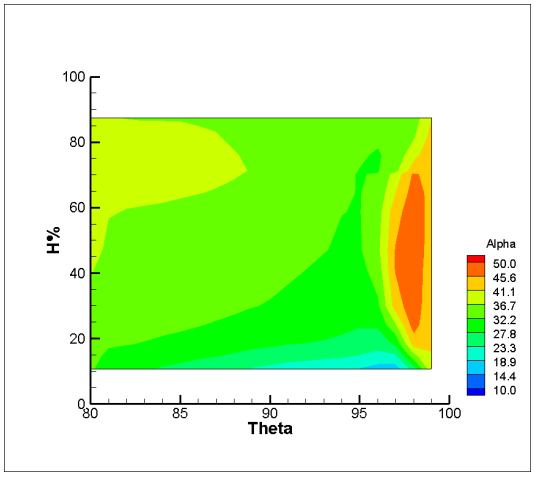

Fig 6.20a: Downstream flow angle visualization in blade passage from probe

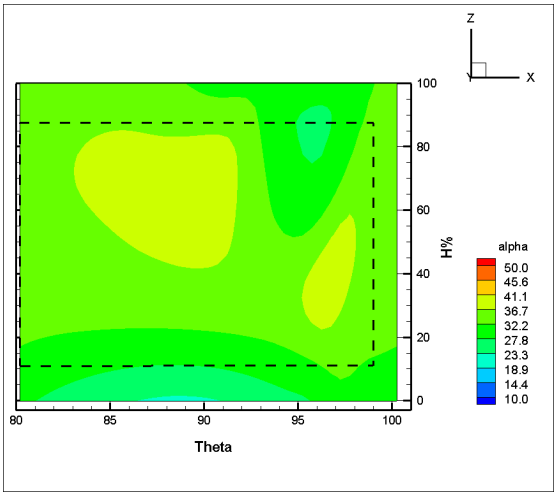

Fig 6.20b: Downstream flow angle visualization in blade passage from CFD, Case: Probe

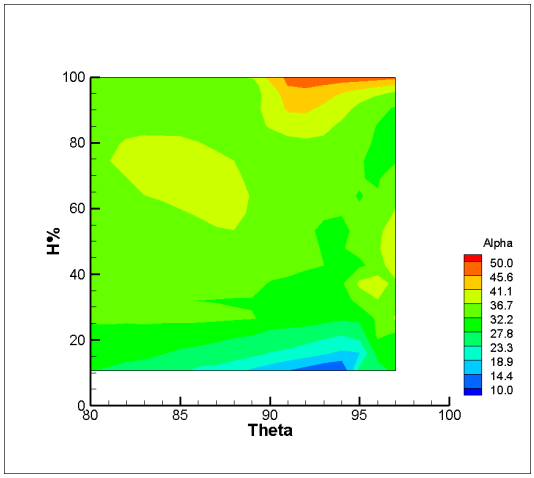

Fig 6.20c: Downstream flow angle visualization in blade passage from LDA

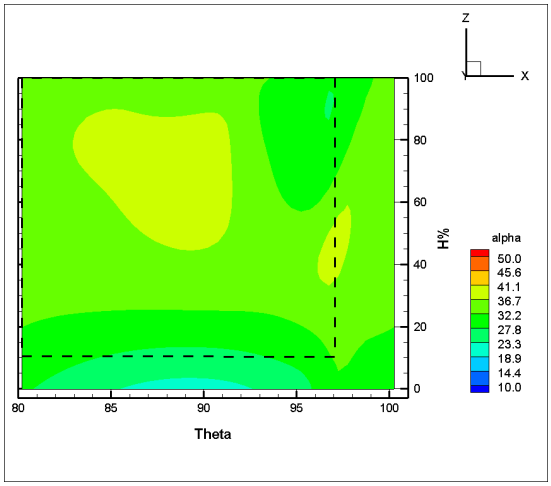

Fig 6.20d: Downstream flow angle visualization in blade passage from CFD, Case: LDA

The downstream flow angle visualized by probe in figure 6.20a shows higher values on the suction surface side all along the blade span indicating higher flow deviation due to strong flow separation on the suction surface. In figure 6.20c, LDA results show small traces of higher flow angles from 20% to 60% span and θ=95° to 97°.

This may also be due to higher flow deviation on the suction surface side of the wake. However, the CFD traces in figures 6.20b,d show similar values of flow angle as compared to experimental LDA values on the suction surface side. We shall compare the flow visualizations of Mach number at the downstream plane between experiments and CFD:

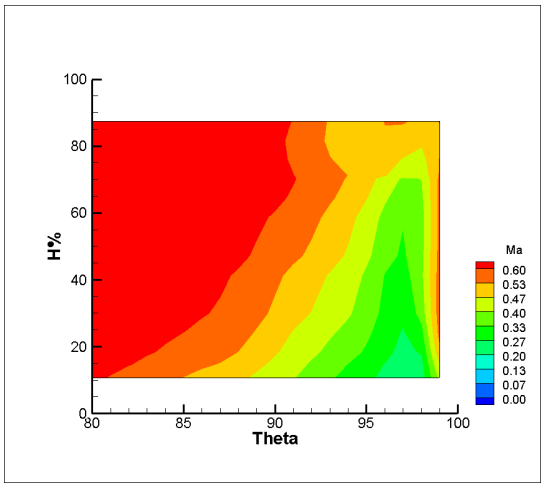

Fig 6.21a: Downstream Mach number visualization in blade passage from probe

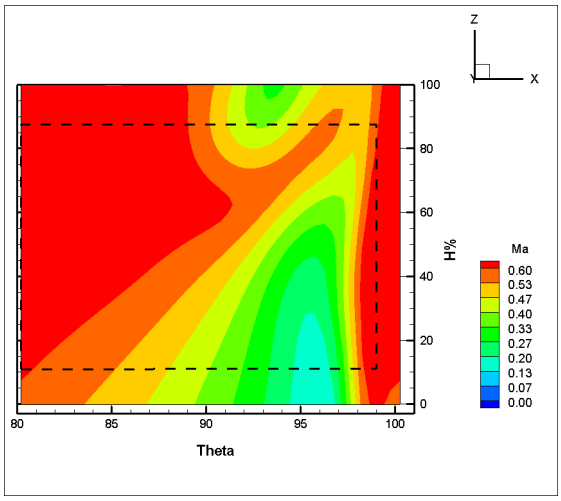

Fig 6.21b: Downstream Mach number visualization in blade passage from CFD, Case: Probe

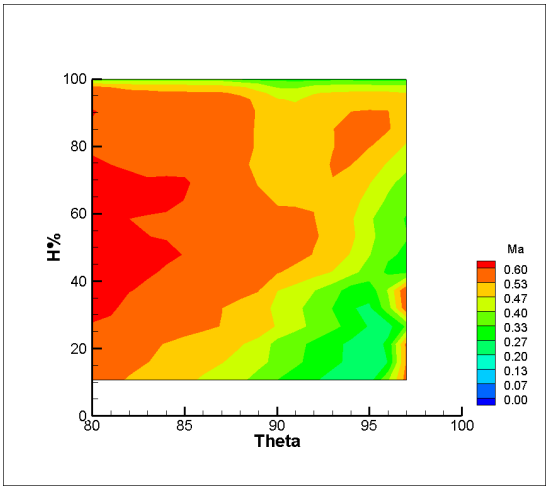

Fig 6.21c: Downstream Mach number visualization in blade passage from LDA

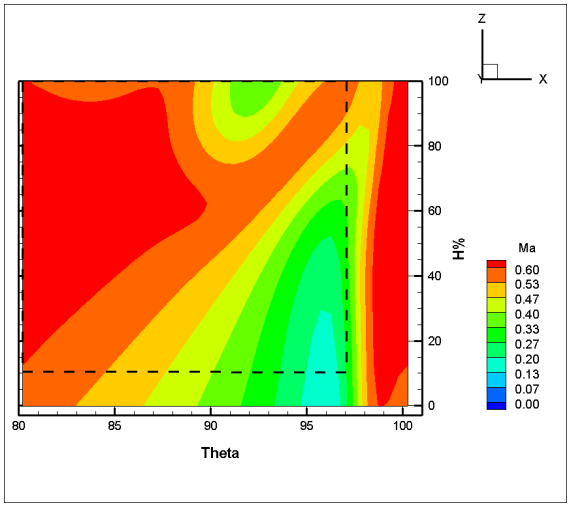

Fig 6.21d: Downstream Mach number visualization in blade passage from CFD, Case: LDA

The CFD downstream Mach number for Case: Probe correlates well with the experimental flow visualization. The difference is observed in the corner separation; the CFD predicts stronger corner separation as compared to experiments (figure 6.21a,b). The tip leakage vortex is stronger in experiments as visualized by LDA due to the higher radial tip clearance. This has an effect of suppressing the corner separation on the hub wall as the vortex transports the energy of the flow in the blade channel towards the separation zone by its rotation. The CFD 'Case: LDA', although modelled with the tip clearance corresponding to the experimental value shows a weaker tip leakage vortex compared to its experimental part. Consequently, the corner separation in CFD is stronger compared to experiment.

6.8.2 TOTAL PRESSURE LOSS COEFFICIENT FOR ALL THE CONFIGURATIONS

The comparison of experimental and CFD results has been done for all the cases in the first campaign of tests. We shall see the total pressure loss coefficient plotted for all the cases studied. Note that all these cases are experimentally measured with the aerodynamic probe.

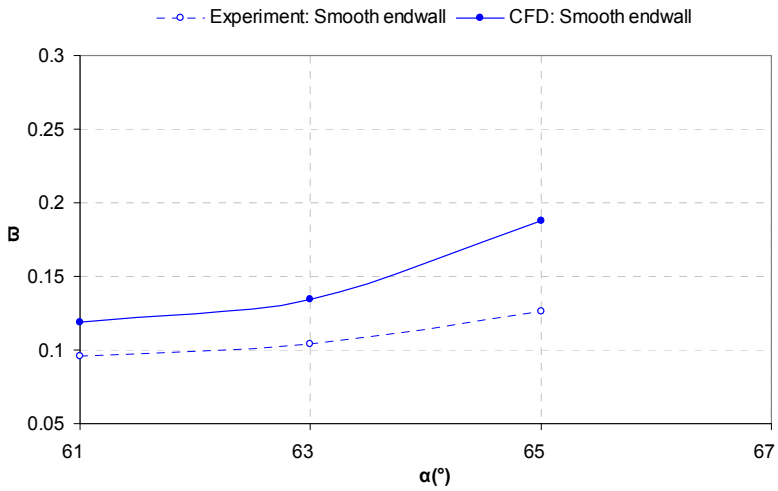

Fig 6.22a: Total pressure loss coefficient for the configuration: Smooth endwall (Experiment/CFD)

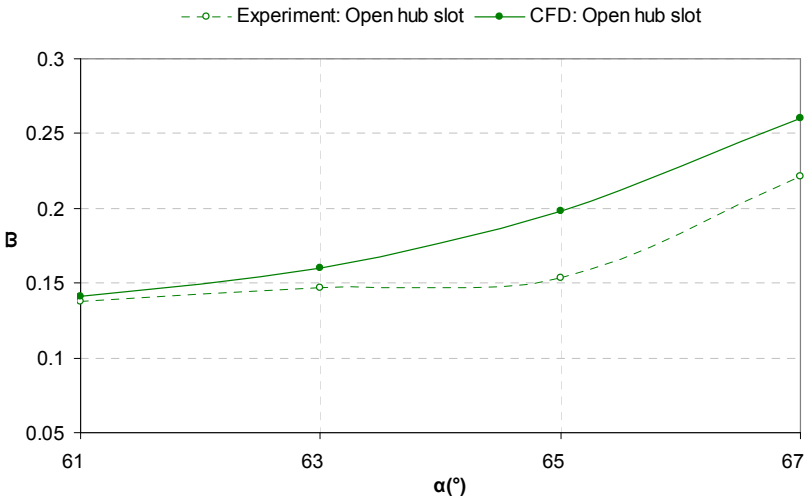

Fig 6.22b: Total pressure loss coefficient for the configuration: Open hub slot (Experiment/CFD)

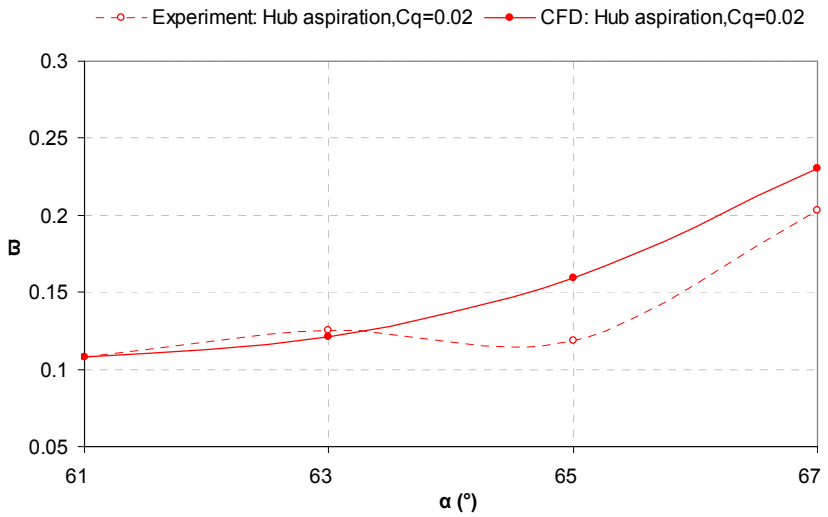

Fig 6.22c: Total pressure loss coefficient for the configuration: Hub aspiration, Cq=0.02 (Experiment/CFD)

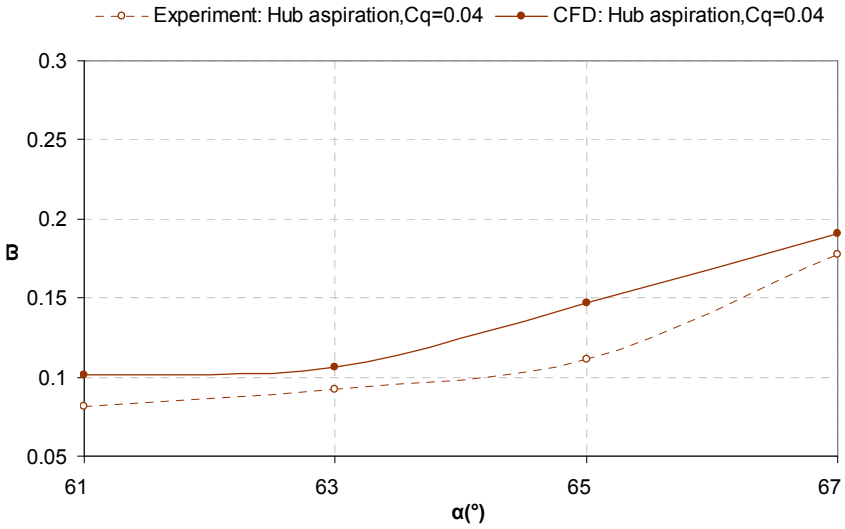

Fig 6.22d: Total pressure loss coefficient ϖ for the configuration: Hub aspiration, Cq=0.04 (Experiment/CFD)

The total pressure loss coefficient ϖ is calculated in CFD and experiments as:

$$\varpi = \frac{P_{T_1} - P_{T_2}}{\frac{\gamma}{2} \cdot P_{S_1} \cdot Ma_1^2} \tag{4.4}$$

Also, ϖ is calculated between 10-90% span as this zone corresponds to the span-wise zone of measurements in experiments.

As seen from the figures 6.22a-d, the CFD and experimental values of ϖ do not correlate very well over the range of the parametric points studied at all the configurations. Generally, CFD tends to yield higher values of ϖ as compared to the experimental values and it is more profound at higher values of α, i.e., CFD predicts higher level of losses than experiments. The operational points where CFD and experiments correlate well in terms of ϖ are:

- α=61° with open hub slot
- α=61°,63° with hub aspiration, Cq=0.02

Interestingly, the CFD and experimental values of ϖ show an increased discrepancy at α=65° for all the configurations; at α=65°, the experimental value of ϖ show a sudden drop. This is more surprising in the configuration of hub aspiration, Cq=0.02 as the experimental value of ϖ at α=65° is found to be lower than ϖ at α=61° and α=63°.

We shall compare the CFD and experimental results at other operating points, we shall compare the results at points corresponding to α=63° and α=65° for all the configurations. Note that the following comparison is done for all the experimental points measured by the probe and the reference point measured by LDA is excluded in this comparison.

6.8.3 SMOOTH ENDWALL

We shall study the comparison of CFD and experimental span-wise mass averaged physical quantities for α=63° and α=65°.

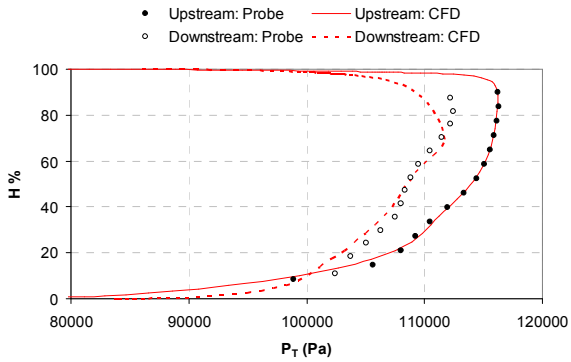

Fig 6.23a: Span-wise profile of total pressure at upstream and downstream planes, Case: Smooth endwall, α=63° (Probe/CFD)

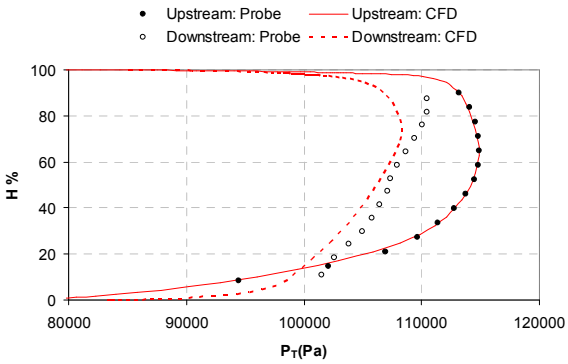

Fig 6.24a: Span-wise profile of total pressure at upstream and downstream planes, Case: Smooth endwall, α=65° (Probe/CFD)

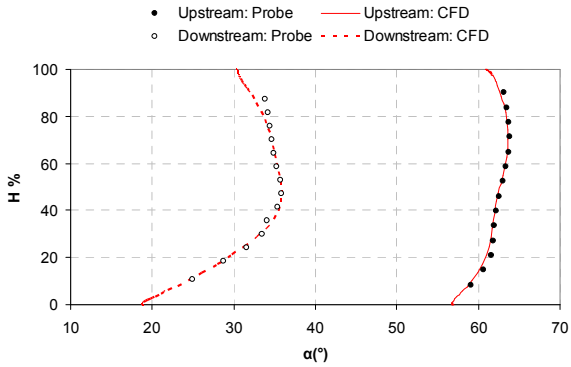

Fig 6.23b: Span-wise profile of flow angle at upstream and downstream planes, Case: Smooth endwall, α=63° (Probe/CFD)

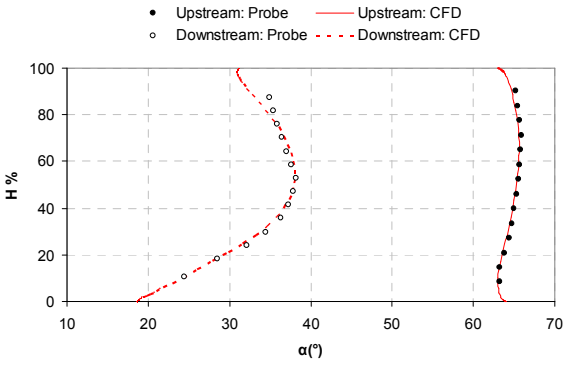

Fig 6.24b: Span-wise profile of flow angle at upstream and downstream planes, Case: Smooth endwall, α=65° (Probe/CFD)

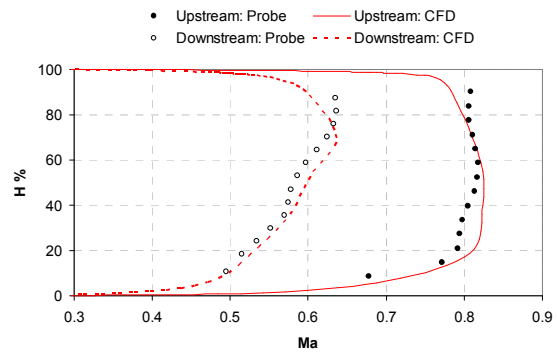

Fig 6.23c: Span-wise profile of Mach number at upstream and downstream planes, Case: Smooth endwall, α=63° (Probe/CFD)

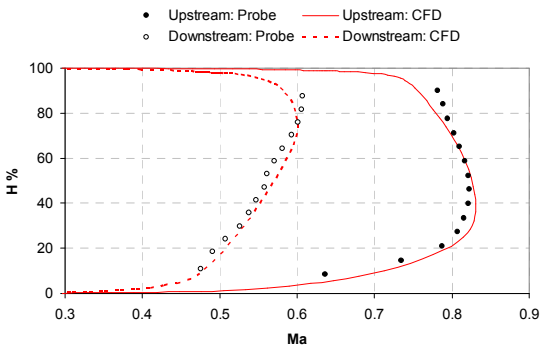

Fig 6.24c: Span-wise profile of Mach number at upstream and downstream planes, Case: Smooth endwall, α=65° (Probe/CFD)

There is good correlation between experimental and CFD values of downstream total pressure, flow angle and Mach number as seen in figures 6.23, 6.24. The CFD values of downstream Mach number are higher than the experimental values from 40% to 70% span as seen in figure 6.23c. Also, the CFD upstream Mach number values are slightly higher than the experimental values implying that the higher losses may result in CFD values due to higher inlet Mach number. The ϖ_{CFD} is 22% higher than ϖ_{test} for α=63° and 32% higher for α=65°.

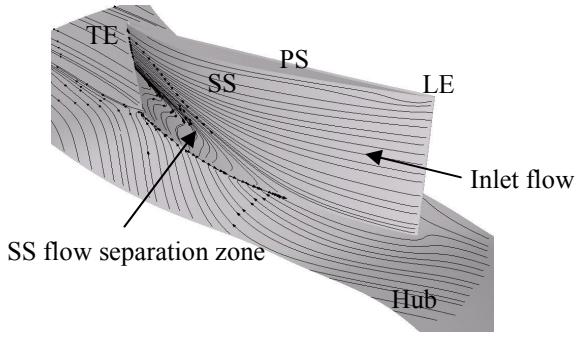

Fig 6.25a: Limiting streamlines on endwall and blade surface, Case: Smooth endwall, α=63° (CFD)

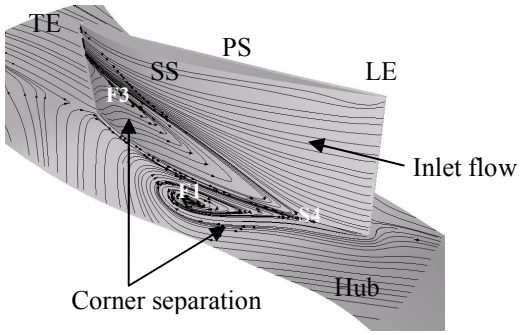

Fig 6.25b: Limiting streamlines on endwall and blade surface, Case: Smooth endwall, α=65° (CFD)

Figures 6.25a,b show limiting streamlines on the hub and suction surface of the blade for the case of CFD at α=63° and α=65° respectively . Flow topologies from experiments are not available; limiting streamlines in CFD cases are presented with the sole intention of understanding the flow structures that may be obtained in experiments. In the present case we observe no corner separation on the hub wall and a zone of flow separation on the suction surface of the blade at α=63°. (figure 6.25a)

In the case of α=65° (figure 6.25b), the boundary layer separates at saddle point S4 in the corner between the blade suction surface and the hub wall. The saddle point is the source of two dividing streamlines on the hub wall and the suction surface respectively. The endwall dividing streamline terminates at the focal point F1 and forms the base of the corner separation vortex on the hub wall. The suction surface dividing streamlines rolls into the focal point F3 on the suction surface.

6.8.4 OPEN HUB SLOT

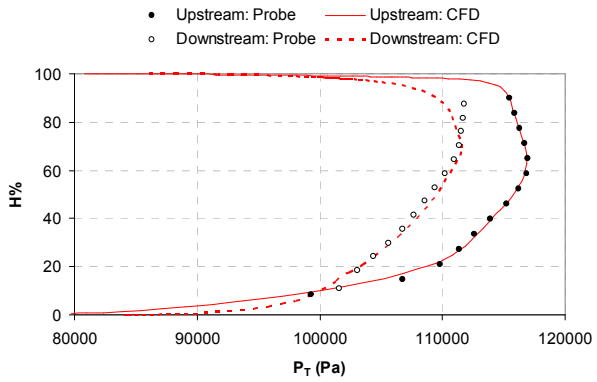

Fig 6.26a: Span-wise profile of total pressure at upstream and downstream planes, Case: Open hub slot, α=63° (Probe/CFD)

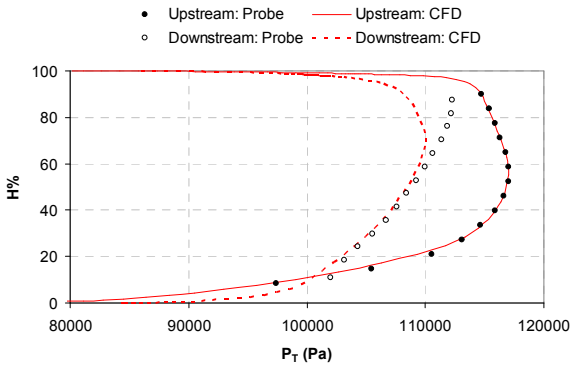

Fig 6.27a: Span-wise profile of total pressure at upstream and downstream planes, Case: Open hub slot, α=65° (Probe/CFD)

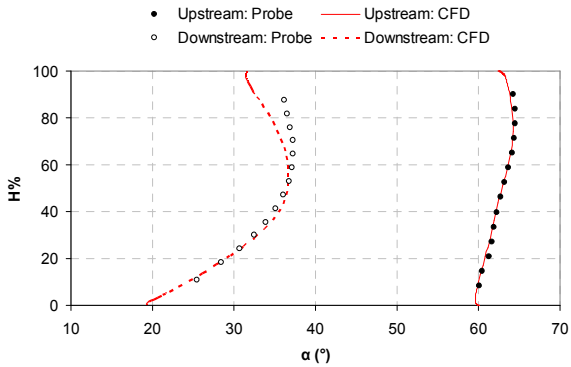

Fig 6.26b: Span-wise profile of flow angle at upstream and downstream planes, Case: Open hub slot, α=63° (Probe/CFD)

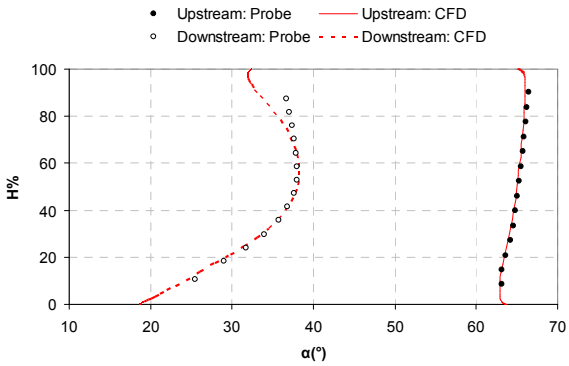

Fig 6.27b: Span-wise profile of flow angle at upstream and downstream planes, Case: Open hub slot, α=65° (Probe/CFD)

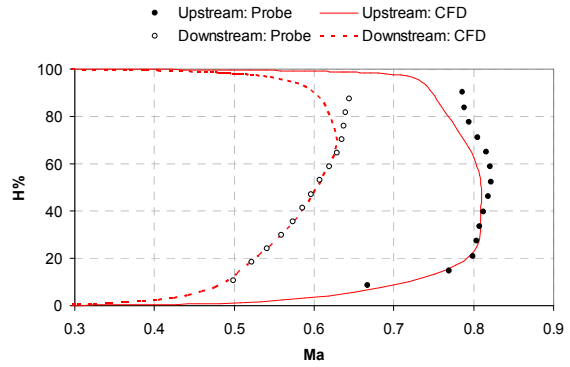

Fig 6.26c: Span-wise profile of Mach number at upstream and downstream planes, Case: Open hub slot, α=63° (Probe/CFD)

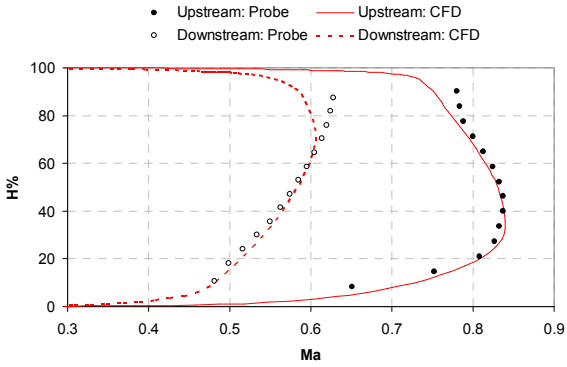

Fig 6.27c: Span-wise profile of Mach number at upstream and downstream planes, Case: Open hub slot, α=65° (Probe/CFD)

There is good correlation between the experimental and CFD values at the downstream plane as seen from figures 6.26, 6.27. The span-wise CFD total pressure correlates well with the experimental value for α=63°, whereas for α=65°, the experimental values of total pressure are significantly higher than CFD values from 60% span. The strong corner separation vortex on the hub wall displaces a large quantity of massflow towards the casing wall. This has the effect of reducing the strength of tip clearance vortex as seen in locally higher (experimental) values of downstream flow angle from figure 6.27b close to the casing wall. Consequently, we observe a higher total pressure build up close to the casing wall and lower total pressure losses.

The CFD flow angle and Mach number correlate well with the experimental values till 60-70% span and then show minor deviations from the experimental values. The ϖ_{CFD} is 8% higher than ϖ_{test} for α=63° and 11% higher for α=65°.

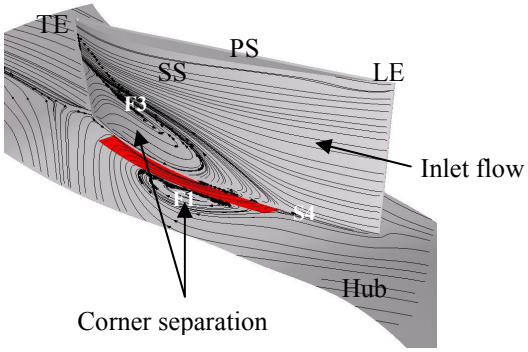

Fig 6.28a: Limiting streamlines on endwall and blade surface, Case: Open hub slot, α=63° (CFD)

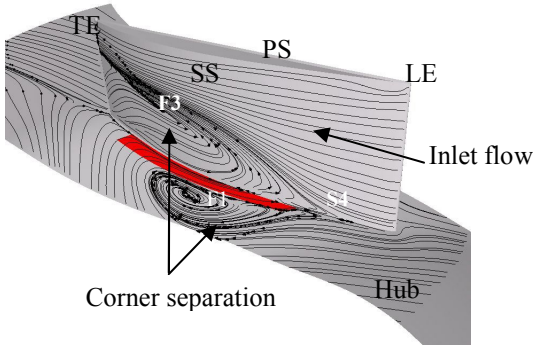

Fig 6.28b: Limiting streamlines on endwall and blade surface, Case: Open hub slot, α=65° (CFD)

The limiting streamlines in figure 6.28a,b show the presence of corner separation and suction surface flow separation. The flow topology is essentially the same in both the cases with the exception of stronger corner separation in the case of α=65°.

From the study of flow topology of the present cases, we understand the influence of open hub slot without active aspiration. The flow enters the aspiration cavity via the open hub slot and then re-circulates between the cavity and the flow path in absence of aspiration to create the downward momentum flux essential to prevent the recirculation. Hence, the flow begins to separate on the hub wall leading to corner separation and the flow separation on the suction surface is intensified as compared to the cases with smooth endwall at the same inlet flow angles. We can conclude that the presence of open hub slot without aspiration is deleterious to the aerodynamic performance of the blade.

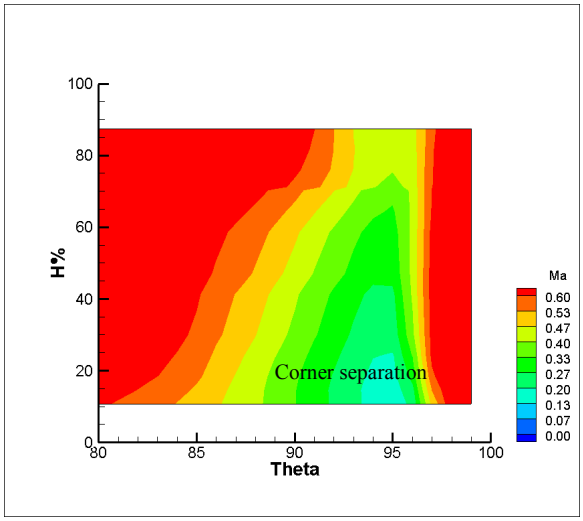

Fig 6.29a: Downstream Mach number visualisation in the blade passage,
Case: Open hub slot, α=65° (Probe)

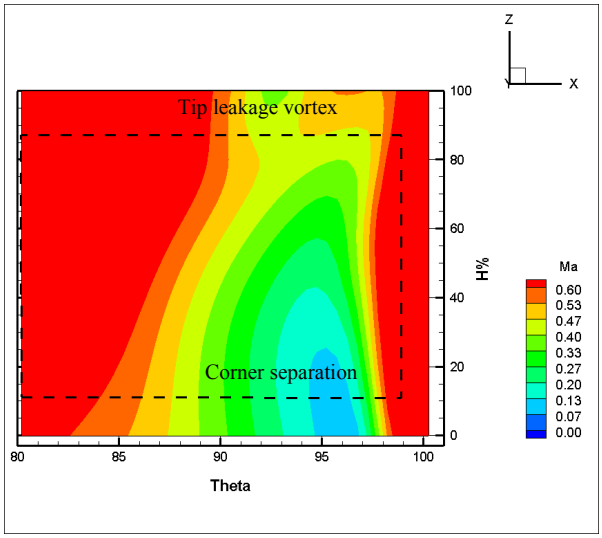

Fig 6.29b: Downstream Mach number visualisation in the blade passage,
Case: Open hub slot, α=65° (CFD)

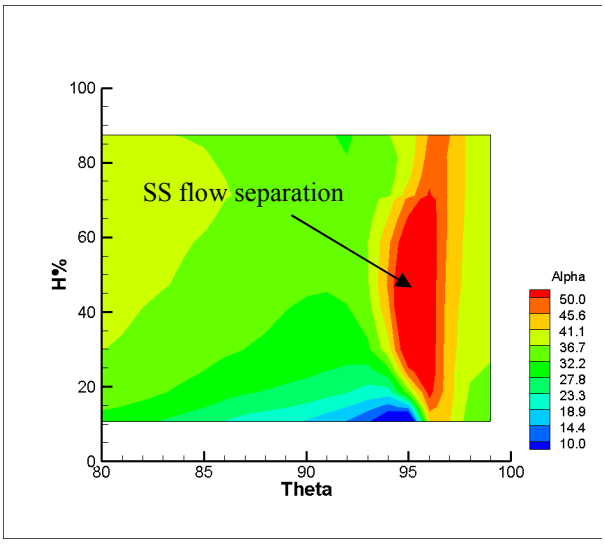

Fig 6.29c: Downstream flow angle visualisation in the blade passage,
Case: Open hub slot, α=65° (Probe)

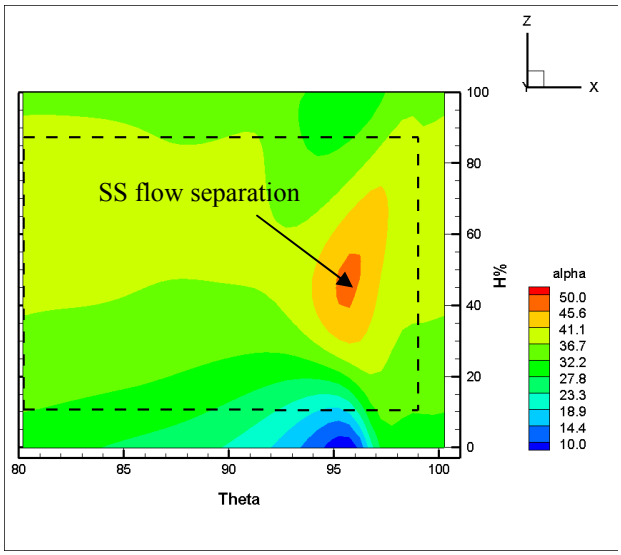

Fig 6.29d: Downstream flow angle visualisation in the blade passage,
Case: Open hub slot, α=65° (CFD)

Figures 6.29a-d show the comparison of downstream visualisations of Mach number and the flow angle between the experiments and CFD for the case of open hub slot at α=65°. The visualisation of Mach number shows a good correlation of the flow structure developed in both the experiments and CFD. The corner separation is clearly visible to be well developed at the hub wall. The tip leakage vortex is visible in CFD (figure 6.29b), while it is not visible in the experimental window, as the probe does not measure the flow close to the casing wall. The downstream flow angle visualised in the experimental windows shows high values on the suction surface along the blade span in figure 6.29c. The flow angle in the CFD window shows a local increase from 30-90% span. The higher flow angle is due to flow separation on the suction surface of the blade. Since the CFD predicts the flow separation well with experiments in this case, the locally high values of the downstream flow angle on the blade span in experiments are surprising.

6.8.5 HUB ASPIRATION, C_q=0.02

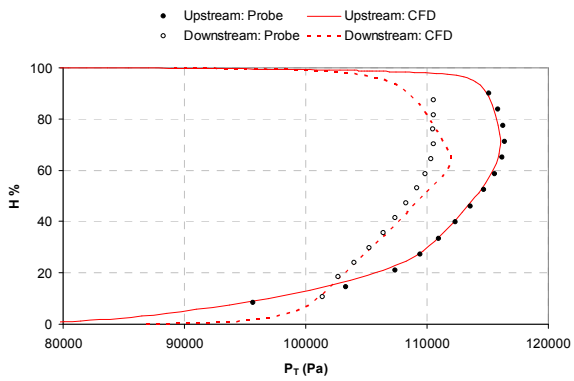

Fig 6.30a: Span-wise profile of total pressure at upstream and downstream planes, Case: Hub aspiration, Cq=0.02, α=63° (Probe/CFD for Case: Probe)

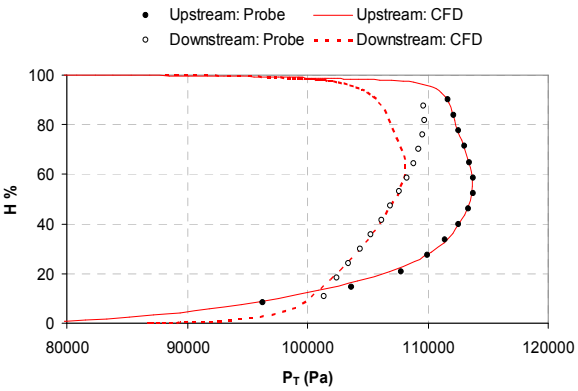

Fig 6.31a: Span-wise profile of total pressure at upstream and downstream planes, Case: Hub aspiration, Cq=0.02, α=65° (Probe/CFD)

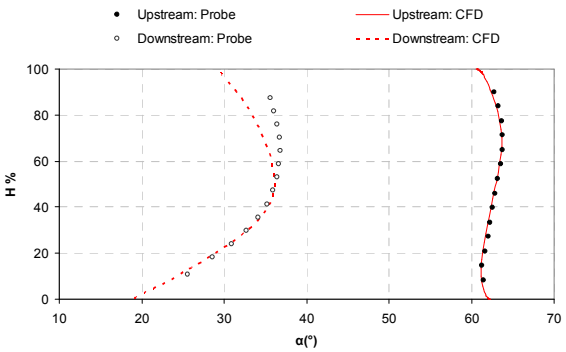

Fig 6.30b: Span-wise profile of flow angle at upstream and downstream planes, Case: Hub aspiration, Cq=0.02, α=63° (Probe/CFD for Case: Probe)

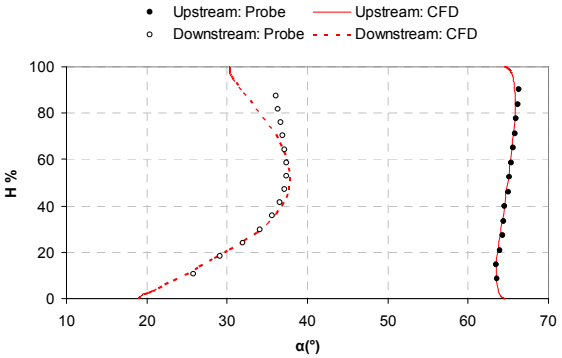

Fig 6.31b: Span-wise profile of flow angle at upstream and downstream planes, Case: Hub aspiration, Cq=0.02, α=65° (Probe/CFD)

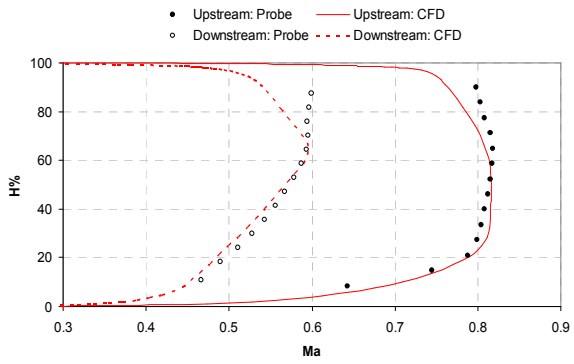

Fig 6.30c: Span-wise profile of Mach number at upstream and downstream planes, Case: Hub aspiration, Cq=0.02, α=63° (Probe/CFD for Case: Probe)

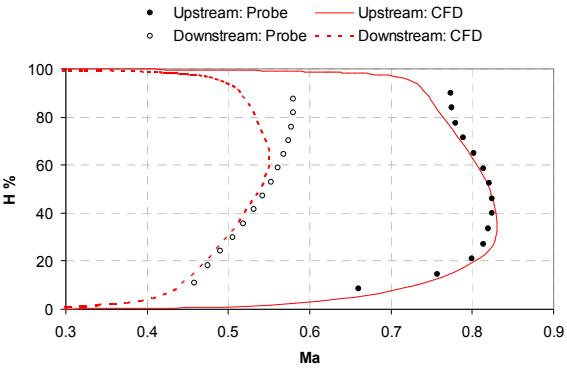

Fig 6.31c: Span-wise profile of Mach number at upstream and downstream planes, Case: Hub aspiration, Cq=0.02, α=65° (Probe/CFD)

rom figures 6.30, 6.31 for the cases of hub aspiration, Cq=0.02 at α=63° and α=65° respectively, we see that the correlation of downstream values is good till 60% span. As with the previous case of α=65°, open hub slot with no aspiration, the downstream span-wise values of experimental total pressure till increases in value till the casing wall.

Furthermore, with hub aspiration in the present cases a higher quantity of massflow passes through the lower and central zones of blade passage due to the downward flow and hence the tip leakage vortex gets stronger due to lower massflow passing through the higher zones of blade passage. As the tip leakage vortex gets stronger, the losses near the casing wall increase and the total pressure gets lower near the casing wall. This effect is clearly visible in the span-wise profile of CFD total pressure whereas the experimental total pressure profile defies this expected evolution. The ϖ_{CFD} is 23.5% higher than ϖ_{test} for α=63° and 25% higher for α=65°.

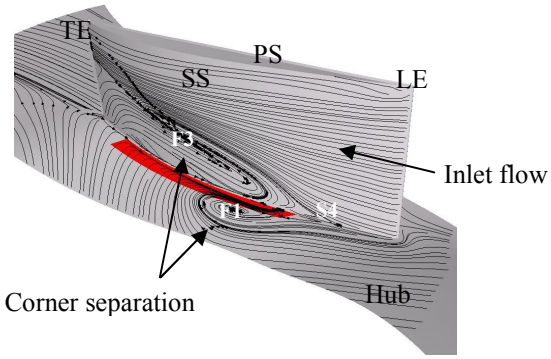

Fig 6.32: Limiting streamlines on endwall and blade surface,
Case: Hub aspiration, Cq=0.02, α=65° (CFD)

The flow topology in figure 6.32 shows the reduction in strength of corner separation on the hub wall by aspiration compared to figure 6.26f without aspiration and with an open slot. The strength of vortex of corner separation on hub wall represented by F1 is reduced as compared to the configurations of smooth endwall (figure 6.25b) and open hub slot (figure 6.28b).

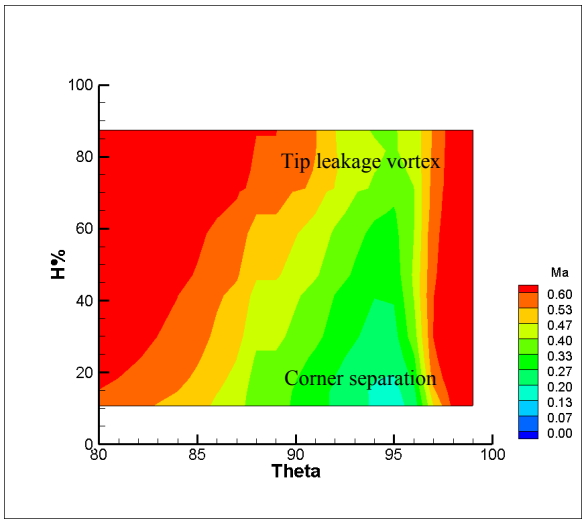

Fig 6.33a: Downstream Mach number visualisation in the blade passage,
Case: Hub aspiration, Cq=0.02, α=65° (Probe)

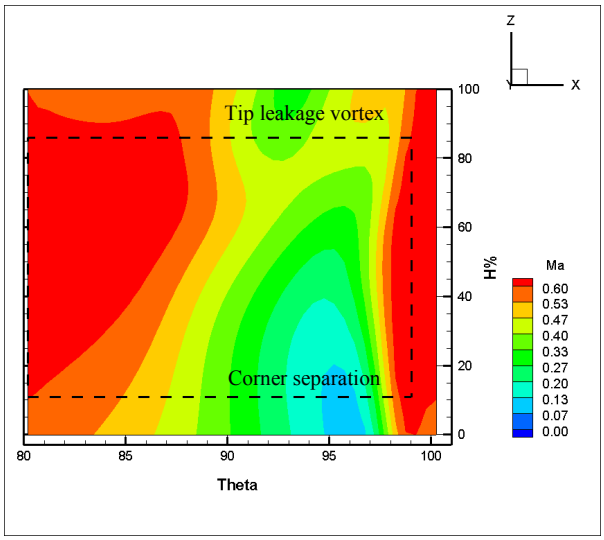

Fig 6.33b: Downstream Mach number visualisation in the blade passage,
Case: Hub aspiration, Cq=0.02, α=65° (CFD)

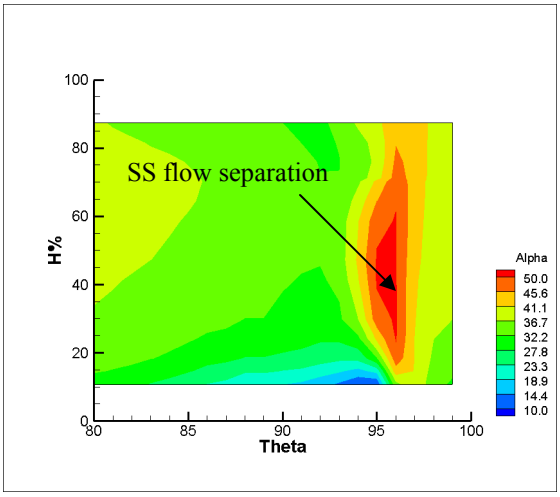

Fig 6.33c: Downstream flow angle visualisation in the blade passage,
Case: Hub aspiration, Cq=0.02, α=65° (Probe)

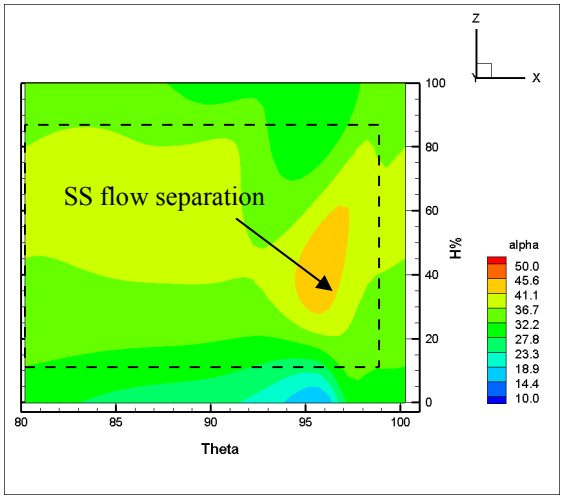

Fig 6.33d: Downstream flow angle visualisation in the blade passage,
Case: Hub aspiration, Cq=0.02, α=65° (CFD)

The corner separation in flow visualisation of downstream Mach number in CFD (figure 6.33b) correlates well with that of experiment (figure 6.33a) and it is found to be slightly stronger than the corner separation in the experiment. The tip leakage vortex in CFD window is also stronger than the tip leakage vortex in experiment. It is distinctly visible near the casing wall in the CFD window and slightly visible in experiment from 80% to 87.5% span. The endwall effects predicted by CFD are stronger than their experimental counterparts indicating higher losses in CFD.

The suction surface flow separation as seen by the downstream flow angle in figures 6.29c,d is found to be larger in tangential extent in CFD. The higher values of downstream flow angle in the wake leaving the suction surface in experiments shows higher span-wise values that is surprising.

From the above analysis, we see that the experimental total pressure continues to increase even near the casing wall where the tip leakage vortex is expected to be responsible for higher level of losses. From figures 6.33a,b we have seen that CFD predicts stronger corner separation and tip leakage vortex than the experiment. Of particular interest is the tip leakage vortex in this case, as CFD and experiment do not correlate well over this phenomenon. The possibility of difference in the tip clearance value between CFD and experiments is ruled out as we have confirmed that CFD and experiment are coherent in their values of tip clearance.

6.8.6 HUB ASPIRATION, C_q=0.04

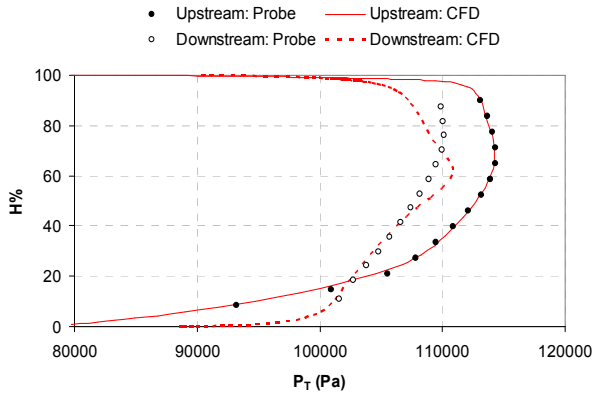

Fig 6.34a: Span-wise profile of total pressure at upstream and downstream planes, Case: Hub aspiration, Cq=0.04, α=63° (Probe/CFD)

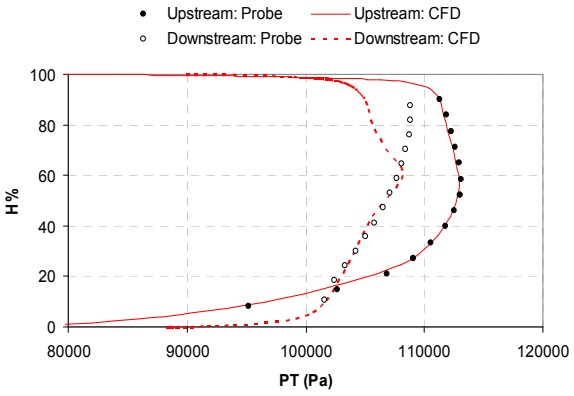

Fig 6.35a: Span-wise profile of total pressure at upstream and downstream planes, Case: Hub aspiration, Cq=0.04, α=65° (Probe/CFD)

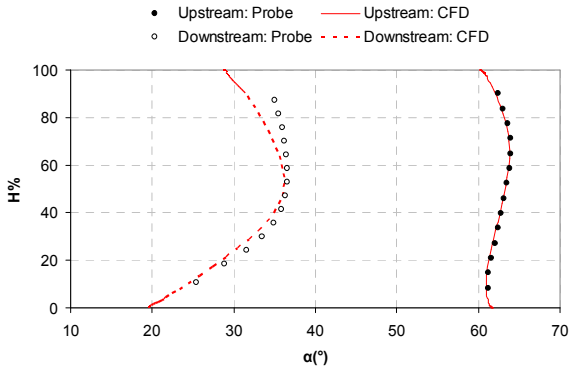

Fig 6.34b: Span-wise profile of flow angle at upstream and downstream planes, Case: Hub aspiration, Cq=0.04, α=63° (Probe/CFD)

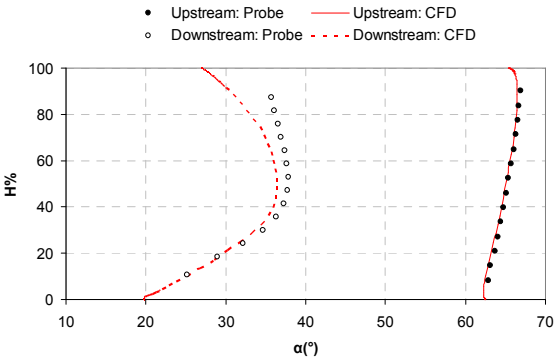

Fig 6.35b: Span-wise profile of flow angle at upstream and downstream planes, Case: Hub aspiration, Cq=0.04, α=65° (Probe/CFD)

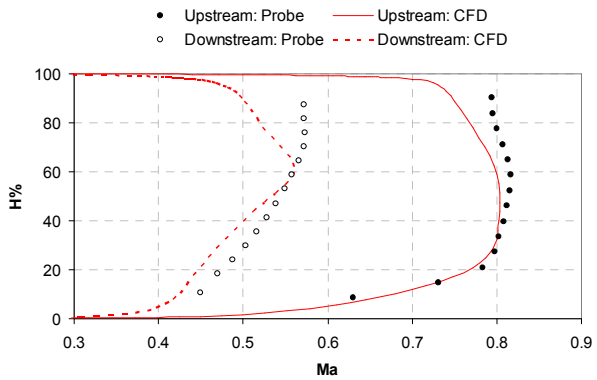

Fig 6.34c: Span-wise profile of Mach number at upstream and downstream planes, Case: Hub aspiration, Cq=0.04, α=63° (Probe/CFD)

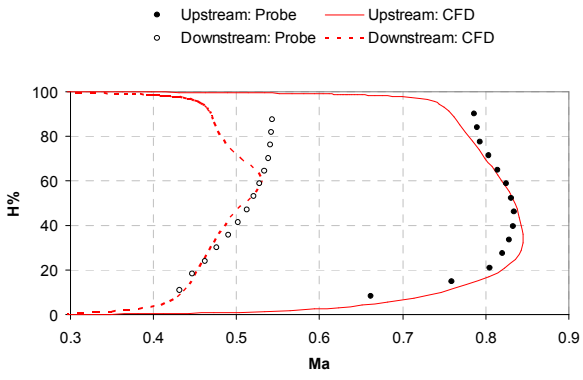

Fig 6.35c: Span-wise profile of Mach number at upstream and downstream planes, Case: Hub aspiration, Cq=0.04, α=65° (Probe/CFD)

In figures 6.34a and 6.35a, the CFD span-wise profile of downstream total pressure increases from hub wall to 60% span due to better control of corner separation with increased aspiration coefficient Cq=0.04. The CFD downstream total pressure profile then falls sharply from 70% span to the casing wall due to stronger tip leakage vortex induced by higher quantity of aspirated massflow as lower quantity of massflow passes near the casing wall. The profile of experimental downstream total pressure shows a small drop in value near the casing wall; there does not appear to be a strong tip leakage vortex in the experiment. The ϖ_{CFD} is 13% higher than ϖ_{test} for α=63° and 24% higher for α=65°.

The correlation between CFD and experiment is good in the profile of downstream flow angle till 60% span for α=63° and 40% span for α=65°; the experimental downstream flow angle exhibits higher values from these limits till the casing wall. The span-wise profiles of experimental and CFD downstream Mach number do not correlate well as seen in figure 6.34c for α=63°; this could be due to the difference in inlet Mach numbers leading to slightly different levels of compressions between the experiment and CFD. In figure 6.35c, the CFD downstream Mach number correlates well with its experimental counterpart till 60% span, after which the experimental values are considerably higher till the casing wall as if the flow is not influenced by the tip clearance vortex.

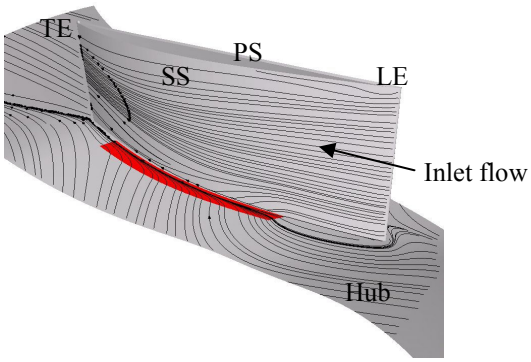

Fig 6.36a: Limiting streamlines on endwall and blade surface, Case: Hub aspiration, Cq=0.04, α=63° (CFD)

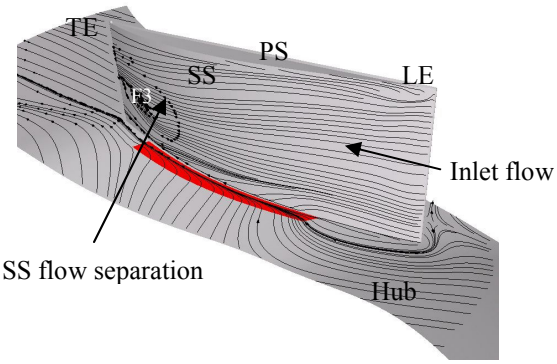

Fig 6.36b: Limiting streamlines on endwall and blade surface, Case: Hub aspiration, Cq=0.04, α=65° (CFD)

The flow topology in figure 6.36a,b shows complete suppression of corner separation and suction surface flow separation with hub aspiration, Cq=0.04 at α=63° and α=65°. The flow separation on suction surface is largely suppressed, however some streamlines are found to spiral around into a focal point F3 near the trailing edge forming a small zone of flow separation.

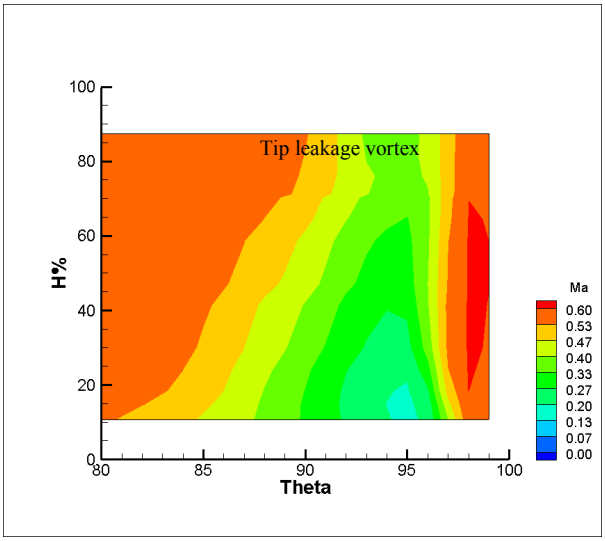

Fig 6.37a: Downstream Mach number visualisation in the blade passage,
Case: Hub aspiration, Cq=0.04, α=65° (Probe)

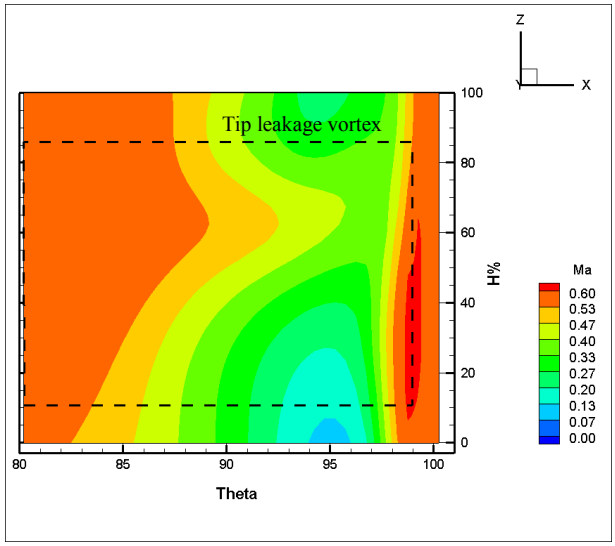

Fig 6.37b: Downstream Mach number visualisation in the blade passage,
Case: Hub aspiration, Cq=0.04, α=65° (CFD)

In figures 6.37a,b showing the Mach number visualisation, we see that the corner separation is suppressed and we find traces of a small zone of low energy flow in CFD and experiment at the hub wall. Also, the tip leakage vortex is distinctly visible in CFD and stronger compared to experiment. While the tip leakage is also visible in experiment, it is weaker than CFD. Although hub aspiration appears to be more effective in experiment, the weaker tip leakage vortex in experiment seems to be surprising.

The results discussed above show that hub aspiration, Cq=0.04 is able to suppress the corner separation completely on the hub wall till α=65°. Recall from the previous CFD studies of chapters 4 and 5 that the operating range of the blade row is limited at α=65° as the corner separation could not be suppressed with hub aspiration, Cq=0.02.

A parametric study at the end of chapter 5 showed that it is possible to suppress the corner separation with hub aspiration, Cq=0.04. However, the CFD studies were not done beyond α=65° to test if the operating range of the blade row could indeed be extended. The experiments without and with hub aspiration have been done beyond α=65° at α=67°. To determine the possibility of an extended operating range of the blade row, we shall briefly compare the experimental and CFD results for the case of hub aspiration, Cq=0.04 at α=67°.

6.8.7 α=67°, HUB ASPIRATION, C_q=0.04

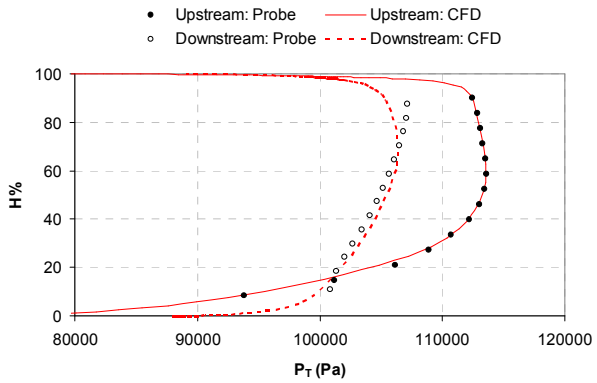

Fig 6.38a: Span-wise profile of total pressure at upstream and downstream planes, Case: Hub aspiration, Cq=0.04, α=67° (Probe/CFD)

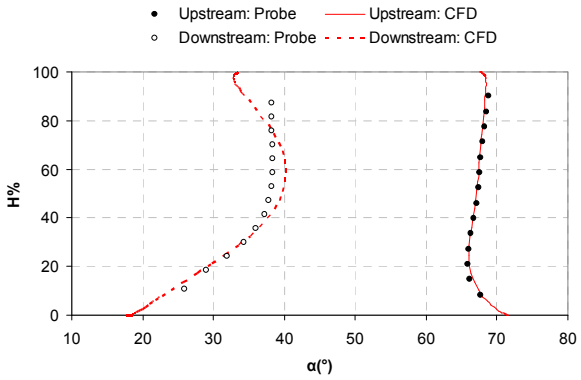

Fig 6.38b: Span-wise profile of flow angle at upstream and downstream planes, Case: Hub aspiration, Cq=0.04, α=67° (Probe/CFD)

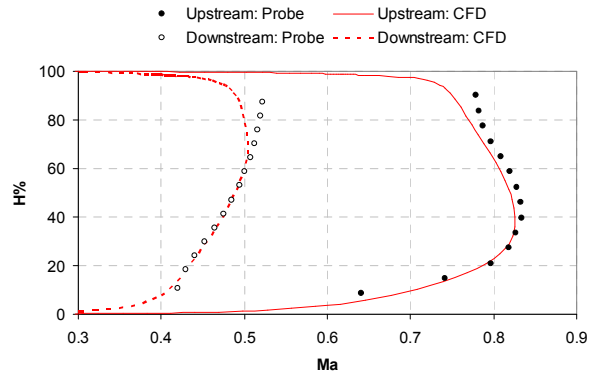

Fig 6.38c: Span-wise profile of Mach number at upstream and downstream planes, Case: Hub aspiration, Cq=0.04, α=67° (Probe/CFD)

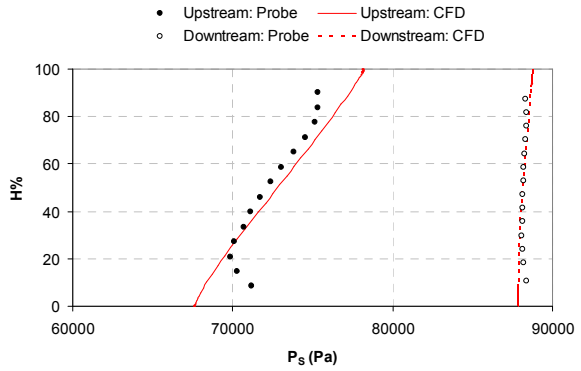

Fig 6.38d: Span-wise profile of static pressure at upstream and downstream planes, Case: Hub aspiration, Cq=0.04, α=67° (Probe/CFD)

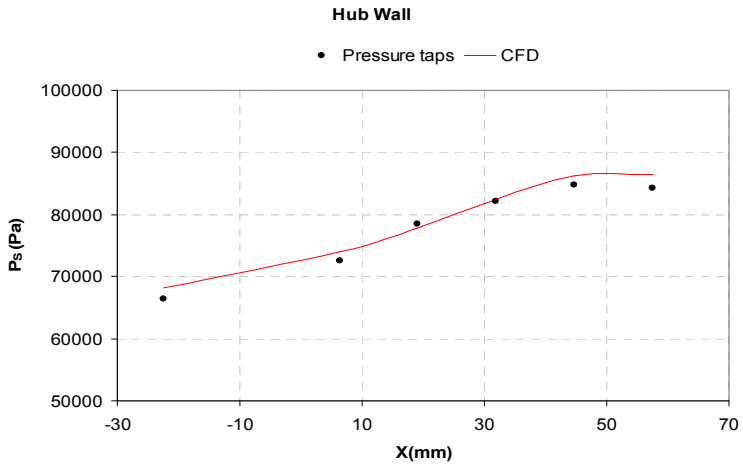

Fig 6.39a: Static pressure on hub wall, Case: Hub aspiration, Cq=0.04, α=67° (Experiment/CFD)

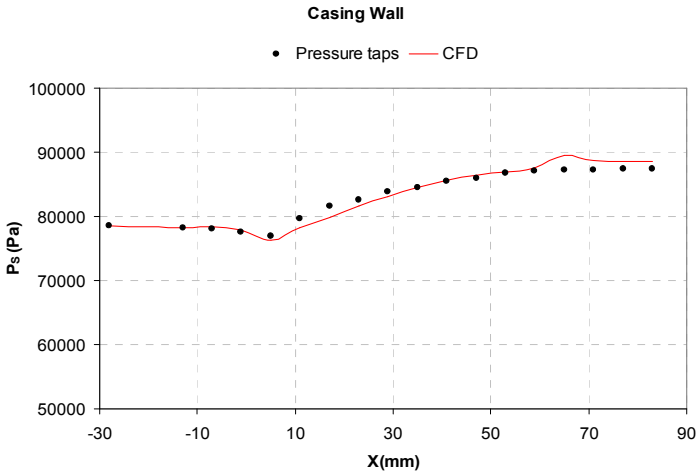

Fig 6.39b: Static pressure on casing wall, Case: Hub aspiration, Cq=0.04, α=67° (Experiment/CFD)

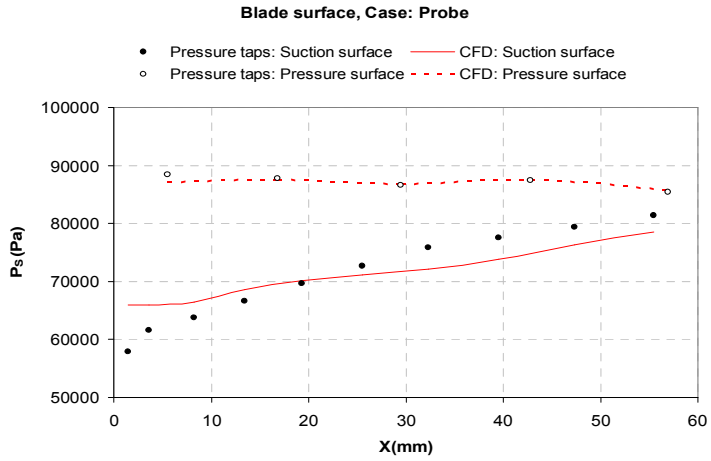

Fig 6.39c: Static pressure on blade surface at mid-span, Case: Hub aspiration, Cq=0.04, α=67° (Experiment/CFD)

The quantitative comparison of the experimental and CFD results is presented in figures 6.38a-d, 6.39a-c. Globally, there is good correlation between all the experimental and CFD flow variables. One exception is the profile of downstream Mach number where the experimental and CFD values are in good correlation till 60% span and then begin to diverge. The ϖ_{CFD} is 7% higher than ϖ_{test}, indicating a good correlation between experiment and CFD.

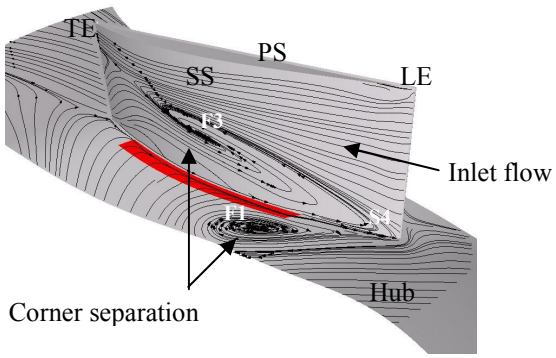

Fig 6.40: Limiting streamlines on endwall and blade surface, Case: Hub aspiration, Cq=0.04, α=67° (CFD)

The flow topology in figure 6.40 shows very strong corner separation with hub aspiration, Cq=0.04 at α=67°. The separation initiates with saddle point S4 very close to the leading edge in the corner between the hub wall and the suction surface. The zone of corner separation on the hub wall is well defined by focal point F2 on the hub wall and the zone of flow separation on the suction surface is well defined by focal point F1. We determine that increasing the quantity of aspirated massflow in the present aspiration configuration does not improve the operating range of the cascade.

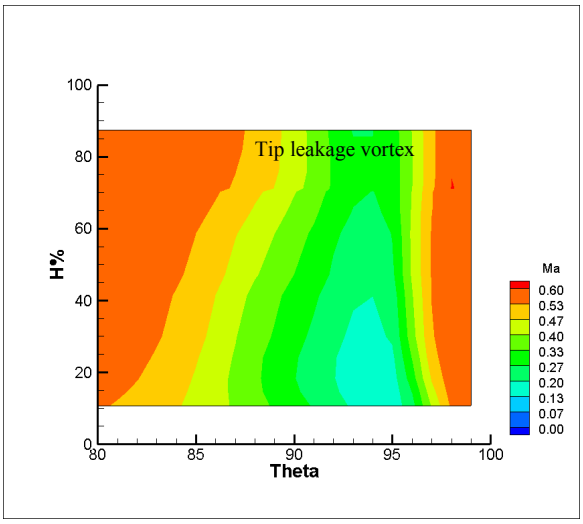

Fig 6.41a: Downstream Mach number visualisation in blade passage, Case: Hub aspiration, Cq=0.04, α=67° (Probe)

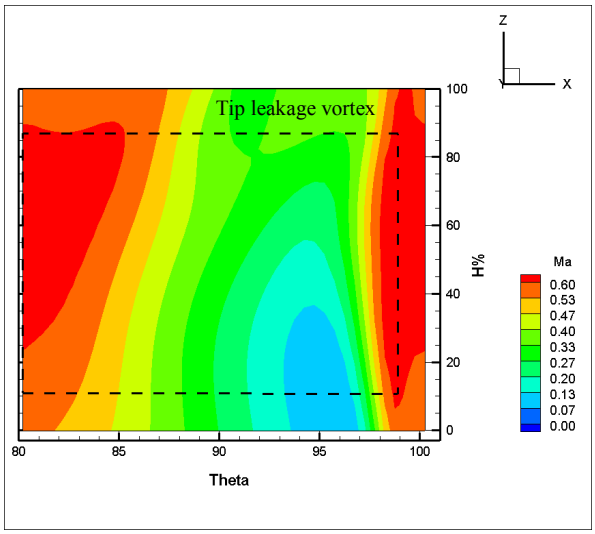

Fig 6.41b: Downstream Mach number visualisation in blade passage, Case: Hub aspiration, Cq=0.04, α=67° (CFD)

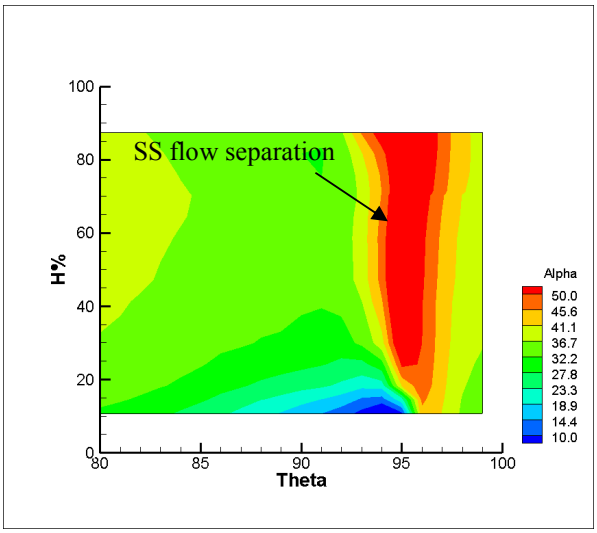

Fig 6.41c: Downstream flow angle visualisation in blade passage, Case: Hub aspiration, Cq=0.04, α=67° (Probe)

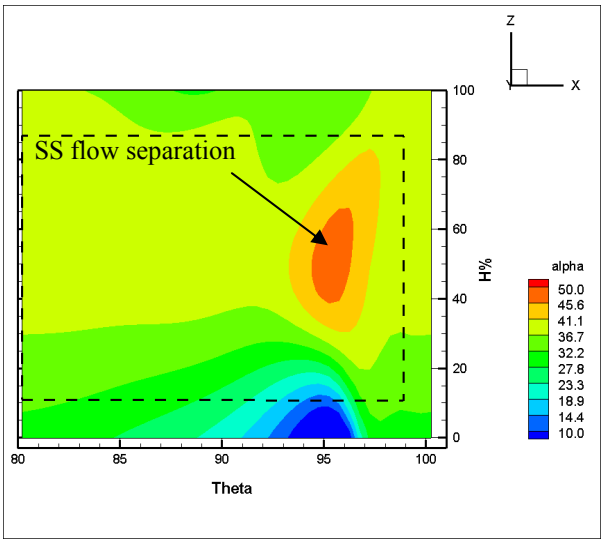

Fig 6.41d: Downstream flow angle visualisation in blade passage, Case: Hub aspiration, Cq=0.04, α=67° (CFD)

From figures 6.41a,b we see the corner vortex strongly developed in experiment and CFD; the tip leakage vortex is also visible in both the cases. In CFD, the corner separation is so strongly developed that the tip leakage vortex is unable to suppress it; it is found to mix in the wake with corner separation. We observe the same effect in experiment but the tip leakage vortex is again found to be weaker than CFD. Figure 6.41d shows the flow separation on the suction surface clearly by high value of downstream flow angle in the wake.

6.9 CONCLUSION

The experiments have been carried out with highly turbulent inlet conditions and the flow variables exhibit strong gradients. The inlet conditions may be not representative of the inlet flow conditions in a real engine environment, as the integral scale of turbulence seems too high.

The discrepancy in experimental measurements by the pressure probe and LDA at the reference point is surprising in terms of Mach number. The discrepancy presented by the measurement techniques remains an open question and should be addressed in the future. In the recent developments carried out at LTT-PFL, there are indications that these discrepancies arise from the non axisymmetry of the test rig.

CFD simulations are done with inlet boundary conditions from experimental measurements with hypothesis in turbulence modelling. The hypothesis is that the dissipation rate of turbulent kinetic energy is modelled using a uniform length scale along the blade span. The span-wise profile of length scale obtained later from LDA has shown significant span-wise evolution and our simplifying hypothesis is not representative of the reality.

The comparison of CFD results with experimental results yields good correlation from hub wall to 60% span for most of the configurations studied. In particular, the extent of the hub corner separation is good for many incidence angles. The numerical modelling with chimera mesh is capable of predicting the flows without and with aspiration at hub wall reasonably well.

The correlation is found to deteriorate in the zone close to the tip walls where CFD predicts stronger tip leakage vortex at casing wall than experiments. Of remarkable difference is the much stronger tip leakage vortex predicted by CFD. This makes CFD results pessimistic as compared to the experimental results with higher total pressure losses. This high tip clearance effect is even higher when aspiration is performed at the hub, as it tends to displace the tip flow towards the hub.

The experimental results show that it is possible to completely suppress the corner separation with hub aspiration, Cq=0.04 at α=65°. However, the improvement in the operating range of the blade row seems unlikely with the present aspiration strategy as demonstrated by the analysis of results at α=67° with hub aspiration, Cq=0.04.

The lower level of endwall effects in experiments is a sign of encouragement for the integration of boundary layer aspiration in a real engine environment. If the experimental inlet conditions can be improved to match the inlet conditions of a real engine then boundary layer aspiration may offer substantial incentive with its potential benefits to integrate in a real engine compressor.

The K-ε turbulence model has its own limitations that contribute to some of the inaccuracies in results of numerical simulations. The K-ε turbulence model (2 equations) is limited in its accuracy to predict flows that are sensitive to strong 3D flow separations. A steady flow separation is not a real phenomenon; it is a result of stationary RANS simulations. Perhaps, a LES (Large Eddy Simulation) technique would be more accurate in predicting such flows.

We recommend better understanding and possible elimination of the discrepancies in flow measurements by probe and LDA for a better comparison.

Flow visualisation techniques on the walls such as pressure sensitive paint or oil may be used to visualise the experimental flow topology. If the flow topologies in experiments and CFD can be compared, we may be able to better understand the limitations of our present numerical modelling.

7. BASELINE BLADE WITH HUB AND PROFILE ASPIRATION

7.1 INTRODUCTION

In chapter 5, we have seen that hub aspiration with Cq=0.02 offers a good control of the corner separation in the stator blade row over the entire operating range of the blade row except at the highest loss incidence point (α=65°). Although the level of total pressure losses is reduced, the corner separation is not suppressed and the operating range of the blade row could be improved.

To further improve the aerodynamic performance of the blade row, the hub aspiration is coupled with the blade profile aspiration. The potential of blade profile aspiration is to reduce or suppress the flow separation on the suction surface of the blade and to increase the diffusion capacity of the blade.

Various blade profile aspiration configurations are investigated to finalize the configuration of the blade profile slot for the second campaign of tests at EPFL. A sensitivity study is carried out to study the influence of various parameters like the slot width, slot length, chord wise slot position, etc. on the aerodynamic performance of the blade row. Three blade slot widths of 2mm, 4mm and 6mm are studied by ONERA and the blade slot width is frozen at 4mm. The sensitivity studies showed that the blade profile slot of width 2mm is susceptible to flow blockage due to lower cross section area for aspiration, blade slot of width 6mm is larger than necessary to aspirate the target mass flow. The blade slots are inclined at 45° to the free stream flow (figure 7.2b). Initial studies have been done to study the slot lengths from 5% to 60%, 80% and 90% span. Blade slot from 5% to 90% span have been retained as a final length parameter due to the robustness requirement for the experiments.

The different blade profile aspiration configurations in CFD studies are tabulated below:

	Slot width (mm)	Slot position (chord)	Slot span
Configuration 1	4	40%	5-90%
Configuration 2	4	60%	5-90%

Table 7: Various blade profile aspiration configurations in CFD studies

The blade slot positions in the above configurations that are shown in figures 7.1a,b:

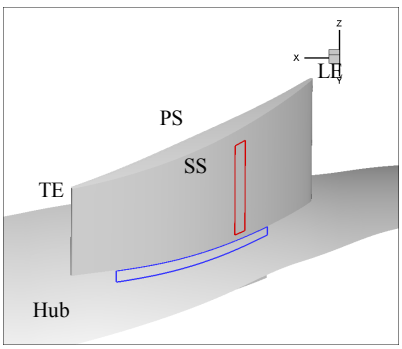

Fig 7.1a: Configuration 1: Blade slot at 40% chord, 5-90% span

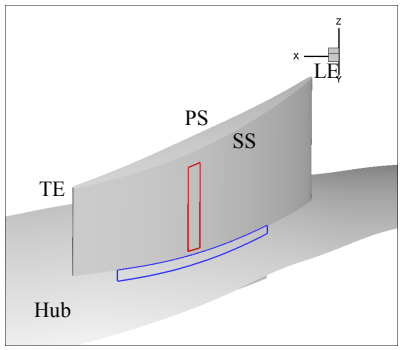

Fig 7.1b: Configuration 2: Blade slot at 60% chord, 5-40% span

The selection of blade aspiration slots is based on two criteria:

- Geometric constraints: The choice of position of blade slots is made under the constraints of fabrication with the inner blade cavity that transports the aspirated fluid from the flow path to the internal blade channels. Close to the leading edge and the trailing edge, the blade is not thick enough to permit the fabrication of the blade slots and their connection with the inner cavity. Hence, the blade slots have to be positioned between 30%c to 70%c.

- Aerodynamic influence: The blade slot configuration at 40%c is to study the influence of the profile aspiration on the hub flow that separates quickly after the leading edge at the highest loss incidence point. Since the hub aspiration is unable to suppress the corner separation, it is interesting to observe the influence of blade profile aspiration in the zones of corner region between the leading edge and mid-chord.

  The blade slot configuration at 60%c is to study the potential improvement in the flow deviation. As it is located to permit higher flow diffusion in the downstream zone after the mid-chord, it also has the potential to collect the separated flow on the hub wall and diffuse it over the span.

7.2 MESH GENERATION

Similar to the technique of hub slot mesh generation, the blade slot mesh is generated independently and then joined with the entire mesh using the Chimera technique of overlapping mesh planes. The meshing technique for blade slots is more complex as it is needed to introduce an intermediate supplementary mesh block "buffer block" between the blade slot mesh and the flow path mesh. The buffer block permits better transfer of information from the flow path mesh to the blade slot by providing a means of better interpolation of points in the entire mesh. It is found that without the presence of buffer block, the CFD simulation fails to converge to a solution.

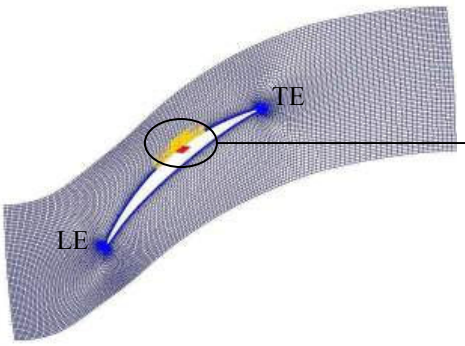

Fig 7.2a: 2D mesh planes with blade slot and the buffer block (blade slot at 60% chord)

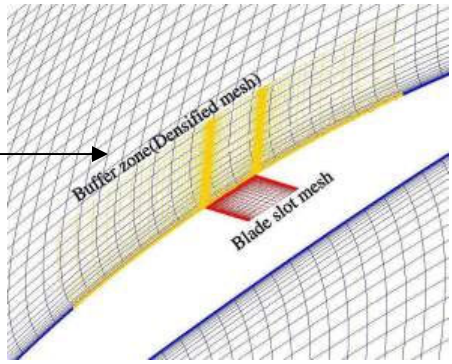

Fig 7.2b: Magnified view of mesh connection (blade slot mesh in red and the buffer block in yellow)

The blade slot mesh is coincident with the buffer block and the buffer block is joined with the flow path mesh by the Chimera technique of overlapping mesh planes. The CFD simulations exhibit a good level of convergence with the buffer block and good stability characteristics in terms of the flow rates and the conservative variables. Note that the CFD studies are done without the inner aspiration cavity in the blade.

7.3 RESULTS AND DISCUSSIONS

The blade profile aspiration studies were done only on the intermediate operational point (α=63°) and the highest loss incidence point (α=65°) to study the gains of profile aspiration in terms of better blade diffusion and its influence on the endwalls. The aspiration coefficient for the blade slot aspiration is Cq=0.02, so when coupled with hub wall aspiration (Cq=0.02), the total aspirated flow coefficient is Cq=0.04.

7.3.1 TOTAL PRESSURE RATIO

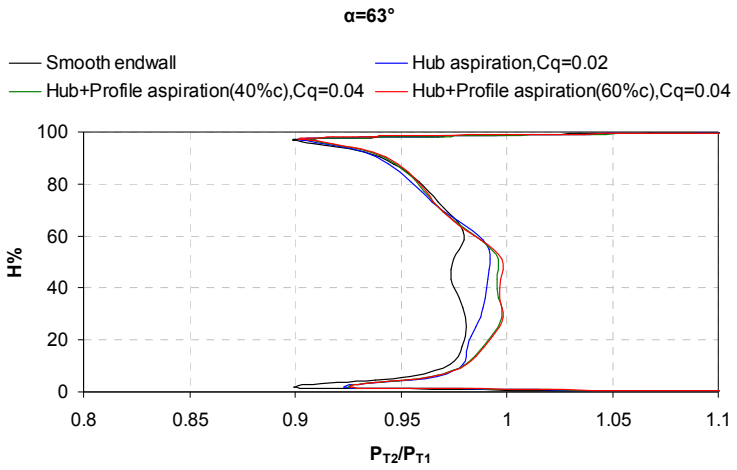

Fig 7.3a: Span-wise profile of total pressure ratio for hub and profile aspiration configurations at α=63°

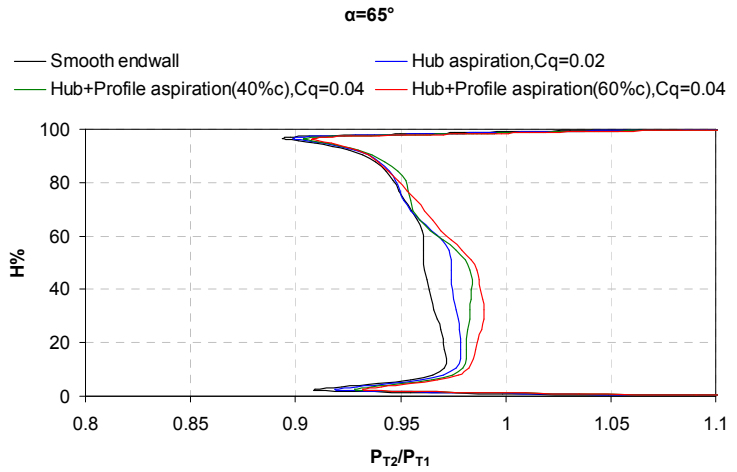

Fig 7.3b: Span-wise profile of total pressure ratio for hub and profile aspiration configurations at α=65°

The influence of hub and blade profile aspiration is clearer on the blade profile away from the endwalls for both the operational points. For both the configurations, the blade profile aspirations offers significant gains in increasing the downstream total pressure as compared to the smooth endwall and the hub aspiration configurations.

At α=63°, hub and blade profile aspiration offers more or less the same level of gains in total pressure. Aspiration configuration with the blade slot at 60% chord offers slightly better gain in total pressure ratio from 40% to 60% span.

At α=65°, aspiration configuration with blade slot at 60% chord offers better gains over all the configurations. Aspiration configuration with blade slot at 40% chord offers better gains over the smooth endwall and hub aspiration configurations but less than blade slot at 60% chord.

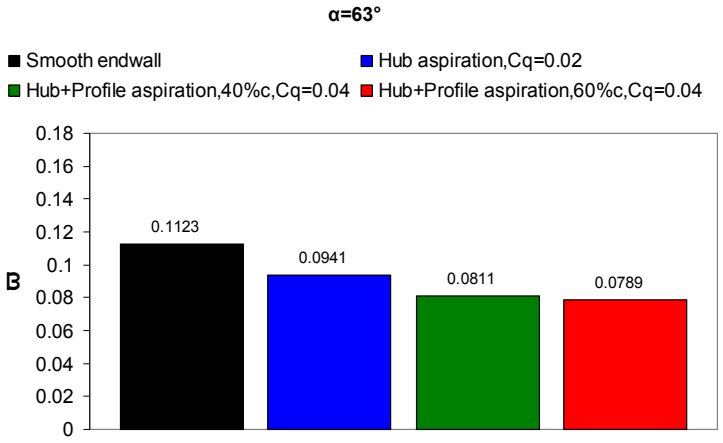

Fig 7.4a: Total pressure loss coefficient ϖ for hub and profile aspiration configurations at α=63°

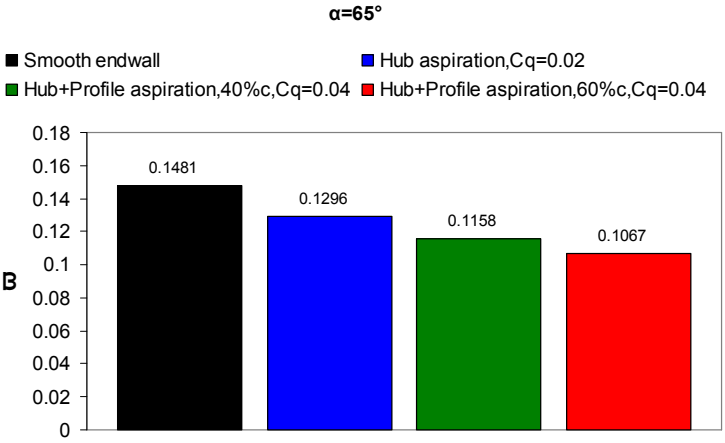

Fig 7.4b: Total pressure loss coefficient ϖ for hub and profile aspiration configurations at α=65°

For the cases of aspiration by hub and blade slots, the total pressure loss coefficient ϖ is calculated as:

$$\varpi = \varpi_{hub} + \varpi_{blade} + \varpi_{flowpath} \tag{7.1}$$

$$\varpi = \left[\left(\frac{Cq_{hub}}{100}\right).\frac{P_{T_1} - P_{T_{hub}}}{\frac{\gamma}{2}.P_{S_1}.Ma_1^2}\right] + \left[\left(\frac{Cq_{blade}}{100}\right).\frac{P_{T_1} - P_{T_{blade}}}{\frac{\gamma}{2}.P_{S_1}.Ma_1^2}\right] + \left[\left(\frac{100 - Cq_{total}}{100}\right).\frac{P_{T_1} - P_{T_2}}{\frac{\gamma}{2}.P_{S_1}.Ma_1^2}\right] \tag{7.2}$$

At α=63°, the total pressure loss coefficient ϖ is reduced by 27% and 28% by the blade profile configurations with blade slots at 40% chord and 60% chord respectively over the baseline configuration of smooth endwall. At α=65°, the total pressure loss coefficient ϖ is reduced by 22% and 28% by the blade profile configurations with blade slots at 40% chord and 60% chord respectively over the baseline configuration of smooth endwall. Recall from chapter 5 that ϖ at α=65° with hub aspiration, Cq=0.04 is 0.1086, i.e., merely 1.7% higher than the aspiration configuration with blade slot at 60% chord.

This shows certain equivalence in the levels of performance achieved by hub aspiration strategy and the hub and profile aspiration strategy. As will be shown later by the analysis of flow topologies in this chapter, the hub aspiration strategy with increased aspirated flow rate is able to eliminate the critical points, whereas the critical points are not completely eliminated by hub and profile aspiration. The flow structures exhibit differences between the two aspiration strategies.

7.3.2 FLOW DEVIATION

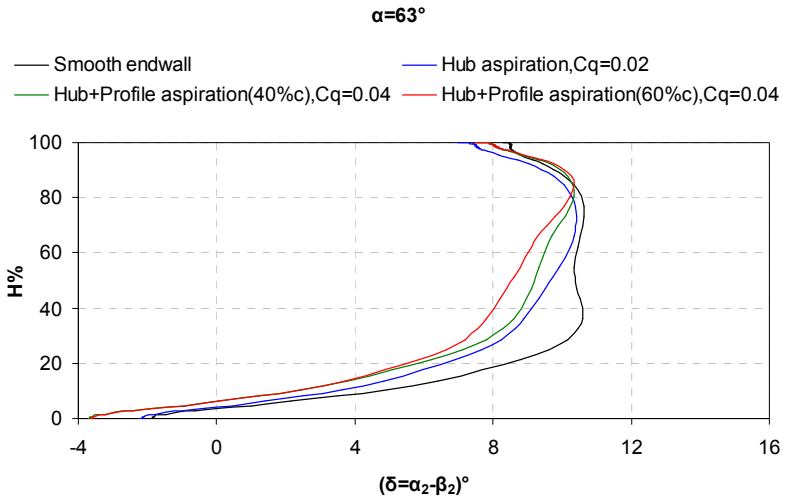

Fig 7.5a: Span-wise profile of flow deviation for hub and profile aspiration configurations at α=63°

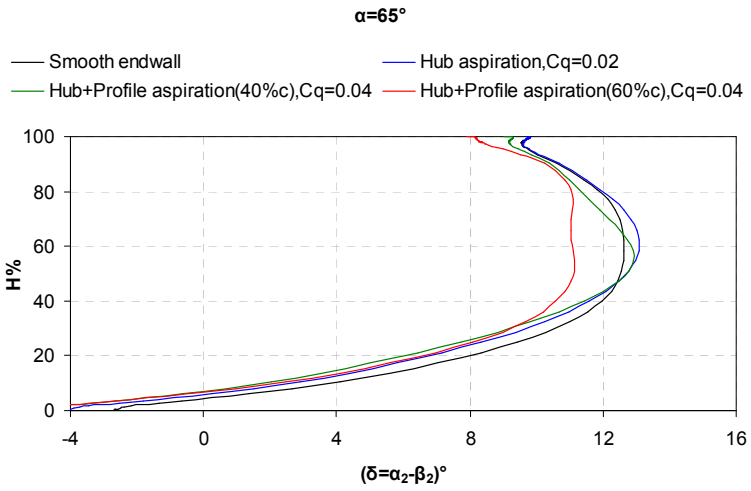

Fig 7.5b: Span-wise profile of flow deviation for hub and profile aspiration configurations at α=65°

As expected the flow deviation at both the points is improved with blade profile aspiration due to increased diffusion on the blade suction surface and consequently thinner wakes.

At α=63°, there is a progressive improvement in span-wise profile of flow deviation with the blade slots aspiration configurations indicating the contribution of the profile aspiration to improve the flow deflection. At α=65° all the configurations, the blade profile aspiration at 40% chord exhibits reduced flow deviation from 60% span to the casing wall. With the blade profile aspiration at 60% chord, the flow deviation is significantly reduced by 2° to 3° from 40% span to the casing wall as compared to the smooth endwall configuration. The corner vortex that climbs up along the blade passage span from hub wall is aspirated along the span by the blade slot leading to thinner wake.

7.3.3 MACH NUMBER

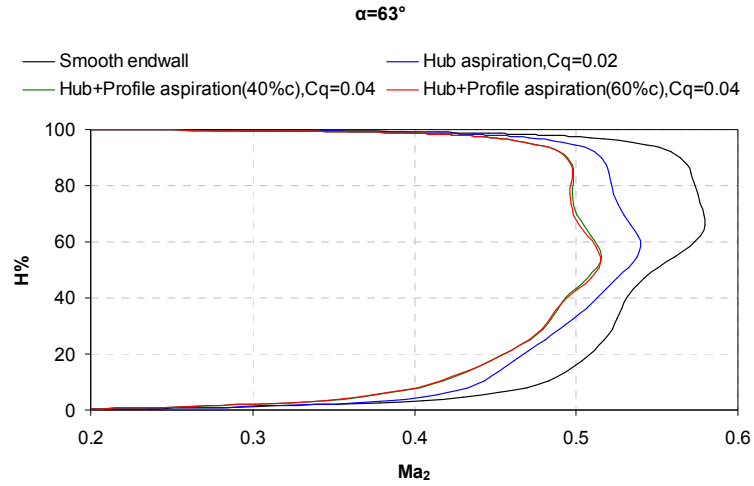

Fig 7.6a: Span-wise profile of downstream Mach number for hub and profile aspiration configurations at α=63°

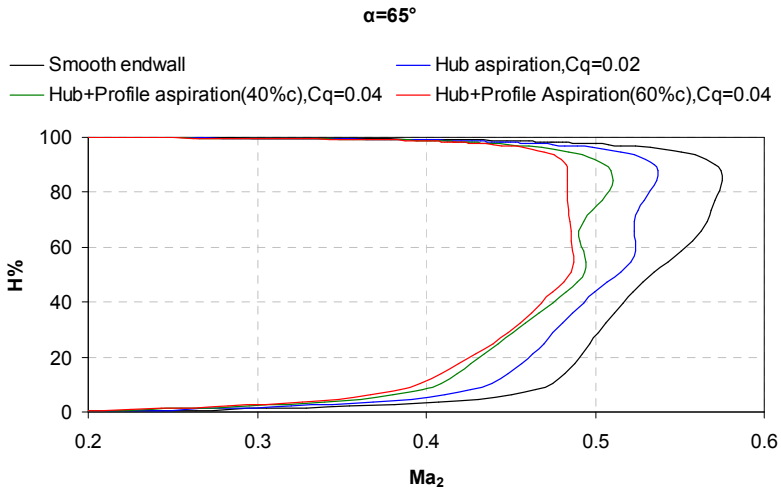

Fig 7.6b: Span-wise profile of downstream Mach number for hub and profile aspiration configurations at α=65°

At α=63°, the Mach number at downstream plane is found to be decelerated to more or less the same level by both the aspiration slots at 40% chord and 60% chord as seen in figure 7.6a. Since the flow separation exists only on suction surface of the blade at α=63°, both the aspiration with blade slots at 40% chord and 60% chord show signs of suppressing the separation with more or less the same level of efficiency.

At α=65°, aspiration with blade slot at 60% chord is more effective than the other configurations at increasing the compression and reducing the downstream Mach number. In particular, blade slot at 60% chord is better than blade slot at 40% chord in improving the compression from 40% span to the casing wall as it aspirates the corner vortex that tends to climb radially in the blade passage from the hub wall.

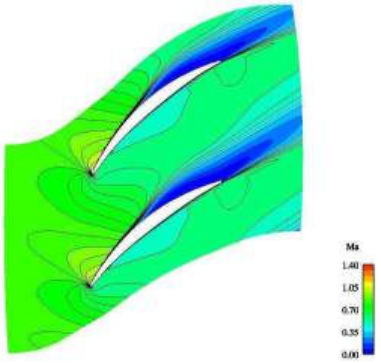

Fig 7.7a: Mach number at 10% span, Configuration: Smooth endwall at α=63°

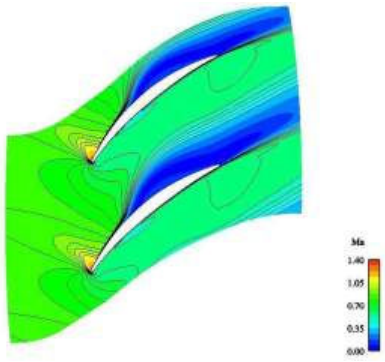

Fig 7.8a: Mach number at 10% span, Configuration: Smooth endwall at α=65°

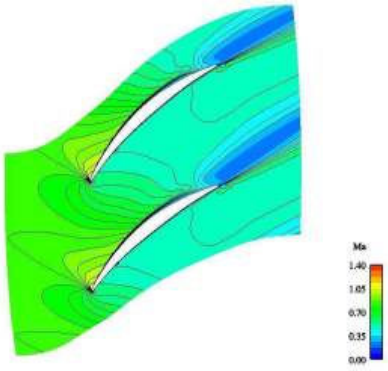

Fig 7.7b: Mach number at 10% span, Configuration: Hub aspiration, Cq=0.02 at α=63°

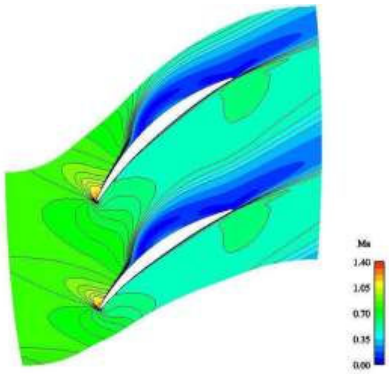

Fig 7.8b: Mach number at 10% span, Configuration: Hub aspiration, Cq=0.02 at α=65°

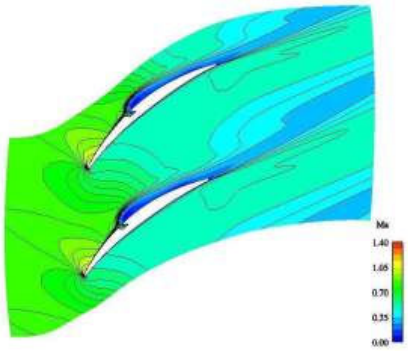

Fig 7.7c: Mach number at 10% span, Configuration: Hub+Profile aspiration (40%c), Cq=0.04 at α=63°

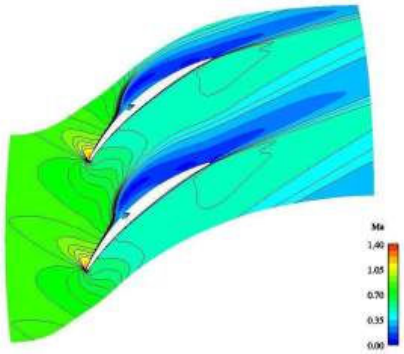

Fig 7.8c: Mach number at 10% span, Configuration: Hub+Profile aspiration (40%c), Cq=0.04 at α=65°

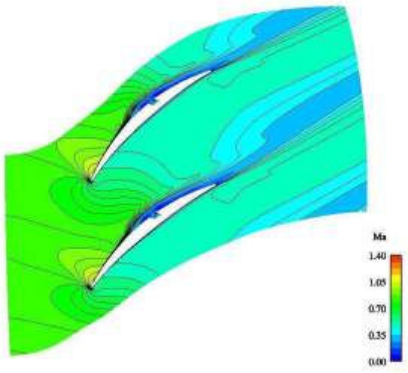

Fig 7.7d: Mach number at 10% span, Configuration: Hub+Profile aspiration (60%c), Cq=0.04 at α=63°

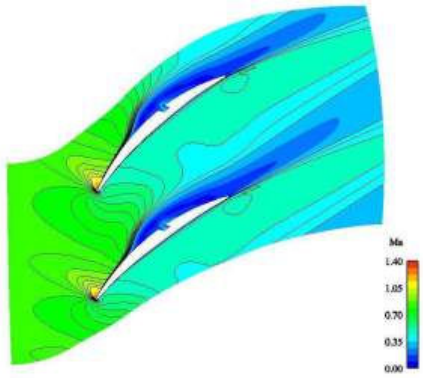

Fig 7.8d: Mach number at 10% span, Configuration: Hub+Profile aspiration (60%c), Cq=0.04 at α=65°

Figures 7.7a-d and 7.8a-d show the Mach number in the blade-to-blade plane at 10% span for various aspiration configurations. The Mach number at 10% span close to the hub wall shows the influence of aspiration configurations on the corner separation.

At α=63°, the corner separation is eliminated by hub aspiration, Cq=0.02. Aspiration with blade slot at 40% chord aspirates the non-separated flow in the fore region of the blade near the leading edge and this has a perturbing effect of slightly decelerating the flow after the slot. It does not provoke a separation and the flow leaves the blade trailing edge in a thinner wake as compared to the smooth endwall and the hub aspiration configuration. We may say that some quantity of the aspirated flow may spill out of the blade slot cavity due to low depth of the aspiration cavity on the blade. This may explain the presence of a thin zone of zero velocity at this configuration. The blade slot at 60% chord exhibits a thinner zone of zero velocity on the blade profile.

At α=65°, the corner separation is slightly reduced with hub aspiration, Cq=0.02 as compared to the smooth endwall configuration. In combination to hub aspiration, aspiration by blade slot at 40% chord has a minor effect on flow structure with zone of separation slightly reduced. Aspiration by blade slot at 60% chord offers better control over corner separation as the zone of separation is reduced but not completely eliminated. The location of separation on the hub wall is virtually uninfluenced by changing the blade slot positions.

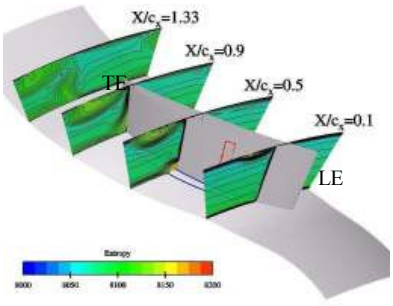

Fig 7.9a: Entropy in blade passage, Configuration: Hub+Profile aspiration (40%c), Cq=0.04 at α=63°

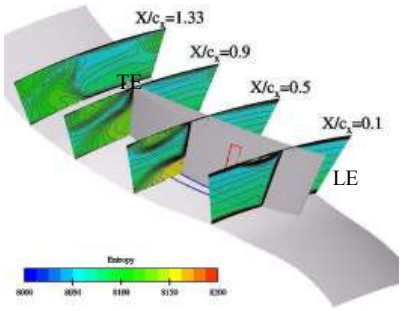

Fig 7.10a: Entropy in blade passage, Configuration: Hub+Profile aspiration (40%c), Cq=0.04 at α=65°

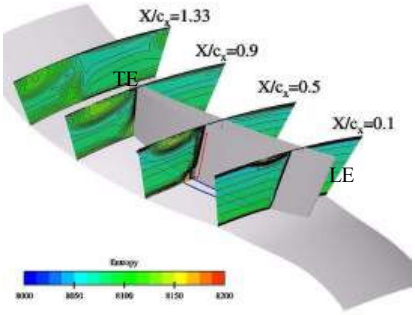

Fig 7.9b: Entropy in blade passage, Configuration: Hub+Profile aspiration (60%c), Cq=0.04 at α=63°

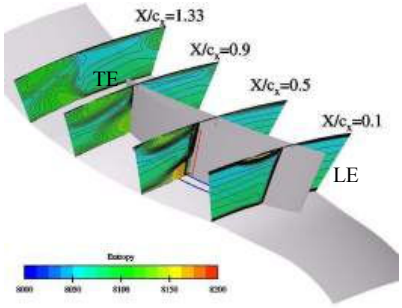

Fig 7.10b: Entropy in blade passage, Configuration: Hub+Profile aspiration (60%c), Cq=0.04 at α=65°

Figures 7.9a,b and 7.10a,b show the chord-wise evolution of flow entropy in the blade passage for aspiration configuration with hub and blade slots.

At α=63°, the aspiration configurations have a very similar effect of effectively removing the low energy fluid from the flow path as it is not highly separated. At α=65°, the corner separation is influenced in different ways by the aspiration configurations. Aspiration with blade slot at 40% chord is clearly not good enough to suppress the corner separation on the hub wall. Downstream of the slot, the corner vortex is found to be strong and propagates as large wake downstream of the trailing edge. Aspiration with blade slot at 60% chord is better at suppressing the corner separation to some extent. The strength of the corner vortex is reduced at the blade slot and then continues to propagate downstream. However, the corner separation is not completely eliminated and thus even with blade profile aspiration the operational margin of the blade row is not improved beyond α=65°.

7.4 ANALYSIS OF FLOW TOPOLOGY

7.4.1 FLOW TOPOLOGY AT α=63°

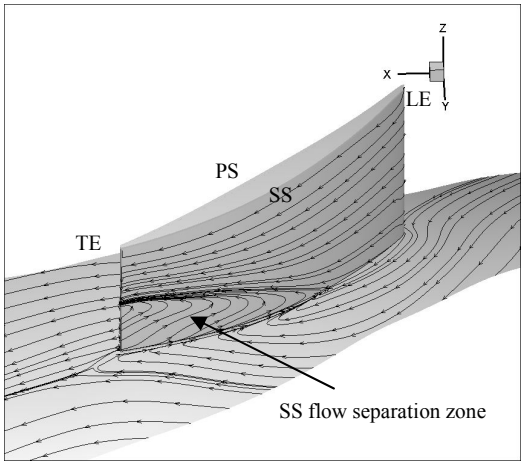

Fig 7.11a: Skin friction lines on hub wall and blade surface, Configuration: Smooth endwall at α=63°

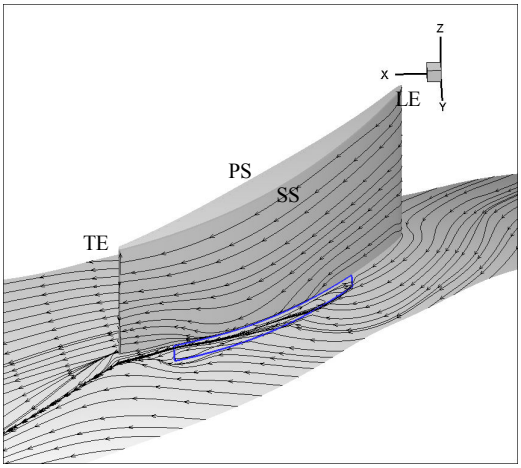

Fig 7.11b: Skin friction lines on hub wall and blade surface, Configuration: Hub aspiration, Cq=0.02 at α=63°

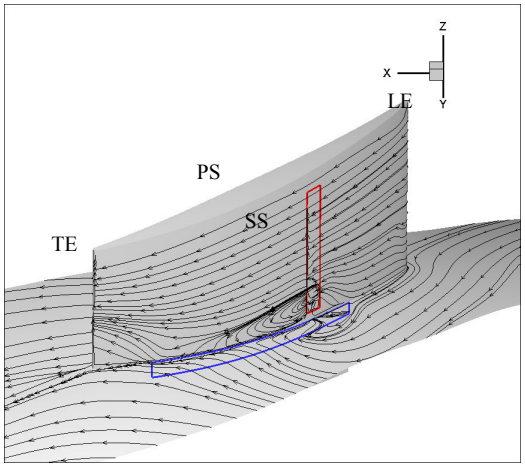

Fig 7.11c: Skin friction lines on hub wall and blade surface, Configuration: Hub+Profile aspiration (40%c), Cq=0.04 at α=63°

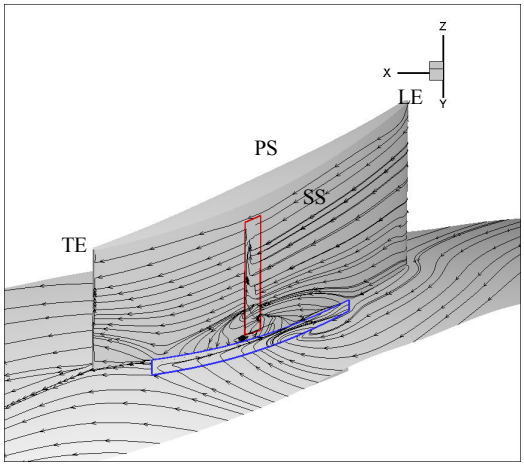

Fig 7.11d: Skin friction lines on hub wall and blade surface, Configuration: Hub+Profile aspiration (60%c), Cq=0.04 at α=63°

The flow separation zone on the suction surface of the blade with no aspiration in figure 7.11a is eliminated by hub aspiration, Cq=0.02 as seen in figure 7.11b. In figure 7.11c, we see the influence of blade slot at 40% chord on the flow structure in the blade passage.

Due to combined effect of hub and blade aspiration at 40% chord, the skin friction lines on the hub wall tend to curve strongly towards the hub slot. Just upstream of the blade slot, the skin friction lines on the suction surface of blade tend to converge and be aspirated in the blade slot. Just downstream of the blade slot we observe a small zone of reversing flow on the blade suction surface. This may be due to recirculation of the flow from the aspiration cavity of the blade slot.

The blade slot at 60% chord exhibits similar flow structures in the flow path. The skin friction lines in the proximities of the blade slots show discontinuous and deformed patterns. Under these circumstances, we are unable to establish the relations between the critical points to define separation and reattachment patterns. It has been verified that CFD simulations are correct and the incompleteness of the flow topology studies with blade aspiration is attributed to the erroneous exploitation of results in post processing, particularly in the proximity of blade slot where the buffer block mesh and the blade mesh (‘O’ block) coincide. Hence, we shall concern ourselves with the comparison of flow structure in the blade passage between different aspiration configurations without emphasizing on the detailed separation patterns, as done in chapters 4 and 5.

7.4.2 FLOW TOPOLOGY AT α=65°

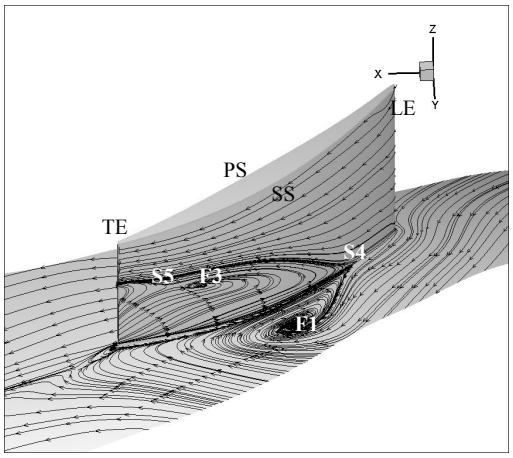

Fig 7.12a: Skin friction lines on hub wall and blade surface, Configuration: Smooth endwall at α=65°

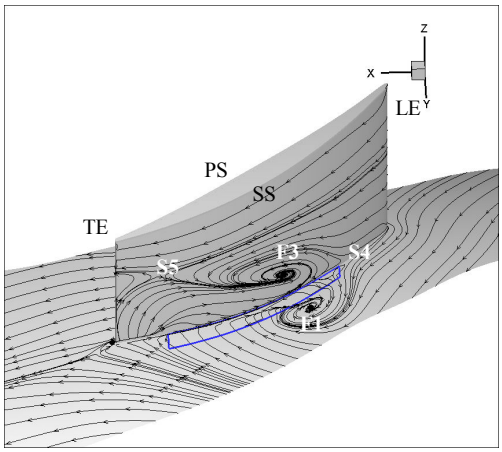

Fig 7.12b: Skin friction lines on hub wall and blade surface, Configuration: Hub aspiration, Cq=0.02 at α=65°

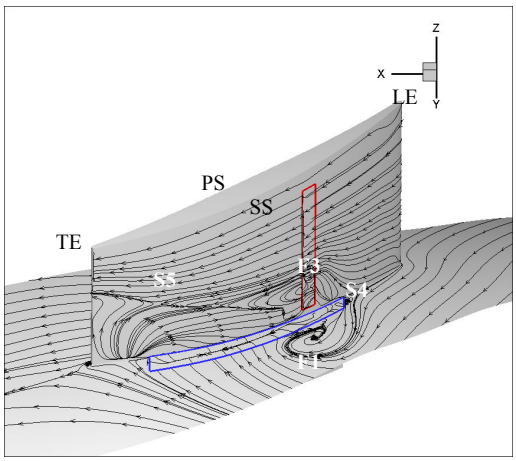

Fig 7.12c: Skin friction lines on hub wall and blade surface, Configuration: Hub+Profile aspiration (40%c), Cq=0.04 at α=65°

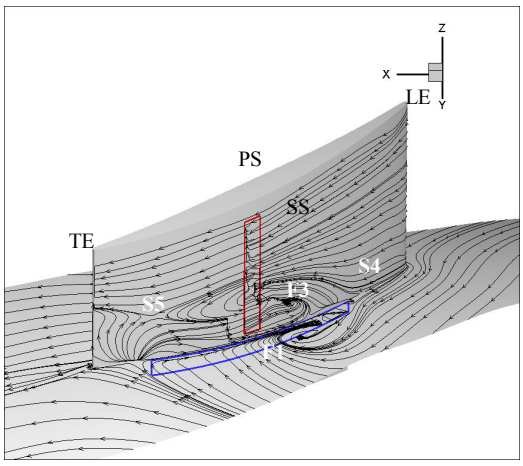

Fig 7.12d: Skin friction lines on hub wall and blade surface, Configuration: Hub+Profile aspiration (60%c), Cq=0.04 at α=65°

The flow topologies at α=65° in the configurations of smooth endwall and hub aspiration, Cq=0.02 (in figures 7.12a,b) have been explained in chapters 4 and 5 already and we shall study the influence of blade aspiration on flow structures. Recall that the focal point of separation F3 on the blade suction surface displaces under the influence of hub aspiration closer to the leading edge due to downward flow in the hub aspiration cavity (figure 7.12b). With the blade slot at 40% chord, the focal point of separation F2 on the blade suction surface is further displaced on the blade slot due to flow being aspirated into the blade suction cavity (figure 7.12c).

On the hub wall, the focal point F1 also experiences the effect of flow being aspirated in the blade slot. Recall from figure 5.21 that a common vortex core connects F1 and F3. The vortex F1 on the hub wall experiences the pulling effect of being drawn into the blade slot and is displaced slightly upstream. However, the strength of vortex F1 on the hub wall is virtually unchanged as the low energy fluid from the base of corner separation mounts into the blade passage and continues to propagate downstream without coming under the influence of blade aspiration.

In figure 7.12d, the blade slot at 60% chord has a more dramatic influence on the flow structure in the blade passage. We can see the convergence of skin friction lines towards the blade slot starting from the leading edge on the blade suction surface. The system of vortices F1 and F3 does not come into direct contact with the blade slot, as the slot is located downstream of F3 on the blade suction surface. The corner separation marked by F1 and F3 mounts in the blade passage, propagates downstream and is aspirated by the blade slot. This effectively reduces the strength of F1 on the hub wall.

Hence, the blade slot located downstream of the zone of flow separation has the potential to render better control on flow separation as it can aspirate the incoming low energy flow stream.

7.5 CHOICE OF THE BLADE SLOT CONFIGURATION FOR THE EXPERIMENTS

All the blade slot configurations failed to completely suppress the corner separation limiting the operating range of the cascade. Moderate success is achieved with the blade slot at 60% chord. Hence, blade profile aspiration with the blade slot located at 60% chord from 5% to 90% span is selected as the final configuration for the second campaign of experiments.

7.6 OPTIMIZATION OF BLADE PROFILE ASPIRATION: FURTHER CFD INVESTIGATION

The objective of this study is to implement the blade aspiration strategies than can possibly surpass the limitation of the operating range of the blade row. For this, we investigate to develop aspiration strategies that may render more efficient control on corner separation.

This study of optimization is based on the control of critical points in the flow topology. In this case we consider the implementation of aspiration on the critical points such as the focal point F3 on the blade suction surface at α=65°. Recall the flow topology on the blade with hub aspiration, Cq=0.02 at α=65°.

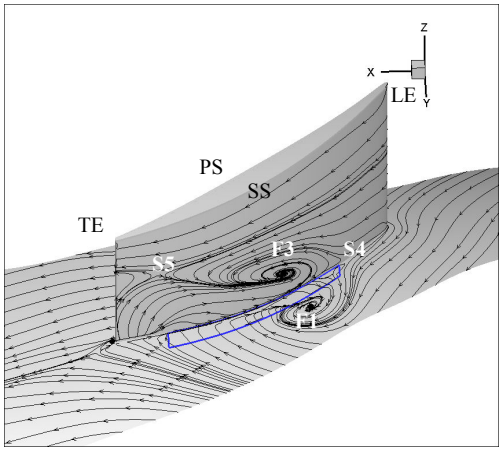

Fig 7.13: Flow topology at the highest loss point α=65° with hub aspiration, Cq=0.02

The focus F1 is the centre of formation of the corner vortex on the hub wall and focus F3 on the suction side is the centre of the separation on the suction side. As already seen in figure 5.21, both F1 and F3 are linked with a vortex core connecting their centres and there is a strong three-dimensional complex interaction of the flow. The saddle point S5 on the suction side is also a point where the re-circulating flow from the aspiration cavity goes into F3, flowing to increase the circulation strength of F3. If F3 can be reduced or eliminated on the blade suction surface we may expect better control of BLS over the flow separation.

Thus, two configurations with aspiration localised on F3 are proposed for better flow control:

- Aspiration slot localized on F3 on the suction surface (50%c, 5-40%H)

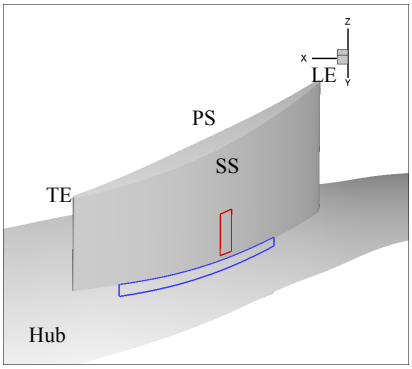

Fig 7.14a: Configuration 1: Blade slot at 50% c, 5-40% span

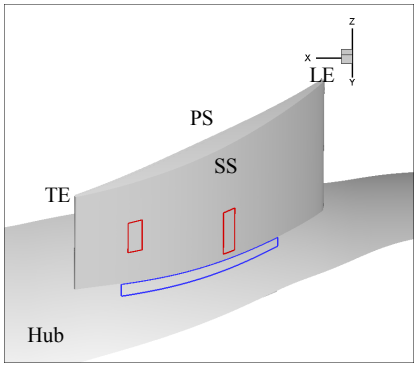

Fig 7.14b: Configuration 2: Blade slots at 50% c, 5-40% span and 82%c, 30-60% span

In the configuration 1 shown in figure 7.14a, the blade slot has a smaller cross section that can allow a lower massflow to be aspirated. The maximum massflow that can be aspirated in the blade slot at 50% chord is 1.5% of the inlet massflow. With hub aspiration, Cq=0.02, the total Cq becomes 0.035. In figure 7.14b, 1% of the inlet massflow is aspirated in each blade slot, hence, along with hub aspiration, Cq=0.02, the total Cq becomes 0.04.

7.7 RESULTS AND DISCUSSIONS

The results of the numerical studies for the above two configurations are compared with the configuration selected for tests: blade slot at 60%chord,5-90% span.

7.7.1 TOTAL PRESSURE LOSS COEFICIENT

Both the aspiration configurations with smaller slots on the blade suction surface are at par with the chosen profile aspiration configuration at α=63° and α=65°. It is interesting to see that the small blade slot at 50% chord offers the same level of total pressure losses with an economy of 0.05% in aspirated massflow as compared to the other two aspiration configurations. Although, the economy of the aspirated flow rate is not very appreciable, we may demonstrate the potential benefits of optimizing the location of aspiration slots.

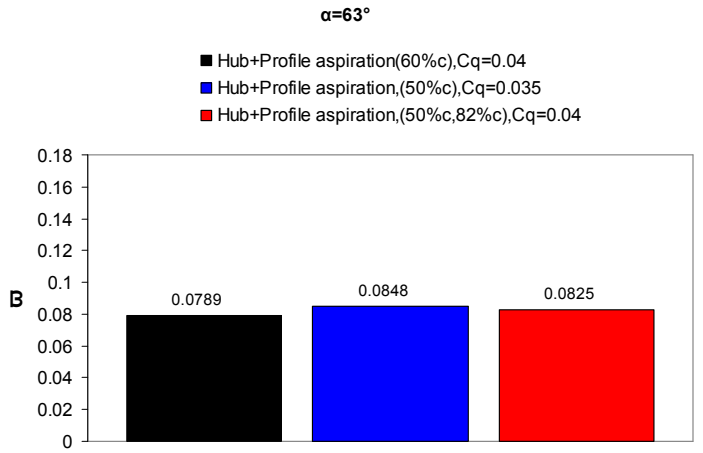

Fig 7.15a: Total pressure loss coefficient ϖ for hub and profile aspiration configurations at α=63°

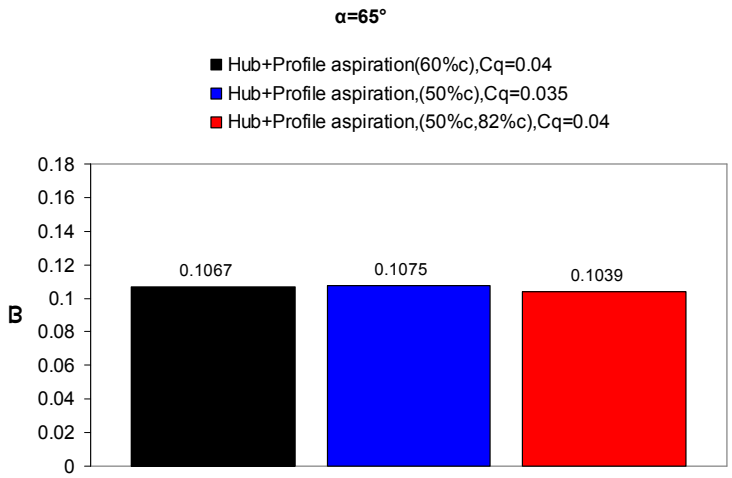

Fig 7.15b: Total pressure loss coefficient ϖ for hub and profile aspiration configurations at α=65°

At α=63°, ϖ is slightly higher for the aspiration configurations with smaller blade slots. The blade slot at 60% chord spans almost the entire span of the blade and hence may be better at diffusing the flow over the blade resulting into a lower ϖ. At α=65°, the blade slot at 50% chord renders a slightly higher ϖ over the blade slot at 60% chord.

7.7.2 FLOW DEVIATION

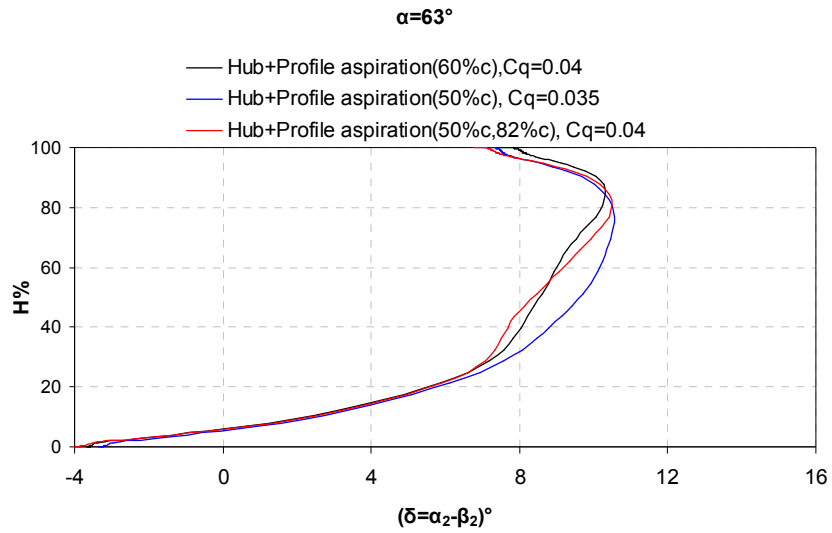

Fig 7.16a: Span-wise profile of flow deviation for hub and profile aspiration configurations at α=63°

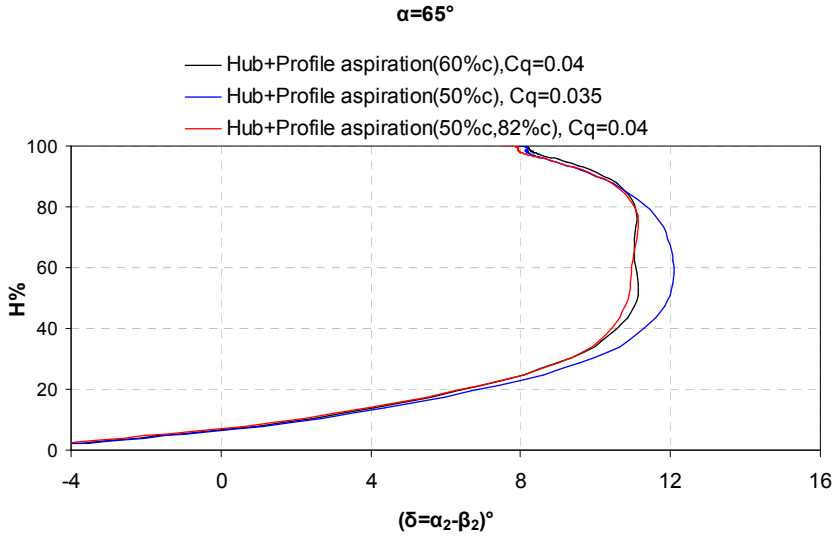

Fig 7.16b: Span-wise profile of flow deviation for hub and profile aspiration configurations at α=65°

The aspiration configuration with blade slot at 50% chord shows a higher flow deviation compared to other configurations due to its control on a very limited surface of the blade. The configuration with blade slots at 50% chord and 82% chord deflects the fluid in the same way as the large slot although located at very different positions along the chord. Positioning the aspiration slots in the aft zones of the blade improves flow deviation leaving the trailing edge as the low energy flow can be accelerated and re-energized under the influence of aspiration.

7.7.3 ENTROPY IN BLADE TO BLADE PLANE

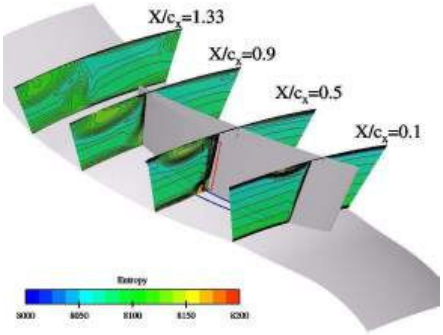

Fig 7.17a: Entropy in blade passage, Configuration: Hub+Profile aspiration (60%c), Cq=0.04 at α=63°

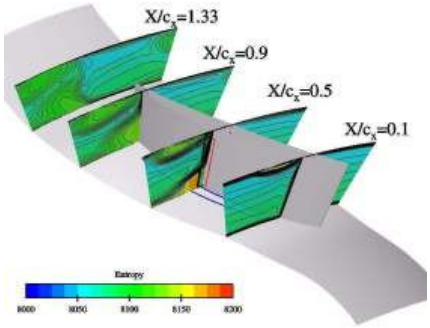

Fig 7.18a: Entropy in blade passage, Configuration: Hub+Profile aspiration (60%c), Cq=0.04 at α=65°

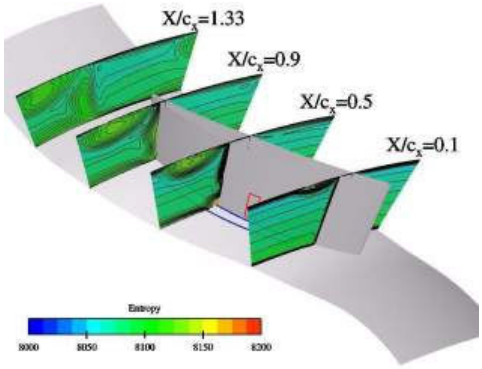

Fig 7.17b: Entropy in blade passage, Configuration: Hub+Profile aspiration (50%c), Cq=0.035 at α=63°

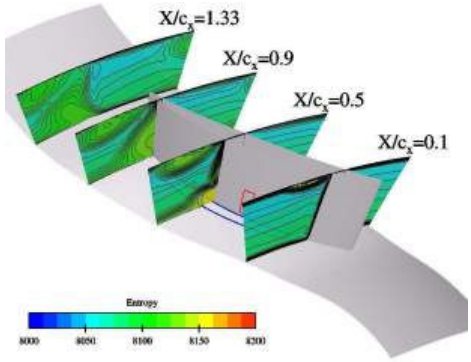

Fig 7.18b: Entropy in blade passage, Configuration: Hub+Profile aspiration (50%c), Cq=0.035 at α=65°

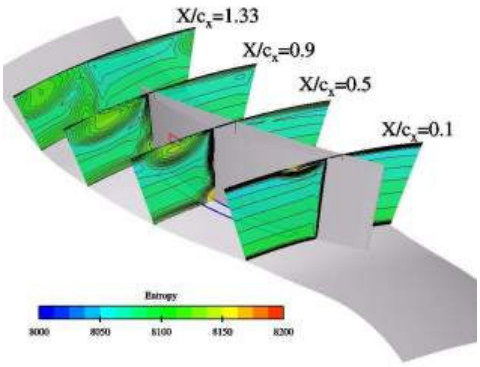

Fig 7.17c: Entropy in blade passage, Configuration: Hub+Profile aspiration (50%c, 82%c), Cq=0.04 at α=63°

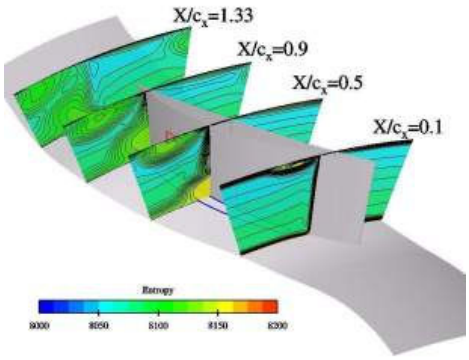

Fig 7.18c: Entropy in blade passage, Configuration: Hub+Profile aspiration (50%c, 82%c), Cq=0.04 at α=65°

There is a definite improvement at α=63° with the small slots. The small slots have suppressed the upstream separation that is found with the large slot placed at 60% chord. The small zone of separation is found to commence at the slot itself, also to consider the influence of the recirculation of the fluid between the slot and the flow path.

At α=65°, the separation upstream of the slot still persists but the extent of separation has been reduced with both the configurations having small slots on the suction side. The separation is still strong enough in magnitude not to be completely suppressed by the presence of small slots on the critical points on the suction side. Positioning the slots further upstream results in displacement of separation point upstream although with a slight improvement in the reduction of the separated zone.

At α=65°, the small slots on the suction side are better at controlling the extent of the corner separation due to their localized control than the large slot. The configuration with two slots on the suction side is able to slightly suppress the thickening of the boundary layer near the casing wall as compared to the configuration with one slot. As the hub corner stall is extremely strong, the small slots offer only minor improvement to the control.

7.8 ANALYSIS OF FLOW TOPOLOGY

7.8.1 FLOW TOPOLOGY AT α=63°

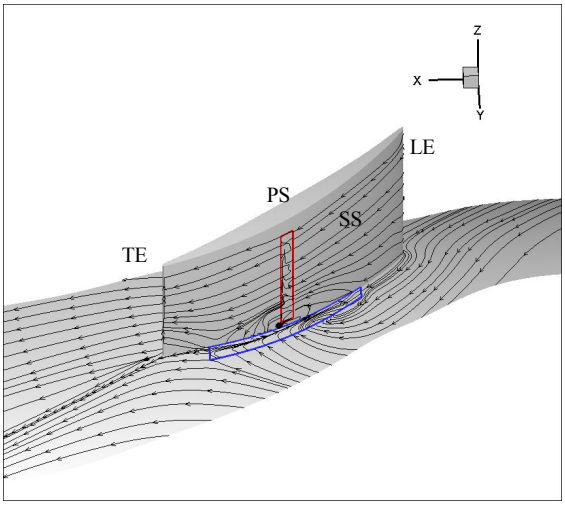

Fig 7.19a: Skin friction lines on hub wall and blade surface, Configuration: Hub+Profile aspiration (60%c), Cq=0.04 at α=63°

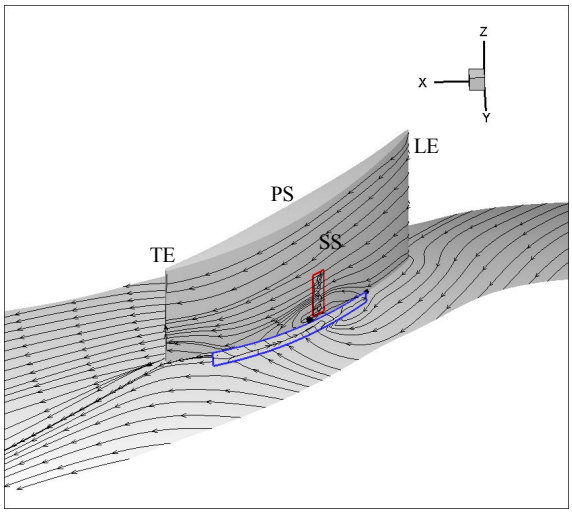

Fig 7.19b: Skin friction lines on hub wall and blade surface, Configuration: Hub+Profile aspiration (50%c), Cq=0.035 at α=63°

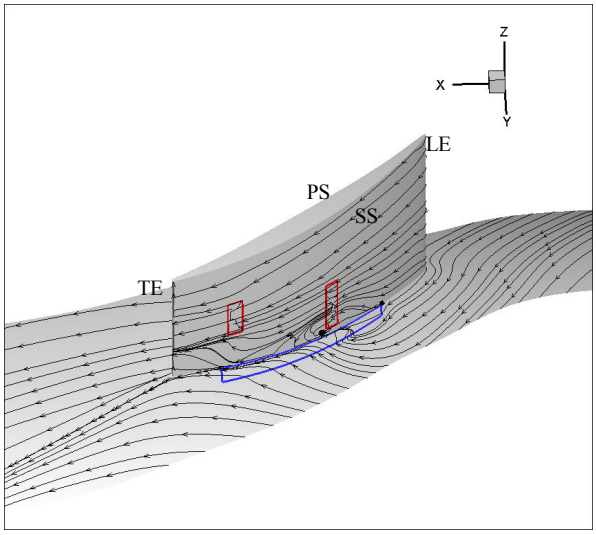

Fig 7.19c: Skin friction lines on hub wall and blade surface, Configuration: Hub+Profile aspiration (50%c, 82%c), Cq=0.04 at α=63°

At α=63°, the flow topologies are very similar for all the three aspiration configurations as shown in figures 7.19a-c. Close to the hub wall, we notice a reduction in the perturbed flow due to recirculation from the blade cavity with small slots.

7.8.2 FLOW TOPOLOGY AT α=65°

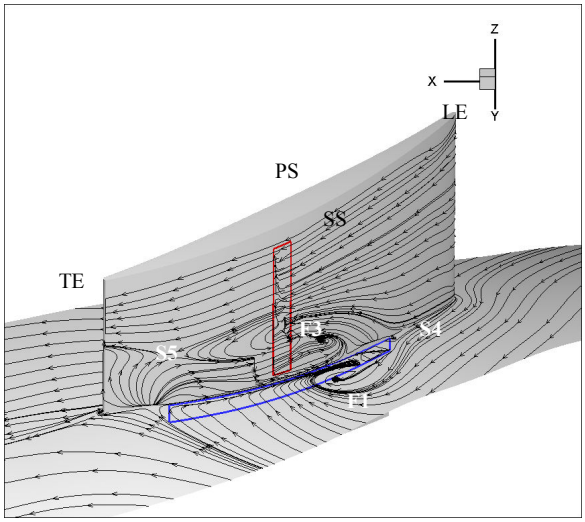

Fig 7.20a: Skin friction lines on hub wall and blade surface, Configuration: Hub+Profile aspiration (60%c), Cq=0.04 at α=65°

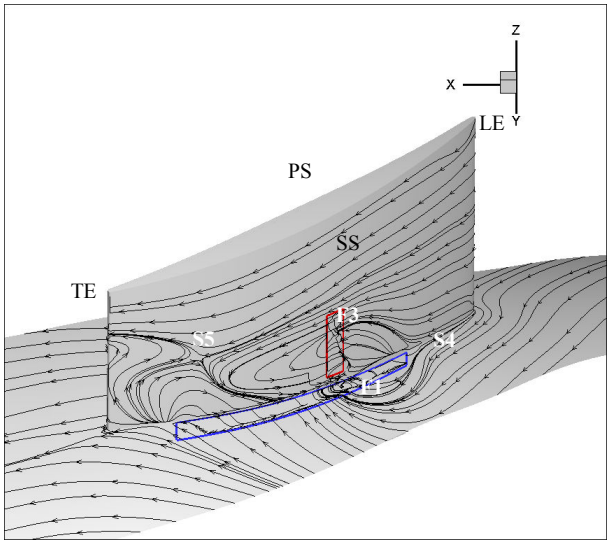

Fig 7.20b: Skin friction lines on hub wall and blade surface,
Configuration: Hub+Profile aspiration (50%c), Cq=0.035 at α=65°

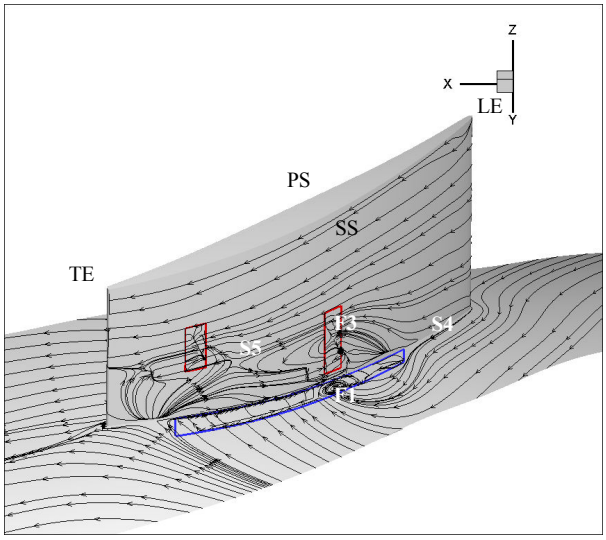

Fig 7.20c: Skin friction lines on hub wall and blade surface,
Configuration: Hub+Profile aspiration (50%c, 82%c), Cq=0.04 at α=65°

From figure 7.20b, we can see that vortex F1 on the hub wall is almost suppressed; F1 is barely visible on the hub slot and F3 is displaced on the blade slot. The saddle point S5 is displaced upstream closer to the blade slot due to strong effect of aspiration from hub wall to mid-span of the blade passage. Although the corner separation is well reduced by the blade slot at 50% chord, flow separation downstream of the blade slot is increased as indicated by the large extent of the saddle point S5.

In figure 7.20c, the flow topology is similar in proximity of the blade slot at 50%c. The corner separation is reduced on the hub wall. The blade slot at 82% chord displaces the saddle point S3 between the two blade slots. With S3 between the two blade slots, the flow diffusion over the blade is improved close to the trailing edge. One may reason that if the blade slot at 82% chord is extended span-wise till hub wall (downwards), there might be more improvement in the flow structure relating to saddle point S5.

7.9 CONCLUSION

The numerical studies of blade profile aspiration with hub aspiration show benefits of improved diffusion on blade suction surface. With the initial configurations of blade slots at 40%c and 60%c, the effect of aspiration with both the slot positions is similar at $\alpha=63°$ with blade slot at 60%c faring slightly better. Most of the improvement is attributed to the improved flow diffusion on the blade profile by blade slot.

The influence of blade profile aspiration is stronger on the operating point of $\alpha=65°$, where the hub corner separation is dominant. Reduction in flow separation on blade suction surface is achieved by the blade slot at 60%c as it is able to aspirate the separated massflow mounting in the blade passage from the hub wall. The low energy separated flow is aspirated and re-energised by the blade slot and leaves the trailing edge with a relatively thinner wake. The corner separation is reduced only marginally on the hub wall and is still strong enough to hinder any gain that can be achieved to improve the operating range of the blade row.

From the analysis of flow topologies, it is clear that the flow recirculation also exists between the blade slot and blade passage. This is interpreted as a limitation of the modelization; the cavity is not deep enough to properly simulate the aspirated flow.

The CFD studies performed by ONERA with complete modelling of the internal blade cavity has shown blade profile aspiration to be more effective as the re-circulation phenomenon is found to be non existent with a deeper aspirated flow passage. We may conclude that the results obtained from the present studies of blade profile aspiration are not demonstrative of the full potential benefits of BLS. This may be verified by the results of experiments with the finalised blade slot at 60%c. However, such verification is beyond the scope of this thesis.

Further CFD studies done with smaller slots positioned on the critical points such as focal point and saddle point on the suction surface have not produced major improvements in the reduction of total pressure losses. However, the objective of developing aspiration strategies to bleed flows at critical points is demonstrated successfully. The rationale to aspirate boundary layer in the cores of separated flows shows that it is possible to reduce the geometric dimensions of the aspiration device, reduce the suction flow rate and still achieve a level of aerodynamic performance similar to the larger slots.

8. CONCLUSION AND FUTURE PROSPECTS

We shall present a brief summary of the actions and the results obtained in this research work and provide the important conclusions.

This thesis aims to study the influence of boundary layer aspiration on the hub wall and blade profile to improve the aerodynamic performance of a stator blade row of a high pressure compressor. The main objective of the thesis is to investigate the influence of aspiration strategies on the hub wall and blade suction surface to control three dimensional flow separations on the test case. Special emphasis is laid on the understanding of flow structures by the study of flow topologies.

The numerical studies on the baseline test case of the stator blade row identify the hub corner separation increasing progressively with incidence. The three dimensional flows are strongly developed, the pressure rise capability of the blade row is hindered and the operating range is limited by the hub corner separation.

The CFD RANS (steady state) simulations reproduce the complex flow topologies of three dimensional flows in the compressor stator blade row with a standard Launder Sharma K-ε turbulence model.

The flow structures on the walls of the blade row have been extensively studied by traces of skin friction lines; this study of flow topologies is instrumental in the comprehension of flow separations. The singularities (critical points) are identified on the walls and the inter-relationship is explained by the topological rules established by Lighthill (1963), Délery [30], Tobak and Peake [31], etc. in case of flow separations. The overall analysis is satisfactory to serve the purpose of developing ideas of implementing flow control in the separated zones.

The advent of hub corner separation with a saddle point in the corner region is identified. Since the saddle point is the source of dividing streamlines that lead to flow separations, it is necessary to implement flow control in the vicinities of the saddle point.

Boundary layer aspiration increases the total pressure ratio by reducing the intensity of flow separations. The aerodynamic blockage is reduced and the exit flow angle is consequently reduced though at the expense of energy that must be compensated in re-utilizing the aspirated massflow.

Aspiration is implemented by an aspiration slot in the corner between the blade suction surface and the hub wall. The influence of aspiration is sensitive to the aspiration flow rate, higher flow rate improves control of flow separation and lower flow rate has a negative effect as it may amplify hub corner separation. The flow topology studies show complex three dimensional flow structures; there is recirculation of flow from aspiration cavity to the blade passage due to weak depression in the cavity. We draw an important conclusion that for the given blade row with the implemented aspiration strategy, it is critical to ensure a strong depression in the aspiration cavity to suppress corner separation.

Increasing the suction coefficient by a factor of two, we demonstrate that the hub corner separation can be suppressed at the highest loss point. Considering the impact of a very high suction flow rate on the global performance of the engine, we do not recommend this strategy. Since, we identified the saddle point in the corner to be the origin of two dividing streamlines on the hub wall and the suction surface respectively as the lines of separation; we extend the hub slot upstream to aspirate the saddle point. The study shows the strategy to be ineffective as the saddle point is displaced further upstream. We draw a conclusion that it is unadvisable to implement aspiration very close to the leading edge of the blade due to the destabilizing effects in this zone.

We apply the Stall indicator and Diffusion parameter by Lei et al. [14] to quantify the hub corner separation on our case. Our results are coherent with the critical limit of the hub corner stall established by the researchers. We recommend using these parameters as design guidelines to have notions of the development of corner separation based on the geometric characteristics of the blade.

The concept of hub aspiration has been studied experimentally at EPFL. With some hypothesis in modelling, the numerical simulations are re-done with the experimental inlet conditions and the results are compared.

The comparison of CFD results with experiments yields good correlation from hub wall to 60% span for most of the configurations studied. In particular, the extent of the hub corner separation is properly reproduced (numerically) at most of the incidence angles. The numerical modelling with chimera mesh is capable of predicting the flows without and with aspiration at hub wall reasonably well. The correlation is found to deteriorate in the zone close to the casing walls where CFD predicts stronger tip leakage vortex at casing wall than experiments. This makes CFD results pessimistic as compared to the experimental results with higher total pressure losses. This tip clearance effect is stronger when aspiration is performed at the hub, as it tends to displace the tip flow towards the hub.

The lower magnitude of endwall effects in experiments is a sign of encouragement for the integration of boundary layer aspiration in a real engine environment. If the experimental inlet conditions can be improved to match the inlet conditions of a real engine then boundary layer aspiration may offer substantial incentive with its potential benefits to integrate in a real engine compressor.

The CFD studies of blade profile aspiration is done by studying the influence of two large blade slots at 40% chord and 60% chord on the blade suction surface along with the hub slot. The results show that most of the improvement is achieved by improved diffusion on the suction surface of the blade. The flow at hub wall is not influenced very much except for some radial push generated by the blade slot on the suction surface. The slot located at 60% chord finally proves its advantages at the highest loss point where it has better control over the hub corner separation, as it is able to re-energize the low momentum separated flow rising in the blade passage from strong hub corner separation. This does not, however, completely eliminate the hub corner separation. The operating range of the blade row does not improve beyond α=65°.

The principle gain of blade profile aspiration (with hub aspiration) is noted in the reduction of total pressure losses: 28% lower losses over the baseline at $\alpha=65°$ as compared to 12% lower losses over the baseline with hub aspiration (but with twice the suction flow rate). Although the gain is important, we may consider the gain to be moderate when considering the complexity of the aspiration configuration to be integrated into the real engine environment.

We further investigate the optimisation of aspiration strategies by the study of flow topologies. The rationale is the implementation of aspiration on cores of flow separation presented by the critical points on the suction surface. This yields two configurations with smaller aspiration slots: first configuration with slot located on the focal point on the suction surface of the blade, second configuration with slot located on focal and saddle points respectively on the suction surface. Both the configurations yield similar results almost at par with the configurations of larger blade slots.

We demonstrate that it is possible to have smaller slot geometries with lower aspirated rates to achieve performance equivalent to those of larger blade slots with higher suction flow rates. Hence, we propose implementation of flow control on the location of critical points for better suppression of flow separation.

We recommend some future prospects:

We recommend employing a denser mesh to verify the non degeneracy criterion developed by Surana et al. [20, 32] on the entire flow field. Also, the effects of wall curvature have to be taken into account to ensure accurate values of critical points on the hub wall. This may ascertain the separation and re-attachment patterns of skin friction lines to provide finer understanding of flow separations. Such an approach may be instrumental to optimise the flow control strategies.

With respect to saddle point in the corner between the blade suction surface and the hub wall, it is recommended to develop a new aspiration strategy for the better control of hub corner separation. This includes a better study to understand the flow structure related to recirculation in the aspiration cavity.

When comparing experimental and numerical results, we are faced with limitations of accurately simulating complex three dimensional phenomena such as the hub corner vortex and the tip clearance vortex that are highly unsteady in nature. The RANS calculations with standard turbulence models are limited in their scope of reproducing highly separated flows. Such a task explicitly demands more sophisticated approach of employing LES (Large Eddy Simulations) or DES (Detached Eddy Simulations) techniques to perform unsteady flow simulations.

Towards the vision of an aspirated compressor, the next step would be to study the influence of aspiration on a complete compressor stage (such as Merchant et al. [5]). Aspiration can be implemented on a rotor and stator together or in one of the two depending upon the flow field. This may be achieved by designing blades optimised for aspiration to achieve higher performance with lower aspirated flow rates. (Dang et al. [8], Godard et al. [27])

As aspiration is done at the expense of energy, it is important to study the feasibility of re-utilising the aspirated massflow in the engine cycle. A system level study accounting for the recovery of aspirated massflow is indispensable. If aspiration is to be rendered feasible for implementation in a real engine environment, it is crucial to have lower pressure drops in the aspiration cavities.

9. APPENDIX

9.1 REFERENCES

[1] Loughery R, Horn JR R, Tramm P (1971) Single stage experimental evaluation of boundary layer blowing and bleed techniques for high lift stator blades, NASA CR 54573

[2] Kerrebrock J.,Reijnen D.,Ziminsky W., Smilg L. (1997) Aspirated Compressors, ASME Paper, 97-GT-525

[3] Kerrebrock J, Merchant A, Drela M, Schuler B (1998) A family of designs for aspirated compressors, ASME paper 98-GT-196

[4] Merchant A (2002) Aerodynamic design and performance of aspirated airfoils, ASME paper GT- 2002-30369

[5] Merchant A, Drela M, Kerrebrock J (2000) Aerodynamic design and analysis of a high pressure ratio aspirated compressor stage ASME paper 2000-GT-619

[6] Schuler B, Kerrebrock J, Merchant A, Drela M (2000) Design, analysis, fabrication and test of an aspirated fan stage, ASME paper 2000-GT-618

[7] Schuler B, Kerrebrock J, Merchant A (2002) Experimental investigation of an aspirated fan stage, ASME paper GT-2002-30370

[8] Dang TQ, Van Rooij MPC, Larosiliere LM (2003) Design of Aspirated Compressor blades using three dimensional inverse method ASME, paper GT-2003-38492

[9] Hubrich K., Bolcs, Ott P. (2004) Boundary layer suction via a slot in a transonic compressor – Numerical parameter study and first experiments, ASME paper GT2004-53758

[10] Kirtley K.R., Graziosi P., Wood P., Beacher B., Shin H.W. (2004) Design and test of an ultra-low solidity flow controlled compressor stator ASME paper GT-2004-53012

[11] Merchant A, Kerrebrock J, Adamczyk J, Braunscheidel E (2004) Experimental investigation of a high pressure ratio aspirated fan stage ASME paper GT-2004-53679

[12] Gummer V., Goller M., Swoboda M. (2005) Numerical Investigation of endwall boundary layer removal on highly loaded axial compressor blade rows ASME paper GT-2005-68699

[13] Chen F., Song Y., Chen H., Wang Z. (2006) Effects of boundary layer suction on the performance of compressor cascades ASME paper GT-2006-90082

[14] Lei V., Spakovszky Z., Greitzer E. (2006) A criterion for axial compressor hub corner stall ASME paper GT2006-91332

[15] Cumpsty N. (1989) Compressor Aerodynamics, Longman Scientific and Technical Publishing

[17] Gad-el-Hak. M., Flow Control. Cambridge University Press, 2000.

[18] Lakshminarayana B., Fluid Dynamics and heat transfer of turbomachinery. Wiley Interscience, 1996.

[19] Merchant A., MIT Thesis - Design and analysis of axial aspirated compressor stages, 1999.

[20] Surana A.,Grunberg O., Haller G. (2006) Exact theory of three-dimensional flow separation. Part1: Steady separation. Journal of fluid mechanics vol.564, pp. 57-106

[21] Gbabedo S., Cumpsty N., Hynes T. (2006) Interaction of tip clearance flow and three dimensional separations in axial flow compressors, ASME paper GT2006-90071

[22] Chakraborty U, Pradeep AM. (2008) Boundary layer control in a compressor cascade using distributed suction, ASME paper GT2008-50225

[23] Hergt A., Meyer R., Engel K (2006) Experimental investigation of flow control in compressor cascades, ASME paper GT2006-90415

[24] Wang S, Qiang X, Lin W, Wang Z (2008) A study of parameter selection principle and internal flow mechanism in a multi-stage low-reaction axial flow compressor, ASME paper GT2008-50554

[25] Gbabedo S, Cumpsty N, Hynes T. (2008) Control of three dimensional separations in axial compressors by tailored boundary layer suction, Journal of Turbomachinery January 2008, Vol. 130 / 011004-1

[26] Song Y, Chen H, Chen F, Wang Z (2007) Effects of air injection on performance of highly loaded compressor cascades, ASME paper GT2007-27062

[27] Godard A, Burguburu S, Leboeuf F (2007) Parametric study of an aspirated diffuser, ETC paper

[28] Gbabedo S, Cumpsty N, Hynes T (2004) Three dimensional separations in axial compressors, ASME paper GT2004-53617

[29] Lord W.K., MacMartin D.G., Tillman T.G. (2000) Flow control opportunities in gas turbine engines, AIAA paper AIAA 2000-2234

[30] Délery J.,(1999) Topologie des écoulements tridimensionnels décollés stationnaires: points singulilers, séparatrices et structures tourbillionaires, Rapport Technique ONERA, RT 121/7078 DAFE

[31] Tobak M., Peake D.J.,(1981) Topology of three dimensional separated flows, NASA-TM-81294

[32] Surana A., Jacobs G.B., Haller G.,(2007) Extraction of separation and attachment surfaces from three dimensional steady shear flows. AIAA Journal, Vol.45, No.6

[33] Sachdeva A., Leboeuf F., Touyeras A., Obrecht T.,(2008) Control of hub corner separation by boundary layer aspiration, Proceedings of the 43rd AAAF

[34] Anderson John D.,(2005) Fundamentals of Aerodynamics, fourth edition. McGraw Hill International.

[35] Study course in three dimensional turbomachinery flows and transonic flows in turbomachinery, Ecole Centrale de Lyon.

[36] E.Colombo (EPFL), P.Ott (EPFL), F.Bario (ECL) (2008) NEWAC internal report Deliverable D5.3.1B; Test report of the first configuration without aspiration.

[37] L.Cambier, M.Gazaix (ONERA), (2002), 40th AIAA Aerospace Science meeting and exhibit, Reno, USA

9.2 TABLE OF FIGURES

9.3 TABLE OF TABLES